QUANTITATIVE MOLECULAR PHYSIOLOGY AT ACTIVE ZONES OF CALYCEAL SYNAPSES IN THE AUDITORY PATHWAY

DISSERTATION

for the award of the degree

"Doctor rerum naturalium" (Dr. rer. nat)

of the Georg-August-Universität Göttingen

within the doctoral program

International Max Planck Research School for Neurosciences

of the Georg-August University School of Science (GAUSS)

submitted by

THEOCHARIS ALVANOS

from Athens, Greece

Göttingen, 2022

THESIS COMMITTEE:

Prof. Dr. Tobias Moser

Institute of Auditory Neuroscience & InnerEarLab, University Medical Center Göttingen

Prof. Dr. Silvio Rizzoli

Dept. of Neuro- and Sensory Physiology, University Medical Center, Göttingen

Prof. Dr. Dr. h.c. Erwin Neher

Dept. of Membrane Biophysics, Max Planck Institute for Multidisciplinary Sciences, Fassberg Campus, Göttingen

MEMBERS OF THE EXAMINATION BOARD:

1st Reviewer: Prof. Dr. Tobias Moser

Institute of Auditory Neuroscience & InnerEarLab, University Medical Center Göttingen

2nd Reviewer: Prof. Dr. Silvio Rizzoli

Dept. of Neuro- and Sensory Physiology, University Medical Center, Göttingen

FURTHER MEMBERS OF THE EXAMINATION BOARD:

Prof. Dr. Nils Brose

Dept. of Molecular Neurobiology, Max Planck Institute for Multidisciplinary Sciences, City Campus, Göttingen

Prof. Dr. Ralf Heinrich

Dept. of Cellular Neurobiology, Schwann-Schleiden Research Centre, Göttingen

Prof. Dr. Martin Göpfert

Dept. of Cellular Neurobiology, Schwann-Schleiden Research Centre, Göttingen

Date of oral examination: November 22nd 2022

"The important thing is not to stop questioning. Curiosity has its own reason for existence. One cannot help but be in awe when he contemplates the mysteries of eternity, of life, of the marvellous structure of reality. It is enough if one tries merely to comprehend a little of this mystery each day"

- Albert Einstein

"Every man, if he so desires becomes sculptor of his own brain"

- Santiago Ramón y Cajal

"Of course it is happening inside your head, Harry, but why on earth should that mean that it is not real?"

- J.K. Rowling

To my family and friends and to never-ending curiosity

Contents

Abstract

Bushy cells (BCs) of the anteroventral cochlear nucleus (aVCN) are the first relay station of ascending auditory information. Sound is transformed from mechanical to electrical stimuli by the inner hair cells of the cochlea and transmitted to the auditory brainstem by spiral ganglion neurons (SGNs). To enable consistent firing of Bushy cells, auditory nerve fibers, arising from SGNs terminate on BCs with large calyceal axosomatic endings, called the endbulbs of Held. Since BCs are tuned to respond with short action potentials, phase lock and entrain to the sound stimulus, endbulbs display pronounced short term depression and fast recovery which allow fast sound-onset coding and consistent synaptic transmission even at high frequencies, produced by high sound intensities. These properties are important for the localization of sound in the azimuth plane and BCs are connected with other nuclei of the auditory brainstem to enable these computations, which crucially depend on precise timing. This thesis sheds new light on the molecular composition of pre-synaptic endbulb active zones and how it is connected with their unique physiology. It also investigates how the auditory system can be modulated by hormone-like neurotransmitters, that are released in a brain-wide fashion and, importantly, are able to tweak the molecular properties of calyceal synapses and active zones of the auditory pathway, affecting physiology.

First, collaborators and I studied synaptic transmission and the cytoarchitecture of mouse endbulb terminals from RIM-BP2 constitutive knockout (KO) mice (See Chapter 1 and Appendix). RIM-BP2 is a protein that belongs to the pre-synaptic cytomatrix of the active (CAZ) and interacts with other members of the CAZ forming a network of interactions that are important for the function of active zones. In its absence, endbulbs of Held elicit smaller evoked post-synaptic currents unto BCs, their synaptic vesicle (SV) release probability (P_{vr}) was reduced and the replenishment rate of new SVs was slower. These effects altered the characteristic endbulb short-term plasticity (STP), especially at higher stimulation frequencies. The effect of RIM-BP2 deficiency on STP was rescued by applying high extracellular Ca^{2+} concentrations. Recovery from SV pool depletion was slower in the KO, which was corroborated by the presence of less SVs close to the pre-synaptic plasma membrane, observed with electron tomography. Immunofluorescence imaging experiments showed that the levels of other CAZ proteins were unaltered at KO endbulbs, but the distance between Ca^{2+} channels and core CAZ components was increased, disrupting the pre-synaptic terminal's cytoarchitecture. We postulate a role of RIM-BP2 in controlling the distance between the SV release machinery and Ca^{2+} and additionally promoting SV tethering and priming, increasing endbulb P_{vr}, possibly through interactions with Munc13-1.

Second, the effects of monoamines on the mouse endbulb of Held synapse were studied, with a focus on mechanisms of pre-synaptic neuromodulation. Immunofluorescence imaging of aVCN slices

revealed pronounced innervation of the lower auditory pathway by noradrenergic and serotonergic fibers, while the presence of dopamine was not as prominent, consistent with existing literature on other rodents and cats. Preliminary experiments with monoamine receptor blockers show that baseline transmission is important for setting up synaptic properties by regulating the amplitude, frequency and kinetics of spontaneous neurotransmitter release events. Evoked release was not similarly affected by the blockers. Application of monoamine receptor agonists, especially norepinephrine (NE), altered the short-term plasticity of endbulbs, reducing P_{vr} and variability of evoked release, while it slowed down the recovery from SV pool depletion. We cautiously interpret these preliminary results, and consider a role of NE in reducing STD and post-synaptic receptor desensitization at endbulbs, promoting onset coding through convergence of subthreshold inputs on BCs.

General Introduction

Imagine yourself standing for a moment to contemplate the beginning of your next adventure. A hike, you've been organizing and preparing since a long time. You set off and the novelty of the Unexplored fills you with excitement. You know, already, that the return trip will feel shorter. Fast forward and you're almost at the end, climbing through a dangerous part of the track. You struggle for a while, your brain floods with noradrenaline, your focus becomes razor-sharp and with careful, co-ordinated movements, engaging all your faculties, you manage to pull through and finish the hike. A sense of accomplishment kicks in as you take a few quick breaths and reach for water, feeling it taste better than it ever did, the subtle effects of serotonin and dopamine starting to spread through your brain. As you relax, an increase in serotonin gives you a surge of gratefulness and you start appreciating the magnificent view, relishing the harmonious beauty of nature all around you. "Is this the point, when inspiration visits us?", you ponder. "It must be at this point, when poetry crystallizes in the poet's thoughts".

We humans, like all animals have the uncanny ability to accurately perceive and interpret the vast world of stimuli around us in ways that guarantee our survival against all odds. On top of that, we are curious, grateful, appreciative, we get excited by novelty and get a kick out of small doses of danger, even though we have overcome many of the challenges to our survival. We owe all of that to the most complicated biological computer, our brain, comprised of billions of tiny processing units, its constituent cells, the neurons. No rudimentary assembly of neurons could be the basis of the incredible complexity that is our human experience. But, when wired together, through special connections called synapses, the possibilities for complex computations become endless. So much so, that today, 128 years since Santiago Ramón y Cajal declared: "The ability of neurons to grow in an adult and their power to create new connections can explain learning", modern neuroscientific research continues to uncover new knowledge about the brain, its neurons and their synapses.

Aim of the study

This study aims to further the knowledge of how synapses transfer signals between neurons with high precision, through the interaction of many tiny molecular machines, called synaptic proteins. One of these is the pre-synaptic protein RIM-Binding Protein 2 and the first part of my study focuses on the consequences of its deletion on the function of synapses in the auditory pathway.

Hormone-like neurotransmitters called neuromodulators are secreted throughout our brain and modulate its activity and connectivity. A very famous neuromodulator is serotonin (5-HT). When we feel pleased or grateful, there is a surge of 5-HT in our brain. Our alertness, on the other hand, our readiness to respond to challenging situations, owes its existence to norepinephrine (NE). Some

synaptic proteins that enable neurons to communicate are subject to changes caused by these neuromodulators. The second part of this study aims to dissect the effects of neuromodulation of pre-synaptic terminals in the auditory pathway by 5-HT and NE.

Neuronal, excitability and synaptic transmission

Neurons and glial cells are the building blocks of the brain. While, glial cells are responsible for maintaining neurons healthy and assist with their metabolism, it is the neurons' purpose to generate and transmit electrical signals along short and long distances to specific points of connection within the brain or body. Neurons have distinct anatomical features and are usually comprised of a cell body, dendrites and an axon. Both the dendrites and the axon display different levels of arborization, a feature that serves to classify neurons in neuronal subtypes or cell-types that serve distinct functions in different neuronal networks (Fig. 1 A – C). The axons of some neurons are enveloped by consecutive segments of a thick, multi-layered sheath, which contains high amounts of myelin and is aptly named the myelin sheath. This sheath is maintained by glial cells and its purpose is to insulate the axon of the neuron, enabling electrical signals to travel with high velocity through long distances (Fig. 1D). Neurons produce electrical signals by allowing the flow of Na^+ and K^+ ions through specialized voltage- gated channels (Hodgkin, 1948; Hodgkin and Huxley, 1952b, 1952a; HODGKIN and HUXLEY, 1952; Hodgkin et al., 1952), called Na_Vs and K_Vs respectively. The equilibrium potential for Na^+ is higher than the resting membrane potential. Thus, when Na_Vs open, in response to the arrival of a suprathreshold depolarizing pulse, which raises the membrane potential (V_m) (Fig. 2 A), a large amount of Na^+ is allowed to flow in the cytosol, further raising the V_m to a peak value of +40mV. This causes the opening of K_Vs, which, since the equilibrium potential is lower than +40, causes K^+ to move out of the cell, pushing the V_m back, to values more negative than the resting potential (close to the equilibrium potential for K^+). The process is reversed, and the V_m returns to its value at rest, through the function of resting K^+ conductances and the Na^+/K^+ ATPase (Skou and Hoffman, 1998), which consumes 1 molecule of adenosine tri-phosphate (ATP), the universal energy currency to actively transport 3 Na^+ ions out of the cell and 2 K^+ inside the cytosol.

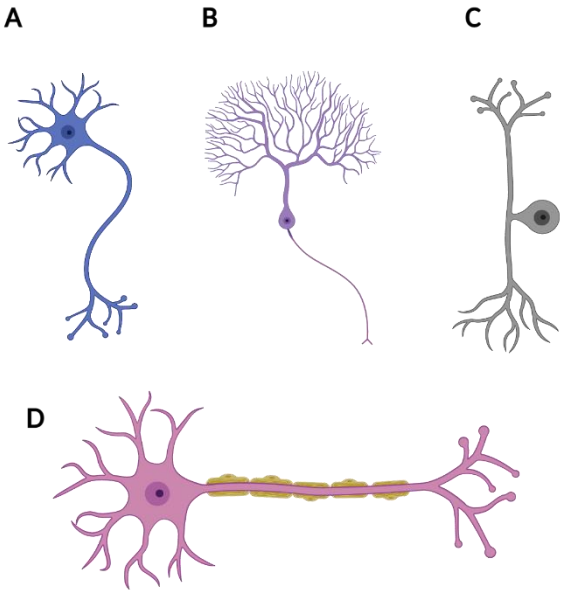

Figure 1: Anatomical diversity of Neurons. A: Motor neuron. B: Purkinje Cell. C: Pseudo-unipolar spinal cord neuron. D: Long projecting neuron with myelinated axon. *Created with Biorender.*

This signal was named the Action Potential (AP) and the pciscrocess that generates it is referred to as “firing”. An AP is fired in an all or nothing fashion once the firing threshold is exceeded and is, in essence, a change in the polarity of the neuronal membrane. A high concentration of Na_Vs is found at the axon-initial segment, at the axon hillock. The AP is generated there, by the integration of subthreshold depolarizing signals arriving through the dendrites or, in auditory synapses, for example, from synaptic inputs directly to the soma. After travelling through one neuron’s axon, it reaches the axon terminals where, through the synapses, it transfers information to a connected neuron. This process is called synaptic transmission.

Electrical synapses

A synapse is a modified point of contact between neurons. Electrical synapses (Fig. 2) allow the bidirectional transfer of an AP from the pre- to the post-synaptic neuron and vice versa. This is enabled by gap junctions (Payton et al., 1969), which consist of many neighbouring connexons. Each connexon is built up as a hexamer of connexins, a family of proteins with more than 20 isoforms in humans and mice (Chi et al., 2008; Connors and Long, 2004; Goodenough, 1974; Henderson et al., 1979). Two connexon hemichannels, one anchored to the pre- and the other to the post-synaptic neuron’s membrane, connect to form a gap-junction channel which links the two cytosols, enabling the flow of ions between the two neurons. Apart from ions, metabolites also get transported through gap-junctions. The distance between the pre- and post-synaptic membranes that comprise an electrical synapse is approximately 2-3 nm (Connors and Long, 2004). Electrical synapses are very reliable in transmitting not only APs, but also subthreshold ionic currents. As such, they are important for the shaping of activity in developing neural networks, by propagating rhythmic patterns of electrical activity and increasing the synchronicity of neighbouring neurons (Hormuzdi et al., 2004; Pereda, 2014). In leech embryos, blockade of electrical synapses between known interacting neurons of a specific behavioural circuit, prevented the sequential formation of chemical synapses between them (Marin-Burgin et al., 2005). Finally, while signalling through electrical synapses is reduced in the adult

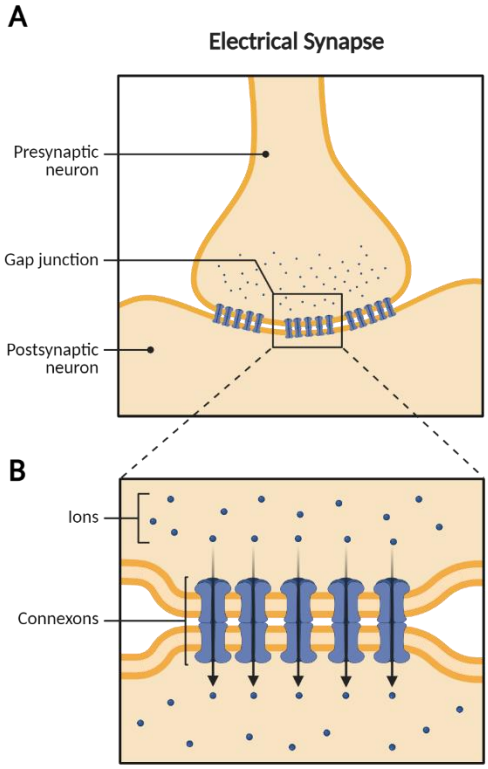

Figure 2: The Electrical Synapse. A: Pre-synaptic terminal contacting the post-synaptic neuron. Connexons provide stability and cytoplasmic continuity between the two neurons B: Zoomed in point of contact. *Created with Biorender.*

mammalian brain, both synapse types may co-exist in adjacent or even the same synaptic terminal of a single neuron's axon (Pereda, 2014; Hormuzdi et al., 2003).

Chemical Synapses

In the adult brain most of the communication between neurons is taken over by chemical synapses. Chemical synaptic transmission occurs through the release of neurotransmitters, which are packaged in small spherical structures, that are ~ 40nm in diameter and made up of a phospholipid bilayer and multiple proteins (Takamori et al., 2006), the synaptic vesicles (SVs). Neurotransmitters are organic compounds, many of which are common amino acids like the excitatory neurotransmitter glutamate. Some others are modified versions of amino acids like γ-aminobutyric acid (GABA), which is synthesized from glutamate and is a common inhibitory neurotransmitter throughout the nervous system. Neurotransmitters are released in the 20 – 50 nm wide synaptic cleft, the intercellular space between the pre- and post-synaptic neuron and exert their action by binding to post-synaptic receptors. These receptors are integral membrane proteins of the post-synaptic neuron's membrane (Fig. 3) and are usually comprised of chemically gated ion channels that, upon binding the neurotransmitter allow the flow of cations or anions into the cytoplasm, exciting or inhibiting the neuron respectively.

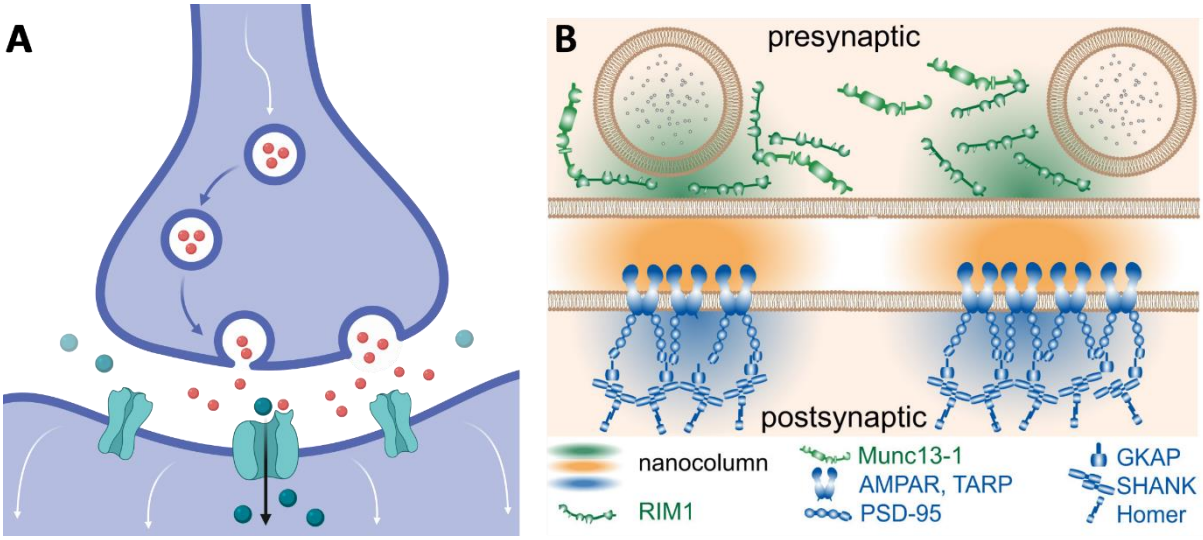

Figure 3: The Chemical Synapse. A: Graphic that depicts the pre- and post-synaptic compartments of a chemical synapse during neurotransmitter release (red spheres). Note the ions (green spheres) that enter the post-synaptic cytoplasm through the receptors after neurotransmitter binding. *adapted from biorender* B: Illustration that shows how pre-synaptic SV release sites are apposed in alignment to post-synaptic receptor clusters. *Image adapted from Biederer, Kaeser et al., 2017*

Complex molecular machinery orchestrates the coordinated release of neurotransmitter in response to an AP, its recovery from the synaptic cleft, the maintenance and turnover of receptors on the post-synaptic membrane and the accurate placement of SV release across the post-synaptic receptors by trans-synaptic signals. Trans-synaptic signalling, consists of interactions between proteins

that anchor to either the pre- and/or post-synaptic membrane and their specific interaction partners across the synaptic cleft. It has been suggested that this trans-synaptic signalling maintains an alignment of pre-synaptic release hot-spots, called active zones (AZs), with post-synaptic receptor island membrane patches that appear dense in an electron microscopy image and are thus named post-synaptic densities (PSDs). This transcellular nano-alignment of synaptic function gives rise to trans – synaptic structures called nanocolumns and ensures the efficiency and reliability of chemical synaptic transmission (Biederer et al., 2017; Tang et al., 2016).

Let us liken chemical transmission to an exchange in the market. If a neuron's type of neurotransmitter is its currency and the total amount of transmitter is the budget, then the coin would surely have to be the content of a single SV. Synaptic transmission occurs in quanta (del Castillo and Katz, 1954). Each quantum can be measured as the post-synaptic current (PSC) generated in response to the fusion of a single SV, also called a mini or a miniature PSC (mPSC). Minis are generated from spontaneous SV fusion and do not result in a post-synaptic current summation that could generate an AP. For the evoked fusion of SVs, voltage gated Ca^{2+} channels (VGCCs or Ca_Vs) are involved, which are placed very close to SV release sites inside AZs. With the arrival of an AP at the pre-synaptic membrane, the plasma membrane gets depolarized resulting in the opening of VGCCs. The influx of Ca^{2+} inside the cytosol creates a transient domain, a sharp gradient of high Ca^{2+} concentration in a limited area around intracellular side of the channel's pore. A family of proteins called Synaptotagmins (further explained below) act as Ca^{2+} sensors and can induce the fusion of the SV and plasma membrane bilayers, resulting in the release of neurotransmitter in the synaptic cleft, and the generation of large evoked excitatory post-synaptic currents (eEPSCs). The time needed from the arrival of the pre-synaptic AP until the generation of the eEPSC is called the synaptic delay and can vary between chemical synapses. On average, partially due to mammals' high body temperatures, chemical transmission is characterized by sub-millisecond synaptic delays. This may largely diminish the advantage in speed that is a feature of electrical transmission (Bennett, 2000) making chemical transmission the prevalent mode of information transfer between neurons.

Ca^{2+} triggered, synchronous SV release is not the only existing mode of transmitter release (Kaeser and Regehr, 2014). The minis that were mentioned above represent another mode called spontaneous transmitter release. In the presence of the Na_V blocker TTX, or in the exposure to extracellular solution containing high Mg^{2+} and no Ca^{2+}, spontaneous release persists. It has been proposed, that spontaneous release, being unable to elicit post-synaptic APs, may have a role in maintaining a baseline activity in synapses that prevents the reduction of synaptic strength or the total detachment and degradation of the pre- and post-synaptic compartments of the synapse. Perturbation of spontaneous release alters the extension pattern of axonal growth cones during development, thus suggesting that spontaneous release constitutes a chemotactic signal for the wiring of emerging

neuronal circuits (Andreae and Burrone, 2018). Asynchronous release is the other mode of release that shares the same SV fusion machinery, has a Ca^{2+} dependence, but occurs usually with a fluctuating synaptic delay or in the aftermath of a synchronous release event. Its Ca^{2+} regulation differs from synchronous release in that it is mediated by Synaptotagmin-7 (Weyrer et al., 2021) instead of Synaptotagmin-1. Doc2s have been identified as crucial factors that mediate Ca^{2+} independent, spontaneous release (Pang et al., 2011). Whether these molecular identifiers can divide all the available vesicles of a terminal into separate modes of release or characterize separate vesicle pools has remained a topic of intense debate. Two different schools of thought have supported, on one hand, that different pools of vesicles contribute to these three modes of neurotransmitter release (Fredj and Burrone, 2009; Sara et al., 2005) and, on the other hand, that the same pool of SVs contributes to all three (Groemer and Klingauf, 2007; Wilhelm et al., 2010; Yang and Xu-Friedman, 2010)

Synaptic vesicle cycle and exocytosis

Synapses are highly active parts of neurons that are often located very far from the cell body and main volume of cytoplasm. It stands to reason, that new functional proteins are needed after many rounds of synaptic activity, which cause wear and tear to the release machinery. SVs themselves are complex secretory organelles that contain a multitude of transmembrane and membrane associated proteins (Takamori et al., 2006). There is, in fact, constant antero- and retrograde flow of cargo, consisting of both SVs and AZ proteins (Juranek et al., 2021), between the synaptic terminals and the cell body, which is necessary for the maintenance of synaptic function and neuronal health.

Neurotransmitter filling and vesicle fusion machinery

SV precursors are generated in the trans Golgi network and trafficked to the synapses via microtubules thanks to the activity of kinesins (Okada et al., 1995). In the case of glutamatergic central synapses, the SVs contain the vesicular glutamate transporter (vGLUT), a multifunctional protein that displays a proton pump ATPase activity, with which it acidifies the SV lumen. VGLUT1, which is found in many central neuronal synapses, generates a proton gradient, which it itself uses to act as a glutamate/proton exchanger. VGLUT1 was recently associated with a channel-like Cl^- conductance (Martineau et al.). It appears that, apart from acidification and proton-gradient- driven refilling, VGLUT1 additionally removes Cl^- from the SV lumen, generating a chloride gradient that can be used by glutamate/Cl^- co-transporters to assist with SV refilling and Cl^- clearance from the intracellular compartment. It has been postulated that some molecular mechanism can regulate the process of vesicle re-filling, which can alter the amount of glutamate in each SV, change the size of the quantum and affect synaptic strength.

Once SVs reach the synapse they are tethered to AZs and then docked, which brings them very close to the plasma membrane of the active zone through several protein-protein interactions. The process of priming follows, during which SVs attain fusogenicity and become release-ready. SV exocytosis is mediated by a family of proteins called **S**oluble **N**-ethylmaleimide-sensitive factor (**N**SF) **A**ttachment **Re**ceptor proteins (SNAREs), which undergo association/disassociation cycles to enable membrane fusion. These proteins contain long α-helical domains and can be subdivided in the vesicular SNAREs (vSNAREs), namely Synaptobrevin or VAMP-2 (1 α-helix) and target SNAREs (tSNAREs), which are syntaxin-1 (1 α-helix) and soluble N-ethylamide factor attachment protein 25 (SNAP-25, 2 α-helices). At the synapse, Synaptobrevin forms a trans-SNARE complex with syntaxin1 and SNAP-25 in a process that has been described as the zippering of the α-helical domains of SNAREs (Söllner et al., 1993). This process exerts the necessary force that pushes the two lipid bilayers together and overcomes the energy barrier for membrane fusion. After fusion, the N-ethylamide sensitive fusion protein (NSF) binds and enzymatically unwinds the trans-SNARE complex thanks to its AAA ATPase activity. In chromaffin cells, it was determined that 3 trans-SNARE complexes need to be formed for the fast fusion of one secretory vesicle (Mohrmann et al., 2010).

Orchestration of fusion: α-SNAPs, NSF, Munc18s & Munc13s

The orchestration of SV fusion is a complicated process that involves many multi-domain proteins. Each of them is connected with other proteins through various domain – domain interactions and binding affinities to cumulatively control trans-SNARE complex assembly and disassembly. As was mentioned above, NSF forms a complex with zippered SNARE proteins and catalyzes their disassembly. A reasonable question is how it gets localized in the SNAREs' vicinity. A protein that can bind cis-SNARE complexes between syntaxin-1 and SNAP 25, called α-SNAP (Fig. 4 B1) is responsible for guiding NSF to active zones (Ma et al., 2016; Winter et al., 2009). These α-SNAP – cis-SNARE complexes are formed after SV fusion and α-SNAP facilitates their disassembly (Fig. 4 B2) (Söllner et al., 1993). NSF – α-SNAP complexes were introduced to preparation of re-constituted liposomes in solution and were able to completely inhibit liposome fusion. α-SNAP alone could mediate this inhibition, partially because it binds syntaxin – SNAP25 dimers and partially because it binds pre-formed trans-SNARE complexes and stabilizes them. Halting fusion before the AP dependent influx of Ca^{2+} is a duty that α- SNAP shares with Munc18s, Munc13s, Synaptotagmins and complexins.

In the absence of Munc13s and Munc18s, fusion would not be possible. SV priming involves the partial zippering of trans-SNARE complexes, which are exposed to unwinding by the omnipresent NSF – α-SNAP duet and need to be protected by stabilizing factors (Rizo, 2022). Many colleagues entertain the notion that Munc18-1 and Munc13s are master regulators of Ca^{2+} triggered release. The undeniable fact is, that in the absence Munc18-1, synaptic transmission is abolished and neurons start

to degenerate (Verhage et al., 2000). Similarly, the deletion of Munc13s 1&2 or the Unc-13 invertebrate homologue completely blocks neurotransmitter release (Aravamudan et al., 1999; Varoqueaux et al., 2002; Verhage et al., 2000). Munc18-1 is a member of the Sec1/Munc18-1 (SM) family of proteins that are required for all forms of SNARE-dependent membrane trafficking. Its four domains (D1, D2, D3a and D3b) form an arch-like shape and a small cavity. That cavity mediates the direct binding of the closed conformation of syntaxin-1 (Dulubova et al., 1999; Misura et al., 2000; Rizo, 2022), which gives Munc18-1 its function of preventing the zippering of the SNAREs, by keeping syntaxin-1 closed (Fig. 4 B3). It has been suggested that Munc18-1 also acts as a template for SNARE zippering, because it can directly bind VAMP-2 (Parisotto et al., 2014; Xu et al., 2010). In liposomes, it was shown that the zippering of SNAREs and liposomal fusion proceeded unimpeded in the absence of Munc18-1 (Weber et al., 1998). In liposomes that were reconstituted with VAMP-2, syntaxin-1 – SNAP25 pre-complexes and Synaptotagmin-1, which stimulates fusion, introduction of NSF and α-SNAP abolished fusion, while the introduction of soluble C-terminal fragments from of Munc18-1 and Munc13-1 rescued the liposomes' ability to fuse (Liu et al., 2016; Ma et al., 2013).

Among Munc13s, Munc-13-1 is the dominant, most abundant isoform in the CNS. Its N-terminal region contains a C_2A domain, and a calmodulin binding sequence (Junge et al., 2004). Its C-terminal region contains a diacylglycerol (DAG) binding C1 domain, a MUN domain and two C_2 domains, C_2B and C_2C (Basu et al., 2007; Pei et al., 2009; Rhee et al., 2002). Like molecular coincidence detectors, C_2 domains gain a high affinity for phospholipids after binding 2 Ca^{2+} ions (Rizo and Südhof, 1998). In the case of Munc13-1, however, only its C_2B domain's activity is intact, binding Phosphatidylinositol 4,5-bisphosphate (PIP_2), a phospholipid that is enriched in neuronal plasma membranes, upon Ca^{2+} entry (Shin et al., 2010). The C_2C domain can also bind to membranes in a Ca^{2+} dependent manner, albeit very weekly (Quade et al., 2019), in contrast to the C_2B. The C_2A domain has the ability to form a Munc13-1 homodimer, by binding to its counterpart, or to form a heterodimer with Rab3 Interacting Molecules, RIMs (Dulubova et al., 2005; Lu et al., 2006). The MUN domain exhibits a remarkable structural similarity to yeast vesicle tethering factors (Li et al., 2011). It can strongly bind the Munc18-1 – suntaxin-1 and Munc18-1 – syntaxin-1 – VAMP-2 complexes with higher affinity for the latter than the former and was, thus, ascribed the role of opening syntaxin-1 to enable trans – SNARE assembly (Ma et al., 2011; Richmond et al., 2001; Wang et al., 2017; Yang et al., 2015). It has been postulated that Munc13-1 can bridge the two bilayers of the SV and plasma membranes (Fig. 4 B4) and, through conformational changes upon exposure to Ca^{2+}, mediate an increase in proximity between them (Fig. 4 B5), while facilitating the zippering of SNAREs (Rizo, 2022).

Regulation of Ca^{2+} triggered release: Synaptotagmins and complexins

Before the entrance of Ca^{2+}, as the trans-SNARE complexes are partially zippered and protected from NSF, the barrier for fusion has become very small and the slightest fluctuation of the intracellular Ca^{2+} concentration can overcome the energy barrier towards fusion. The process described here as priming, or in molecular terms, partial trans-SNARE complex assembly has a morphological correlate, observed by EM tomography studies which is called docking (Imig et al., 2014). The regulation of Ca^{2+} evoked release is a task handled partially by Synaptotagmins, proteins with tandem C_2 domains in their cytoplasmic regions, a C_2A and a C_2B domain. Synaptotagmin-1, an example neuronal Synaptotagmin is associated with the SV membrane and can bind the SNARE complex through its C_2B domain. The details of this interaction have been the focus of a number of studies, some suggesting that a polybasic region of the C_2B binds an acidic region of the SNARE complex (Brewer et al., 2015) and others indicating the formation of a primary interface with the SNARE complex by two regions of the C_2B domain (Zhou et al., 2015). Experiments with nanodiscs, containing SNARE complexes anchored on PIP2 and phosphatidyl serine (PS), showed that in the absence of Ca^{2+} the C_2AB binds to SNAREs via the aforementioned primary interface (Voleti et al., 2020). In the absence of Synaptotagmin-1 synchronous release is impaired, but spontaneous release is increased, an increase that is sensitive to the knockdown of Synaptotagmin-7 (Bacaj et al., 2013). It appears that Synaptotagmins compete for Ca^{2+} binding and that the relative amount and positioning of different isoforms relative to the Ca^{2+} channel clusters might be a way to regulate the relative contributions from different modes of release.

One of the protein families that have instigated intense debate around their precise function are complexins, a group of small soluble proteins that bind the SNARE complex with high affinity (McMahon et al., 1995). It was proposed that complexins “clamp” SVs before fusion, stabilizing trans-SNARE complexes at an all but completely zippered state preventing them from mediating fusion before the entry of Ca^{2+} (Melia, 2007). This function of complexins is thought to underly the high degree of synchronicity that Ca^{2+} evoked transmitter release displays at many synapses. The deletion of all 3 isoforms, complexins-1,2,3, decreased the probability of SV release (P_{vr}) at both excitatory and inhibitory synapses in the mouse brain (Xue et al., 2008). Hearing in mice was impaired when complexin-1 was deleted, but triple knock – out (tKO) mice for complexins 2,3 and 4 as well as 3,4 double KOs (dKOs) exhibited normal hearing (Strenzke et al., 2009). Synaptic transmission at the endbulb of Held synapse became less reliable in the absence of complexin-1, peak firing rates of post-synaptic bushy cells in the cochlear nucleus were reduced and the variability of first spike latencies was increased, impairing synchronized transmission and reliable transfer of auditory information. Similar results, namely aberrant action potentials of the post-synaptic neurons and increased asynchronous release, were reported at the calyx of Held synapse after deletion of complexin-1 (Chang et al., 2015).

In another study, the C-terminal sequence of complexin-1 was introduced in cultured complexin-1 KO neurons and could assist Synaptotagmins in priming SVs and clamping their fusion, but it was not able to fulfil its postulated role of activating Synaptotagmin for Ca^{2+} evoked release (Kaeser-Woo et al., 2012). Autaptic neuron cultures from the mouse forebrain and mass cultured hippocampal neurons were subjected to acute genetic perturbation of complexin-1. In these experiments, the absence of complexin did not unclamp spontaneous release, but reduced overall P_{vr} and partially suppressed all modes of neurotransmitter release (López-Murcia et al., 2019). The conclusion from the forebrain neuron experiments was that complexins are facilitators of SV fusion, but are dispensable for clamping it. Finally, it was recently reported that accessory helix of complexin-1 binds the SV membrane proximal regions of VAMP2 and SNAP25 in the partially formed trans-SNARE (Fig. 4 B6) complex and prevents spontaneous SV fusion (Malsam et al., 2020).

The last milliseconds before evoked release

Multiple attempts to develop a model consolidating the plethora of interactions between separate domains of Synaptotagmins, SNAREs and complexins have fallen short of the challenge. Newly emerging data have continuously thwarted the establishment of the sequence of events following Ca^{2+} entry at the pre-synaptic terminal. The binding of C_2AB to the SNARE complex that is anchored on PS and PIP2 rich nanodiscs appears to be the dominant version of what takes place in the absence of Ca^{2+} (Brewer et al., 2015; Rizo, 2022). This binding is likely to be mediated by the primary interface allowing the C_2B's polybasic region to bind to PIP_2. This view is compatible with an arrangement of complexin that binds to the SNARE complex and extends its accessory helix to bind the SV membrane bound regions of VAMP2 and SNAP25, preventing the final step of trans-SNARE complex formation (Fig. 4 B7, B8). A cryo-EM study supports this notion, suggesting that Synaptotagmin-1 releases the SNARE complex upon the binding of Ca^{2+} (Grushin et al., 2019) and binds to the plasma membrane (He et al., 2017a).

Synaptic vesicle cycle and endocytosis

Synapses undergo SV exocytosis at rates much higher than the rate of arrival of new SV precursors from the cell body. The continuous activity displayed by synapses has to be sustained by some mechanism of SV recovery. This process is called endocytosis and involves, essentially, the emergence of an SV that, in a regulated fashion buds-off and gets snipped from a larger source of membrane, like an organelle or the plasma membrane itself. After SV fusion, the release site may be inaccessible to new vesicles, limiting the rate of SV exocytosis until the fused SVs membrane and proteins are laterally cleared (Neher, 2010) towards pre-synaptic membrane patches that surround the AZ, called the peri-active zones (Haucke et al., 2011; Rizzoli, 2014; Watanabe et al., 2013). There

endocytosis can proceed without impeding the fusion of new vesicles during sustained activity. The SV then will get acidified, refilled with neurotransmitter and undergo the aforementioned priming steps to regain its fusogenicity. The distinct endocytic pathways that an SV may take (Fig. 5) have fueled intense debate over decades. Depending on the level of activity of a synaptic terminal, structurally and molecularly distinct mechanisms of membrane retrieval are called upon to handle the task of re-generating SVs. Using a variety of methods (reviewed in Saheki and De Camilli, 2012), these mechanisms have been identified as morphological correlates of different endocytic pathways. These include clathrin-mediated endocytosis, kiss-and-run, bulk endocytosis, ultrafast and clathrin independent endocytosis.

Clathrin and its major adaptor protein 2 (AP-2) are involved in the formation of clathrin coated pits, invaginations of membrane that are enveloped by the clathrin lattice. This chicken-wire-like structure is made up of many trimers of clathrin heavy chains with three bound light chains, called the clathrin triskelia (McMahon and Boucrot, 2011). The initial membrane curvature is made possible by the action of BAR domain containing proteins like endophilin, amphiphysin, SNX9/SNX18 and tuba (Itoh and De Camilli, 2006; Milosevic et al., 2011). This is a pre-requisite for the recruitment of clathrin triskelia around the budding vesicle. Clathrin was initially regarded as being necessary for the entire process of endocytosis, but it was later shown that the clathrin coat is removed from the SV by endophilin, immediately after it separates from the plasma membrane (Milosevic et al., 2011). The invaginating membrane that generates the SV forms a neck that is connected to the plasma membrane and needs to be severed for the completion of the process. This function is performed by dynamin which polymerizes around the neck and exerts the necessary force to separate the two membrane bilayers for the completion of endocytosis. A number of auxiliary factors maintain a uniform size and protein content of SVs in synaptic terminals, binding all the necessary proteins before they diffuse from the plasma membrane in the AZ vicinity and ensuring that they are included in the fully formed SV. (Granseth et al., 2006; Saheki and De Camilli, 2012). In addition, or alternatively AP-2 supports synaptic vesicle reformation from endocytosed membrane compartments (Jung et al., 2015a; Kononenko et al., 2014).

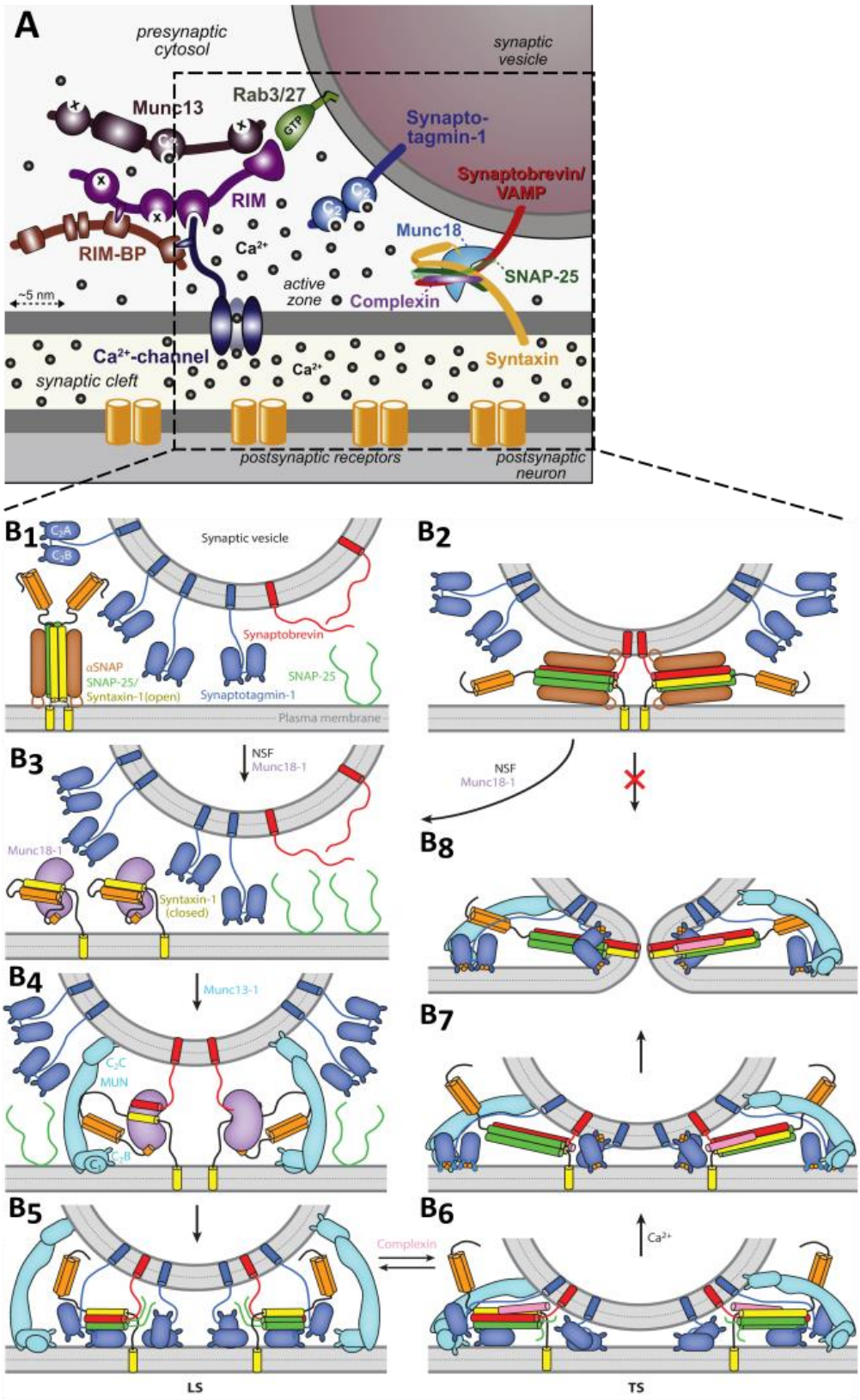

Figure 4: The molecular machinery of neurotransmitter release. A: Illustration that depicts the SV release in the context of various molecular organizers of the active zone. *Image taken from Südhof, 2013.* B1 – B8: Series of illustrations outlining key steps of a working model that attempts to consolidate the knowledge about transmitter release to-date, spanning from priming to fusion pore opening. B1: Diagram showing the postulated positions of synaptobrevin, Synaptotagmin-1 on the SV

membrane and the localization of α-SNAP on the plasma membrane, bound to a SNAP-25 – syntaxin-1 complex. B2: α-SNAP prevents the spontaneously formed trans-SNARE from mediating fusion by binding them. B3: Syntaxin-1 adopts a closed conformation by binding to Munc-18-1. Syntaxin-1 in closed conformation, bound to Munc18-1 may remain bound to the membrane after NSF disassembles that trans-SNARE complex, and may constitute a release site for Munc13-1 to bind, once an SV arrives. B4 – B5: Munc13-1 binds the SV with its C2C domain and the plasma membrane with its C1 – C2B region. By opening syntaxin-1 it may enable Munc18-1 to bind synaptobrevin, forming a template complex for the initiation of fusion, once SNAP25 binds to syntaxin and synaptobrevin. This process may be facilitated by Synaptotagmin-1, which can bind SNAP25, but is not shown on the illustration. By opening syntaxin, Munc13-1 promotes fusion, but also, by forming homodimer clusters, may inhibit the formation of many SNARE complexes. The position of Munc13-1 at this point is rather perpendicular to the membrane and this could be a hallmark of the loose primed state (LS, explained later). B6: The binding of complexin may enable further, yet not complete zippering of the trans-SNARE complex, bringing the SV and plasma membranes closer together and forcing Munc13-1 to obtain a slanted orientation in order to maintain the bridging of the two membranes. This may be a hallmark of the tight primed state (TS). Complexin and Synaptotagmin stabilize this state to prevent premature fusion and increase the synchronicity of evoked release. B7 – B8: When Ca2+ enters the cell after the arrival of a pre-synaptic AP, it binds to Synaptotagmin-1 and forces it to dissociate from SNARE complex, allowing final zippering and SV fusion. *Image and legend adapted from Rizo, 2022.*

Kiss and run, still a controversial mode of endocytosis, involves the immediate retrieval of the cavity generated by a fusing SV (Ceccarelli et al., 1979). This mode, also called cavicapture, necessitates the partial collapse of a fusing SV (Alabi and Tsien, 2012) and could potentially bypass the need for lateral clearance of SV proteins and reassembly by clathrin mediated endocytosis, supporting faster SV recovery (He et al., 2006). Bulk endocytosis occurs in response to the rapid fusion of a great number of vesicles during prolonged bouts of intense synaptic activity (Clayton and Cousin, 2009; Clayton et al., 2008). Very close to AZs, large invaginations of membrane appear and get snipped off by dynamin to create large cistern-like structures. In inner hair cells of the auditory pathway these cisterns can reach 400 nm in diameter (Kamin et al., 2014; Neef et al., 2014). The bulk mode of membrane retrieval appears to be rather unspecific, but considering that it takes place at peri-active zones during rapid fusion and lateral clearance, it is reasonable to expect that a large number of SV proteins will be included in the newly formed cisterns.

Ultrafast endocytosis was discovered in hippocampal synapses through the use of optogenetic neuronal activation and high pressure freezing. This allowed the capture of endocytic events and their localization in peri-active zones relative to the AZ. Watanabe et al., 2013 showed that in physiological temperatures, membrane retrieval peaks in the first 50 – 100 ms after the stimulating light pulse. Large invaginations of membrane were observed, which could amount to retrieved membrane material equivalent to 4 SVs. The application of latrunculin-A, an actin polymerization blocker, led to a drastic reduction of captured endocytic events in electron tomograms of hippocampal synapses.

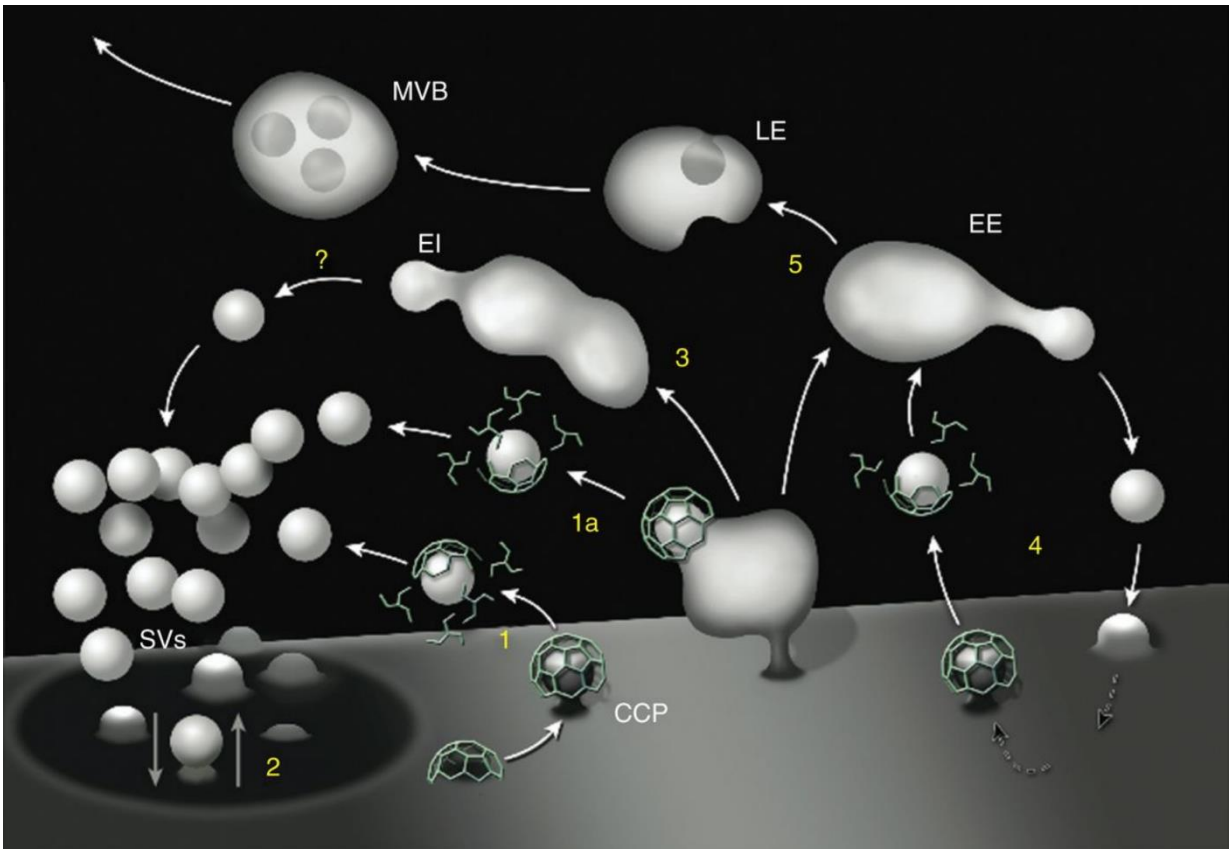

Figure 5: Endocytic Pathways: Schematic diagram depicting membrane trafficking in synaptic terminals, illustrating distinct SV recycling and endocytic pathways. 1,1a: Membrane retrieval through the formation of Clathrin coater pits directly at the plasma membrane or after the formation of endocytic intermediates, by ultrafast (not shown) or bulk endocytosis (3). 2: Kiss and run, 3: Bulk endocytosis, 4: Clathrin mediated housekeeping membrane retrieval 5: early endosome formation (EE) as well as traffic to the cell body through late endosome (LE) and multivesicular body (MVB) formation. *Image taken from Saheki and De Camilli, 2012.*

Finally, clathrin independent endocytosis, was identified in hippocampal neurons (Soykan et al., 2017) and is mediated predominantly by formin-dependent actin assembly, which produces endosome like vacuoles. Clathrin – dynamin mediated membrane fission lies downstream of bulk (Neef et al., 2014), ultrafast and clathrin-independent endocytosis and may be one of the mechanisms behind the conversion of cisterns, endosome-like vacuoles and other endocytic intermediates to regular sized SVs.

Synaptic vesicle pools

Biochemical, physiological and imaging experiments on synaptic terminals were part of multiple attempts to categorize SVs into distinct pools, separated by different molecular markers, implicated in different functional states and showing different motility or appearing at different distances from a pre-synaptic terminal's plasma membrane respectively. One of the longest standing models involves three distinct vesicle pools (Alabi and Tsien, 2012; Neher, 1998; Rizzoli and Betz, 2005; Schikorski and Stevens, 2001) that contribute to neurotransmitter release with different numbers of SVs and at different intensities or time scales of stimulation. These are (Fig. 6) the readily releasable

pool (RRP), the recycling pool and the reserve (Rizzoli and Betz, 2005) or resting pool (Alabi and Tsien, 2012).

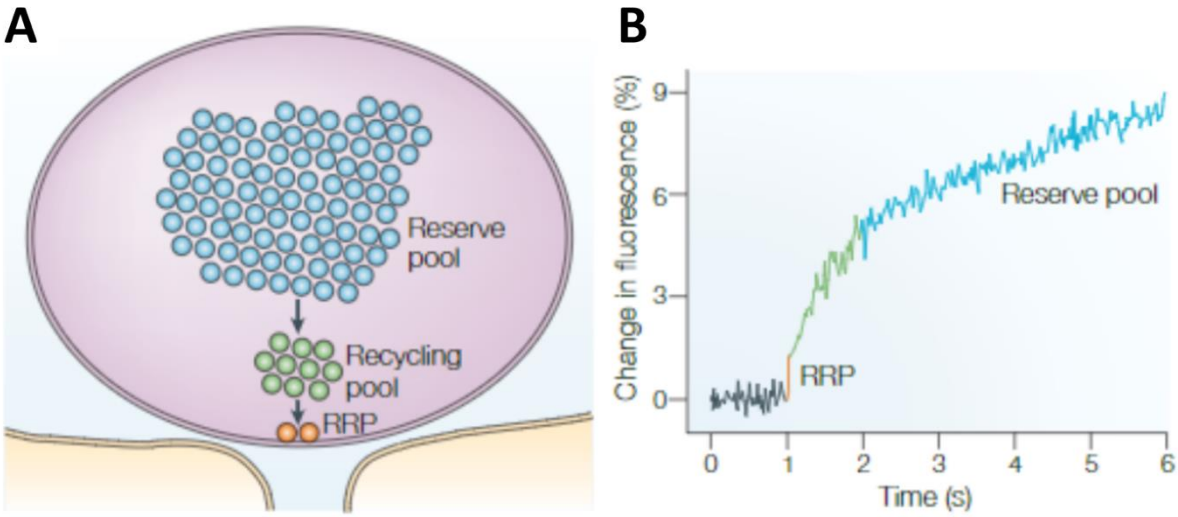

Figure 6: Model of synaptic vesicle pools. A: The three SV pool model, presented in relative to the percentage of SVs included in each of them (RRP: 1-2%, Recycling Pool: 10 – 15%, Reserve Pool: 80 – 90%) and perpendicular distance from the plasma membrane, a morphological proxy of fusogenicity. B: The three kinetic components of exocytosis from goldfish bipolar cell terminals, visualized and measured as the FM1-43 dye fluorescence increase (Neves and Lagando., 1999). *Images taken from Rizzoli and Betz., 2005*

Synaptic strength is defined as the magnitude of a post-synaptic depolarization that a pre-synaptic action potential can elicit by triggering SV fusion. The number of SVs included in the RRP (5-9 at individual hippocampal boutons) has received a lot of attention, partially due to its weighted contribution to synaptic strength. The RRP is rapidly depleted by 5-15 stimuli delivered at high frequency (Elmqvist and Quastel, 1965; Richards et al., 2003; Schneggenburger et al., 1999) or after 1 second of exposure to a hypertonic shock (Rosenmund and Stevens, 1996). This pool represents approximately 1-2% of all available SVs at a terminal, that are usually found docked to the plasma membrane and therefore, immobile in resting terminals. Not all docked SVs are necessarily release ready (Rettig and Neher, 2002). Estimates from the calyx of Held synapse ascribe 1500 – 4000 SVs to the RRP, which can be further subdivided into a fast and a slow component (Sakaba and Neher, 2001), released within 3 and 30 ms respectively, or within 0.9 and 4ms in mature calyces (Chen et al., 2015). Interestingly, at room temperature, the fast component recovers within the first 5-10 seconds (single exponent τ = 6.7s, (Lee et al., 2010; Sakaba and Neher, 2001)) after RRP depletion, while the slow component recovers within the first 100ms. A superprimed, more fusogenic sub-pool of SVs within the RRP (Schlüter et al.2006) has been thought to underlie inter-synapse variability and possibly explain short-term pre-synaptic plasticity (STP) and its modulation (Lee et al., 2012, 2013a; Pofantis et al., 2021; Taschenberger et al., 2005; Xue et al., 2018).

The reserve pool of SVs contains 10 – 15% of the total SVs in a terminal and takes over neurotransmitter release under sustained moderate stimulation. Its SV numbers are maintained by

cycles of release and endocytosis (Rizzoli and Betz, 2005). Recycling SVs eventually mature and join the resting pool of SVs (Denker and Rizzoli, 2010; Denker et al., 2011; Rizzoli and Betz, 2004), which contains 80 – 90% of the total SVs. To mobilize SVs from the reserve pool, a particularly intense, high-frequency and probably non-physiological sustained stimulation is required. This inert pool of SVs is maintained by slow clathrin mediated endocytosis which allows the capture of SV proteins that might diffuse laterally out of the terminal and into the axonal membrane. The reserve pool could act as depot or capture point of SV proteins that are involved in SV recycling (Denker et al., 2011).

Cytomatrix of the Active Zone: Orchestrators of neurotransmitter release

The trigger for Ca^{2+} triggered neurotransmitter release is provided by the opening of VGCCs. A closer look at the active zone unveils the existence of many proteins at high copy numbers, that cumulatively form the cytomatrix of the active zone (CAZ), a network of interactions between multidomain proteins called the CAZ proteins. It is postulated that the dense projections appearing on EM tomograms of pre-synaptic terminals may represent the dense network of CAZ proteins (Südhof, 2012). Among them, we find Bassoon, Piccolo, RIMs, RIM-Binding Proteins, Cytomatrix of the Active zone – associated Structural protein (CAST) and its close relative from the same protein family, ELKS, CAPS, Liprins-α. Some of these proteins and their interactions are responsible for regulating SV docking and recycling (Garner et al., 2000), some of them are candidates for generating putative SV release sites, while others may determine the precise positioning of release sites and VGCCs relative to them.

The assembly of the active zone during development begins at the trans-Golgi network, where active zone components are loaded into precursor vesicles called Piccolo-Bassoon-Transport Vesicles (PTVs) and delivered to synapses via microtubules (Ahmari et al., 2000; Bury and Sabo, 2011; Dong et al., 2010; Dresbach et al., 2006; Fairless et al., 2008; Fejtova et al., 2009; Maas et al., 2012; Shapira et al., 2003; Tao-Cheng, 2007a; Zhai et al., 2001). While some studies have suggested that PTVs recruit most known CAZ proteins and deliver them to the AZ, more recent work indicates at least three types of precursors carrying, as pre-formed complexes, Piccolo-Bassoon-CAST/ELKS, RIM-Neurexin-CASK-VGCCs or RIM-Neurexin-CASK-Munc13 (Bury and Sabo, 2011; Gundelfinger et al., 2016; Maas et al., 2012; Tao-Cheng, 2007b). Once delivered to the AZ, these proteins assemble into the fully formed CAZ network, by interacting with neurexins, neuroligins and other trans-synaptic molecules (Siddiqui and Craig, 2011; Waites et al., 2005)

Piccolo and Bassoon: The hub of the cytomatrix interaction network

Piccolo and Bassoon are large proteins with very high sequence similarity (Fig. 7). Their predicted structure involves few N-terminal zinc finger domains followed by extended coiled-coil (CC) structures (Tom Dieck et al., 1998; Wang et al., 1999). Through their second CC region Piccolo and

Bassoon may interact with each other (Fenster et al., 2000), while their CC3 region probably mediates their interaction with CAST/ELKS, which results in them being trafficked together to the AZ. The homologous region between amino acids 2869–2899 allows both proteins to interact with RIM-BPs, through which, Bassoon can position P/Q VGCCs in AZs of central (Davydova et al., 2014), retinal (Tom Dieck et al., 2005) and inner hair cell ribbon synapses (Frank et al., 2010). The C- terminal polyQ region of Bassoon has been shown to interact with Munc13-1 and Mover, while on the side of Piccolo, the C terminal C_2A and C_2B domains enable its interactions with Rim2 and the L-Type VGCC $Ca_V1.2$ (Fujimoto et al., 2002; Shibasaki et al., 2004). Experiments on synapses of the auditory pathway have yielded results that confirm these interactions. Disruption of Bassoon at the endbulb of Held synapse led to elongated PSDs which in turn resulted in higher quantal size (Mendoza Schulz et al., 2014), while the frequency of miniature EPSCs was unaffected. SV replenishment was slower in the absence of BSN and RRP estimates were smaller for high frequency trains. Additionally, Munc13-1 levels at endbulb AZs were reduced in the absence of Bassoon. P_{vr} estimates in Bassoon deficient endbulbs were reduced for higher frequency trains (200, 333Hz).

When the perturbation of Piccolo was investigated at the endbulb of Held, P_{vr}, it was shown, similar to the Bassoon KO, that SV replenishment was slowed down and the levels of RIMs at endbulb synapses were reduced (Butola et al., 2017). Additional removal of one functional Bassoon allele in the Piccolo KO background exacerbated the slow replenishment phenotype, while a reduction in P_{vr} became prominent as a result of the manipulation. Deletion of Piccolo's exon 14 did not cause any synaptic phenotypes in hippocampal neurons, due to compensation by other Piccolo isoforms.

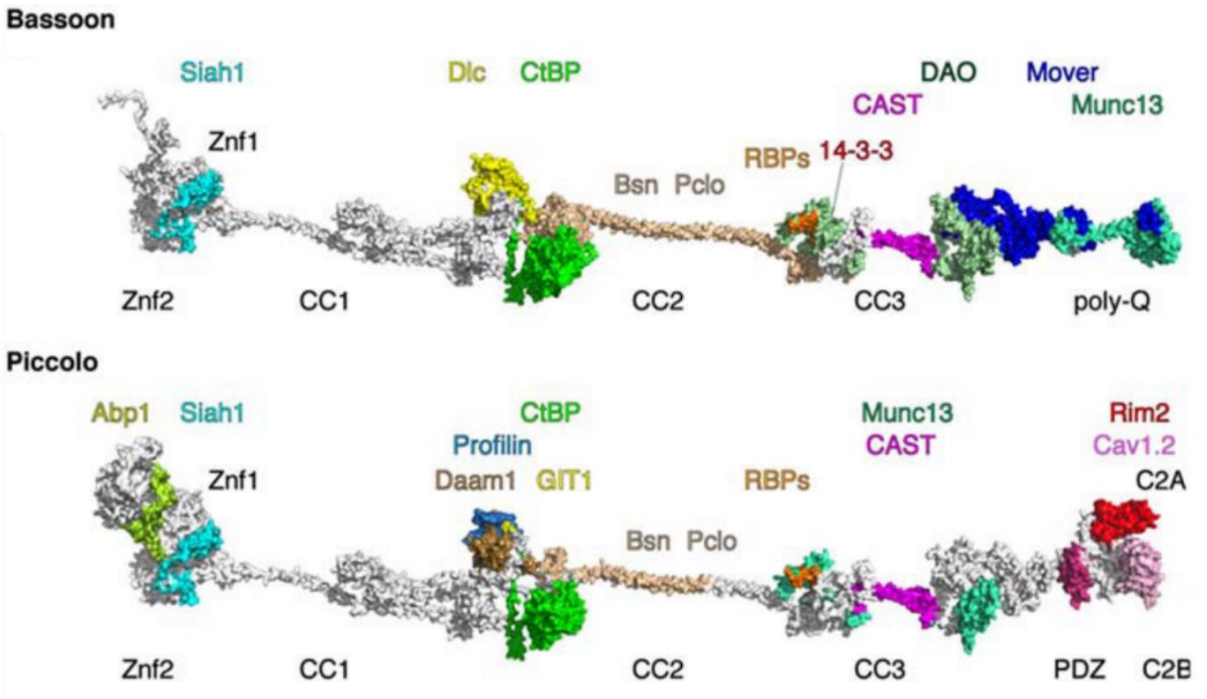

Figure 7: In silico modelling of the structure of Bassoon and Piccolo: The domains are outlined and coloured where binding sites for interactions with other CAZ proteins have been described. The colouring corresponds to the colour of the protein, with which Piccolo or Bassoon bind. *Image taken from Gundelfinger et al., 2016*

Subsequent knock-down of these isoforms robustly inhibited the polymerization of F-actin, revealing a role of Piccolo in the regulation of actin dynamics that could explain its aforementioned contribution to the replenishment phenotype, which was shown in earlier studies of Piccolo deficient neurons (Leal-Ortiz et al., 2008; Mukherjee et al., 2010; Waites et al., 2011). When Piccolo and Bassoon were both removed from hippocampal neurons, however, aberrant protein degradation was observed in pre-synaptic terminals, suggesting that the two proteins, in concert, regulate protein turnover in AZs, by interactions with ubiquitination and protein degradation pathways (Waites et al., 2013). Knockdown of both proteins led to the appearance of autophagosomes in pre-synaptic terminals. The loss of bassoon was sufficient to trigger pre-synaptic autophagy, suggesting a selective role of bassoon in regulating autophagy, possibly via the Atg5-12 complex, since the re-introduction of an Atg5 binding sequence from bassoon could rescue synapses from aberrant autophagy (Okerlund et al., 2018).

One of Bassoon's interaction partners is the SV attached phospho-protein Mover (Kremer et al., 2007). Mover is heterogeneously expressed among synapses of the mammalian brain. Genetic manipulations of Mover differentially affected Mossy fiber and Schaffer collateral synapses in the hippocampus. Schaffer collateral synapses were unaffected by the deletion of Mover, while mossy fiber synapses showed increased synaptic facilitation, an effect that was stronger in younger synapses or synapses that were exposed to higher extracellular Ca^{2+} concentration (Viotti and Dresbach, 2019). In the calyx of Held, RNAi mediated knockdown of Mover increased P_{vr} without affecting the pre-synaptic Ca^{2+} influx, as was verified by Ca^{2+} uncaging experiments. Mover, therefore, was postulated to negatively regulate Ca^{2+} evoked release in certain synapses (Körber et al., 2015). When Mover was knocked out, however, the observed effect was a reduction of P_{vr} which could be specifically attributed to more reluctant tight primed state vesicles, when SV pools were modelled with a sequential LS - TS transition model (Lin et al., 2022; Neher and Taschenberger, 2021; Pofantis et al., 2021).

RIMs and RIM-BPS interact with Munc-13s and Ca_Vs to produce species- and synapse – specific outcomes

RIMs (Wang et al., 1997) have long been regarded as central AZ organizers and rightfully so. Several isoforms of RIM1 and RIM2 have been described (Wang and Südhof, 2003), but we will focus on the structure of RIM1α and RIM2α, as they are the only isoforms that contain all the domains of the respective RIM1 and RIM2 genes. Both proteins contain an N-terminal Zn^{2+} finger domain, some central PDZ and C_2 domains. Through the Zn^{2+} finger domain, RIM, as was already mentioned, forms a heterodimer with Munc13-1, in essence activating it, by preventing its autoinhibitory homodimerization (Deng et al., 2011). Another interaction, that also contributes to RIMs priming

function is that between the α-helices surrounding the Zn^{2+} finger domain, which bind to the activated, GTP – bound form of Rab3, a protein that is found on all SVs (Gracheva et al., 2008). Through its central PDZ domain, RIM binds to ELKS and P/Q – VGCCs. Upon deletion of this domain, evoked release in neurons is impaired, has a higher Ca^{2+} requirement and becomes desynchronized (Kaeser et al., 2011). Conditional KO of RIMS in the calyx of Held led to decreased pre-synaptic Ca^{2+} currents (I_{ca}) and evoked release (Han et al., 2011). Ca^{2+} uncaging was used to bypass the VGCC trafficking function of RIM and uncover, in this large terminal, an effect of RIM's deletion in SV priming, which was a dramatic reduction in the size of the RRP, and the intrinsic Ca^{2+} sensitivity of release. Both RIM2a KO and RIM1/2 DKO in hair cells led to reduction of the pre-synaptic Ca^{2+} channel complement and decreased vesicle replenishment to the RRP possibly by contributing to SV tethering to the AZ membrane (Jung et al., 2015b; Picher et al., 2017). In contrast, conditional KO of RIM1/2 in rods of the mouse retina did not affect the levels of expression for L-Type VGCCs, but led to profoundly reduced Ca^{2+} currents, an effect that was not reproduced in heterologous expression systems. It appears that in rod terminals, the interaction of RIMs with certain L-type VGCCs facilitates the influx of Ca^{2+}, which is necessary for the release of SVs (Grabner et al., 2015). The proline rich regions of RIM interact with RIM-BPs, which also tether P/Q VGCCs. In hippocampal synapses, the expression of the central RIM PDZ domain combined with a proline rich region, similar to the one with which RIM-BP tethers VGCCs, rescues Ca^{2+}release in RIM lacking synapses (Kaeser et al., 2011).

Since a publication on RIM-BP's function in the auditory endbulb of Held synapse is included in Chapter 2, only a brief account of recent findings on RIM-BPs will be included here. Three different RIM-BP isoforms, RIM-BP1, 2 and 3 have been identified, with RIM-BP2 being the dominant CNS isoform. RIM-BP2 contains one central and two C-terminal SH3 domains, three central Fibronectin 3 domains channels and a proline rich domain. RIM-BPs were discovered as molecules that bind RIMs through their central SH3 domain and tether N-type and L-type VGCCs through their PxxP domain to the SV priming apparatus. As such, RIM-BPs promote tight Ca^{2+} - secretion coupling and ensure the reliability of synaptic transmission (Acuna et al., 2015; Grauel et al., 2016; Hibino et al., 2002; Luo et al., 2017; Wang et al., 2000). Work in *C. Elegans* and mouse neurons showed that RIM-BPs and RIMS redundantly regulate the trafficking of VGCCs to the synaptic terminals and the spatial coupling between VGCCs and SV release (Acuna et al., 2016; Kushibiki et al., 2019). Work in inner hair cell ribbon synapses has shown that RIM-BPs are required for normal sound coding in mice, while RIM-BP2 was found to positively regulate the number of $Ca_V1.3$ channels, stabilizes their slow inactivation kinetics and enables indefatigable release, a hallmark of glutamate release in the cochlea (Krinner et al., 2017, 2021; Ortner et al., 2020).

Re-evaluation of the early central synapse findings uncovered a larger variety of phenotypes by testing the interactions between RIMs, RIM-BPs and Munc13-1 in different central systems.

Contradicting the Grauel et al. study on hippocampal stellate cell synapses, Brockmann et al., 2019 showed that RIM-BPs are important in priming SVs by recruiting Munc13-1 in mossy fiber synapses formed by hippocampal granule cells. Specifically, the Munc13-1 C_2B domain KW mutation (K726W, Shin et al., 2010) co-immunoprecipitated more strongly with RIM-BP2, suggesting a dynamic interaction between the two proteins which switches upon the entry of Ca^{2+} and is mediated by the C_2B domain (Brockmann et al., 2020). Further evidence for the involvement of RIM-BP2 in priming came from experiments in RIM1/2-RIM-BP1/2 quadruple KO (qKO) neurons, where the viral re-introduction of RIM1α and RIM-BP2 was sufficient to rescue the observed priming deficits (Brockmann et al., 2020). Importantly, RIM-BP deletion in *Drosophila melanogaster* neuromuscular junction (NMJ) synapses, resulted in very severe disruptions of synaptic integrity, unlike what has been observed in the mouse (Liu et al., 2011). RIM-BP was found to not only tether SVs to Bruchpilot (BRP), the invertebrate homologue of ELKS, but also to be necessary for BRP scaffolding, a central part of AZs at NMJs. The C-terminal SH3 domains act as an interaction hub for RIMs, Munc13 and VGCCs, bridging synaptic vesicle recruitment to release sits (Petzoldt et al., 2020). Additionally, multivalent binding between the proline rich regions of RIM and SH3 domains of RIM-BP promotes the formation of condensates in synaptic terminals, a phenomenon that has been described as liquid-liquid phase separation (LLPS). The cytoplasmic tails of N- and P/Q-type VGCCS bind to RIM and RIM-BP as described above. These interactions lead to VGCC cytoplasmic tail enrichment in the condensates and promote the formation of the condensed state, which might affect N- and P/Q- type VGCC clustering at the AZ (Wu et al., 2019).

CAST/ELKS and α-liprins in the dynamic re-organization of the AZ

The names CAST and ELKS used to refer to the same protein (Südhof, 2012), the latter being the first name given to it when it was first described as a target of the RET tyrosine kinase pathway (Nakata et al., 1999). When it was found that ELKS is an active zone protein its name was changed to CAST (Takao-Rikitsu et al., 2004). Both names have been used interchangeably to describe a protein with two coding genes in mammals (Kaeser et al., 2009), producing very similar structures, largely made up of coiled coil regions, one of which is shorter in what is now called ELKS leaving CAST as the name for the protein with the longer central CC domain (Inoue et al., 2006). ELKS was found to bind Rab6 in a GTP dependent manner (Monier et al., 2002), as well as the PDZ domain of RIM (Wang et al., 2002). These interactions involve ELKS in a mechanism of axonal cargo capture, whereby vesicles marked by Rab6 are transferred through the axons, captured by the abundant ELKS molecules and brought to the AZ through the interaction with RIMs or maybe through the interaction between RIMs and Piccolo (Nyitrai et al., 2020). CAST, through its N- and C-terminal regions interacts with the β(4)-subunit of VGCCs and weakly with the α(1)-subunit (Kiyonaka et al., 2012). In the AZs of mouse rods,

the deletion of CAST resulted in smaller active zones (Dieck et al., 2012). It was later found that both CAST and ELKS are necessary for the development and maintenance of normal rod terminal structure, prevent the appearance of ectopic ribbons and maintain normal pre-synaptic Ca^{2+} currents to enable normal visual processing (Dong et al., 2018). Similarly, developing calyces of Held lacking both CAST and ELKS were smaller in area and volume. The levels of the two proteins were seemingly linked, whereby deletion of CAST would lead to increased levels of ELKS at calyx AZs (Radulovic et al., 2020). Mature calyces of Held lacking CAST and ELKS showed normal AP evoked transmission, but had less Ca_V clusters in their AZs (Dong et al., 2018). The RRP and rate of replenishment were reduced in the absence of both proteins, while the P_{vr} was increased (Dong et al., 2018). The necessity of both CAST and ELKS for neuronal development was apparent also in the mouse forebrain, where local ablation of the two proteins led to embryonic lethality (Hagiwara et al., 2020).

Another family of CAZ proteins are liprins. A- and β-liprins consist of LH1 and LH2, two highly conserved motifs, also known as "liprin homology domains" in their N-terminal coiled coil domain. At their C-terminal, liprins contain three SAM domains, which are commonly found in proteins that homo- or hetero-dimerize and can also mediate low affinity interactions with other proteins (Serra-Pages et al., 1995). Deletions of α-liprins in *C.elegans* and *D.melanogaster* disrupted the size of the AZs and the accumulation of SVs in its vicinity (Dai et al., 2006; Kaufmann et al., 2002; Zhen and Jin, 1999). The role of α-liprins in murine synapses remained elusive until recently, when new light was shed on the organization of active pre-synaptic terminals in the context of liquid liquid phase separation (LLPS). Liprin-α_1 was characterized as an interaction partner of the dystrophin associated glycoprotein complex (DSG) in murine NMJ PSDs, which ascribes the role of NMJ formation and maintenance to liprin-α_1, through its interaction with DSG (Bernadzki et al., 2017).

When liprin-α_2 and liprin-α_3 were immunolabelled and imaged with superresolution microscopy at synaptic terminals, it was shown that liprin-α_3 colocalizes more with Bassoon, RIM-BPs, Munc13 and ELKS than liprin-α_2. Deletion of liprin-α_3 led to smaller PSDs and less SVs per hippocampal bouton, reduced SV tethering with a concomitant translocation of liprin-α_2 to AZs, hinting at a compensatory mechanism. Physiological evaluation of the liprin-α_3 KO neurons showed impaired evoked release (Wong et al., 2018). The role of liprin-α_2 was identified as a synaptic organizer and interaction partner of neurexin1β and CASK, a protein of the MAGUK family, which has an active CAM Kinase domain. CASK binds a valine-tryptophan-valine motif, which is highly conserved in murine liprins and is also is found on mint1. Mint1 binds CASK and prevents the interaction with liprin-α_2. In a bivalent ion dependent manner, probably through the presence of Ca^{2+} during synaptic activity, the affinity of CASK for liprin-α_2 increases and CASK binds liprin-α_2 bridging it as such to a neurexin1β-CASK-mint1 complex. Through this interaction liprins and CASK stabilize neurexins at synapses. This phenomenon is reversed during inhibition of synaptic activity (LaConte et al., 2016).

Recent work elucidated the role of liprin-α_2 dimerization and oligomerization in dynamic AZ compartmentalization (Liang et al., 2021). The transition of liprin-α_2 from the dimer to the oligomer state leads to the LLPS of the ELKS2 N-terminal segment. This drives an increase of RIM1α in the ELKS condensates. The ELKS-RIM1α condensates could not, in contrast to RIM1α-RIM-BP2 condensates, assemble clusters of VGCCs. This finding is indicative of a mechanism by which liprin-α_2 dictates the dynamic compartmentalization of core AZ proteins, promoting changes in the priority of interactions between them and effectively tuning pre-synaptic evoked release (Liang et al., 2021).

Interestingly, liprin-α_3 also undergoes LLPS upon phosphorylation by protein kinase C (PKC) at serine 760 (Emperador-Melero et al., 2021). In its phosphorylated state liprin-α_3 recruits RIM1α and Munc13-1, enriching them in membrane attached condensates. Upon PKC activation, synaptic levels of RIM-1α and Munc13-1 were increased, which was not observed when protein kinase A (PKA) was activated in culture via the administration of forskolin. Similarly, the activation of CAM kinase 2 (CAMKII), via the administration of caffeine, could not reproduce the enrichment results seen with PKC. The functional relevance of this interaction was tested on hippocampal neurons that lacked liprin-α_2 and liprin-α_3. These DKO neurons displayed reduced levels of RIM1α and Munc13-1 at active zones, while the levels of $Ca_V2.1$ and synapsin-1 were increased. The readily releasable pool of these neurons was reduced. In the DKO background, expression of liprin-α_2 did not rescue the RRP phenotype, while re-introduction of liprin-α_3 could fully recover the size of the RRP. Emperador-Melero et al. additionally tried re-introducing a mutated version of liprin-α_3, where the serine 760 phosphorylation was blocked and this manipulation abolished the previously observed rescue. The image that emerges from these two studies is that of α-liprins as activity dependent or phosphorylation dependent re-organizers of the CAZ network of protein-protein interactions, with functional implications for important synaptic properties and, potentially, for synaptic plasticity.

Synaptic plasticity

Neurons receive repetitive stimuli through their synapses. Depending on the circuit or brain area the frequency and intensity of stimulation during physiological activity may differ. The molecular background for how dynamic synaptic transmission can be has already been discussed. Derived from the Greek verb “πλάσσειν”, meaning “to mold, to shape”, plasticity is the ability, the propensity to be shaped or molded. Multiple plasticity processes act on the short and long term to enhance and suppress synaptic transmission, giving rise to facilitation, post-tetanic potentiation and depression respectively (Zucker and Regehr, 2002). For the scope of this thesis, pre-synaptically driven short-term plasticity (STP), acting over tens of milliseconds to seconds, and the factors that may be involved in it will be introduced.

The Ca^{2+} dependence of release renders it malleable to changes in pre-synaptic Ca^{2+} concentration. Depending on the directionality of this change, paired-pulse facilitation (PPF) or depression (PPD) may be observed in the responses to two stimuli delivered with short inter-stimulus intervals (ISIs). Post-tetanic potentiation, short term depression and facilitation happen simultaneously in the same synaptic terminal (Dittman et al., 2000; Pan and Zucker, 2009; Regehr, 2012; Zucker and Regehr, 2002), but their relative contribution to the observed change in net synaptic strength depends on the initial release probability and the pattern of activity that the pre-synaptic terminal is exposed to.

To quantify the strength of synapses, one reverts to the quantal theory of transmitter release (del Castillo and Katz, 1954; Fatt and Katz, 1952). As introduced already, the quantum or quantal size, is a singles SV's content, determined from measurements of post-synaptic responses to its release (mEPSCs, Fatt and Katz, 1950). The strength of a synapse is the response, or post-synaptic current (PSC) that is elicited when several quanta (q) are released from multiple pre-synaptic release sites (N), coordinated by AP-driven Ca^{2+} influx, and with certain release probability (P_{vr}). Release probability of an SV is the product of the probability that it occupies a release site ($P_{occ.}$) before the arrival of the AP and the probability that it will successfully fuse after the AP's arrival ($P_{succ.}$) so that $P_{vr} = P_{occ.} * P_{succ.}$ (Neher, 2017). This leads to a simple way of determining a synapse's strength as:

$$\boldsymbol{PSC = N * P_{vr} * q}$$

Through the development of electrophysiological techniques, one can determine PSC and q experimentally, by measuring eEPSCs and mEPSCs respectively. Then, this framework can be used to calculate the parameters N and P_{vr} (Neher, 2017; Schneggenburger and Neher, 2000; Schneggenburger et al., 1999).

Short-term depression (STD) is a form of STP found commonly in synapses that connect to stimulus – onset coding cells. One model that explains the paired pulse depression, observed in depressing synapses is the SV pool depletion model. It posits that during the first of two stimuli delivered with a short ISI, a fraction ***F*** of the total RRP vesicles ***S*** is released, each producing quantal currents ***q*** amounting to a first eEPSC with current amplitude $A_1 = F * S * q$. Upon arrival of the second stimulus the size of the RRP will be $S - F * S$ and the amplitude of the EPSC in response to the second stimulus will be $A_2 = F * (S - F * S) * q$, or $A_2 = F * (1 - F) * S * q$. The paired pulse ratio will be $A_2/A_1 = 1 - F$. This model makes the assumptions that a large fraction of the RRP is released during the first stimulus, that no replenishment occurs between the two pulses and that the P_{vr} does not change between the two stimuli, making the P_{vr} proportionate to the initial probability of release. The model describes well the STD of many synapses, including the auditory pathway's calyx (Scheuss et al., 2002) and endbulb of Held (Cao and Oertel, 2010b). Difficulties arise with the paired pulse

depression of cultured hippocampal neuron synapses (Chen et al., 2004), which the model fails to account for.

Prolonged depression occurs after long exposure to high frequency stimulation leading to the depletion not only of the RRP, but also of the recycling pool. In hippocampal autaptic synapses this type of depression occurred only after 1000 stimuli delivered at a frequency of 9Hz, which managed to deplete the recycling pool (Stevens and Wesseling, 1999). When studying STD, one must not overlook the possibility that the pre-synaptic I_{ca} may also decrease during long high frequency stimulation, as was seen in the calyx of Held (Forsythe et al., 1998).

Pre-synaptic terminals employ a variety of proteins that intercept Ca^{2+} upon its entry to the cytosol, sharpening the high concentration domains around VGCC pores and buffer it after channel closing, leading to the collapse of said domains. However, during high frequency stimulation, the time needed to perform these processes may be limited and the clearance of Ca^{2+} may not be able to keep up with the subsequent AP involved influx, leading to endogenous buffer saturation and the build-up of residual Ca^{2+}. The residual Ca^{2+} - buffer saturation hypothesis (Katz and Miledi, 1968) has been the first to explain paired pulse facilitation or short-term facilitation (STF). It predicts that the increased Ca^{2+} concentration in response to subsequent pulses of high frequency trains will lead to more quanta being released, augmenting post-synaptic responses. However, the amount of residual Ca^{2+} is much smaller than the local Ca^{2+} concentration that drives SV release and would account for a very small fraction of observed facilitation in many synapses. Hence this model fails to describe PPF for most synapses (Regehr, 2012). An alternative explanation predicts that a slow Ca^{2+} sensor with high affinity can explain STF. Synaptotagmin-7 has 2 times higher k_{on} for Ca^{2+} than Synaptotagmin-1 and 60 times larger k_{off}, meaning that its Ca^{2+} driven activity persists for longer periods of time. Introducing Synaptotagmin-7 at climbing fiber to Purkinje cell cerebellar synapses promoted short term facilitation (Weyrer et al., 2021), supporting the Syt7 explanation of STF.

Synaptic heterogeneity and multiple primed states

STP can vary widely between synapses, but even synapses of the same type can display a high variability of STP patterns. As was introduced briefly in sections 1.5 and 1.7, CAZ proteins regulate the exocytosis of SVs and may influence the relative contributions of different pools to neurotransmitter release. In the cerebellum, electrophysiological recordings at the mossy fiber to granule cell synapse revealed a slow component of the RRP that recovered in several seconds after stimulation (Hallermann et al., 2010).

Positional priming was put forward as a theory that could explain the contributions of slow and fast components based on the distance of their constituent SVs from VGCCs and the ability of those SVs to “sense” changes in Ca^{2+} levels during stimulation and STP. It posits that during influx of

Ca^{2+}, fast vesicles fuse and slower vesicles undergo a positional change, that is strongly dependent on Ca^{2+} (Wadel et al., 2007), getting closer to the nanodomains to become fusogenic (Meinrenken et al., 2002). One could test this theory and overcome the postulated limitation of positional priming by uniformly elevating Ca^{2+} concentration in the pre-synaptic terminal through uncaging experiments. A wide range of Ca^{2+} concentrations were indeed, tested and, surprisingly, both the slow and the fast components of SV release persisted, suggesting that the defining property behind the division of the two components is the intrinsic change in Ca^{2+} sensitivity of the SV fusion machinery (Wölfel et al., 2007).

Electrical stimulation of the calyx of Held confirmed the division of the RRP into a fast pool, with slow replenishment and a slow pool with fast replenishment (Taschenberger et al., 2016). Another study indicated that the recovery of the fast pool obstructs the fast recovery of the slow pools, hinting at a sequential maturation mechanism, whereby SVs have to pass the slow stage to become fusion competent (Lee et al., 2012, 2013b). Superpriming is a term that describes the priming state of a subset of vesicles that get released during the first stimuli of a train, which have a higher release probability than normally-primed SVs (Schlüter et al., 2006).

The model of CAZ protein mediated regulation of the fusion machinery that was described before (see General Introduction) consolidates recent molecular and electrophysiological findings (Rizo, 2022) in the light of a new explanation for the process of SV priming. A theory of transition between a loosely primed state (LS) and a tightly primed state (TS) was put forward by Neher and Brose (2018). Recent work on the function of the Munc13s, showed that replacing Munc13-1 with Munc13-2 does not affect activity dependent priming but leads primed SVs to fall back to a de-primed state (He et al., 2017b). The resulting reduction in spontaneous release could be rescued by blocking NSF activity. These data indicate that Munc13-1 and Munc18-1 prevent de-priming by protecting partially zippered SNARE complexes from NSF mediated disassembly. Thus, Neher and Brose proposed that neurotransmitter release should be regarded as a three-step process involving:

1. Initial loose docking of SVs at the AZ membrane. Partial SNARE zippering and loosely organized SV fusion machinery (LS), due to the increase in intracellular Ca^{2+}, occurring within 20 – 50 ms during sustained high frequency activity.
2. A reversible (He et al., 2017b; Kusick et al., 2020) transition to a tightly primed state (TS) which is slow at resting synapses but can happen within 1-5ms at high Ca^{2+} concentrations and
3. Ca^{2+} triggered SV fusion, which occurs with sub-millisecond kinetics.

This two-step priming scheme allows the categorization of different synapses based on the fraction of their vesicles that are in the TS state at rest (Fig. 8). Not all release sites are occupied by SVs in the TS

state and synapses can, therefore, be classified depending on the probability of finding a release site occupied by a TS SV (P_{TS}). Then, synapses like CA3 – CA1 hippocampal synapses or the vertebrate NMJ will have a low P_{TS} and will facilitate as SVs transition from LS to TS during repetitive stimulation, a hallmark of tonic synapses. A depressing synapse on the other hand will have a high P_{TS} and as the TS SVs are depleted before LS SVs can state-transition to replenish them, the eEPSC amplitudes will decay, which characterizes phasic, onset-coding synapses. This model was recently corroborated with electrophysiological experiments in rat calyces of Held (Lin et al., 2022) and, in contrast to previous SV pool and priming models, can capture the diversity observed not only between different types of synapses, but also between synapses of the same type that alter their synaptic efficacy in an activity dependent manner.

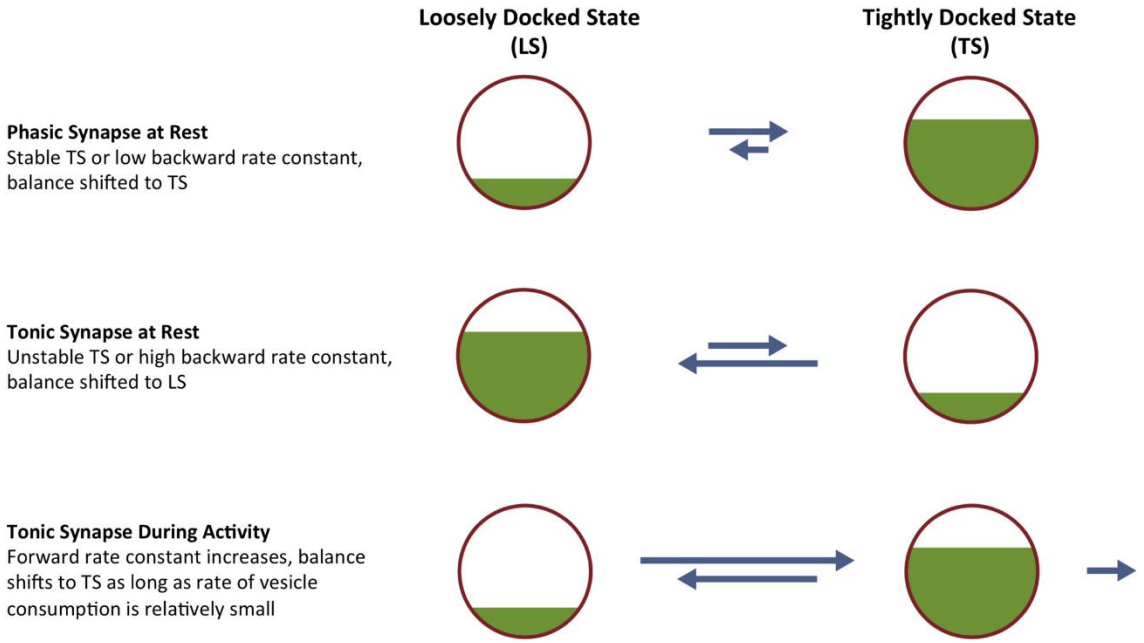

Figure 8: Synapses categorized based on the initial distribution of SVs between the LS and TS state. *Image taken from Neher and Brose (2018).*

Auditory pathway: An exemplary system for the study of pre-synaptic plasticity.

A hallmark of audition is the need for fast and temporally precise synaptic transmission to capture the constant presence and fluctuating features of naturally occurring sounds. The evolutionarily selected features of the auditory system that serve this purpose are calcium domains that tighten after the onset of hearing and during postnatal development, ribbon synapses for indefatigable release and diverse P_{TS} synaptic contacts to the auditory brainstem to enable a variety of computations for the decoding of sound (Kopp-Scheinpflug and Tempel, 2015; Moser et al., 2006; Trussell, 1997; Wichmann, 2015).

Sound is a sensory modality that is transmitted as pressure waves, local repeated changes in the density of molecules in the medium that it is transmitted. Such pressure waves arrive, commonly

through the air at the outer ear and are redirected by the pinna to the ear canal, where it stimulates the tympanic membrane. The vibration of the tympanic membrane is then transmitted through three ossicles of the middle ear, called the malleus (hammer), the incus and the stapes to the oval window of the cochlea of the inner ear. The membranous lid of the oval window transmits the mechanical energy to the fluid filled cavities of the cochlea, the scala tympani, the scala vestibuli and the scala media. The mechanical properties of the cochlea's scala media and basilar membrane change from the base to the apex of the cochlea's snail-like structure. This allows the transmitted vibrations to travel and resonate at specific points along the length of the cochlea. At the point of resonance, the basilar membrane and the organ of Corti that are housed inside the scala media will oscillate with the frequency of the sound stimulus. The organ of Corti houses 3-4 rows of outer hair cells (OHCs) and one row of inner hair cells (IHCs). The name hair cell is aptly descriptive of hair like structures that these cells carry on their membrane, which are called stereocilia. These stereocilia harbour mechanically gated potassium channels at their tips, which open upon deflection of the caused by the sound-induced basilar membrane oscillations. The depolarized OHCs display electromotility which leads to synchronized contractions upon stimulation with sound, a phenomenon that renders OHCs the natural mechanical amplifier of oscillations in the cochlea (Brownell, 1990; Liberman et al., 2002). The IHC graded receptor potentials travel to their basal membrane where, via L-type VGCCs, they stimulate the release of glutamate unto 5-20 separate spiral ganglion neuron (SGN) boutons (Nouvian et al., 2006). Each IHC – SGN connection harbours ribbon synapses that ensure indefatigable release.

The SGNs relay the auditory information to the cochlear nucleus (CN) of the brain stem (Rutherford et al., 2012). Upon entry to the CN, the SGN axons bifurcate into two branches (Fekete et al., 1984): the ascending and the descending branch. Ascending auditory nerve fibers (ANFs) innervate two major types of principal cells in the anterior ventral cochlear nucleus (aVCN), the Bushy cells (BCs) and Stellate cells (SCs). BCs receive their name due to their distinct morphology. From a round-shaped soma with an eccentric nucleus stems a primary dendrite that forms a bush of complex arborizations very close to the cell body. SCs, on the other hand, have a multipolar star-like morphology with many long dendrites that branch away from the cell body. SCs are innervated by ANFs with bouton-like glutamatergic axonal projections to their dendrites (Cant, 1981). Two groups of BCs have been identified so far with distinct morphologies and AP firing (Cao and Oertel, 2010b), namely small spherical BCs (SBCs) and globular BCs (GBCs), harking to their cell-body shape and size. Both types receive large glutamatergic modified axon terminals from ANFs, called the endbulbs of Held that harbour hundreds of AZs, releasing SVs in response to a single AP. Mouse GBCs receive 4-6 modified endbulbs of Held, which are smaller in area and cytoplasmic volume (Fig. 9) than the 2-3 endbulbs found on SBCs (Cao and Oertel, 2010b). The convergence of inputs and synchronized release of glutamate, results in enhanced phase-locking of BCs to the frequency of the sound stimulus (Brenowitz

et al., 1998; Howard and Rubel, 2010; Joris et al., 1994; Trussell, 1999) compared to SGNs, which receive information from only 1 ribbon synapse (Liberman, 1982).

The SBCs project to the medial superior olivary complex (MSO), providing excitatory input to its principal neurons. Depending on the direction of sound source in the azimuth plane, two types of interaural localization cues are generated, the interaural time differences (ILDs) and the interaural level differences (ILDs). Low frequency sounds (Grothe et al., 2010) are localized based on ITDs, which create detectable phase shifts between the sound signals arriving from each cochlea. This cue can be computed at the MSO by comparing the timing of arrival of excitation from contralateral and ipsilateral SBCs (Liang et al., 2002)(Fitzpatrick et al., 1997; Yin and Chan, 1990). The ability of endbulbs of Held to accurately transmit the temporal properties of incoming sound stimuli to SBCs becomes very crucial for computing ITDs. GBCs, on the other hand, form a long axon that projects contralaterally to the next nucleus of the auditory pathway, the medial nucleus of the trapezoid body (MNTB), where it gives rise to an even larger calyceal glutamatergic terminal called the calyx of Held. The glutamatergic calyx to principal neuron (PN) synapse constitutes a point of signalling reversal, where the excitatory input from the calyx stimulates a glycinergic inhibitory neuron that, in turn, innervates the Lateral superior olivary complex (LSO). Through this GBC-calyx of Held-PN-LSO connection, the LSO can coincidently detect (von Gersdorff and Borst, 2002) the timing of contralateral inhibitory input and ipsilateral excitatory input from SBC axons, to compute ILDs.

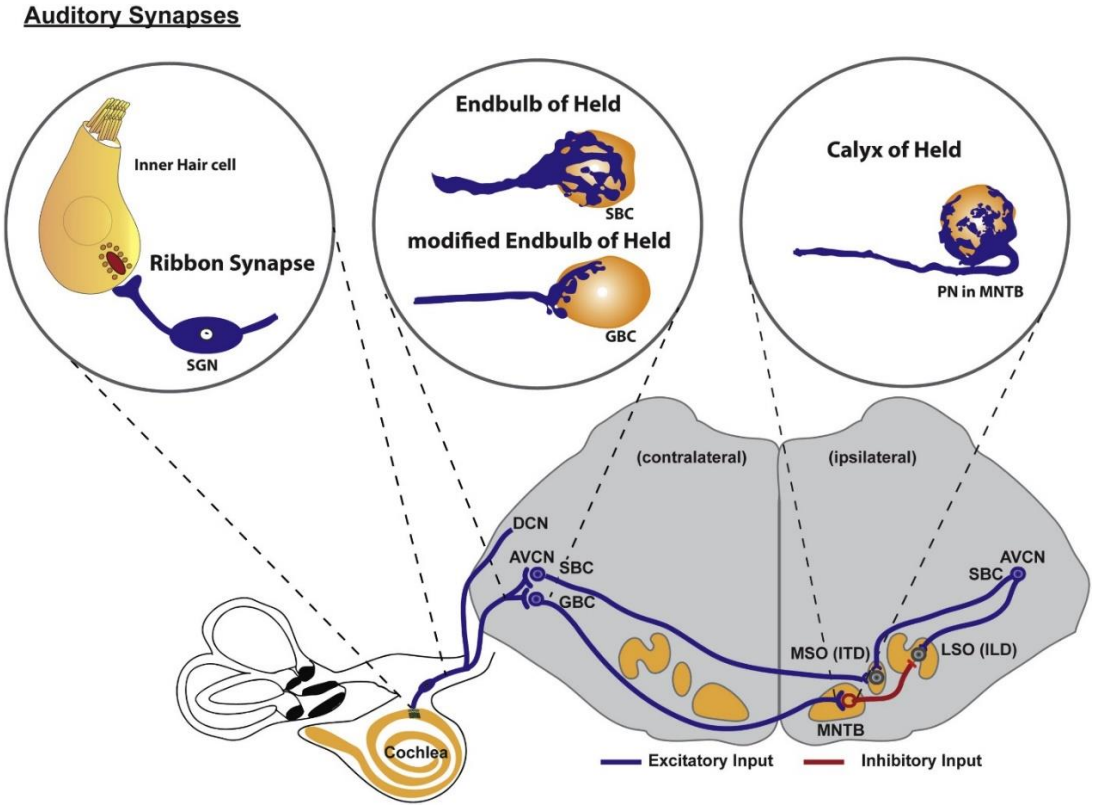

Figure 9: Lower auditory pathway. Illustration depicting the connectivity between the cochlea and the first relays of auditory information in the brain- STEM. The nuclei that are involved in the computation of binaural cues for sound localization in the azimuth plane are depicted. *Image taken from Yu & Goodrich (2014)*

The ease of access for acute brain-stem slice preparations, the amenability of large calyceal terminals to pre-synaptic recordings and the large eEPSCs, generated from many SVs fusing in parallel render the lower auditory system ideal for studies of the neurotransmitter release machinery (Cao and Oertel, 2010b; Chen et al., 2015; Lin et al., 2011; Moser and Beutner, 2000).

Chapter 1: RIM-Binding Protein 2 Organizes Ca2+ Channel Topography and Regulates Release Probability and Vesicle Replenishment at a Fast Central Synapse

Tanvi Butola*, Theocharis Alvanos*, Anika Hintze, Peter Koppensteiner, David Kleindienst, Ryuichi Shigemoto, Carolin Wichmann and Tobias Moser

* These authors contributed equally to the work

Journal of Neuroscience 2021; 7742

Appendix

DOI: https://doi.org/10.1523/JNEUROSCI.0586-21.2021

Detailed author contribution of Theocharis Alvanos:

- Experimental work and analysis
    - Performed whole cell patch-clamp recordings for:
        - Transmitter release (Fig. 1 B-G; Fig.3)
        - Short-term depression analysis (Fig. 5, 10; Table 2, 4)
        - Recovery from pool depletion (Fig. 7)
    - Performed immunohistochemistry, confocal and STED imaging for:
        - Semi-quantitative assessment of protein levels (Fig.9, 11)
        - Spatial and structural properties of $Ca_V2.1$ & BSN clusters (Fig. 12, 13, 14; Table 5)
- Wrote and edited parts of the manuscript

Chapter 2: Pre-synaptic neuromodulation at the mouse endbulb of Held synapse

2.1. Introduction

The more complex the environment an animal lives in, the higher the need for brain adaptability becomes. Among animals, mammalian and especially primate brains display remarkable adaptability. Brain development is completed outside the mother's womb and depends heavily on experience, learning and memory. Synaptic plasticity has been postulated to be the basis for these phenomena. As such, synapses have been rigorously investigated to a high level of detail in regards to their ability to remodel themselves for many decades. The concept of meta-plasticity, coined by W.C. Abraham and M.F. Bear (Abraham and Bear, 1996) refers to the plasticity of plasticity, the determination of the activity-dependent changes a synapse will undergo based on its current synaptic "state". Extrinsic influences, such as the level of synaptic inhibition, the presence of modulatory transmitters like monoamines or the hormonal environment that a synapse is exposed to, can set or tweak this synaptic state. The result of this process is that the same synapse may facilitate or depress after being exposed to activity, due to transient differences in its molecular composition, that it underwent before the arrival of activity or due to certain types of modulation. Neuromodulation is one manifestation of meta-plasticity, whereby neuromodulators, neurotransmitters that mainly act through metabotropic receptors, elicit secondary messenger cascades and alter the metabolism and transcription in other synapses or cells, priming them for plasticity. Synaptic plasticity and neuromodulation act in symphony to enable behavioural adaptability and enhance fitness in complex and demanding environments.

2.1.1 Neuromodulator receptors and G-Proteins

Neuromodulator is a term that describes a neurotransmitter with a modulatory action. "Classical" neurotransmitters, such as D-glutamate, glycine and GABA, are famous for binding to ionotropic receptors and being the main mediators of neuronal excitation and inhibition in many areas of the brain. Neuromodulators exert their influence on neuronal circuits primarily by modulating the synaptic transmission of other synapses, instead of eliciting brisk post-synaptic potentials. Instead of ligand-gated ion channels, neuromodulators act mainly though metabotropic receptors that are coupled to trimeric guanine-nucleotide-binding proteins (G – proteins) and are, hence called G – protein coupled receptors (GPCRs). GPCRs are integral plasma membrane proteins with seven transmembrane domains. Upon binding of their ligand, they allosterically activate G-protein

heterotrimeric complexes, made up of alpha (α), beta (β) and gamma (γ) subunits. G – proteins are turned on when they are bound to guanine tri-phosphate (GTP) and are off when bound to guanine bi-phosphate (GDP). Upon receptor-ligand interaction, GPCRs undergo conformational changes that are transferred to the Gα subunit. $G\alpha_s$, $G\alpha_q$ and $G\alpha_i$ are different isoforms of the alpha subunit that upon activation, can stimulate and inhibit intracellular cascades respectively. Gα exchanges GTP for GDP and dissociates from Gβ, γ creating two active parts of the original heterotrimeric complex that are both capable of initiating intracellular cascades, altering transcription, directly affecting metabolism through protein-protein interactions, or influencing the cell's homeostasis.

Among neuromodulators, are dopamine (DA), norepinephrine (NE) and serotonin (5-HT). They act through a wide range of GPCRs, even though, a few ligand-gated ion channels can be found among their receptors (e.g. 5HTR3). Conversely, though both D-glutamate and GABA act through ionotropic receptors mainly, a few of their receptors are actually GPCRs, like the metabotropic glutamate receptor family (mGluRs) or the modulatory $GABA_B$ receptors. GPCRs have been found on the somata, dendrites and some pre-synaptic terminals of many glutamatergic and GABAergic neurons. Two very common GPCR initiated pathways that have been investigated in neurons are:

- the $G\alpha_s$ – activated and $G\alpha_i$ – inhibited adenylate cyclase pathway that increases or decreases cytosolic levels of cyclic adenosine monophosphate (cAMP). cAMP levels modulate the activity of the late effector protein kinase A (PKA).
- The $G\alpha_q$ activated phospholipase C (PLC) pathway that leads to increases cytosolic levels of second messenger molecules diacylglycerol (DAG) and Inositol triphosphate (IP_3). High levels of cytosolic DAG increase the activity of the late effector protein kinase C (PKC)

2.1.2 Neuromodulators' brain-wide volume secretion

Similar to how physicists can detect the dark energy of the universe through its interaction with measurable phenomena, neuroscientists can detect the effects of neuromodulators, by measuring the changes they elicit on neuronal circuits and synapses. A common feature of DA, 5-HT and NE is that they are synthesized in very specific locations in the brain and the neurons that synthesize them project diffusely throughout the brain (Fig. 10 A), concomitantly tweaking multiple areas and functions of the brain. DA is synthesized in the substantia nigra and the ventral tegmental area, 5-HT in the Raphe nuclei and NE in the locus coeruleus. AP – evoked Ca^{2+} influx, RIMs, Munc13s and Synaptotagmin-1 are necessary for the release of neuromodulators (Fig. 10 B; Liu et al., 2021). Even though they share these factors with conventional synapses, neuromodulation secretion employs a mode of release called volume transmission, where the neurotransmitter diffuses away

from the release site and forms a gradient of concentration (Fig. 10 B). One neuromodulator-filled SV can, therefore activate receptors that are expressed on the membranes of neurons at different distances from the release site, have different affinities and a distinct spatial niche of activation along the concentration gradient.

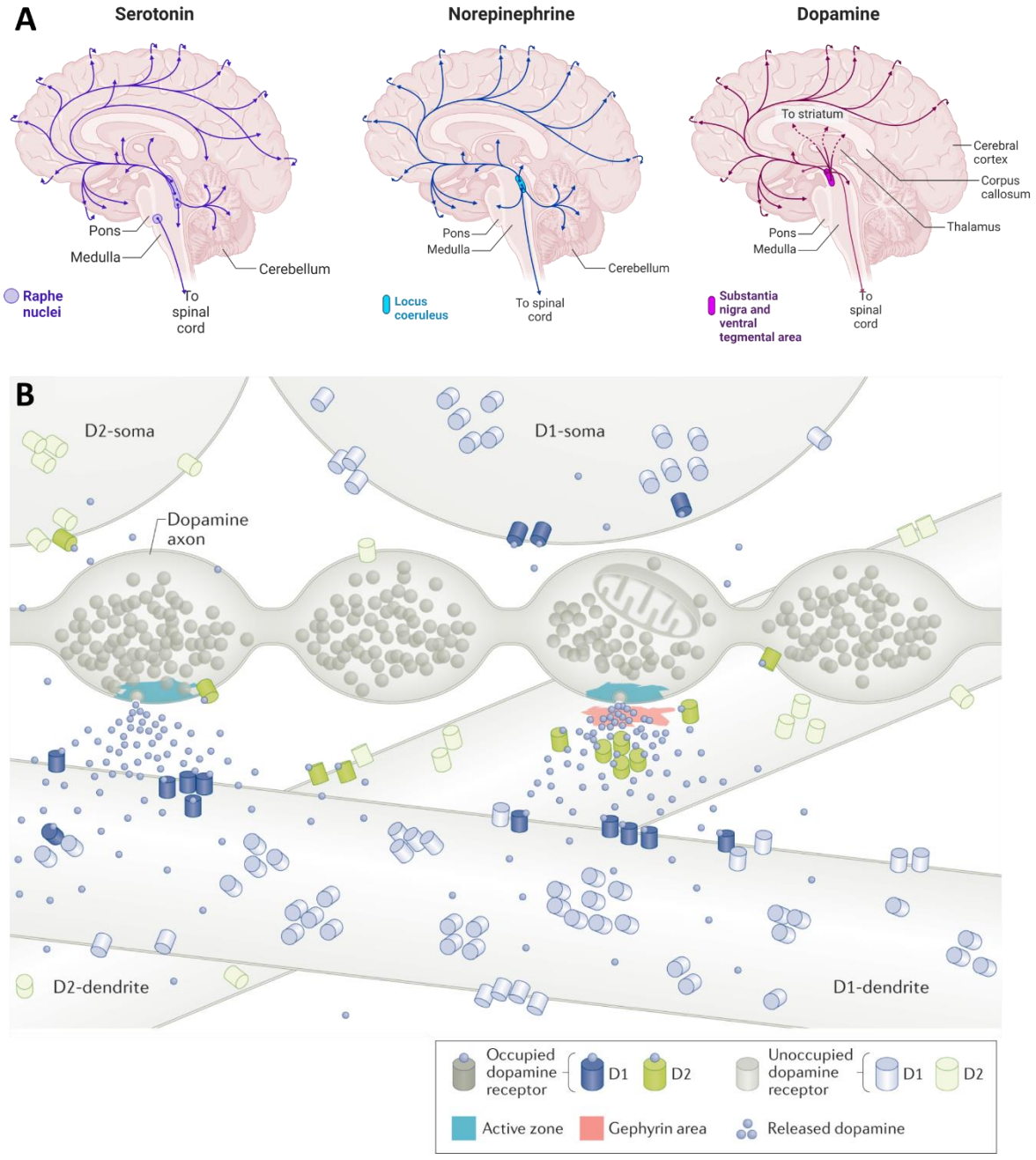

Figure 10: Neuromodulator release in the brain. A: Illustration that depicts the brain areas, where the cell bodies that synthesize serotonin (5-HT), Norepinephrine (NE) and dopamine (DA) are located. The projection patterns of said neurons are also displayed. Image created with BioRender. B: Model of striatal dopamine transmission. Two striatal neurons are shown that are receptive to DA, albeit they express different DA receptors. While the dendrite of D1R expressing neuron responds to volume transmission (left active varicosity, panel B), the one that contains D2Rs forms post-synaptic appositions and receives synaptic transmission from the dopamine releasing varicosity of the dopaminergic neuron's long projecting axon (right varicosity, panel B). The left varicosity, affects, at the distal edges of the neurotransmitter concentration gradient, some receptors on the D2 dendrite. Conversely, the synaptic transmission depicted at the right varicosity creates some

neurotransmitter spillover that reaches and activates a few D1Rs on the D1 dendrite. *Image adapted from Lie, Goel & Kaeser (2021)*.

2.1.3 Neuromodulation of plasticity

At the behavioural level, some old studies showed that long-term memory storage is enhanced during stress (reviewed in McGaugh and Roozendaal, 2002). This is mediated by the endocrine stress response from the adrenal glands, through secretion of cortisol that leads to activation of locus coeruleus neurons. This in turn leads to secretion of NE in the amygdala, which, in concert with the hippocampus, stores the memory of the event that caused the stress response. NE administration was shown to increase the retention of information with low emotional content, that were not retained in the absence of NE (Groch et al., 2011; McGaugh and Roozendaal, 2002). Interestingly, Takeuchi et al., (2016) showed that the distinct effects of NE and DA release are interconnected. The secretion of dopamine during a novel experience affected the firing rate of Locus coeruleus neurons, which released NE in the amygdala and that, in turn, coupled with postulated release of DA in the hippocampus, promoted the enhanced incidental long-term memory storage of the novel experience (Clewett and Murty, 2019; Terhune et al., 2016; Thorp et al., 2020). These modulatory effects can upregulate the efficiency of incidental memory storage based on either a positive or negative emotional context and may also underlie reward driven learning processes.

2.1.3.α Neuromodulation of Long-term and spike-timing dependent plasticity

Some mechanisms that underlie memory formation involve different forms of plasticity, the effect they exert on the post-synaptic compartments of synapses and on neuronal excitability (Brzosko et al., 2019). The aforementioned emotional priming of plasticity and memory by NE and DA has been proven to involve a regulatory mechanism, whereby NE controls the incorporation of α-amino-3-hydroxy5-methyl-4-isoxazolepropioninc acid receptors (AMPARs) on the post-synaptic membrane of glutamatergic synapses (Hu et al., 2007a). AMPARs are heterotetrametric complexes of subunits GluR1-4. At resting membrane potentials, they drive the bulk of glutamate driven EPSCs, depolarizing the membrane. N-Methyl-D-aspartate receptors (NMDARs) open at a depolarized potential and respond to glutamate, further depolarizing the post-synaptic membrane. The voltage dependence of NMDAR opening is due to a Mg^{2+} ion that blocks the intracellular side of the pore forming complex. Upon sufficient depolarization by AMPARs, NMDARs open and allow the flow of cations, among which Ca^{2+} into the post-synaptic cytosol. This activates Ca^{2+}/calmodulin kinase 2 (CaMKII), which is responsible for phosphorylating many targets that lead to the induction of long-term potentiation (LTP). Among the phosphorylation targets of CaMKII are the GluR1 subunits of AMPARs, which are phosphorylated at several major C-terminal sites. Serine 831 and Serine 845 have been extensively

studied, one being phosphorylated by CaMKII and PKC, while the other by PKA. Phosphorylation of these sites on GluR1 regulates the AMPAR channels kinetics (Banke et al., 2000; Barria et al., 1997) and synaptic incorporation (Ehlers, 2000; Esteban, 2003; Qin et al., 2005). Interestingly, NE can hijack this mechanism and, through β-adrenoreceptors, cause the phosphorylation of these two serines (Hu et al., 2007b). Electrophysiology experiments conclude that NE facilitates the induction of LTP, a mechanism that becomes defective in the presence of GluR1s with mutated serine 831 and 845. Thus, NE can prime a synapse for plasticity by changing its membrane bound AMPAR content, making it easier for NMDAR dependent induction of LTP (O'Dell et al., 2010).

The regulation of dendritic excitability may also regulate NMDARs and the induction of plasticity. In hippocampal pyramidal neurons, $K_V4.2$ potassium channels generate rapidly activating and inactivating K^+ transients that activate at hyperpolarized potentials and prevent the back-propagation of an AP from the cell to the dendrites (Hoffman and Johnston, 1999; Hoffman et al., 1997). Activation of β_1 – adrenoreceptors was shown to downregulate the presence and conductance of $K_V4.2$ channels at hippocampal dendrites. If the kinetics or amplitude of these transients are modulated by NE, an AP may back propagate to reach the dendrite, lift the magnesium block and allow NMDARs to respond to glutamate, promoting the induction of LTP. Serotonin has also been shown to modulate potassium outward currents, albeit in olfactory neurons (Gao et al., 2013). Small conductance Ca^{2+} activated potassium channels (SK channels) are also found on dendrites, are activated by Ca^{2+} and prevent the back propagation of APs. SKs are modulated by the cAMP-AC-PKA pathway and are another target of neuromodulation by NE and β-adrenoreceptors (Faber et al., 2008; Ren et al., 2006).

Serotonin was also shown to regulate neuronal excitability by modulating hyperpolarization activated cyclic nucleotide gated channels (HCN channels) that are expressed at the axon initial segment of neurons (Ko et al., 2016). Finally, at the visual cortex, spike timing dependent plasticity (STDP) induced eligibility traces of LTP or long-term depression (LTD) were induced by exposure to coincidental pre- and post-synaptic spikes, a protocol that is called spike timing (ST) stimulation. If the pre-synaptic neuron is stimulated first and the post-synaptic follows up with a burst of activity, an LTP eligibility trace is generated (pre-post ST). Conversely if a pre-synaptic spike occurs after the post-synaptic burst, an LTD eligibility trace is generated (post-pre ST). These traces may decay and never turn to long-lasting changes, an effect that for LTP is called de-potentiation. The stabilization of those traces was induced with 10 seconds of iontophoretic application of 50μM NE or 5-HT after the ST conditioning. NE specifically stabilized the pre-post LTP inducing pathway without affecting the post-pre pathway. Conversely, iontophoretic application of 5-HT specifically stabilized the LTD eligibility

trace and post-pre pathway. Optogenetic activation of endogenous monoamine release replicated those results in the visual cortex (He et al., 2015).

What already becomes apparent is that rigorous scientific work has been devoted to modulatory effects on the post-synaptic side of a synapse undergoing plasticity. With the advent of optogenetics, Ca^{2+} and transmitter imaging and improvement of fluorescence and structural microscopy, neuromodulation is a re-emerging theme in synaptic research (Brzosko et al., 2019).

2.1.3.β Neuromodulation of the pre-synapse

The focus on post-synaptic action of neuromodulators does not exclude the possibility that there are modulatory pathways regulating neurotransmitter release in the pre-synapse. In fact, an increasing amount of evidence shows that G-protein pathways, especially those driven through cAMP – AC – PKA, IP3 and DAG – PLC – PKC are capable of modulating Ca^{2+} evoked release (Gekel and Neher, 2008; He et al., 2017b; de Jong and Verhage, 2009; Rhee et al., 2002; Wierda et al., 2007). Neuromodulator control of those pre-synaptic pathways is relatively underexplored in the context of short-term plasticity and the newer insights on SV priming, de-priming and SV pools (Lin et al., 2022; Neher and Brose, 2018; Rizo, 2022).

Nevertheless, early experiments showed that β-adrenoreceptors, through cAMP signaling, can increase VGCC conductance, by modulating single channel open time or the probability of channel opening (Gray and Johnston, 1987). The effect was measured with whole cell and cell-attached voltage clamp, indicating that the VGCCs were positioned post-synaptically and could contribute to the induction of LTP. In rat hippocampal autapses, pre-synaptically apposed α_2 – adrenoreceptors caused inhibition of eEPSCs, which ranged from 12 to 100% reduction in amplitude (Boehm, 1999). In contrast to NE, mGluR activation inhibited both eEPSCs and evoked inhibitory post-synaptic currents (eIPSCs). Similar to mGluR activation, incubation with 5-HT on led to inhibition of both eIPSCs and eEPSCs in dissociated rat basolateral amygdala (BLA) neurons (Koyama et al., 1999) and motorneurons (Singer and Berger, 1996; Singer et al., 1996).

In the developing calyx of Held, Leão and Von Gersdorff (2002) showed that NE downregulates the pre-synaptic I_{Ca} by 20% and suppressed the amplitude of AMPAR and NMDAR eEPSCs by 40-60% during postnatal days 6-9. Surprisingly, this allowed the post-synaptic neuron to fire at higher frequencies, due to the abolition of the NMDAR-mediated depolarization block. The effect was reduced during later stages of synapse development and seemingly abolished in the mature calyx of Held. This developmental effect was recently shown to rely on a developmentally declining incorporation of GluA2 containing Ca^{2+} permeable AMPARs (CP-AMPARs) in the membrane of the PNs of the MNTB that are post-synaptic to the calyx (Lujan et al., 2019). Perhaps the mechanism that gets triggered by NE alters the incorporation of CP-AMPARs in the post-synaptic membrane.

The calyx was also modulated by extracellular application of forskolin, which increases intracellular cAMP as well as by intracellular application of cAMP. This led to the activation of Epac, a protein the gets activated by cAMP with an EC_{50} = 40μM, higher than that of PKA. The two known isoforms of Epac, Epac1 and Epac2 are expressed in some parts of the neonatal mammalian brain, but only Epac2 maintains high expression levels in the adult brain (Kawasaki et al., 1998). The potential synergistic action of PKA and Epac in neuromodulation has not been elucidated. Epac can activate Rap1 and Rap2 effector proteins leading to the activation of the MEK – ERK kinase pathways, which can effect long-lasting changes in translation and metabolism in the cell. It can also directly activate Ryanodine receptors, leading to release of Ca^{2+} from intracellular stores (Kang et al., 2003). Epac signaling at the calyx of Held strongly potentiated eEPSCs, by increasing P_{vr} and RRP size and increased the speed of recovery from RRP depletion (Kaneko and Takahashi, 2004; Sakaba and Neher, 2003).

Norepinephrine signaling through β_1 – adrenoreceptors and Epac2 was recently studied in the cerebellar parallel fiber to granule cell synapse (Martín et al., 2020). NE and isoprotenerol, a β_1 – adrenoreceptor agonist strongly potentiated eEPSCs from 100.9% to 194%. The RRP was increased, asynchronous release was potentiated and the PPR was reduced, indicating an increase in P_{vr}. The effect was sensitive to the application of metoprolol, a β_1 – adrenoreceptor blocker, the genetic ablation of Epac2 and the pharmacological block of Epac2. Pharmacologically blocking PKA did not alter the effect of NE or isoprotenerol. In this circuit the potentiation of pre-synaptic release is required for parallel fiber LTP (Martín et al., 2020).

The postulated mechanism of pre-synaptic neuromodulation involves Epac and PKA as targets of converging pathways that down- or upregulate neurotransmitter release from pre-synaptic terminals. Recent experiments on autaptic neurons derived from human induced pluripotent stem cells (Patzke et al., 2019), showed that the phosphorylation of synapsin-1, an SV associated protein is controlled by PKA, which is subject to neuromodulation by NE, 5-HT and endocannabinoids (Patzke et al., 2019, 2021). 5-HT exposure led to pre-synaptic increases in cAMP and phosphorylation of synapsin-1, which caused it to dissociate from SVs. NE and endocannabinoids had the inverse effect of reducing cAMP and promoting dephosphorylation of synapsin-1. In its non-phosphorylated form synapsin-1 associates with SVs and forms LLPS condensates, which might promote SV clustering close to the AZs of a pre-synaptic terminal (Milovanovic et al., 2018; Patzke et al., 2019). Making matters even more complicated, a connection between cAMP – Epac and PKC signaling exists, whereby Epac activates PLCε, PKC and CamKII (Oestreich et al., 2009). Whether this pathway bears any importance to the modulation of neuronal networks and synapses has not been elucidated thus far.

Functioning alongside the $G\alpha_s/G\alpha_i$ cAMP dependent cascades, is the Ga_q pathway that activates PLC and PKC. Early evidence showed that spinal neurons' mEPSCs can be differentially

modulated by 5-HT. Some terminals displayed a transient suppression during incubation with 5-HT, some others a transient facilitation and a third group showed long-lasting facilitation of mEPSCs, recorded in a Ca^{2+} free and high [Mg^{2+}] solution (Hori et al., 1996). This long-lasting effect was mimicked by bath application of PdBu and blocked by calphostin C, an inhibitor of PKC activity. The same terminals that showed long potentiation of mEPSCs, displayed long-term eEPSC potentiation. Application of forskolin did not have an effect on eEPSC potentiation, meaning that PKA is not involved in generating this effect. PKC activation, probably through 5HT2Rs activates the release machinery and potentiates spinal neuron synapses. A possible target of the PLC – PKC pathway is Munc13-1 whose activity is upregulated by the presence of Ca^{2+} and DAG (Lipstein et al., 2021; Rhee et al., 2002; Xu et al., 2017). This pathway has not received as much attention as the cAMP – PKA pathway as a potential route of neuromodulation, even though the potentiating influence of phorbol esters on transmitter release have been known for decades (Hori et al., 1996; Lee et al., 1993; Lou et al., 2005).

2.1.3γ Neuromodulators in the cochlear nucleus

The experiments on the calyx of Held show that there is prominent innervation of the MNTB by noradrenergic and serotonergic fibers. Little is known however about the endbulb of Held to BC synapse in the aVCN. Experiments by Klepper and Herbert (1991) on rats uncovered the prominent presence of NE releasing fibers in all subdivisions of the rat aVCN. Serotonergic fibers were not as abundant in the rostral aVCN, but a higher density was described for the DCN's granular and molecular cell layer. It was thought that, since both modulators are synthesized in neurons that project diffusely throughout the brain, the innervation of the aVCN probably is part of a general modulatory system and does not constitute a specific pathway of neuromodulation of auditory function (Ebert and Ostwald, 1992). Interestingly, however, 5-HT was observed with in vivo single-unit experiments to differentially affect the firing rates of primary-like responding neurons when anesthetized rats were exposed to sound stimuli. Compared to the large inhibition of GABA and glycine, 5-HT predominantly generated modest inhibition up to 60% of evoked firing rates. Some neurons showed both inhibition and a delayed excitation leading to higher firing rates. The authors conclude that different auditory neurons express a range of 5HTRs that mediate these varying effects.

The presence of low voltage activated K_V1 and HCN channels on BCs of the aVCN (Cao et al., 2007b; Leão et al., 2005; Oertel et al., 2008) shorten the time window for subthreshold input summation on BCs and reduce the refractory period after the generation of an AP (Kuenzel, 2019). This is not unique to BCs and in fact is more pronounced on Octopus cells, coincidence detectors in the CN that have an order of magnitude smaller membrane resistance and faster time constants than those of BCs. These channels are targets of neuromodulators in other systems and could potentially be influenced by the secretion of NE or 5-HT in the CN.

Endbulbs of Held elicit huge suprathreshold EPSCs unto BCs. The predominant in vitro pattern of STP is short-term depression, albeit with high inter-synapse variability, which is reduced in synapses converging on the same BC (Oleskevich et al., 2000; Yang and Xu-Friedman, 2012a). Endbulb pre-synaptic I_{Ca}, measured by Ca^{2+} imaging, was downregulated due to the activation of the metabotropic $GABA_B$ receptor activation via its specific agonist baclofen (Chanda et al., 2011). This result is suggestive of neuromodulation at the endbulb that could be potentially mediated by the release of NE or 5-HT.

The variability that was reported by Yang & Xu-Friedman (2012) was also observed in our work with the endbulb of Held synapse (Butola et al., 2017; Mendoza Schulz et al., 2014 & Chapter 1 of this thesis). We hypothesized that neuromodulation underlies the observed variability of neurotransmitter release at the endbulb of Held synapse and can potentially describe the dynamic role of BCs in sound information processing and binaural-cue generation. In order to test and scrutinize this hypothesis some preliminary, yet encouraging experimental data will be presented and discussed in the following sections.

2.2. Materials and Methods

2.2.1 Animals

This second part of the study includes experiments performed exclusively on Bl6N animals, which were housed and provided from the animal facility of the Fassberg Campus of the Max Planck Institute for Multidisciplinary Sciences. For information on the RIM-BP2 KO animals, please refer to the relevant Materials and Methods section of the publication in the Appendix. The animal housing of BL6N animals followed a 12-hour light/dark cycle with food and water constantly provided ad libitum. All of the experiments performed here complied with the guidelines of the German animal welfare act and were approved by the board for animal welfare of the University Medical Center Göttingen and the animal welfare office of the state of Lower Saxony.

2.2.2 In vitro acute slice electrophysiology

Mouse pups at 15 – 21 postnatal days of age were used for the harvesting of brainstem tissue. The pups were sacrificed by decapitation. In some cases, a brief exposure to CO_2 was preformed to facilitate handling. After decapitation the scull was opened with an incision between the eyes and a dorsal cut reaching and cutting through the first vertebra. Two quick cuts were performed along the lambda sutures to get rid of the skull. The optic and facial nerves were severed with a scissor to allow for the brain to be dissected out of the skull. This process lasted 25 – 40 seconds. The brains were immediately immersed in ice cold cutting solution (Table 1) and pinned, dorsal side down, on a wax stage. With the ventral side of the brainstem exposed, the meninges were removed with curved forceps and a mid-sagittal cut was performed using a straight razor, splitting the brain in two hemispheres. Scissors were used to cut between the cerebellum and the occipital lobe of each hemisphere in order to separate the hind-brain from the fore-brain. The two blocks of hind-brain, containing brain-stem and cerebellum, were glued with cyanoacrylate glue, (Loctite 401, Henkel) medial side down, on the stage of a Leica (Wetzlar, Germany) VT 1200S vibratome. The lateral side of both brain blocks was facing upwards and towards the advancing blade. A vibration amplitude of 1.5 mm was used and the blade was placed at the height of the cerebellar flocculus. Cerebellar tissue was sectioned at an advancing speed of 0.05 – 0.1 mm/sand discarded. Thereafter, a speed of 0.02 mm/s was used to obtain 150µm thick parasagittal slices of the cochlear nucleus. The slices were incubated in artificial cerebro-spinal fluid (aCSF, Table 1) for a total of 30 minutes in a 35°C water bath (Julabo, Seelbach, Germany), after which they were maintained in aCSF at room temperature (23 – 25 °C) until recording. The pH of both the cutting solution and the aCSF was adjusted to 7.4. The osmolarity was,

in mOsm, 310 for the aCSF and 320 for the cutting solution. Both solutions were continuously aerated with carbogen (95% O_2, 5% CO_2). An EPSC10 USB patch clamp amplifier was used for all recordings and was driven by the Patchmaster software (HEKA Elektronik GmbH, Reutlningen, Germany). The sampling interval was set to 25µs and the filter at 7.3 kHz. For better visualization of the slice's cell layers and auditory nerve fibers (ANFs), differential interference contrast (DIC) microscopy was used on and Axioscope 2 FS plus microscope (Carl Zeiss GmbH, Oberkochen, Germany) with a 40x water immersion, 0.8 numerical aperture objective (Carl Zeiss GmbH). All recordings were performed at near physiological temperature (33 – 35°C). The bath solution flowed through an in-line heater element (SH-27B with TC-324B controller, Warner Instruments LLC, Holliston, MA, USA). The temperature of the solution was monitored by a thermistor placed between the opening of the inflow tube and the slice in the recording chamber.

aCSF 2mM Ca^{2+}

Compound Name (Source)	**Concentration (mM)**
Glucose (Merck)	13
NaCl (Merck)	125
$CaCl_2$ (Merck)	2
$MgCl_2$ (Merck)	1
$NaHCO_3$ (Merck)	26
NaH_2PO_4 * H_2O (Merck)	1.25
KCl (Merck)	2.5
Na-Pyruvate (Merck)	2
Na L-ascorbate (Merck)	0.7

Intracellular solution

Compound name (Source)	**Concentration (mM)**
K-gluconate (Merck)	108
HEPES (Merck)	9
EGTA (Merck)	9
Na_2Phosphocreatine (Merck)	14
ATP-Mg (Merck)	4
GTP-Na (Merck)	0.3
$MgCl_2$ (Merck)	4.5
QX-314 (Merck)	1

Cutting Solution

Compound Name (Source)	**Concentration (mM)**
Glucose (Merck)	20
Sucrose (Merck)	120
NaCl (Merck)	50
$CaCl_2$ (Merck)	0.2
$MgCl_2$ (Merck)	6
$NaHCO_3$ (Merck)	26
NaH_2PO_4 * H_2O (Merck)	1.25
KCl (Merck)	2.5
Na-Pyruvate (Merck)	2
Na L-ascorbate (Merck)	0.7
Na L-Lactate (Merck)	3

Table 1: Solutions used for acute slice in vitro electrophysiology. All compounds used are listed with their concentrations. QX314 stands for N-(2,6-dimethylphenylcarbamoylmethyl) triethylamonium Chloride, an intracellular sodium channel blocker.

Borosilicate filamentous glass capillaries (GB150F, Inner diameter: 0.86mm | Outer Diameter: 1.50mm | Length: 80mm, Science Products GmbH, Hofheim, Germany) were used to pull patch pipettes on a P-87 micropipette puller (Sutter Instruments Co., Novato, CA, USA). The resistance at the tip of the pipette was strictly 2.5 – 3.5 MOhms to avoid increases of the series resistance (R_s) over long recordings. The pipettes were filled with intracellular solution (details on Table 1), which additionally contained 1mM of either Alexa – 488 or Alexa – 568 (Invitrogen / Fisher Scientific, Schwerte, Germany). The pH of the solution was adjusted to 7.4 and its osmolarity to 325 mOsm, in order to prevent osmotic collapse of the patched neuron, preserve the cell's vigour and prevent fluctuations of the R_s over long recordings. Voltage clamp experiments were performed with a V_{hold} = -70mV, corrected for a liquid junction potential of 12mV. Only cells with R_s values less than 8 MOhms were included in the analysis. Residual R_s was compensated offline using a custom Igor Script, which was kindly provided by Erwin Neher, utilizing the algorithm developed by Stephen Traynelis (1998). Afferent fiber stimulation was performed using a monopolar electrode to deliver stimulating currents through a stimulus isolator (A360 World Precision Instruments, Sarasota, FL, USA). 10 – 20µA of current were injected at a distance of approximately 3 – 4 cell diameters (60 – 80 µm) away from the patched cell on the surface of the slice to elicit action potentials (APs) from ANFs. Even higher amplitudes were injected at the point where the auditory nerve enters the cochlear nucleus if a fiber could not be located in the vicinity of the patched BC.

For the recordings of monoamine pharmacological blocking, the solution used as control, was based on aCSF (Table 1), which was additionally supplemented with 1mM Kynurenic acid (Abcam, Waltham, USA), a low affinity AMPAR antagonist, to prevent saturation and desensitization of AMPARs and 100µM Cyclothiazide (from Biotrend, Wangen, Zurich, Switzerland or from Adooq Bioscience, Irvine, California, USA) a positive allosteric AMPAR modulator that blocks desensitization. The bath solution also included 2µM Strychnine hydrochloride (Merck) a glycine receptor blocker and 10µM Bicuculine methchloride, a $GABA_A$ receptor antagonist. The two preliminary experiments described in the subsequent result section, involved two modified versions of this control solution.

One of them included 10µM of the atypical antipsychotic Risperidone (Merck Biochemichals, GmbH, Germany), which blocks a range of serotonin, dopamine and norepinephrine receptors (details on Table 2) and a second version additionally contained 10µM Amisulpride, an antiemetic - antipsychotic and 1µM Pindolol (Tocris Bio-Techne GmbH, Wiesbaden-Nordensstadt Germany), a non-selective beta blocker. The chosen concentrations are larger than five times the higher K_i (Table 2) of each blocker and were chosen to ensure successful blocking of their targets in the in vitro setup. Administered together, these three compounds can block most known monoaminergic receptors and their respective signaling cascades (Table 2). One type of experiment consisted of sequentially

exposing synapses to the control solution (as described above) and, after performing afferent fiber stimulation, switching to the solution which included all 3 monoamine receptor blockers. In the second type of experiment the control solution was exchanged for one that additionally contained only Risperidone.

Risperidone	
Target - function	**Ki**
5-$HT_{1A/B/D}$ - antagonist	14 - 400 nM
5-$HT2_{A/B/C}$ - inverse agonist	0.2 - 60 nM
5-$HT5_A$ - antagonist	200 nM
5-HT_6 - antagonist	2000 nM
$5HT_7$ - antagonist (irreversible)	7nM
Adrenergic $\alpha_{1A/B}$ - antagonist	5 - 9 nM
Adrenergic $\alpha_{2A/B/C}$ - antagonist	1 - 100 nM
Dopamine D_1 - antagonist	240 nM
Dopamine $D_{2/3/4}$ - antagonist	3.5 - 4.5 nM
Dopamine D_5 - antagonist	300 nM

Amisulpride	
Target - function	**Ki**
5-$HT_{1B/D}$ - antagonist	1700 nM
5-$HT2_B$ - antagonist	13 nM
5-HT_7 antagonist/inverse agonist	11 nM
Adrenergic $\alpha_{2A/C}$ - antagonist	1500 µM
Dopamine $D_{2/3}$ antagonist	3 nM

Pindolol	
Target - function	**Ki**
5-HT1A antagonist	15-80 nM
β1 - antagonist	2 nM
β2 - antagonist	5 nM
β3 - antagonist	45 nM

Table 2: Detailed accounting of the monoamine receptor blockers' range and efficacy of action. The targets of Risperidone, Amisulpride and Pindolol are displayed next to the respective efficacy of the drug in blocking that target.

The experiments, which included the activation of monoaminergic signaling by administration of L-Norepinephrine hydrochloride (NE, Sigma – Aldrich, Munich, Germany) or 5-HT hydrochloride (Sigma – Aldrich, Munich, Germany) were performed with a similar control solution as described above. However, in this case, Cyclothiazide was excluded. This change was intended to limit the potential modulatory effects of Cyclothiazide on pre-synaptic potassium channels on the ANF membrane. Thus, the study of short-term plasticity would not be impeded by potential changes in the pre-synaptic AP duration and the resulting calcium influx I_{Ca}. To measure the effect of NE on endbulb glutamate release, 100 µM of NE were added in the bath solution, following the guidelines set by Leão et al., 2002 and their work on the immature rat calyx. 5-HT was administered at 10µM through the bath solution. The recordings of afferent fiber stimulation resumed after 3 minutes had passed after the exchange of the control solution for the one containing either neuromodulator.

2.2.3 Immunohistochemistry and immunofluorescence imaging

Coronal brain slices were used for immunofluorescent labelling. P15 – p23 pups were decapitated and after dissection the brain was cut at the pons – midbrain junction between the

cerebellum and the occipital lobe. The hindbrain block was immediately immersed in 2-Methylbutane (Sigma – Aldrich, Taufkirchen, Germany), which was brought to -20°C on dry ice. After snap-freezing the brain was transferred to a pouch made of aluminum foil, containing Tissue Tek mounting medium (Thermo-Fisher Scientific, Schwerte, Germany), where it was embedded for sectioning. 30µm thick sections were obtained with a Leica cryostat (Wetzlar, Germany), whose chamber and objective temperatures were set to -20°C and -22°C respectively. Sectioning advanced from caudal to nasal and all sections, obtained prior to the emergence of the 7th cranial nerve, were discarded (Fig. 11). When the 7th cranial nerve emerged the presence of the AVCN subdivision was confirmed using a stereomicroscope (Leica). All subsequent slices that contained the AVCN were picked up with electrostatically charged microscope slides (SuperFrost Plus, Thermo Fisher Scientific, Schwerte, Germany). For the positive control stainings of the Locus coeruleus (LC) and the medial Raphe nuclei, the same slices as those containing aVCN were used, since they conveniently contain substantially large parts of those regions. Where necessary, further sectioning into more nasal parts of the brain was performed. To prevent thawing, the microscope slides were instantly placed on the air vent outlets of the cryostat's sectioning chamber, where they remained until a batch of approximately 10 slides could either be transferred to the -20°C freezer for long term storage or directly fixed by immersion for 5 minutes in ice cold 3% heat-depolymerized Paraformaldehyde (PFA) diluted in PBS. The 150 µm thick slices with neurobiotin filled cells were instead fixed for 30 minutes in Formaldehyde (FA) at room temperature. Afterwards they were washed in PBS for 10 minutes to halt fixation and blocked with GSDB as described above. Subsequent steps were identical to what was described above, except for mounting, where double sided tape spacers of 120µm thickness were used to flank the slice before the application of Molwiol. This way, the coverslip's weight would not smash into the thicker tissue, which would result in better preservation of structural integrity of the brain tissue.

After fixation, the slides were kept for 10 minutes in ice cold PBS to halt fixation and then washed for 1 hour at room temperature in goat serum dilution buffer, which contained in 16% normal goat serum, 450 mM NaCl, 0.3% Triton X-100, and 20 mM phosphate buffer (PB, pH 7.4). The slides were then incubated in primary antibodies diluted in GSDB for 3 hours in a wet chamber at room temperature. Four washing steps followed that lasted 10 minutes each, two of them with wash buffer (450 mM NaCl, 0.3% Triton X-100 and 20mM PB) and two more with PBS.

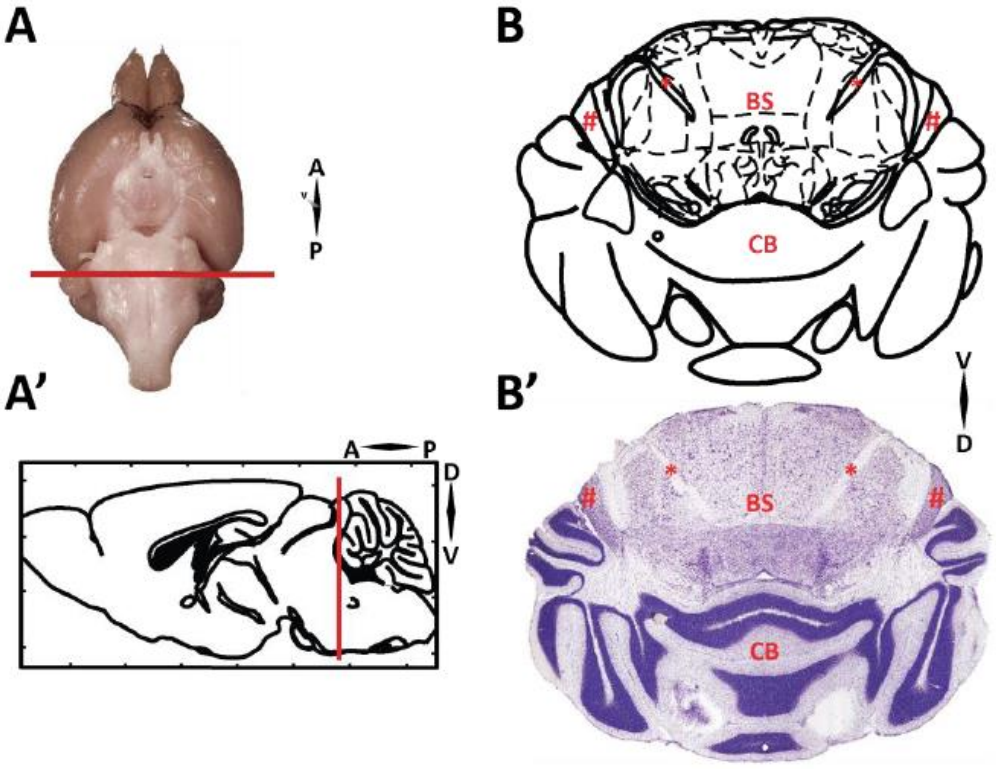

Figure 11: Preparation of sagittal slices of the aVCN. **A:** Ventral view of the mouse brain. The solid line indicates the target for the coronal sectioning on the mouse brain. **A':** Sagittal view of the mouse brain. The solid line indicates the position of interest for the coronal sectioning. **B:** Sketched coronal view of the mouse brain. **B':** Stained coronal section of the mouse brain showing the brain-stem (BS), cerebellum (CB), anterior ventral cochlear nucleus (aVCN, marked as #) and the 7th cranial nerve (facial nerve) that was used as a landmark during sectioning (marked as *).

The slides were then incubated with secondary antibodies overnight at 4°C and, afterwards, washed twice with Wash Buffer and twice more with PBS as before. Before mounting, the slides were maintained in 5mM PB for 10 minutes and were then mounted with a drop of Molwiol (Carl Roth GmbH, Karlsruhe, Germany) and covered with a thin glass coverslip.

Confocal and STED images were acquired using a three-colour confocal / two-colour STED microscope (Abberior GmbH), equipped with a 488 nm (Ar), a 561nm (He/Ne) and a 640nm excitation laser, a 775 nm laser for STED (1.2W) and a 100x oil immersion objective (1.4 NA, Olympus).

Unless otherwise stated, the antibodies used in this part of the study were purchased from Synaptic Systems GmbH, Göttingen, Germany. The specific antibodies used were:

Primary antibodies: mouse-anti-Norepinephrine transporter (NET, 1:200), rabbit-anti-vesicular monoamine transporter 2 (VMAT2, 1:200), rabbit-anti-tyrosine hydroxylase (TH, 1:200, Merck - Calbiochem), rabbit-anti-Serotonin transporter (5HTT, 1:500), guinea-pig-anti dopamine transporter (DAT, 1:200), guinea-pig-anti-vesicular glutamate transporter 1 (VGLut1, 1:1000), rabbit-anti-VGlut1 (1:200).

Secondary antibodies: streptavidin-AF-568-conjugate (1:500, Invitrogen molecular probes, Themo Fisher Scientific), goat-anti-guinea-pig 568 (1:200, Invitrogen molecular probes), goat-anti-rabbit 635p

(1:200, STED, Abberior, Göttingen, Germany), goat-anti-mouse 635p (1:200, STED, Abberior) goat-anti-rabbit 488 (1:200, Mobitec-Invitrogen).

2.2.4 Data analysis

Electrophysiology data were analysed using Igor Pro (Wavemetrics, Lake Oswego, OR, USA). Evoked release was analysed using custom Igor scripts, while miniature EPSCs were detected, analysed and plotted using Neuromatic (Rothman and Silver, 2018). Confocal z-stacks and STED images were processed with the NIH ImageJ software (Schneider et al., 2012). Figures were assembled for display using open source vector graphic software Inkscape (https://inkscape.org). The data were compared to normal distributions using the Jarque – Bera test and the variances were compared with F-test. Statistical significance of differences between groups of normally distributed data was determined by unpaired student's t-test. The Mann-Whitney U-test was used in the cases of non-normally distributed data. The threshold for statistical significance was $p < 0.05$ depicted on figures as *. **, ***, **** indicate p values smaller than 0.01, 0.001, 0.0001 respectively. Statistics were performed using MATLAB (Mathworks).

2.3 Results

2.3.1 Monoamine secretory varicosities in the mouse cochlear nucleus

Previous studies employed biochemical and immunohistochemical analysis of auditory brainstem tissue and identified the prominent presence of norepinephrine (NE) and serotonin (5-HT) in the ventral subdivision of the cochlear nucleus (Thompson and Thompson, 2001: cat; Klepper and Herbert, 1991: rat). To study the monoaminergic innervation in the mouse AVCN in detail, I performed immunohistochemistry on coronal cryosections and parasagittal vibratome sections of the mouse auditory brainstem. The vesicular glutamate transporter 1 was targeted by a guinea-pig anti-VGLUT1 antibody and used as a context marker for all the two-colour immunostainings. I aimed to identify monoamine releasing terminals in the close vicinity to VGLUT1 -positive large pre-synaptic terminals representing endbulbs of Held in the AVCN formed by ANFs on BCs. STED imaging of 20µm thick cryosections revealed the presence of vesicular monoamine transporter 2 (VMAT2) positive terminals in the direct vicinity of endbulbs and BCs (Fig. 12, A). Furthermore, immunolabeling against SERT (Fig. 12 C, STED) confirmed the presence of 5-HT releasing varicosities. NE transporter (NET) labelling resulted in clear identification of NE releasing varicose terminals (Fig. 12 B), but also showed large, dense appositions suggestive of clustering around the dendritic stalk of BCs (Fig. 12 F). To control for possible artefacts in the apparent morphology of the NET labelling, I imaged slices of the locus coeruleus (LC, Fig 2.3 G), the main source of NE in the brain. In the LC the anti-NET antibody labelled large structures with a hollow center, presumably the principal cells of the LC. Directly after the medial border of the LC, large appositions started to appear, similar to what was observed in the AVCN. I next used 150µm thick vibratome slices, to patch BCs and fill them with neurobiotin over 10 – 15 minutes. During the infusion with neurobiotin, I performed current clamp recordings to confirm the identity of the patched cell as a BC, via its electrophysiological properties. After removal from the microscope and 30 minutes of fixation the slices were stained with 488 – VGlut1, 568 – streptavidin and 635p – NET and imaged with a confocal microscope. This longer fixation effectively abolished large NET appositions, while the chains of varicose terminals were maintained (Fig. 12 H). I can, thus safely conclude that NET positive varicosities are diffusely projecting and apposed around the endbulbs and BC somata in the AVCN.

Dopaminergic innervation of the AVCN has not been reported thus far in the literature to our knowledge. Nevertheless, I stained 20 µM cryosections against tyrosine hydroxylase, the key enzyme involved in DA biosynthesis. I saw TH-positive appositions crowning endbulbs around a BC soma (Fig. 12 D). However, the presence of TH is not a specific identifier of dopaminergic signalling since DA is the substrate of Dopamine beta hydroxylase, the enzyme that synthesizes NE. I, therefore stained

against the dopamine transporter (Fig. 12 E) and found very weak or nonspecific signalling. This allowed us to verify that the TH positive varicosities are in fact NE releasing varicosities and that DA seems not to be released specifically in the vicinity of BCs in the AVCN. In order to verify the signal yielded in the NET, TH and SERT stainings, I labelled slices of the Locus coeruleus (Fig. 12 I, J) and the Medial Raphe nuclei (Fig. 12 K, L) respectively as positive controls.

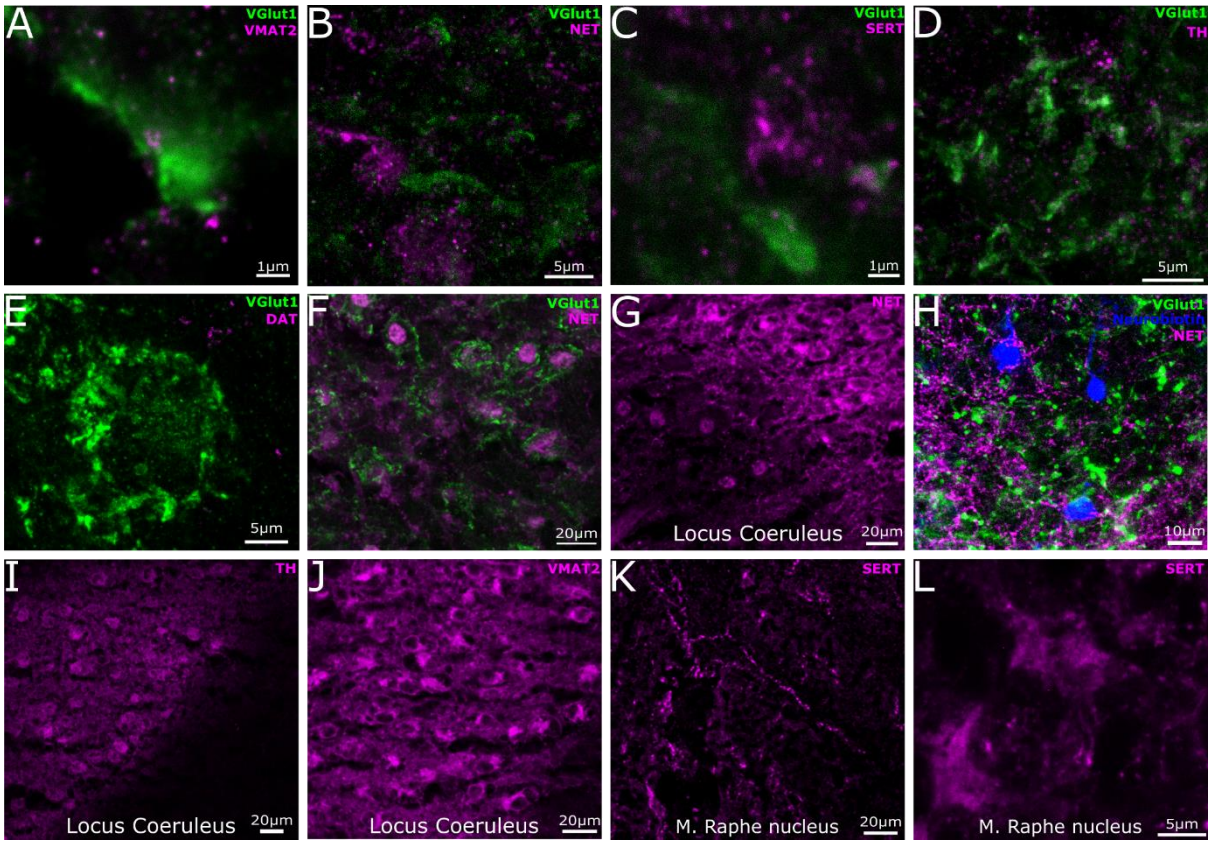

Figure 12: Serotonergic and Noradrenergic innervation of the anteroventral cochlear nucleus. STED and confocal immunofluorescence microscopy analysis of monoaminergic pre-synaptic terminals near bushy cells and endbulbs of Held. **A:** A Coronal brainstem section was imaged with STED microscopy. A large calyceal endbulb of Held terminal is depicted, labelled by VGLut1 (green). VMAT2 appositions (magenta) are localized near the endbulb at sub-micrometer distance. **B:** Confocal overview of NET positive (magenta) chains of varicosities, some of which appear juxtaposed to endbulbs of Held (green) that outline the BC soma. **C:** STED overview shows part of a BC soma outlined by an endbulb of Held. SERT positive terminals (magenta) are shown neighbouring the endbulb and also colocalizing with a smaller VGLut1 positive bouton-like structure. **D:** Maximal intensity projection from a confocal z-stack of an entire BC. The BC soma can be identified by the 3-4 endbulb terminals that surround it. One of the endbulbs appears to be crowned by puncta of tyrosine hydroxylase (magenta), indicating the presence of dopaminergic or noradrenergic transmission. **E:** Maximal intensity projection of a confocal z-stack shows endbulbs (green) surrounding a BC soma. There is little or no DAT (magenta) labelling, suggesting that there is no prominent direct dopaminergic innervation of the endbulb to BC synapse. **F:** Maximal intensity projection from An AVCN slice was imaged at 20x magnification. Endbulbs (green) indicate the position of BC somata. The signal from NET (magenta) outlines chains of varicose terminals that originate from the LC and project diffusely in the AVCN. Additionally, large dense appositions are observed on every principal cell of the AVCN that is depicted. **G:** A NET labelled slice of LC shows intense and widespread signal revealing cell-like structures with intense labelled membrane and a hollow center, which likely represents the cell nucleus of NE releasing neurons. At the medial border of the LC the signal is comprised chains of varicosities and dense oval-like appositions that were also seen in the AVCN. **H:** Confocal imaging of the surface layer of a 150µm thick vibratome AVCN slice. BCs were filled with neurobiotin through a patch pipette, the slice was fixed in FA for 30 minutes and stained with 568-strepatvidin (blue: BC somata), guinea pig- anti VGlut1 (green: endbulbs) and rabbit-anti-NET (635p: NE releasing terminals). The longer fixation that was applied in this case resulted in the absence of dense appositions of NET, suggesting that this pattern, as observed in F and G is an artefact of short fixation of the brainstem tissue. **I – L:** Positive control immunostainings of the LC where strong TH (**I**) and VMAT2 (**J**) labelling is expected. **K** and **L** depict the medial raphe nuclei where strong SERT labelling is found on the somata of groups of neurons that secrete 5-HT.

2.3.2 Preliminary results indicate an effect of monoamines on spontaneous release.

Next, I looked for direct proof of functional alterations of endbulbs due to monoaminergic innervation. To prove this, I started by employing pharmacological blockage of monoamine receptors. I reasoned that the postulated baseline monoamine release might exert an effect, which I can uncover by its pharmacological ablation. To that end, I used three compounds with a wide range of inhibitory action on monoaminergic receptors: Risperidone, Amisulpride and Pindolol (for details on their targets, see Fig. 13 and section 2.2 – materials and methods). I designed an experiment where I would apply all three of these blockers via the bath solution on acute slices of the AVCN. This way I would effectively deactivate any and all secondary messenger cytoplasmic cascades in response to monoamine binding to endbulbs that may affect the release of glutamate from the endbulb or the AMAR content on the BC membrane.

In a preliminary experiment with all 3 drugs, the mEPSC amplitude (Fig. 14 A_{ii}, B_{ii}, C) of one cell increased by 50% (Mean ± SEM; control: 58.49 ± 2.96 pA; n = 31, inhibition of monoamine signalling: 90.64 ± 2.65 pA, n=131). The frequency of mEPSCs (Fig. 14 A_i, B_i, D) was also affected and almost tripled (control: 1.92Hz, monoamine block: 5.43Hz) whereas mEPSC kinetics was unaltered. The change in frequency is indicative of a pre-synaptic effect and the increase in mEPSC amplitude points to a post-synaptic effect.

<u>Risperidone</u>

5-HT1A/B/D antagonist.	K_i – 14-400 nM
5-HT2A/B/C inverse agonist.	K_i – 0.2-60 nM
5-HT5A antagonist.	K_i – 200 nM
5-HT6 antagonist.	K_i – 2000 nM
5-HT7 antagonist (irreversible)	K_i – 7 nM
Adrenergic a1A/B antagonist	K_i – 5-9 nM
Adrenergic a2A/B/C antagonist	K_i – 1-100 nM
Dopamine D1 antagonist.	K_i – 240 nM
Dopamine D2/3/4 antagonist.	K_i – 3.5-4.5 nM
Dopamine D5 antagonist.	K_i – 300 nM

<u>Amisulpride</u>

5-HT1B/D antagonist.	K_i – 1700 nM
5-HT2B antagonist.	K_i – 13 nM
5-HT7 antagonist/inverse agonist.	K_i – 11 nM
Adrenergic a2A/C antagonist.	K_i – 1500 µM
Dopamine $D_{2/3}$ antagonist.	K_i – 3 nM

<u>Pindolol</u>

5-HT1A antagonist.	K_i – 15-80 nM
Adrenergic b1 antagonist.	K_i – 2 nM
Adrenergic b2 antagonist.	K_i – 5 nM
Adrenergic b3 antagonist.	K_i – 45 nM

Figure 13: Pharmacological block of monoamine receptors with blockers. Risperidone, Amisulpride and Pindolol with a list of their targets and Ki concentrations.

I expected that the 3-blocker approach would potentially result in concomitant activation and inhibition of modulatory pathways. I reasoned that blocking such a wide range of receptors could elicit a simultaneous response through G_α, G_i, or G_{aq}. The fact that I already saw a preliminary result was encouraging, but further scrutiny with this approach would be halted by issues with the interpretation

of the data. I, therefore reverted to single drug experiments, using the atypical antipsychotic Risperidone and recorded mEPSCs at V_{hold} = -70mV. As shown in Fig. 13, Risperidone still blocks all 5-HT and DA signalling, but spares the noradrenergic β-receptor pathways, which have been involved in the regulation of plasticity before. What could be readily observed as a result of this manipulation (Fig. 14 E_i, F_i, H) was an increase of the mEPSC frequency (control: 5.93 ± 1.03 Hz, Risperidone: 19.08 ± 1.52Hz), consistent with the above experiment with 3 blockers combined. Risperidone also increased the amplitude (Fig 2.3.3 E_{ii}, F_{ii}, G). In terms of kinetics, Risperidone caused a reduction of the rise time (Fig. 14 I, control: 123.52 ± 3.71 µs, Risperidone: 108.88 ± 3.39 µs), decay time (Fig. 14 J, control: 110.75 ± 8.13 µs, Risperidone: 86.81 ± 2.94 µs) and full width at half maxima (Fig. 14 K, control 283.05 ± 9.99 µs, Risperidone: 215.23 ± 3.92 µs). Risperidone is expected to spare NE signaling through β-adrenoreceptors. It is possible that allowing baseline neurotransmission through these receptors was what made all the difference between the two manipulations.

2.3.3 Evoked glutamate release at endbulbs of Held is mildly affected by the ablation of monoamine signaling

The preliminary effect on mEPSC frequency led me to further test the hypothesis that monoamines regulate the glutamatergic pre-synaptic terminals to adjust synaptic strength. Using a monopolar electrode, I performed afferent fiber stimulation and probed for the effect of the same blockers on evoked glutamate release at the endbulb of Held (Fig. 15 A, B). It became immediately apparent that the effects of the blockers are not as drastic on evoked release as I previously observed in preliminary experiments on spontaneous release. Specifically, the amplitude of the first eEPSC ($eEPSC_1$) from a 100Hz train of 50 stimuli was not significantly altered in the presence of Risperidone (Fig. 15 C, control: 3.46 ± 0.67 nA, Risperidone: 2.75 ± 0,38 nA).

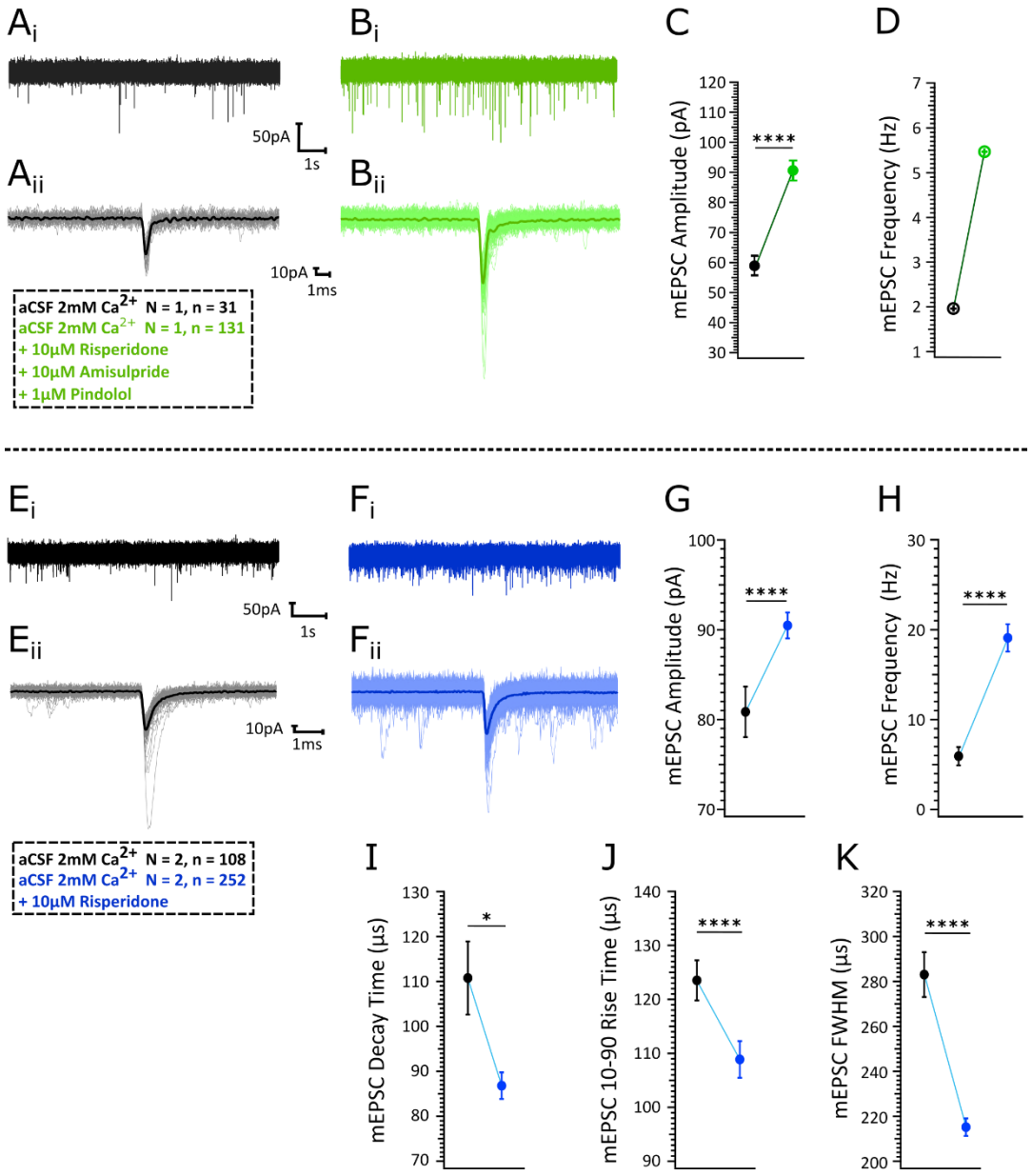

Figure 14 Bath application of monoamine receptor blockers alters spontaneous synaptic transmission at the endbulb of Held synapse. A_i, B_i: 10 second excerpt from a 60 second recording of mEPSCs of a BC held at -70mV and sequentially exposed to the control and the blocker containing solution (solution compositions are detailed in the box inset). **A_{ii}, B_{ii}**: The mEPSCs that were used for the calculation of kinetics are overlaid in light colours (gray and light green respectively) along the average waveform which is overlaid and displayed in darker colours (black and dark green). **C:** The amplitude of mEPSCs was increased due to the application of the 3 blocker compounds. The data points (black: control, dark green: monoamine block) represent the mean amplitude for all the mEPSCs captured in a 60 second recording. The error bars represent the standard error of the mean. **D:** The mEPSC frequency was increased in the absence of monoaminergic signalling. The circular data points represent single measurements of mEPSC frequency from a BC before and after the application of the monoamine receptor blockers. **E_i, F_i**: 10 second excrept from a 60 second recording of mEPSCs of a BC sequentially exposed to the control and the Risperidone containing solution (details in the box inset). **E_{ii}, F_{ii}:** Individual mEPSC traces are overlaid and displayed in gray (control) and light blue (Risperidone) along the average waveform which is overlaid and displayed in black (control) and dark blue (Risperidone). **G:** The amplitude of mEPSCs was increased due to the application of Risperidone. The grand mean of 2 cells is depicted by the dark dots and the error bars represent the SEM. **H:** Bath-applied Risperidone causes an increase in mEPSC frequency. It also resulted in shorter mEPSCs by affecting the Decay time (**I**), 10-90 Rise Time (**J**) and full width at half maxima (**K**). Data are plotted as mean estimates for all BCs included in the analysis. The error bars depict the standard error of the mean. Normality was tested with the Jarque–Bera test. Statistical significance for normally distributed data was tested with student's t-test, while for non-normally distributed the Mann-Whitney U-test was used instead. *n.s. $p \geq 0.05$; *$p < 0.05$, **$p < 0.01$, ***$p < 0.001$, ****$p<0.0001$, N: number of BCs, n: number of pooled mEPSCs.*

What was consistent with the effect of Risperidone on mEPSCs was a sharpening of the release kinetics, namely a significant reduction in the eEPSC 10-90 rise time (Fig. 15 D, control: 191.99 ± 3.76 µs, Risperidone: 175.59 ± 3.06 µs; *p=0.017, student's t-test*). The change in rise time was not followed by alterations of decay time or FWHM. I calculated the time difference between the stimulus artifact and the time point where the eEPSC amplitude reaches 10% as a consistent proxy for synaptic delay. This measurement uncovered a tendency towards shorter synaptic delay in the presence of Risperidone compared to control, which, however, did not reach statistical significance (Fig. 15 E). Neither the amplitude nor the kinetics of evoked release changed during the incubation with the 3 blockers (Fig. 15 B).

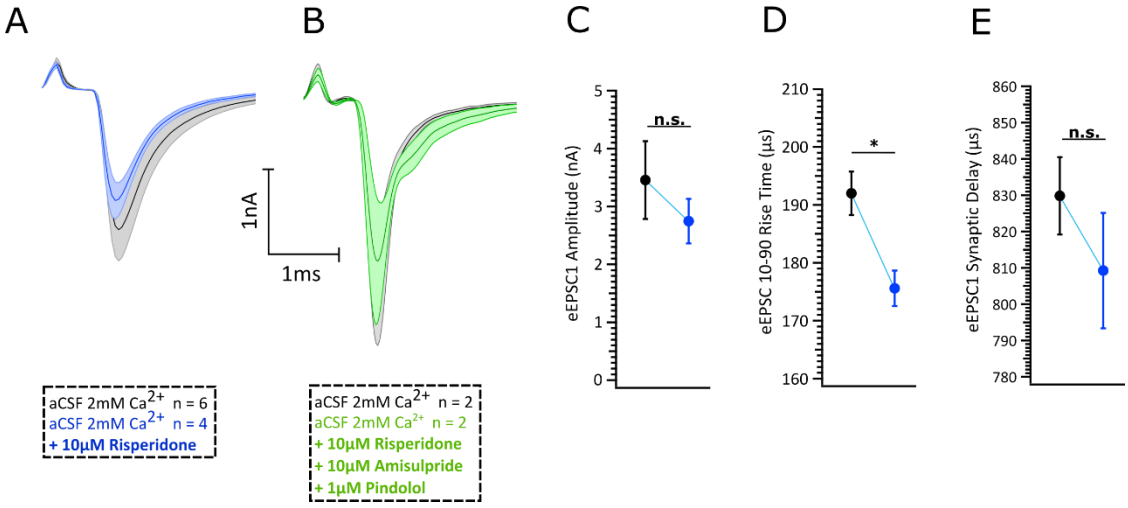

Figure 15: Bath application of monoamine receptor blockers affects the kinetics of evoked release. A, B: ANFs synapsing on BCs were stimulated at a frequency of 100Hz. The resulting trains of eEPSCs were averaged and the $eEPSC_1$ waveform was plotted. The thinner lines outlining the filled light-coloured areas represent the SEM. Data are plotted as mean estimates for all BCs included in the analysis. The error bars depict the standard error of the mean. The amplitude and kinetics of $eEPSC_1$ was not altered when Risperidone, Amisulpride and Pindolol were applied simultaneously. **C:** When BCs were exposed to only Risperidone, the $eEPSC_1$ amplitude was comparable to that measured with the control solution. **D:** Switching from control to Risperidone supplemented solution resulted in faster $eEPSC_1$ kinetics. The 10-90 rise time was significantly reduced when endbulb – BC synapses were exposed to the blocker. **E:** The synaptic delay, which is the time difference between the stimulus artefact and the onset of the eEPSC tended to be shorter during Risperidone incubation, but the difference was not statistically significant. Data are plotted as grand mean estimates from the pooled averages of all the BCs included in the analysis. Normality was tested with the Jarque–Bera test. Statistical significance for normally distributed data was tested with student's t-test, while for non-normally distributed the Mann-Whitney U-test was used instead. *n.s. p ≥ 0.05; *p < 0.05, **p < 0.01, ***p < 0.001, ****p<0.0001, n: number of BCs.*

2.3.4 Evoked release after 5-HT or NE exposure

The experiments with inhibitors of monoaminergic receptors involvement of monoaminergic neuromodulation in the AVCN and specifically at the endbulb of Held – BC synapse. Co-application of

Amisulrpide, Pindolol and Risperidone or sole application of Risperidone led to an increase of the mEPSC frequency and the latter also affected the kinetics of evoked release.

To further disentangle the intricate mechanism of monoaminergic modulation, I chose to apply 5-HT and NE through the bath solution. Previously the quantal concentration of dopamine that could reach nearby receptors was estimated at 1µM (reviewed in Liu et al., 2021). I reasoned that 5-HT and NE, which are also released by varicosities, need to reach at least similar concentrations to affect receptors in the direct vicinity. I decided to use higher than physiological concentrations of either NE and 5-HT (100µM and 10µM) and compared the evoked release of glutamate from endbulbs of Held before and after the application of each neuromodulator. The effects of pre-synaptic neuromodulation of glutamatergic terminals by 5-HT and NE were recently investigated on autaptic human IPSC neurons in culture (Patzke et al., 2019). A bi-directional manipulation of evoked glutamate release was reported via the pre-synaptic neuromodulator-mediated change in the levels of cAMP and PKA dependent phosphorylation of Syn1. Following the same thread, I expected to detect opposing effects of 5-HT and NE at the mouse endbulb of Held synapse.

However, when I incubated mouse AVCN slices with 5-HT supplemented aCSF, the amplitude of evoked release was not significantly affected by the manipulation (Fig. 16 A_i, B_i, control: 1.72 ± 0.23 nA, 5-HT: 1.45 ± 0.34 nA, *p = 0.59, Mann-Whitney U-test*). Similarly, the 10 ms ISI PPR, a rough proxy of SV release probability was statistically indistinguishable between 5-HT treated and control synapses (Fig. 16 C_i, control: 0.92 ± 0.05, 5-HT: 1.07 ± 0.13, *p =0.2, student's t-test*). While facilitating trains of eEPSCs seemed more prevalent during 5-HT incubation, when the data were pooled and statistically compared, the observed trend of higher PPR was not found to be significant. Unlike the effects of Risperidone, 5-HT did not affect the kinetics of evoked SV release. The synchronous nature of endbulb SV release was unaffected, shown by the comparable $eEPSC_1$ synaptic delay (Fig. 16 D_i, control: 1004.79 ± 33.93 µs, 5-HT: 985.62 ± 39.24 µs, *p = 0.82*) and 10-90 rise time (Fig. 16 E_i, control: 214.31 ± 13.90 µs, 5-HT: 215.92 ± 32.60 µs, *p = 0.24*). The decay time (Fig. 16 F_i) and the FWHM (Fig. 16 G_i) were not affected by the 5-HT incubation. This could indicate either that the closing kinetics of AMPARs are not directly modulated at the BC soma, or that whatever effect is there cannot be detected while the synaptic cleft is flooded with glutamate perhaps due to the recruitment of other, potentially opposing modulatory signals, such as mGLURs.

Another set of afferent fibers were stimulated while being sequentially exposed first to control solution and immediately after to aCSF supplemented with 100 µM NE. It was previously reported that NE reduces eEPSC amplitudes at the immature rat calyx (Leão and Von Gersdorff, 2002) as well as the PPR and increases the RRP size of glutamatergic parallel fiber to granule cell synapses in the mouse cerebellum (Martìn et al., 2019). In stark contrast to those observations, panels A_{ii} and B_{ii} of Figure 2.7

show that neither the $eEPSC_1$ amplitudes (control: 1.72 ± 0.23 nA, NE: 2.06 ± 0.71 nA, *p > 0.5*) nor the PPR (control: 0.92 ± 0.05, NE: 0.97 ± 0.08, *p = 0.97, Mann-Whitney U-test*) were significantly altered when the synapses were exposed to 100 µM of NE. The non-significant trend toward larger amplitudes of NE $eEPSC_1$ seems to particularly contrast findings by Patzke et al., (2019).

The bath-application of NE did not significantly alter the kinetics of evoked release. Consistently through our "before-after modulation" recordings, the synaptic delay values of individual synapses observed during NE exposure tended to decrease compared to those observed from the same cells in control solution, but it did not reach statistical (Fig. 12 D_{ii}, control: 1004.79 ± 33.93 µs, NE: 921.22 ± 45.63 µs, *p = 0.21*). No significant differences were observed in the 10-90 Rise time (Fig. 12 E_{ii}), Decay time (Fig. 12 F_{ii}) or FWHM (Fig. 12 G_{ii}). Interestingly, the trial-to-trial variability, measured as the coefficient of variation (C.V.) for of the $eEPSC_1$ amplitude was significantly reduced in the presence of NE (control: 0.19 ± 0.03, NE: 0.07 ± 0.01, ***p = 0.0038***, Student's t-test). There was no significant change of $eEPSC_1$ C.V. upon 5-HT application (control: 0.19 ± 0.03, 5-HT: 0.12 ± 0.02, *p = 0.0935*, Student's t-test). Unlike the variability of eEPSC amplitude the 10ms ISI PPR variability was not affected by either neuromodulator.

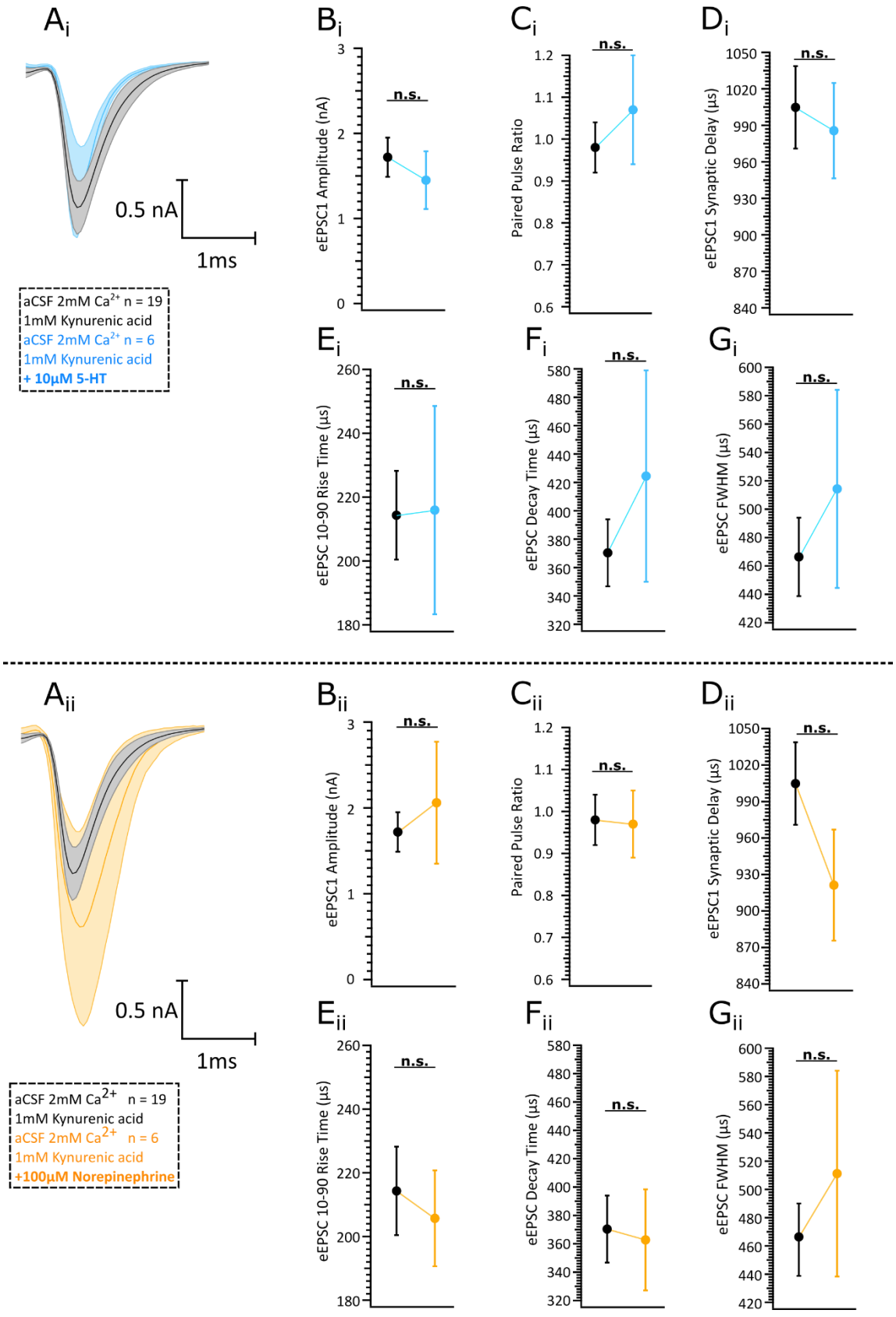

Figure 16: Bath application of neuromodulators does not affect the kinetics of evoked release at the endbulb of Held. A_i, A_{ii}: The $eEPSC_1$ of average 100Hz trains are plotted as thick black (control) and blue (5-HT) lines. The thinner lines outlining the filled light-coloured areas represent the SEM. **B_i, B_{ii}**: The amplitude of endbulb eEPSCs recorded from BCs during exposure to monoamines is comparable to that of eEPSCs recorded during bath application of 1mM Kynurenic acid. **C_i, C_{ii}**: The paired

pulse ratio, calculated by dividing the amplitude of $eEPSC_2/eEPSC_1$, was not affected by the exposure to monoamines. **D_i, D_{ii}**: The time needed from the arrival of the stimulating pulse until the onset of the eEPSC, called the synaptic delay was neither affected by bath-applied 5-HT nor NE. **E_i, E_{ii}, F_i, F_{ii}, G_i, G_{ii}**: Endbulb eEPSCs recorded from BCs at near physiological temperature have stable kinetics through long recordings with 1mM kynurenic acid (black) and subsequent exposure to either 5-HT or NE. Data are plotted as grand mean estimates from the pooled averages of all the BCs included in the analysis. Normality was tested with the Jarque–Bera test. Statistical significance for normally distributed data was tested with student's t-test, while for non-normally distributed the Mann-Whitney U-test was used instead. *n.s. $p \geq 0.05$; *$p < 0.05$, **$p < 0.01$, ***$p < 0.001$, ****$p<0.0001$, n: number of BCs.*

2.3.5 Short-term plasticity during train stimulation is largely unaffected by 5-HT and NE application

A core feature of the endbulb of Held synapse is its rather stereotyped pattern of short-term depression. Due to the high release probability of the endbulb SVs, most of the high P_{vr} vesicles fuse during the first few stimuli of a train. This can be appreciated for the exemplary responses to 50, 100 and 200 Hz stimulation in panels A_i, B_i and C_i of Figure 2.8. After the first few eEPSCs, the ones following have 60% or less of the amplitude of the largest eEPSC in the train. This was true also for the trains recorded from endbulbs that were exposed to 5-HT (Fig. 17 A_{ii}, B_{ii}, C_{ii}) and NE (Fig. 17 A_{iii}, B_{iii}, C_{iii}).

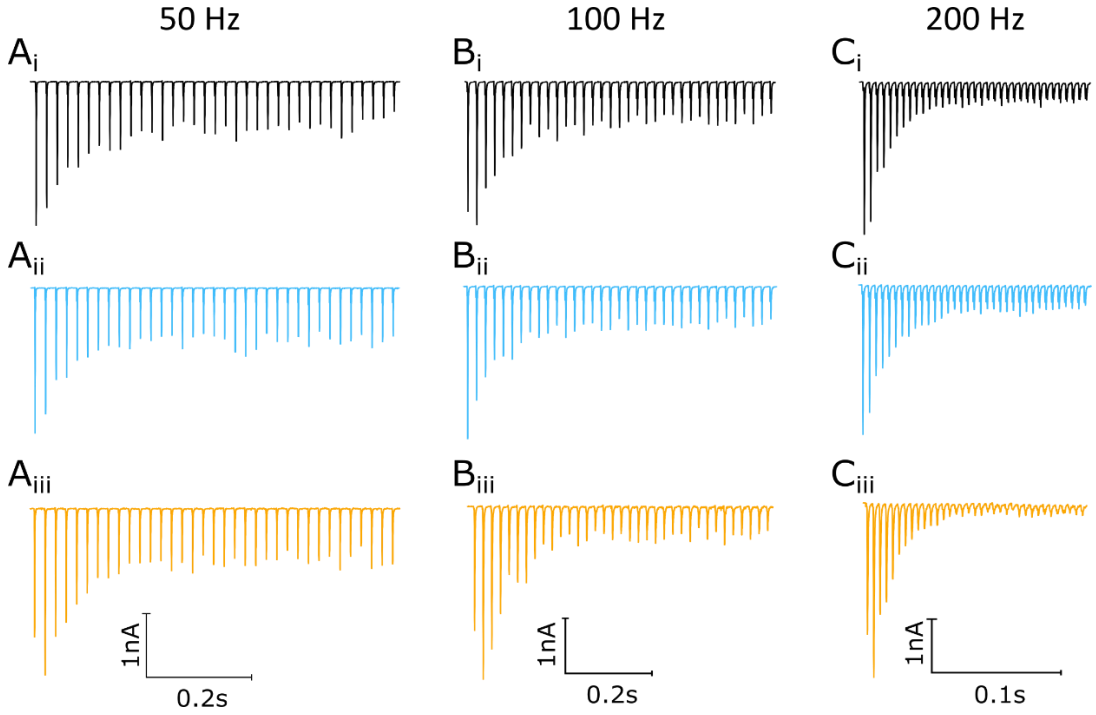

Figure 17: Analysis of release probability and RRP size. A_i, B_i, Ci: Representative traces of eEPSCs in response to trains of 35 stimuli delivered at 50 Hz (Ai), 100 Hz (Bi) and 200Hz frequencies. The trains recorded from a BC that was exposed to 1mM Kynurenic acid dissolved in aCSF containing $[Ca^{2+}]$. **A_{ii}, B_{ii}, C_{ii}:** Representative traces eEPSCs recorded from BCs exposed to the same aCSF containing 1mM Kynurenic acid, which was additionally supplemented with 10µM 5-HT. **A_{iii}, B_{iii}, C_{iii}:** Representative traces eEPSCs recorded from BCs exposed to the same aCSF containing 1mM Kynurenic acid, which was additionally supplemented with 100µM NE. The effects of the two neuromodulators on the short-term plasticity of the endbulbs of Held were calculated using the SMN and EQ methods as described in the publication attached to chapter 1 of this thesis. The results from pooling all the traces of control, 5-HT and NE treated synapses are quantified in Table 3.

I used the SMN and EQ methods to quantify the release probability, size of the readily releasable pool, the tau of the exponential depression of eEPSC amplitudes and the replenishment rate of SVs into the RRP. RRP size, calculated with both methods was unaltered by 5-HT and NE exposure (Table 3). The SV release probability, calculated with the EQ method was also unchanged between the three conditions. The SMN method returned an increased P_{vr} at 50 Hz frequency in synapses exposed to 5-HT, whereas a similar trend for NE did not reach statistical significance. This change of P_{vr} did not persist in 100 and 200 Hz frequency of stimulation. Interestingly, at 200Hz frequency of stimulation, 100 µM NE caused a small, yet significant decrease in the SMN estimate of P_{vr} and, consistent with a reduced P_{vr}, an increase in the tau (τ) of depression.

Frequency	Parameter	1mM Kynurenic acid	1mM Kynurenic acid + 10 µM 5-HT	1mM Kynurenic acid + 100 µM NE	P-values	
50Hz	**RRP EQ**	266.69 ± 44.26	187.59 ± 51.39	229.39 ± 50.60	0.31 T	0.62 T
	P_{vr} EQ	0.15 ± 0.1	0.17 ± 0.03	0.15 ± 0.01	0.63 T	0.81 T
	RRP SMN	129.96 ± 23.85	76.36 ± 19.23	94.14 ± 17.94	0.12 T	0.28 T
	Tau	3.46 ± 0.31	2.77 ± 0.34	3.24 ± 0.42	0.34 M	0.90 M
	P_{vr} SMN	0.26 ± 0.02	0.40 ± 0.03	0.34 ± 0.04	***0.005 T***	0.19 T
	Replenishment	0.64 ± 0.08	0.54 ± 0.13	0.51 ± 0.07	0.56 T	0.27 T
100Hz	**RRP EQ**	254.08 ± 39.13	168.20 ± 45.41	269.84 ± 48.05	0.22 T	0.23 M
	P_{vr} EQ	0.17 ± 0.01	0.22 ± 0.02	0.16 ± 0.03	0.11 M	0.54 T
	RRP SMN	164.98 ± 27.21	112.03 ± 32.50	151.74 ± 41.33	0.28 T	0.49 T
	Tau	4.32 ± 0.29	3.96 ± 0.62	4.64 ± 0.33	0.65 T	0.43T
	P_{vr} SMN	0.26 ± 0.02	0.29 ± 0.04	0.26 ± 0.04	0.62 T	0.85 T
	Replenishment	0.94 ± 0.11	0.90 ± 0.20	0.84 ± 0.12	0.998 T	0.77 M
200Hz	**RRP EQ**	219.92 ± 39.28	253.70 ± 73.53	206.95 ± 28.68	0.85 M	0.91
	P_{vr} EQ	0.23 ± 0.01	0.20 ± 0.03	0.18 ± 0.03	0.36 T	0.498 M
	RRP SMN	178.12 ± 29.43	204.30 ± 66.06	152.15 ± 31.53	0.75 T	0.62 T
	Tau	3.98 ± 0.22	4.83 ± 0.55	4.77 ± 0.15	0.23 T	***0.021 T***
	P_{vr} SMN	0.26 ± 0.02	0.22 ± 0.03	0.20 ± 0.01	0.44 T	***0.012 T***
	Replenishment	1.13 ± 0.16	1.04 ± 0.19	0.63 ± 0.28	0.74 T	0.27 T

Table 3: Quantification of Short-term plasticity analysis: Tau (t): time constant of single exponential fit to the decay of eEPSC during the stimulation train. Replenishment: rate of vesicle replenishment. RRP: readily releasable pool. Pr: release probability. PPR: paired pulse ratio, amplitude of the second EPSC of the train normalized to the amplitude of the first EPSC. Data are presented as grand mean ± SEM, derived from averaging over the mean estimates of all the BCs included in the analysis. The data distribution was compared to a normal distribution with the Jarque–Bera test and the comparability of the variances was verified with the F-test. For data that could not be distinguished from a normal distribution, the statistical significance of differences was tested with unpaired Student's t test (shown in the table as T). For data that were not normally distributed, the Mann–Whitney U test was used instead (shown in the table as M). A value of $p = 0.05$ was set as the threshold for statistical significance. Statistically significant differences are shown in bold italics.

2.3.6 NE, not 5-HT slightly slows down the recovery from RRP depletion

In order to further scrutinize the RRP dynamics and how they may be modulated by neuromodulators, I studied recovery from short-term depression. Since the endbulb of Held synapse naturally responds to high frequency of stimulation I used 100Hz trains of 50 stimuli to deplete the RRP and subsequently delivered a test pulse resulting in an eEPSC in different intervals after the last stimulus of the main train (Fig. 18 A, B). The intervals used were 25, 50, 75, 100, 250 ms to assess fast recovery from depression. I also used 1, 2, 4, 8, 10, 12 and finally 16 second intervals, at which point the eEPSCs were identical in amplitude to those recorded at the beginning of the 100Hz train.

I tracked the ratio of recovery calculated as $eEPSC_{test}$ / $eEPSC_1$. The recovery ratio average estimates for control and 5-HT were fitted with double exponential. The double exponential fit yields a fast and a slow component of recovery from depletion. Consistent with the finding of unaltered SV replenishment from the SMN analysis, recovery was not affected by 5-HT. The estimates at each recovery interval were comparable between control and 5-HT conditions (Fig. 18 C). There was a trend towards faster recovery in the sub second range (fast recovery: $\tau_{1\text{ - control}}$ = 150 ± 4ms, $\tau_{1\text{ – 5-HT}}$ = 46.4 ± 13ms) but none of the mean recovery ratio estimates at individual intervals was significantly altered due to 5-HT.

Next, I tested the effect of NE on recovery by recording first in 1mM kynurenic acid and then switching the bath solution to aCSF supplemented with 100µM NE and repeating the recording on the same cells. I was surprised to find that at the endbulb of Held the recovery ratio at the 2 seconds interval was significantly lower than control (Fig. 19 C). When I tried to fit the trajectory of the recovery ratio of control conditions, I got, as before the lowest chi-square values with a double exponential fit. The recovery data from the NE incubation were, on the other hand, better fitted using a single exponential fit. Taken together these findings suggest that NE slows the recovery from short term depression.

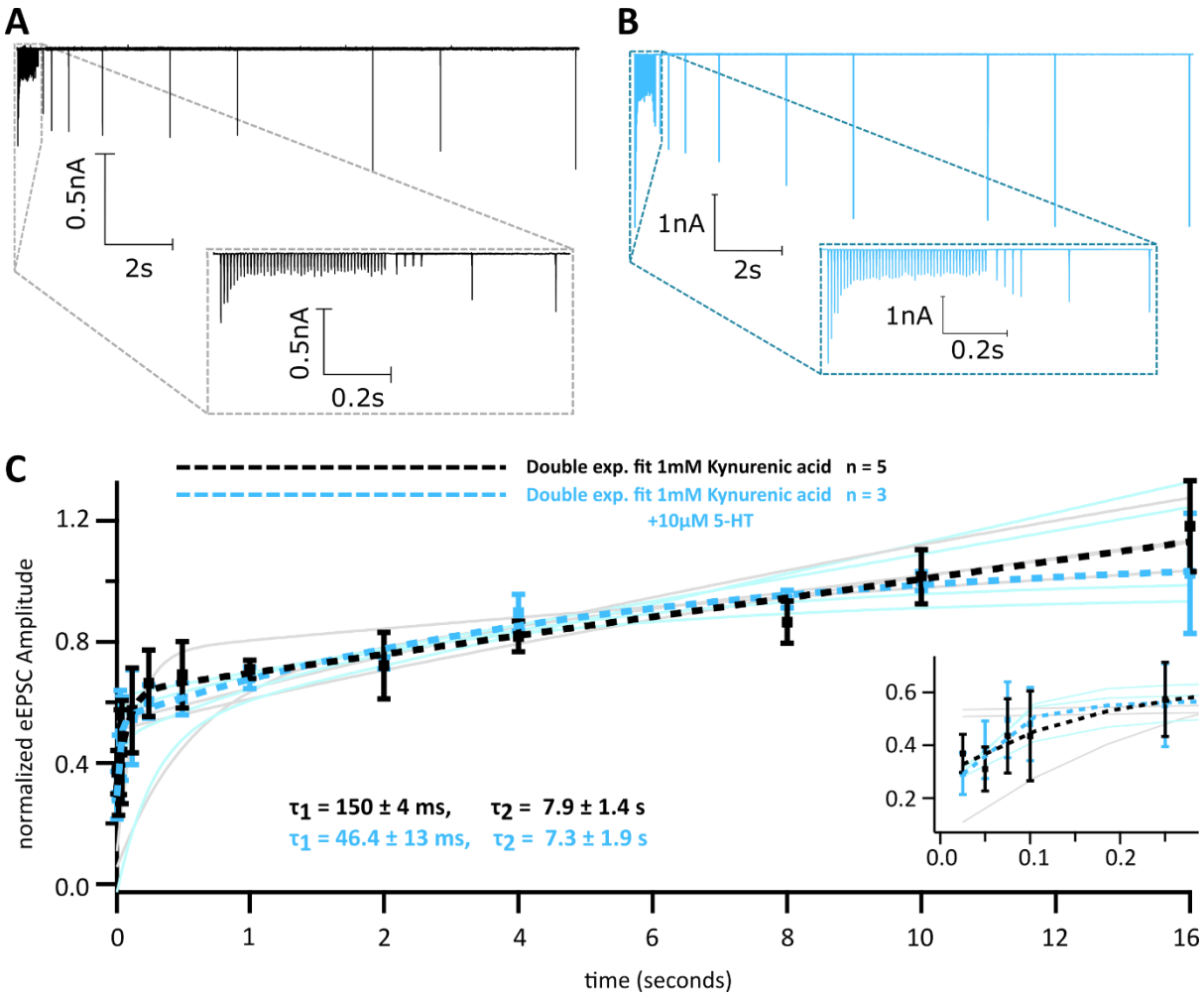

Figure 18: Analysis of recovery from short term depression during activation of serotonergic signalling by 5-HT. A, B: Averaged traces of eEPSCs elicited by trains of 50 stimuli delivered at 100Hz stimulation frequency. The main train is followed by test pulses delivered at 0.025, 0.05, 0.075, 0.1, 0.25, 0.5, 1, 2, 4, 8, 10, 12 and 16 second intervals. The test pulses are overlayed on the main train and a small inset shows a zoomed in version of the same average trace, in the shorter interval range. **C:** The double exponential fits are plotted as dashed lines against the recovery interval duration. Data are plotted as grand mean of per-cell average recovery estimates ± SEM. Fits from single cells are also overlayed in gray (Kynurenic acid) and light blue (5-HT). The tau of each component is given as a text box inset below the fits. Details regarding the type of fit and the composition of the bath solutions used in these recordings are given as a text box inset between panels A, B and C. The data distribution was compared to a normal distribution with the Jarque–Bera test and the comparability of the variances was verified with the F-test. For data that could not be distinguished from a normal distribution, the statistical significance of differences was tested with unpaired Student's t. For data that were not normally distributed, the Mann–Whitney U test was used instead. A value of *p = 0.05* was set as the threshold for statistical significance. *n = number of cells*

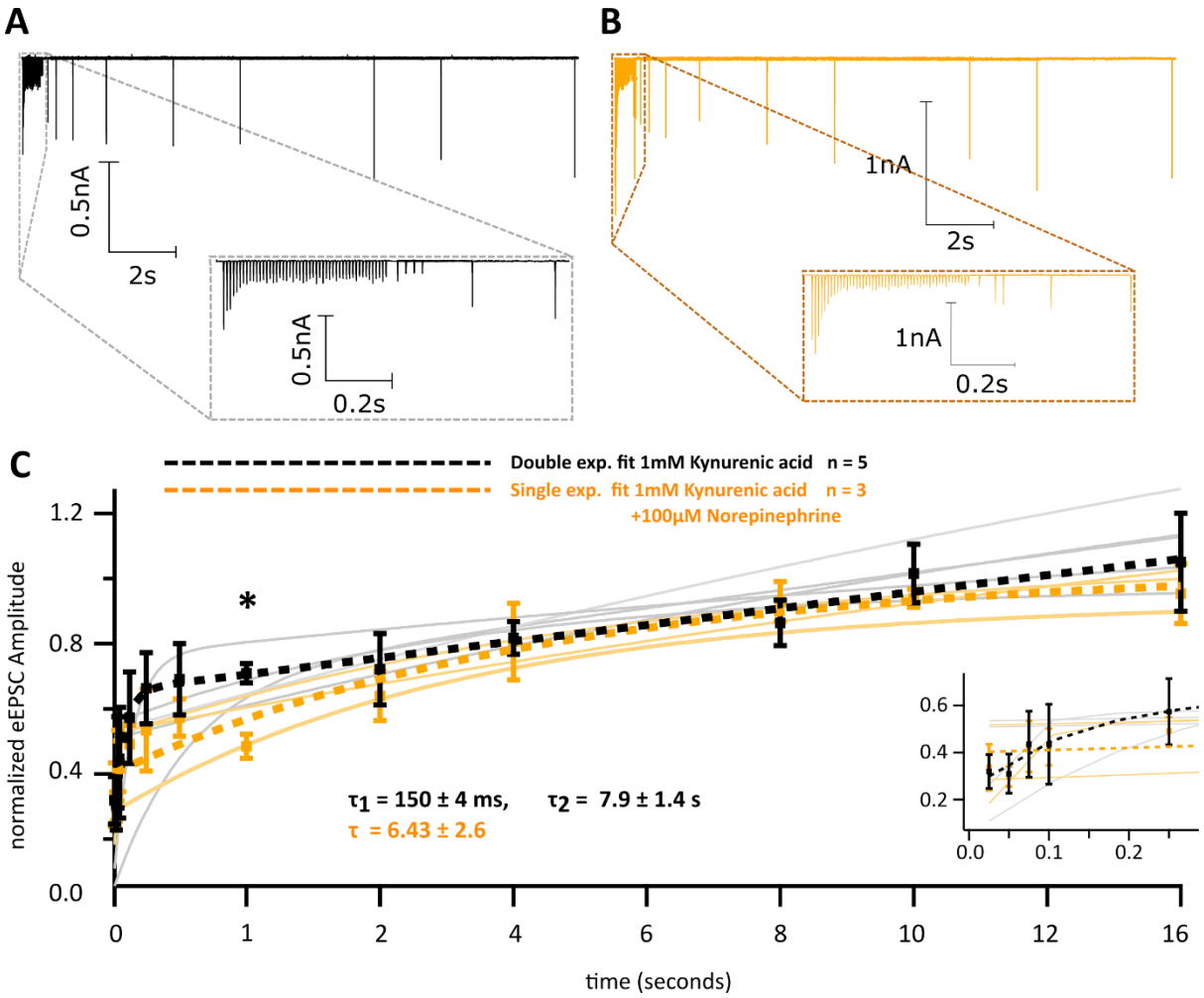

Figure 19: Analysis of recovery from short term depression during activation of serotonergic signalling by NE. A, B: Averaged traces of eEPSCs elicited by trains of 50 stimuli delivered at 100Hz stimulation frequency. The main train is followed by test pulses delivered at 0.025, 0.05, 0.075, 0.1, 0.25, 0.5, 1, 2, 4, 8, 10, 12 and 16 second intervals. The test pulses are overlayed on the main train and a small inset shows a zoomed in version of the same average trace, in the shorter interval range. **C:** The double exponential fits are plotted as dashed lines against the recovery interval duration. Data are plotted as grand mean of per-cell average recovery estimates ± SEM. Fits from single cells are also overlayed in gray (Kynurenic acid) and light orange (NE). The tau of each component is given as a text box inset below the fits. Details regarding the type of fit and the composition of the bath solutions used in these recordings are given as a text box inset between panels A, B and C. The data distribution was compared to a normal distribution with the Jarque–Bera test and the comparability of the variances was verified with the F-test. For data that could not be distinguished from a normal distribution, the statistical significance of differences was tested with unpaired Student's t. For data that were not normally distributed, the Mann–Whitney U test was used instead. A value of p = 0.05 was set as the threshold for statistical significance. *n = number of cells*

2.4. Discussion

The role of neuromodulators on synaptic transmission was studied at the endbulb of Held synapse. Initially, immunofluorescence, confocal and STED imaging provide evidence for the presence of serotonergic and noradrenergic varicosities innervating the AVCN. Preliminary experiments using blockers of monoamines provide support for the notion that baseline secretion of neuromodulators affects the fusogenicity of pre-synaptic SVs. Electrophysiological data from preliminary experiments support a neuromodulation of SV fusogenicity at endbulbs during baseline neurotransmission, by its pharmacological ablation. More solid, yet still preliminary experimental data show that neuromodulators do not affect evoked transmitter release, but mildly influence short-term synaptic plasticity and recovery from RRP depletion.

2.4.1 Neuromodulator releasing varicosities juxtaposed to the endbulb of Held – Bushy Cell Synapse

Previous fluorescent immunolabelling experiments in the cat (Thompson & Thompson, 2001) involved the stereotactic injection of the anterograde tracer biotinylated dextran amine (BDA) in the medial raphe nuclei, combined with concurrent visualization of 5-HT with fluorescein. Tissue processing involved transcranial perfusion with PFA. Similarly, in the rat, Klepper and Herbert (1991) employed immunofluorescent labelling of perfused brains targeting 5-HT and dopamine beta hydroxylase (dbh). Better tissue cytoarchitecture can be achieved by using perfused tissue and a better image of the entire chain of varicosities can be obtained by directly staining against the neurotransmitter itself.

In my study, I used methylbutane snap frozen brains to derive coronal cryosections and briefly fixed those sections by immersion in ice cold PFA, as was described before for successful stainings and semi-quantitative analysis of Munc13-1 at endbulbs (Mendoza Schulz et al., 2014). I expect to not achieve tissue preservation similar to that shown in perfused brains, but have so far observed that many antibodies against membrane bound, or, generally non-soluble markers function very well with this fixation protocol. To increase our chances of success I tracked monoaminergic innervation of the aVCN by labelling against known membrane bound proteins, which should be found only on monoaminergic terminals, namely the serotonin transporter (5-HTT), dopamine transporter (DAT) and norepinephrine transporter (NET). The presence of dopaminergic fibers cannot be excluded, but additional, explorative immunolabelling protocols must be explored to ensure that the signal from DAT stainings is specific and biologically meaningful. These results are consistent with an old biochemical study predicting predominant modulation by NE, a smaller presence of 5-HT and minor contributions by DA in the cochlear nucleus of the rat (Cransac et al., 1995). Our snap-freezing and

post-fixation protocol revealed very large appositions of NET directly on the soma of principal aVCN cells. I was tempted to interpret this signal as a specialized dendritic apposition. The beauty of imaging in the auditory brainstem is that the positive control, the staining of locus coeruleus against NET is dorsally positioned on the same slice as the aVCN. I imaged LC neurons and discovered that, while the membrane of noradrenergic neurons was labelled, as expected, at the medial border of the LC, non-specific nuclear labelling appeared on neurons of a neighbouring brain-stem region.

Turning to 150µM thick vibratome slices, I filled and labelled the BC soma and dendrites with neurobiotin – streptavidin and co-labelled VGLUT1 and NET. I employed longer fixation in this experiment and saw no co-localization of NET signal with the nucleus or dendrites of BCs. I conclude that LC neurons project with varicose fibers throughout the aVCN and do not form specialized axo – somatic or axo – dendritic terminals. This is consistent with the idea put forward by Ebert and Ostwald (1992), who predict that neuromodulation of the auditory brainstem is not specific to auditory function, but is, instead part of a generalized modulatory response.

Taken together, my confocal and STED imaging data provide the first morphological evidence in the mouse of noradrenergic and serotonergic varicosities being juxtaposed to the mouse endbulb of Held synapse. Future work should employ markers for inhibitory synapses to investigate whether modulation of endbulbs or BCs is to some extent occurring by modulatory effects on inhibitory terminals. The distances observed between the NET, 5-HT and vMAT2 positive varicosities and the endbulb VGLUT1 labelling would certainly allow this possibility.

2.4.2 Acute effects of abolishing baseline neuromodulator signaling

Years of treating affective disorders, such as depression or schizophrenia have yielded many anti-psychotic compounds, blocking a multitude of monoamine receptors and thereby addressing the pathophysiology. I turned to risperidone and amisulpride, two atypical anti-psychotic drugs that prevent serotonergic, dopaminergic and α-adrenergic signaling, targeting most known families of the respective receptors. I additionally applied Pindolol, a drug that is used in treatments of hypertension and is effective at blocking β-adrenergic neurotransmission. My approach was to gather proof-of-principle data for pre-synaptic neuromodulation of the endbulb of Held, by collecting recordings of eEPSCs from the same cells sequentially exposed to the control and blocker-containing bath solution. Maintaining a BC alive long enough for these recordings is well within the limits of our expertise. The limiting factor of these experiments is the health and robustness of the ANF that is being stimulated, which may run down or altogether stop releasing glutamate in the course of an experiment that is more than 30 minutes long. Therefore, my focus on gathering evoked release data in the presence of the blockers came at the cost of collecting mEPSC data by holding the cells at -70mV. In one BC that was stable for almost 50 minutes, I recorded mEPSCs and sequentially exposed first to control and

then to blocker-containing bath solutions. At physiological temperatures (33°C), the pharmacological abolition of baseline monoaminergic signaling resulted in higher frequency and amplitude of mEPSCs. The same effect was observed on two other BCs when Risperidone was applied without the addition of amisulpride and Pindolol, meaning that these two blockers are dispensable for blocking neuromodulation of spontaneous transmitter release. A temporal sharpening of mEPSCs, a reduction of their kinetics accompanied the changes of frequency and amplitude upon exposure to Risperidone. Hence, while our ability to draw cell-type specific and generalizable biological conclusions from a small number of recorded cells is limited, pooling the mEPSC kinetics and performing a paired comparison of before-after blocker incubation yielded some first indications for neuromodulation of the endbulb of Held synapse.

The upregulation of mEPSC frequency points to a pre-synaptic effect that is either independent of Ca^{2+} dependent priming, acting perhaps through alterations of Munc13-1 activity, or is capable of causing fluctuations of intracellular Ca^{2+}, by mobilizing Ca^{2+} release from intracellular stores. The pathway that fits this description and has been reported before to cause lasting facilitation of mEPSC frequency is the Ga_q PLC – PKC pathway (Hori et al., 1996), which may converge on Munc13-1 (Lipstein et al., 2021; Rhee et al., 2002). Activation of PLC would also increase intracellular levels of IP3 leading to release of Ca^{2+} from the endoplasmic reticulum. The broad range of monoamine receptors targeted by Risperidone could cause concurrent inhibition and activation of intracellular pathways to occur during its application. Activation of PLC through $G\alpha_q$ could be occurring alongside activation or inhibition of cAMP – Epac/PKA pathways through $G\alpha_s/G\alpha_i$ activation. The net outcome seems to be explained by a transition of some SVs to a tighter state of priming, which in the presence of baseline monoamine secretion would be reversed. It would be a stretch to claim that neuromodulators arrest spontaneous release, especially since total block of monoaminergic signaling does not account for the complex positioning of different receptors along the concentration gradients of the secreted monoamines (see section 2.1 and Fig. 10). A more detailed immunohistochemical study of receptor families and subtypes, their pattern of distribution at BC and endbulb membranes, as well as more functional data of endogenous monoamine release are needed to test this hypothesis.

The increased mEPSC amplitude and sharper kinetics may be due to alterations of the post-synaptic GluaA3-4 containing AMPARs. The possibility that blocking monoamines results in more AMPARs being incorporated in post-synaptic BC membrane islands, or that there is a spatial tightening or pre-existing AMPARs needs to be tested with superresolution microscopy, as a possible way to explain the faster 10-90 rise time. The fact that this effect persists in the probing of eEPSC kinetics means that even at close – to – saturating glutamate concentrations in the synaptic cleft, AMPAR activation, affinity or nano-columnar arrangement of the entire endbulb of Held is affected by the

absence of baseline monoaminergic signaling. The effects on mEPSC decay time may be explained by an increased speed of glutamate re-uptake, although a mechanism that would induce such a change based on monoaminergic receptor activation has not yet been described.

While baseline monoamine secretion seems to affect spontaneous release, the amplitude and decay time of AP – triggered Ca^{2+} – evoked release were not affected. A key consideration for the afferent fiber stimulation experiments is that one cannot exclude that, while stimulating ANFs with electrical pulses, concomitant evoked release of monoamines can also be stimulated. Perhaps the level of monoamine receptor blocking was not sufficient to obstruct monoaminergic signaling in the presence of higher neuromodulator concentrations. It is also possible that the higher glutamate concentrations create sufficient spillover away from the nanocolumnar organization of AZ – AMPAR PSDs to activate mGluRs, which have been shown to affect pre-synaptic release and post-synaptic excitability. The pre-synaptic effects of modulation can be isolated by including GDP-βs, a non-hydrolysable form of GDP in the intracellular solution of the BC patching pipette (Martín et al., 2020), which would help clarify and compare the effect of monoamines with described mGluR effects on Ca^{2+} – evoked release (Chanda et al., 2011). Another possible explanation is that evoked and spontaneous release are indeed dependent on different mechanisms of regulation (Kaeser and Regehr, 2013). Such a hypothesis will need to be tested by complicated experiments involving paired recordings and pharmacological manipulation of the pre-synaptic cytosolic milieu, for which the calyx of Held may be a more suitable system, primarily due to its larger size.

2.4.3 Saturating concentrations of NE and 5-HT do not acutely affect evoked neurotransmitter release at endbulbs of Held

Direct evidence of neuromodulation of auditory synapses by 5-HT and NE was already provided by two studies in the immature calyx of Held (Leão and Von Gersdorff, 2002; Mizutani et al., 2006). Both these studies contain recordings from immature calyces of Held performed at room temperature (25°C). I used similar concentrations of 5-HT and NE to characterize their effect on evoked release. In contrast to the findings at the calyx, neither NE nor 5-HT significantly changed the amplitude or kinetics of eEPSCs. I used post-onset of hearing mice, aged p15 – p23. Leão and Von Gersdorff (2002) reported a reduction of the NE effect on the calyx during development, which could also underlie the absence of evoked release modulation at endbulbs. I noted a significantly reduced trial-to-trial variability of eEPSC amplitudes, measured as the coefficient of multiple recordings from the same cell as well as a consistent yet non-significant reduction in synaptic delay. Considering that the spatial coupling between VGCCs and exocytosis tightens during postnatal development (Yu and Goodrich, 2014), both at the calyx and at the endbulb, it is possible that the effect of NE in mature calyceal synapses is to reduce variability and increase reliability of synaptic transmission. The

implications of such a change in reliability might result in BCs better coding the temporal features of a sound stimulus. Improved phase locking (Fettiplace and Fuchs, 1999; Kuenzel, 2019) might result from the release of NE, which would enable better sound localization, but such a hypothesis needs to be tested with more elegant experimental methods, involving optogenetic activation of endogenous monoamine release.

2.4.4 NE affects STP and recovery from pool depletion

My efforts to study the effects of neuromodulators on STP at endbulbs of Held were geared towards utilizing the sequential two step priming model that was developed by (Neher and Taschenberger, 2021) and used to recapitulate the variability of short – term plasticity and P_{vr} at the calyx of Held (Lin et al., 2022). To that end, I deviated from using Cyclothiazide in our aCSF based bath solutions and instead reverted to only supplementing aCSF with 1mM of Kynurenic acid, which should be sufficient to prevent post-synaptic receptor saturation and desensitization. While 19 BCs were successfully recorded in control solution with afferent fiber stimulation, using high frequency trains, conditioned trains and stimuli to measure recovery from train depletion, very few of them survived the sequential exposure to neuromodulator containing solutions (6 BCs fully recorded with 5-HT and 6 with NE). Thus, this preliminary dataset is not ready to be processed with non-negative matrix factorization and STP was instead analyzed using the Schneggenburger, Meyer, Neher estimations (Meyer et al., 2001) of P_{vr}, RRP, tau of depression and replenishment rate, as well as the Elmqvist & Quastel (Elmqvist and Quastel, 1965) estimations of RRP and P_{vr}. As such, I did not have access to recordings of 333 Hz to probe high frequency dependent depletion as I did, for example in the study of RIM-BP2 KO endbulbs' synaptic transmission (Chapter 1 and Appendix of this thesis).

The estimates yielded from 100Hz and 200Hz trains should sufficiently capture the neuromodulator induced changes in P_{vr}. However, the mild reduction of P_{vr}, caused by NE at 200Hz and the significantly increased P_{vr} caused by exposure to 5-HT, estimated at 50Hz should both be interpreted with caution. The SMN method does not account well for lower frequencies that do not sufficiently deplete the RRP. Judging from the data on RIM-BP2, a change in P_{vr} becomes more pronounced with increased frequency, which is not the case for the 100Hz and 200Hz trains during 5-HT exposure. It could be that at 50Hz frequency, the 20ms ISI is sufficient to cause a transition of reserve pool SVs to the LS state for many SVs, which was predicted to last 20 – 50 ms during sustained activity. This effect would not influence STP during shorter ISIs at 100 or 200Hz and would not be captured by the currently used estimates for P_{vr}, which assume that replenishment does not occur during the train, based on the depletion model for STP. Such speculation needs to be based on future results using the sequential priming model and be corroborated by changes in recovery from pool

depletion caused by 5-HT, which I have not detected thus far. I would therefore refrain from making a big claim on the finding that 5-HT enhances P_{vr}, until more data can support it.

On the other hand, even though there is also little data on STP during NE exposure, the resulting reduction of P_{vr} during 200Hz trains is reminiscent of the effect I observed when RIM-BP2 deficient endbulbs were exposed to high frequency trains, namely an exacerbation of P_{vr} reduction with higher frequency of stimulation. Such a putative effect of NE is better supported by the fact this neuromodulator slows down recovery from pool depletion. This result must be interpreted with caution, not only due to the limited number of recordings, but also because both some control and NE incubated synapses failed to release any SVs during the very short intervals of recovery. At two seconds interval there were no failures to generate eEPSCS, which allowed us to quantify a significant reduction in the recovery ratio caused by NE. However, to generate meaningful fits of the recovery ratio for all tested intervals, more recordings will need to be acquired. Recently, definitive proof for the role of Munc13-1 in recovery from SV pool depletion was shown by Lipstein et al. (2021). Considering the preliminary experiments with Risperidone that increased mEPSC frequency, I conclude that NE, through its release in the aVCN regulates fusogenicity of SVs, STP at high frequencies and the recovery from SV pool depletion at the endbulb of Held synapse.

General Discussion

Hans Held first described calyceal synapses in 1893 in his work: “Die Zentralle Gehörleitung”, describing the cytoarchitecture and neuronal connectivity of the lower central auditory pathway. Two synapses are now named after him, the endbulb of Held and the calyx of Held. Silver nitrate stainings of the calyx of Held inspired the famous drawings of this giant terminal by the father of modern neuroscience, Santiago Ramón y Cajal. They were brought to public view during his Nobel Prize lecture in 1906. Ever since, calyceal synapses have fascinated neuroscientists for many different reasons. Here at last, were easily accessible central synaptic terminals that one can manipulate with direct pre-synaptic measurements. They carry the heavy burden of transmitting information about the onset and phasic temporal properties of sound stimuli, employing tight regulation of Ca^{2+}- evoked release. Unique adaptations for increased synaptic strength in a single synaptic connection are the large size of these terminals and their many release sites, accommodated by their calyceal cytoarchitecture. They can generate huge post-synaptic responses that allow the scrutiny of pre-synaptic synaptic protein function based on the quantal theory of neurotransmitter release (del Castillo and Katz, 1954). Even though they were long thought of as accurate relays of ascending auditory information, they receive a multitude of inhibitory and modulatory inputs that affect sound processing and behavioural salience (Kuenzel, 2019). Due to their high release probability, they are uniquely poised for, and have indeed provided insights on short term plasticity and its influence on synapses, neuronal circuits, on the flow and encoding of information.

Bushy cell physiology and the encoding of sound localization

Bushy cells can be subdivided in spherical and globular bushy cells. The distinction is based on their morphology and physiology (Friauf and Ostwald, 1988; Smith et al., 1993). Large spherical BCs receive few large endbulbs of Held and are positioned rostrally in the aVCN, while small spherical BC receive smaller, but still few endbulbs, are located more caudally in the aVCN and have a smaller size, which led to their subcategorization. In mice, which lack low frequency hearing, the presence of large spherical bushy cells is extremely rare, making it very difficult to draw a clear distinction between SBC subtypes (Cao and Oertel, 2010a; Lauer et al., 2013). Experiments in cat and the Mongolian gerbil, which both possess pronounced low frequency hearing, allow a clear distinction between SBC subtypes (Bazwinsky et al., 2008; Sento and Ryugo, 1989). The size of the endbulbs that each bushy cell receives depends on the characteristic frequency, defined by the tonotopic position of the spiral ganglion neuron that extends an axonal terminal to them (Sento and Ryugo, 1989). Globular BCs receive always smaller endbulbs than SBCs, which have been named “modified” endbulbs of Held (Spirou et al., 2005).

ANFs and BCs can both be distinguished during in vivo recordings after exposure to sound stimuli, by their similar shapes of peri-stimulus histograms, which have a primary-like shape. The oscillatory nature of the mechanical stimuli that trigger IHC mechano-gated channels to open is reflected in their graded receptor potentials and the fusion rate of glutamate-containing SV fusion at their basal membrane. Thus, specific phases of the stimulus cycle are picked up by SGNs and BCs. Phase locking (Goldberg and Brown, 1969), describes the ability of a cell to consistently fire an AP, timed to coincide with a particular phase of the stimulus cycle. This can be measured by the vector strength, with values near 1 meaning perfect synchrony and values near 0 indicating no synchronous firing. Studies that performed comparisons of SGN and BC vector strength showed improved synchronicity in BCs compared to ANFs (Keine and Rübsamen, 2015; Kuenzel et al., 2011). Accurate transmission of phase information is necessary for the computation of ITDs at the MSO and localization of low frequency sounds in the azimuth plane. Timely transmission is also crucial for the timely stimulation by GBCs of the contralateral PNs of the MNTB through the calyx of Held (von Gersdorff and Borst, 2002). The resulting glycinergic output of PNs is coincidently detected at the LSO to enable ILD computation and high frequency sound localization on the azimuth plane. The accuracy of BCs and their ability to entrain to a stimulus, meaning to fire APs, without skipping stimulus cycles, even at high frequencies, depends on their physiological properties and the accuracy of their inputs.

Endbulbs of Held elicit very fast eEPSCs unto BCs, largely due to composition of the BC membrane, which hosts a high density of AMPARs containing $GluA_3$ subunits, with rapid on and off kinetics (Rubio et al., 2017). Endbulb eEPSCs have high initial P_{vr}, which is accompanied by pronounced short-term depression (Abbott and Regehr, 2004; Oleskevich et al., 2004; Wang et al., 2010; Yang and Xu-Friedman, 2009), yet very high Ca^{2+} dependent replenishment rates of SVs (Yang & Xu-Friedman, 2008, 2015). This becomes crucial during repetitive, high frequency stimulation and allows the endbulb to consistently generate eEPSCs. It is at this point of maximally depressed eEPSCs that entrainment probably depends on the convergence of inputs that BCs receive (Xu-Friedman and Regehr, 2005). In this context, the first part of this study becomes very relevant. The expression of RIM-BP2, a core CAZ protein, at endbulbs is responsible for positioning elements of the CAZ and Ca^{2+} in a tight cytoarchitectural configuration opposite of post-synaptic receptor islands, increasing the probability of post-synaptic AMPAR activation. Furthermore, through the postulated interaction with Munc13-1 (Brockmann et al., 2019), RIM-BP2 ensures fast replenishment of the SV pool during sustained high frequency activity. These effects were beautifully captured by systems physiology experiments, which show a reduction in the reliability of BC AP generation in response to a sound stimulus, when RIM-BP2 is absent from endbulbs of Held.

To enable entrainment, the BC AP must be shorter than the stimulus cycle. In BCs the $K_V3.1$ type of high-voltage activated K^+ channels ensure the rapid repolarization of an AP (Cao et al., 2007). A high specificity of AP firing to strong inputs is achieved by the expression of potassium channels of the K_V1 family (Cao et al., 2007a) which activate at low conductances and produce a high resting outward K^+ conductance, called low voltage activated K^+ conductance (g_{KVLA}). This conductance interacts with low voltage activated cation conductances (g_H) that produce slow depolarizing currents, shortening the BC refractory period (Cao et al., 2007a; Oertel et al., 2008) These elements contribute to the BCs low membrane resistance and fast time constants, limiting the time window for summation of subthreshold inputs, allowing only strong inputs, namely the converging endbulbs to drive the firing of BCs (McGinley and Oertel, 2006). Narrowband inhibition from tuberculoventricular cells of the DCN and wideband inhibition from D-Stellate cells of the VCN may shape the thresholds of BC firing, by targeting their namesake dendrites (Campagnola and Manis, 2014; Doucet and Ryugo, 2006). This might become crucial for shaping BC activity in vivo, where the P_{vr} of endbulbs is thought to be lower than what was observed in in vitro experiments (Borst, 2010).

The HCN channels that are expressed in bushy cells are modulated by the concentration of cAMP in the cytoplasm. As such they constitute a potential target for many modulatory systems that, acting through GPCRs (see 2.1.1) can regulate AP firing thresholds and timing at BCs. With that in mind, the second part of this study appears very important. Though I can show only pre-synaptic effects of neuromodulators thus far, future work will be directed in answering how 5-HT and NE can shape not only the transmitter release of endbulbs, but also the excitability and onset coding properties of BCs and how this is relevant for the function of the sound localization circuit.

Neuromodulation of STP and the implications for endbulb – Bushy Cell transmission

P_{vr} and STP shape the activity of synaptic terminals during sustained activity and the output of neuronal networks that encode features of sensory stimuli. While neuromodulation has been widely studied in the context of neuronal excitability (Brzosko et al., 2019), mechanistic is only starting to emerge on how neuromodulators affect feedforward plasticity, driven by pre-synaptic transmitter release (Abbott and Regehr, 2004; Patzke et al., 2019, 2021). Synapsin-1 has been identified as a key target for neuromodulation of the pre-synapse through G-protein pathways that control the intracellular concentration of cAMP (See 2.1.3β). This protein also participates in the formation of condensates in the pre-synaptic cytoplasm, a phenomenon which is named liquid-liquid phase separation. Whether these condensates form functional subcellular compartments or whether they act as reserves of functional proteins is still a matter of debate. Interestingly, many CAZ proteins contain domains that can form LLPS condensates (see General Introduction), among which one finds

RIM-BPs, ELKS and α-liprins. Notably, the phosphorylation of α-liprins by PKC can lead to recruitment of RIMS and Munc13s at membrane proximal condensates, potentially allowing the emergence of new release sites. Interestingly that interaction dissociates RIMs from condensates including RIM-BPs and the cytoplasmic tails of VGCCS. Such a pathway could, therefore bi-directionally control the availability of CAZ proteins at the membrane and the clustering of VGCCs at the membrane. Combined with the effects of Synapsin-1, which, when phosphorylated, mediates a reduction of SV clustering in the pre-synaptic terminal, these mechanisms could be the target of neuromodulation of many parameters that define STP. The pathway of neuromodulation through PLC – PKC, which could modulate Munc13-1 activity through DAG and the availability of CAZ proteins at the AZ through liprins and LLPS, is also an important, albeit underexplored avenue for neuromodulation. Of note is the fact that there are two splice variants of P/Q VGCCs, the main drivers of calyx and endbulb of Held synaptic transmission. $Ca_V2.1$ EFa and $Ca_V2.1$ EFb, generate synaptic depression and synaptic facilitation respectively in hippocampal neurons. In a neuron their relative amounts and contributions to pre-synaptic I_{Ca} are regulated in a homeostatic fashion (Thalhammer et al., 2017). The involvement of such a mechanism in the auditory brainstem has not yet been investigated, but is an interesting candidate mechanism for mediating the diversity of STP observed in calyceal terminals(Lin et al., 2022; Taschenberger et al., 2016; Yang and Xu-Friedman, 2012b)

Recent attempts to explain STP diversity between different types of synapses, or even synapses of the same kind were accompanied by a re-evaluation of the process of SV priming and neurotransmitter release (Neher and Brose, 2018; Neher and Taschenberger, 2021; Rizo, 2022). The two-step priming model, wherein RRP SVs undergo a transition from LS to TS is accompanied by models of Munc13-1 conformational changes from the perpendicular orientation relative to the plasma membrane to a slanted orientation. This change is favoured by the binding of DAG and Ca^{2+} to the C1 domain (Xu et al., 2017). The slanted orientation may bring SVs closer to the membrane, potentially making the clamping of Ca^{2+} evoked release by complexins and Synaptotagmins necessary to maintain a high P_{TS} (Rizo, 2022). The accumulation of residual Ca^{2+} during sustained activity and the potential modulation by $G\alpha_q$ – PLC – DAG and IP3 may affect the equilibrium between LS and TS states. The cAMP pathway may influence PKC activity through Epac2 and may thus promote the phosphorylation of many pre-synaptic target proteins, such as α-liprins, altering synaptic strength through LLPS.

Pre-synaptic $GABA_B$ receptors have been shown to modulate pre-synaptic I_{Ca} at endbulbs and calyces of Held, lowering P_{vr} and reducing AMPAR desensitization (Chanda et al., 2011; Takahashi et al., 1996). Crucially, this tuned BC function in vitro from a relay, needing input from one endbulb to fire an AP, to a co-incidence detector, requiring the concomitant activation of two inputs to generate

an AP. Notably, GABA can be co-released with glycine and acts on $GABA_BRs$ in concentrations as low as 10µM. This opens the possibility that endbulb neurotransmitter release and BC AP firing thresholds can be modulated simultaneously. Depressing synapses can be seen as low pass filters, since their P_{vr} dwindles faster the higher the frequency of stimulation gets (Abbott and Regehr, 2004). Modulation of endbulbs of Held seems to effect of switch on BCs coding, contradicting the simplistic view that wants them acting only as accurate relays of sound information.

Adding to this complexity, nicotinic and muscarinic receptors have been shown to be expressed in BCs and the secretion of acetylcholine from descending pathways can also control BC firing thresholds. Importantly, cholinergic innervation of cochlear hair cells exerts an inhibitory effect on IHC synaptic transmission and SGN firing, while at the same time it lowers BC firing thresholds. This effect could be important for the detection of sounds in noisy environments (Reviewed in Kuenzel, 2019).

Recently, three separate transcriptomic datasets revealed the expression of DA, NE and 5-HT receptors on SGN membranes (Li et al., 2020; Shrestha et al., 2018; Sun et al., 2018). Yet, their precise localization on the SGN compartments has not yet been investigated. Do the IHC contacting boutons or the aVCN terminating axons express these receptors, or both? These questions are the necessary focus of future work that will help elucidate how the volume secretion of monoamines at different points of the auditory pathway tweaks the system in a behaviourally relevant way.

In this context, I provide the first, preliminary evidence that NE decreases P_{vr} at endbulbs of Held, decreases the variability of Ca^{2+}-evoked release, reduces STD at high frequencies and slows down recovery from SV pool depletion. Considering the aforementioned findings on GABA and acetylcholine, an image emerges where NE may tweak the BCs into acting as coincidence detectors during heightened states of arousal. Despite these intriguing findings, a more detailed dissection of the involved mechanisms is necessary.

The absence of an effect on evoked release seems quite puzzling. It is possible that both pre-synaptic and post-synaptic effects are simultaneously driven by volume NE secretion, potentially involving the expression of different receptors in each side of the endbulb synapse. To dissect the pre-synaptic contributions alone, future experiments will include a non-hydrolysable form of GTP in the intracellular solution of the BC – patching pipette, similar to what was described by Martín et al., 2020. This manipulation will eliminate any post-synaptic neuromodulator activity by arresting all potential G-protein mediated alterations of AMPAR dynamics and eEPSC kinetics.

I have stressed how endbulbs and calyces of Held provide a unique opportunity of studying the pre-synaptic release machinery. In light of the focus that Munc13-1 has received as a key priming factor mediating the LS – TS transition, pre-synaptic recordings that measure the Ca^{2+} dependence of

SV release under the influence of bath applied neuromodulators are very crucial to further dissect, which part of the CAZ – SV release machinery is affected by NE and 5-HT. Such experiments also allow the manipulation of the pre-synaptic cytosolic milieu. Adding to the intracellular solution 1-oleoyl-2-acetyl-sn-glycerol (OAG), a DAG variant and, in separate experiments U73122, a PLC inhibitor, would allow the dissection of neuromodulator GPCR – coupled $G\alpha_q$ – mediated influence on SV priming, possibly through influence of the Munc13-1 slanted state and LS – TS equilibrium (Lee et al., 2013b; Neher and Brose, 2018; Rizo, 2022; Xu et al., 2017).

Neuromodulators are released through long axons with chains of sequentially positioned varicosities. However not all varicosities are consistently active (Liu et al., 2021). It is important, when studying the neuromodulation in a brain region to assess the active sites of endogenous release and whether they form meaningful patterns across the dimensions of that region. This is particularly important in the cochlear nucleus, where a tonotopic representation of the sound frequencies encoded in the cochlea is preserved (Campagnola and Manis, 2014). An elegant way to address this is to virally transfect the cells in the aVCN with fluorescent indicators that are modified versions of neuromodulator GPCRs coupled with fluorescent proteins. Upon binding of the released neurotransmitter, these indicators emit fluorescence (Sabatini and Tian, 2020) and allow the characterization of the spatial extent and, depending on their signal to noise ratio, the amount of release. Thus, the possibility that sparse neuromodulator release in the aVCN preferentially affects certain tonotopic positions can be explored. Not all varicosities release in the volume secretion mode. Some release sites display a more synapse like organization. Therein lies the limit of our pharmacological manipulations. The implementation of methods such as optogenetics, which enable control of neuronal activity by light will generate physiologically relevant secretion of neuromodulators (Boyden, 2015; Deisseroth, 2015). This method will be necessary to uncover their mode of action in the aVCN, and is already a staple of studies that probe their effects on synaptic plasticity (He et al., 2015).

Outlook

Synaptic function in vivo is of course not fully recapitulated by in vitro experiments as was already discussed regarding the difference between in vitro and in vivo P_{vr} (Borst, 2010). Additional mechanisms may be involved in the regulation of synaptic function. Letellier et al. (2016) demonstrated that astrocytes, which are sensitive to the activity of neurons and provide them with metabolites, are also involved in modulating synaptic function. Through the activation of astrocyte NMDARs and L-type VGCCS, converging pre-synaptic inputs on the same neuron show more diverse synaptic plasticity in hippocampal neuron networks. This effect was tested both in dissociated cultures, lacking the in vivo neuronal network topology and in acute slice preparations. Blocking

NMDARs and L-type channels in astrocytes caused the rapid correlation of converging pre-synaptic inputs. It is possible that neuromodulation of NMDARs and L-type VGCCs can also occur in astrocytes. While little is known about whether astrocytes express monoamine receptors, such a possibility would be an interesting connection between the history of neuronal activity, homeostasis and modulation of plasticity. Synapses have long been considered bipartite, formed of a pre-synaptic terminal and the post-synaptic dendrite or soma. The consideration of the influence of astrocytes would elevate the complexity to that of a tripartite synapse.

Between neurons and astrocytes and in the clefts of synapses one does not find simply empty space filled with aCSF, but instead a space filled with macromolecules, including collagen and glycoproteins which combined with other factors form the extracellular matrix. Complex forms of modified extracellular matrix, such as the perineuronal nets, which surround the cell bodies and proximal processes of neurons, are receiving a lot of attention as to their implication in plasticity, learning and memory (Shen, 2018). These structures are highly dynamic, undergo turnover and need to be loosened for the development of structural hallmarks of plasticity, such as the appearance of new dendritic spines, ready to receive new synaptic connections. Notably, extracellular matrix elements are modified and regulated by the action of matrix metalloproteinases, some of which interact with receptors of neuromodulators (Bijata et al., 2022; Dankovich et al., 2021; Gorinski et al., 2019) and their dysregulation is involved in crippling neuromodulator – related pathologies such as depression. Immediately, the consideration of the extracellular matrix and its potential involvement in synaptic plasticity increases the perceived complexity of synaptic function.

The preservation of all the elements of the tripartite synapse and ECM is possible to an extent with acute slice preparations. Since mature endbulbs and calyces of Held do not employ L-type VGCCs nor NMDA receptors, the application of blockers against them is bound to specifically affect the postulated modulatory influence from astrocytes, uncovering its presence through its ablation and the resulting effect on STP measured at BCs with afferent fiber stimulation. Additionally, it is possible to manipulate the function of metalloproteinases, or incubate the slices with collagenase and investigate how the dysregulation or degradation of the ECM influences pre-synaptic plasticity. At a higher level, behavioural experiments need to address the effect of neuromodulators on hearing with tasks that are relevant for the animals, such as sound localization, gap detection, auditory cued learning etc. Such experiments demand the recording from awake animals with concomitant stimulation of neuromodulator release at different parts of the auditory pathway. While some surgical approaches allow the opening of cranial windows and insertions of optical fibers for superficial stimulation, more complex systems will need to be developed to control secretion in deeper parts of auditory nuclei.

It is a fact that the focus on 5-HT, NE and DA systems stems from the critical effects of their dysfunction on behaviour, leading to disorders such as depression or schizophrenia that have devastating effects on the human population. The more we learn about their function in neuronal networks, the more we integrate post and pre-synaptic mechanisms of functions from a wide range of diversely regulated synapses, the better our chances not only to predict the system – specific pathology or identify risk factors, but also to begin looking for treatments. To that end, our work on the influence of neuromodulators in the aVCN furthers the current understanding pre-synaptic neuromodulation of plasticity and its impact on neuronal networks.

Bibliography

Abbott, L.F., and Regehr, W.G. (2004). Synaptic computation. Nature *431*, 796–803. https://doi.org/10.1038/NATURE03010.

Abraham, W.C., and Bear, M.F. (1996). Metaplasticity: the plasticity of synaptic plasticity. Trends Neurosci. *19*, 126–130. https://doi.org/10.1016/S0166-2236(96)80018-X.

Acuna, C., Liu, X., Gonzalez, A., and Südhof, T.C. (2015). RIM-BPs Mediate Tight Coupling of Action Potentials to Ca2+-Triggered Neurotransmitter Release. Neuron *87*, 1234–1247. https://doi.org/10.1016/j.neuron.2015.08.027.

Acuna, C., Liu, X., and Südhof, T.C. (2016). How to Make an Active Zone: Unexpected Universal Functional Redundancy between RIMs and RIM-BPs. Neuron *91*, 792–807. https://doi.org/10.1016/j.neuron.2016.07.042.

Ahmari, S.E., Buchanan, J.A., and Smith, S.J. (2000). Assembly of pre-synaptic active zones from cytoplasmic transport packets. Nat. Neurosci. 2000 35 *3*, 445–451. https://doi.org/10.1038/74814.

Alabi, A.R.A., and Tsien, R.W. (2012). Synaptic Vesicle Pools and Dynamics. Cold Spring Harb. Perspect. Biol. *4*, a013680. https://doi.org/10.1101/CSHPERSPECT.A013680.

Andreae, L.C., and Burrone, J. (2018). The role of spontaneous neurotransmission in synapse and circuit development. J. Neurosci. Res. *96*, 354–359. https://doi.org/10.1002/JNR.24154.

Aravamudan, B., Fergestad, T., Davis, W.S., Rodesch, C.K., and Broadie, K. (1999). Drosophila Unc-13 is essential for synaptic transmission. Nat. Neurosci. *2*, 965–971. https://doi.org/10.1038/14764.

Banke, T.G., Bowie, D., Lee, H.K., Huganir, R.L., Schousboe, A., and Traynelis, S.F. (2000). Control of GluR1 AMPA receptor function by cAMP-dependent protein kinase. J. Neurosci. *20*, 89–102. https://doi.org/10.1523/JNEUROSCI.20-01-00089.2000.

Barria, A., Muller, D., Derkach, V., Griffith, L.C., and Soderling, T.R. (1997). Regulatory phosphorylation of AMPA-type glutamate receptors by CaM-KII during long-term potentiation. Science *276*, 2042–2045. https://doi.org/10.1126/SCIENCE.276.5321.2042.

Basu, J., Betz, A., Brose, N., and Rosenmund, C. (2007). Munc13-1 C1 domain activation lowers the energy barrier for synaptic vesicle fusion. J. Neurosci. *27*, 1200–1210. https://doi.org/10.1523/JNEUROSCI.4908-06.2007.

Bazwinsky, I., Härtig, W., and Rübsamen, R. (2008). Characterization of cochlear nucleus principal cells of Meriones unguiculatus and Monodelphis domestica by use of calcium-binding protein immunolabeling. J. Chem. Neuroanat. *35*, 158–174. https://doi.org/10.1016/J.JCHEMNEU.2007.10.003.

Bennett, M.V.L. (2000). Electrical synapses, a personal perspective (or history). Brain Res. Rev. *32*, 16–28. https://doi.org/10.1016/S0165-0173(99)00065-X.

Bernadzki, K.M., Gawor, M., Pęziński, M., Mazurek, P., Niewiadomski, P., Rędowicz, M.J., and Prószyński, T.J. (2017). Liprin-α-1 is a novel component of the murine neuromuscular junction and is involved in the organization of the post-synaptic machinery. Sci. Reports 2017 71 *7*, 1–12. https://doi.org/10.1038/s41598-017-09590-7.

Biederer, T., Kaeser, P.S., and Blanpied, T.A. (2017). Transcellular Nanoalignment of Synaptic Function. Neuron *96*, 680–696. https://doi.org/10.1016/j.neuron.2017.10.006.

Bijata, M., Bączyńska, E., Müller, F.E., Bijata, K., Masternak, J., Krzystyniak, A., Szewczyk, B., Siwiec, M.,

Antoniuk, S., Roszkowska, M., et al. (2022). Activation of the 5-HT7 receptor and MMP-9 signaling module in the hippocampal CA1 region is necessary for the development of depressive-like behavior. Cell Rep. *38*. https://doi.org/10.1016/J.CELREP.2022.110532/ATTACHMENT/21436879-294C-4D38-BED7-980967FAD7C7/MMC1.PDF.

Boehm, S. (1999). Pre-synaptic α2-adrenoceptors control excitatory, but not inhibitory, transmission at rat hippocampal synapses. J. Physiol. *519*, 439–449. https://doi.org/10.1111/J.1469-7793.1999.0439M.X.

Borst, J.G.G. (2010). The low synaptic release probability in vivo. Trends Neurosci. *33*, 259–266. https://doi.org/10.1016/J.TINS.2010.03.003.

Boyden, E.S. (2015). Optogenetics and the future of neuroscience. Nat. Neurosci. *18*, 1200–1201. https://doi.org/10.1038/nn.4094.

Brenowitz, S., David, J., and Trussell, L. (1998). Enhancement of synaptic efficacy by pre-synaptic GABA(B) receptors. Neuron *20*, 135–141. https://doi.org/10.1016/s0896-6273(00)80441-9.

Brewer, K.D., Bacaj, T., Cavalli, A., Camilloni, C., Swarbrick, J.D., Liu, J., Zhou, A., Zhou, P., Barlow, N., Xu, J., et al. (2015). Dynamic binding mode of a Synaptotagmin-1-SNARE complex in solution. Nat. Struct. Mol. Biol. *22*, 555–564. https://doi.org/10.1038/NSMB.3035.

Brockmann, M.M., Maglione, M., Willmes, C.G., Stumpf, A., Bouazza, B.A., Velasquez, L.M., Grauel, M.K., Beed, P., Lehmann, M., Gimber, N., et al. (2019). RIM-BP2 primes synaptic vesicles via recruitment of Munc13-1 at hippocampal mossy fiber synapses. Elife *8*. https://doi.org/10.7554/eLife.43243.

Brockmann, M.M., Zarebidaki, F., Camacho, M., Grauel, M.K., Trimbuch, T., Südhof, T.C., and Rosenmund, C. (2020). A Trio of Active Zone Proteins Comprised of RIM-BPs, RIMs, and Munc13s Governs Neurotransmitter Release. Cell Rep. *32*, 107960. https://doi.org/10.1016/j.celrep.2020.107960.

Brownell, W.E. (1990). Outer Hair Cell Electromotility and Otoacoustic Emissions. Ear Hear. *11*, 82–92. .

Brzosko, Z., Mierau, S.B., and Paulsen, O. (2019). Neuromodulation of Spike-Timing-Dependent Plasticity: Past, Present, and Future. Neuron *103*, 563–581. https://doi.org/10.1016/j.neuron.2019.05.041.

Bury, L.A.D., and Sabo, S.L. (2011). Coordinated trafficking of synaptic vesicle and active zone proteins prior to synapse formation. Neural Dev. *6*. https://doi.org/10.1186/1749-8104-6-24.

Butola, T., Wichmann, C., and Moser, T. (2017). Piccolo promotes vesicle replenishment at a fast central auditory synapse. Front. Synaptic Neurosci. *9*, 1–21. https://doi.org/10.3389/fnsyn.2017.00014.

Campagnola, L., and Manis, P.B. (2014). A Map of Functional Synaptic Connectivity in the Mouse Anteroventral Cochlear Nucleus. J. Neurosci. *34*, 2214–2230. https://doi.org/10.1523/jneurosci.4669-13.2014.

Cant, N.B. (1981). The fine structure of two types of stellate cells in the anterior division of the anteroventral cochlear nucleus of the cat. Neuroscience *6*, 2643–2655. https://doi.org/10.1016/0306-4522(81)90109-3.

Cao, X.-J., and Oertel, D. (2010a). Auditory Nerve Fibers Excite Targets Through Synapses That Vary in Convergence, Strength, and Short-Term Plasticity. J. Neurophysiol. *104*, 2308–2320. https://doi.org/10.1152/jn.00451.2010.

Cao, X.J., and Oertel, D. (2010b). Auditory nerve fibers excite targets through synapses that vary in convergence, strength, and short-term plasticity. J Neurophysiol *104*, 2308–2320. https://doi.org/10.1152/jn.00451.2010.

Cao, X.-J., Shatadal, S., and Oertel, D. (2007a). Voltage-Sensitive Conductances of Bushy Cells of the Mammalian Ventral Cochlear Nucleus. J. Neurophysiol. *97*, 3961–3975. https://doi.org/10.1152/jn.00052.2007.

Cao, X.J., Shatadal, S., and Oertel, D. (2007b). Voltage-sensitive conductances of bushy cells of the mammalian ventral cochlear nucleus. J. Neurophysiol. *97*, 3961–3975. https://doi.org/10.1152/JN.00052.2007/ASSET/IMAGES/LARGE/Z9K0060782480011.JPEG.

del Castillo, J., and Katz, B. (1954). Quantal components of the end-plate potential. J. Physiol. *124*, 560–573. https://doi.org/10.1113/JPHYSIOL.1954.SP005129.

Ceccarelli, B., Grohovaz, F., and Hurlbut, W.P. (1979). Freeze-fracture studies of frog neuromuscular junctions during intense release of neurotransmitter. II. Effects of electrical stimulation and high potassium. J. Cell Biol. *81*, 178–192. https://doi.org/10.1083/JCB.81.1.178.

Chanda, S., Oh, S., and Xu-Friedman, M.A. (2011). Calcium imaging of auditory nerve fiber terminals in the cochlear nucleus. J. Neurosci. Methods *195*, 24–29. https://doi.org/10.1016/j.jneumeth.2010.11.008.

Chang, S., Reim, K., Pedersen, M., Neher, E., Brose, N., and Taschenberger, H. (2015). Complexin stabilizes newly primed synaptic vesicles and prevents their premature fusion at the mouse calyx of held synapse. J. Neurosci. *35*, 8272–8290. https://doi.org/10.1523/JNEUROSCI.4841-14.2015.

Chen, G., Harata, N.C., and Tsien, R.W. (2004). Paired-pulse depression of unitary quantal amplitude at single hippocampal synapses. Proc. Natl. Acad. Sci. U. S. A. *101*, 1063–1068. https://doi.org/10.1073/PNAS.0307149101.

Chen, Z., Das, B., Nakamura, Y., DiGregorio, D.A., and Young, S.M. (2015). Ca2+ channel to synaptic vesicle distance accounts for the readily releasable pool kinetics at a functionally mature auditory synapse. J. Neurosci. *35*, 2083–2100. https://doi.org/10.1523/JNEUROSCI.2753-14.2015.

Chi, N.C., Shaw, R.M., Jungblut, B., Huisken, J., Ferrer, T., Arnaout, R., Scott, I., Beis, D., Xiao, T., Baier, H., et al. (2008). Genetic and physiologic dissection of the vertebrate cardiac conduction system. PLoS Biol. *6*, e109. https://doi.org/10.1371/journal.pbio.0060109.

Clayton, E.L., and Cousin, M.A. (2009). The molecular physiology of activity-dependent bulk endocytosis of synaptic vesicles. J. Neurochem. *111*, 901–914. https://doi.org/10.1111/j.1471-4159.2009.06384.x.

Clayton, E.L., Evans, G.J.O., and Cousin, M.A. (2008). Bulk synaptic vesicle endocytosis is rapidly triggered during strong stimulation. J. Neurosci. *28*, 6627–6632. https://doi.org/10.1523/JNEUROSCI.1445-08.2008.

Clewett, D., and Murty, V.P. (2019). Echoes of Emotions Past: How Neuromodulators Determine What We Recollect. ENeuro *6*. https://doi.org/10.1523/ENEURO.0108-18.2019.

Connors, B.W., and Long, M.A. (2004). ELECTRICAL SYNAPSES IN THE MAMMALIAN BRAIN. Annu. Rev. Neurosci *27*, 393–418. https://doi.org/10.1146/annurev.neuro.26.041002.131128.

Cransac, H., Cottet-Emard, J.M., Pequignot, J.M., and Peyrin, L. (1995). Monoamines (noradrenaline, dopamine, serotonin) in the rat cochlear nuclei: endogenous levels and turnover. Hear. Res. *90*, 65–71. https://doi.org/10.1016/0378-5955(95)00147-X.

Dai, Y., Taru, H., Deken, S.L., Grill, B., Ackley, B., Nonet, M.L., and Jin, Y. (2006). SYD-2 Liprin-α organizes

pre-synaptic active zone formation through ELKS. Nat. Neurosci. *9*, 1479–1487. https://doi.org/10.1038/nn1808.

Dankovich, T.M., Kaushik, R., Olsthoorn, L.H.M., Petersen, G.C., Giro, P.E., Kluever, V., Agüi-Gonzalez, P., Grewe, K., Bao, G., Beuermann, S., et al. (2021). Extracellular matrix remodeling through endocytosis and resurfacing of Tenascin-R. Nat. Commun. *12*. https://doi.org/10.1038/S41467-021-27462-7.

Davydova, D., Marini, C., King, C., Klueva, J., Bischof, F., Romorini, S., Montenegro-Venegas, C., Heine, M., Schneider, R., Schröder, M.S., et al. (2014). Bassoon specifically controls pre-synaptic P/Q-type Ca2+ channels via RIM-binding protein. Neuron *82*, 181–194. https://doi.org/10.1016/j.neuron.2014.02.012.

Deisseroth, K. (2015). Optogenetics: 10 years of microbial opsins in neuroscience. Nat. Neurosci. *18*, 1213–1225. https://doi.org/10.1038/nn.4091.

Deng, L., Kaeser, P.S., Xu, W., and Südhof, T.C. (2011). RIM proteins activate vesicle priming by reversing autoinhibitory homodimerization of munc13. Neuron *69*, 317–331. https://doi.org/10.1016/j.neuron.2011.01.005.

Denker, A., and Rizzoli, S.O. (2010). Synaptic vesicle pools: an update. Front. Synaptic Neurosci. *2*. https://doi.org/10.3389/FNSYN.2010.00135.

Denker, A., Bethani, I., Kröhnert, K., Körber, C., Horstmann, H., Wilhelm, B.G., Barysch, S. V, Kuner, T., Neher, E., and Rizzoli, S.O. (2011). A small pool of vesicles maintains synaptic activity in vivo. Proc. Natl. Acad. Sci. *108*, 17177–17182. https://doi.org/10.1073/pnas.1112688108.

Dieck, S.T., Specht, D., Strenzke, N., Hida, Y., Krishnamoorthy, V., Schmidt, K.F., Inoue, E., Ishizaki, H., Tanaka-Okamoto, M., Miyoshi, J., et al. (2012). Deletion of the pre-synaptic scaffold CAST reduces active zone size in rod photoreceptors and impairs visual processing. J. Neurosci. *32*, 12192–12203. https://doi.org/10.1523/JNEUROSCI.0752-12.2012.

Dittman, J.S., Kreitzer, A.C., and Regehr, W.G. (2000). Interplay between Facilitation, Depression, and Residual Calcium at Three Pre-synaptic Terminals. J. Neurosci. *20*, 1374–1385. https://doi.org/10.1523/JNEUROSCI.20-04-01374.2000.

Dong, B., Nakai, H., and Xiao, W. (2010). Characterization of Genome Integrity for Oversized Recombinant AAV Vector. Mol. Ther. *18*, 87–92. https://doi.org/10.1038/mt.2009.258.

Dong, W., Radulovic, T., Goral, R.O., Thomas, C., Suarez Montesinos, M., Guerrero-Given, D., Hagiwara, A., Putzke, T., Hida, Y., Abe, M., et al. (2018). CAST/ELKS Proteins Control Voltage-Gated Ca 2+ Channel Density and Synaptic Release Probability at a Mammalian Central Synapse. Cell Rep. *24*, 284-293.e6. https://doi.org/10.1016/j.celrep.2018.06.024.

Doucet, J.R., and Ryugo, D.K. (2006). Structural and functional classes of multipolar cells in the ventral cochlear nucleus. Anat. Rec. A. Discov. Mol. Cell. Evol. Biol. *288*, 331–344. https://doi.org/10.1002/AR.A.20294.

Dresbach, T., Torres, V., Wittenmayer, N., Altrock, W.D., Zamorano, P., Zuschratter, W., Nawrotzki, R., Ziv, N.E., Garner, C.C., and Gundelfinger, E.D. (2006). Assembly of active zone precursor vesicles: obligatory trafficking of pre-synaptic cytomatrix proteins Bassoon and Piccolo via a trans-Golgi compartment. J. Biol. Chem. *281*, 6038–6047. https://doi.org/10.1074/JBC.M508784200.

Dulubova, I., Sugita, S., Hill, S., Hosaka, M., Fernandez, I., Südhof, T.C., and Rizo, J. (1999). A conformational switch in syntaxin during exocytosis: Role of munc18. EMBO J. *18*, 4372–4382. https://doi.org/10.1093/emboj/18.16.4372.

Dulubova, I., Lou, X., Lu, J., Huryeva, I., Alam, A., Schneggenburger, R., Südhof, T.C., and Rizo, J. (2005). A Munc13/RIM/Rab3 tripartite complex: From priming to plasticity? EMBO J. *24*, 2839–2850. https://doi.org/10.1038/sj.emboj.7600753.

Ebert, U., and Ostwald, J. (1992). Serotonin modulates auditory information processing in the cochlear nucleus of the rat. Neurosci. Lett. *145*, 51–54. https://doi.org/10.1016/0304-3940(92)90201-H.

Ehlers, M.D. (2000). Reinsertion or degradation of AMPA receptors determined by activity-dependent endocytic sorting. Neuron *28*, 511–525. https://doi.org/10.1016/S0896-6273(00)00129-X.

Elmqvist, D., and Quastel, D.M. (1965). A quantitative study of end-plate potentials in isolated human muscle. J. Physiol. *178*, 505–529. https://doi.org/10.1113/jphysiol.1965.sp007639.

Emperador-Melero, J., Wong, M.Y., Wang, S.S.H., de Nola, G., Nyitrai, H., Kirchhausen, T., and Kaeser, P.S. (2021). PKC-phosphorylation of Liprin-α3 triggers phase separation and controls pre-synaptic active zone structure. Nat. Commun. 2021 121 *12*, 1–17. https://doi.org/10.1038/s41467-021-23116-w.

Esteban, J.A. (2003). AMPA receptor trafficking: a road map for synaptic plasticity. Mol. Interv. *3*, 375–385. https://doi.org/10.1124/MI.3.7.375.

Faber, E.S.L., Delaney, A.J., Power, J.M., Sedlak, P.L., Crane, J.W., and Sah, P. (2008). Modulation of SK channel trafficking by beta adrenoceptors enhances excitatory synaptic transmission and plasticity in the amygdala. J. Neurosci. *28*, 10803–10813. https://doi.org/10.1523/JNEUROSCI.1796-08.2008.

Fairless, R., Masius, H., Rohlmann, A., Heupel, K., Ahmad, M., Reissner, C., Dresbach, T., and Missler, M. (2008). Polarized Targeting of Neurexins to Synapses Is Regulated by their C-Terminal Sequences. J. Neurosci. *28*, 12969–12981. https://doi.org/10.1523/JNEUROSCI.5294-07.2008.

Fatt, P., and Katz, B. (1950). Some Observations on Biological Noise. Nat. 1950 1664223 *166*, 597–598. https://doi.org/10.1038/166597a0.

Fatt, P., and Katz, B. (1952). Spontaneous subthreshold activity at motor nerve endings. J. Physiol. *117*, 109–128. https://doi.org/10.1113/JPHYSIOL.1952.SP004735.

Fejtova, A., Davydova, D., Bischof, F., Lazarevic, V., Altrock, W.D., Romorini, S., Schöne, C., Zuschratter, W., Kreutz, M.R., Garner, C.C., et al. (2009). Dynein light chain regulates axonal trafficking and synaptic levels of Bassoon. J. Cell Biol. *185*, 341–355. https://doi.org/10.1083/JCB.200807155.

Fekete, D.M., Rouiller, E.M., Liberman, M.C., and Ryugo, D.K. (1984). The central projections of intracellularly labeled auditory nerve fibers in cats. J. Comp. Neurol. *229*, 432–450. https://doi.org/10.1002/CNE.902290311.

Fenster, S.D., Chung, W.J., Zhai, R., Cases-Langhoff, C., Voss, B., Garner, A.M., Kaempf, U., Kindler, S., Gundelfinger, E.D., and Garner, C.C. (2000). Piccolo, a pre-synaptic zinc finger protein structurally related to Bassoon. Neuron *25*, 203–214. https://doi.org/10.1016/S0896-6273(00)80883-1.

Fettiplace, R., and Fuchs, P.A. (1999). Mechanisms of hair cell tuning. Annu. Rev. Physiol. *61*, 809–834. https://doi.org/10.1146/ANNUREV.PHYSIOL.61.1.809.

Fitzpatrick, D.C., Batra, R., Stanford, T.R., and Kuwada, S. (1997). A neuronal population code for sound localization. Nature *388*, 871. .

Forsythe, I.D., Tsujimoto, T., Barnes-Davies, M., Cuttle, M.F., and Takahashi, T. (1998). Inactivation of pre-synaptic calcium current contributes to synaptic depression at a fast central synapse. Neuron *20*, 797–807. https://doi.org/10.1016/S0896-6273(00)81017-X.

Frank, T., Rutherford, M.A., Strenzke, N., Neef, A., Pangršič, T., Khimich, D., Fetjova, A., Gundelfinger,

E.D., Liberman, M.C., Harke, B., et al. (2010). Bassoon and the synaptic ribbon organize Ca2+ channels and vesicles to add release sites and promote refilling. Neuron *68*, 724–738. https://doi.org/10.1016/j.neuron.2010.10.027.

Fredj, N. Ben, and Burrone, J. (2009). A resting pool of vesicles is responsible for spontaneous vesicle fusion at the synapse. Nat. Neurosci. *12*, 751–758. https://doi.org/10.1038/NN.2317.

Friauf, E., and Ostwald, J. (1988). Divergent projections of physiologically characterized rat ventral cochlear nucleus neurons as shown by intra-axonal injection of horseradish peroxidase. Exp. Brain Res. *73*, 263–284. https://doi.org/10.1007/BF00248219.

Fujimoto, K., Shibasaki, T., Yokoi, N., Kashima, Y., Matsumoto, M., Sasaki, T., Tajima, N., Iwanaga, T., and Seino, S. (2002). Piccolo, a Ca2+ sensor in pancreatic beta-cells. Involvement of cAMP-GEFII.Rim2. Piccolo complex in cAMP-dependent exocytosis. J. Biol. Chem. *277*, 50497–50502. https://doi.org/10.1074/JBC.M210146200.

Gao, S., Guo, X., Liu, T., Liu, J., Chen, W., Xia, Q., Chen, Y., and Tang, Y. (2013). Serotonin modulates outward potassium currents in mouse olfactory receptor neurons. Physiol. Res. *62*, 455–462. https://doi.org/10.33549/PHYSIOLRES.932413.

Garner, C.C., Kindler, S., and Gundelfinger, E.D. (2000). Molecular determinants of pre-synaptic active zones. Curr. Opin. Neurobiol. *10*, 321–327. https://doi.org/10.1016/S0959-4388(00)00093-3.

Gekel, I., and Neher, E. (2008). Application of an Epac activator enhances neurotransmitter release at excitatory central synapses. J. Neurosci. *28*, 7991–8002. https://doi.org/10.1523/JNEUROSCI.0268-08.2008.

von Gersdorff, H., and Borst, J.G.G. (2002). Short-term plasticity at the calyx of held. Nat Rev Neurosci *3*, 53–64. https://doi.org/10.1038/nrn705.

Goldberg, J.M., and Brown, P.B. (1969). Response of binaural neurons of dog superior olivary complex to dichotic tonal stimuli: some physiological mechanisms of sound localization. J. Neurophysiol. *32*, 613–636. https://doi.org/10.1152/JN.1969.32.4.613.

Goodenough, D.A. (1974). BULK ISOLATION OF MOUSE HEPATOCYTE GAP JUNCTIONS Characterization of the Principal Protein, Connexin. J. Cell Biol. *61*, 557–563. https://doi.org/10.1083/JCB.61.2.557.

Gorinski, N., Bijata, M., Prasad, S., Wirth, A., Abdel Galil, D., Zeug, A., Bazovkina, D., Kondaurova, E., Kulikova, E., Ilchibaeva, T., et al. (2019). Attenuated palmitoylation of serotonin receptor 5-HT1A affects receptor function and contributes to depression-like behaviors. Nat. Commun. *10*. https://doi.org/10.1038/s41467-019-11876-5.

Grabner, C.P., Gandini, M.A., Rehak, R., Le, Y., Zamponi, G.W., and Schmitz, F. (2015). RIM1/2-mediated facilitation of cav1.4 channel opening is required for Ca2+-stimulated release in mouse rod photoreceptors. J. Neurosci. *35*, 13133–13147. https://doi.org/10.1523/JNEUROSCI.0658-15.2015.

Gracheva, E.O., Hadwiger, G., Nonet, M.L., and Richmond, J.E. (2008). Direct interactions between C. elegans RAB-3 and Rim provide a mechanism to target vesicles to the pre-synaptic density. Neurosci. Lett. *444*, 137–142. https://doi.org/10.1016/j.neulet.2008.08.026.

Granseth, B., Odermatt, B., Royle, S.J.J., and Lagnado, L. (2006). Clathrin-mediated endocytosis is the dominant mechanism of vesicle retrieval at hippocampal synapses. Neuron *51*, 773–786. https://doi.org/10.1016/J.NEURON.2006.08.029.

Grauel, M.K., Maglione, M., Reddy-Alla, S., Willmes, C.G., Brockmann, M.M., Trimbuch, T., Rosenmund, T., Pangalos, M., Vardar, G., Stumpf, A., et al. (2016). Rim-binding protein 2 regulates release probability by fine-tuning calcium channel localization at murine hippocampal synapses. Proc.

Natl. Acad. Sci. U. S. A. *113*, 11615–11620. https://doi.org/10.1073/pnas.1605256113.

Gray, R., and Johnston, D. (1987). Noradrenaline and beta-adrenoceptor agonists increase activity of voltage-dependent calcium channels in hippocampal neurons. Nature *327*, 620–622. https://doi.org/10.1038/327620A0.

Groch, S., Wilhelm, I., Diekelmann, S., Sayk, F., Gais, S., and Born, J. (2011). Contribution of norepinephrine to emotional memory consolidation during sleep. Psychoneuroendocrinology *36*, 1342–1350. https://doi.org/10.1016/J.PSYNEUEN.2011.03.006.

Groemer, T.W., and Klingauf, J. (2007). Synaptic vesicles recycling spontaneously and during activity belong to the same vesicle pool. Nat. Neurosci. *10*, 145–147. https://doi.org/10.1038/NN1831.

Grothe, B., Pecka, M., and McAlpine, D. (2010). Mechanisms of Sound Localization in Mammals. Physiol. Rev. *90*, 983–1012. https://doi.org/10.1152/physrev.00026.2009.

Grushin, K., Wang, J., Coleman, J., Rothman, J.E., Sindelar, C. V., and Krishnakumar, S.S. (2019). Structural basis for the clamping and Ca^{2+} activation of SNARE-mediated fusion by synaptotagmin. Nat. Commun. *10*, 2413–2413. https://doi.org/10.1038/S41467-019-10391-X.

Gundelfinger, E.D., Reissner, C., and Garner, C.C. (2016). Role of Bassoon and Piccolo in Assembly and Molecular Organization of the Active Zone. Front. Synaptic Neurosci. *7*, 19. https://doi.org/10.3389/FNSYN.2015.00019/XML/NLM.

Hagiwara, A., Hamada, S., Hida, Y., and Ohtsuka, T. (2020). Double deletion of the active zone proteins CAST/ELKS in the mouse forebrain causes high mortality of newborn pups. Mol. Brain *13*, 1–7. https://doi.org/10.1186/S13041-020-0557-X/FIGURES/3.

Hallermann, S., Fejtova, A., Schmidt, H., Weyhersmüller, A., Silver, R.A., Gundelfinger, E.D., and Eilers, J. (2010). Bassoon Speeds Vesicle Reloading at a Central Excitatory Synapse. Neuron *68*, 710–723. .

Han, Y., Kaeser, P.S., Südhof, T.C., and Schneggenburger, R. (2011). RIM determines Ca2+ channel density and vesicle docking at the pre-synaptic active zone. Neuron *69*, 304–316. https://doi.org/10.1016/j.neuron.2010.12.014.

Haucke, V., Neher, E., and Sigrist, S.J. (2011). Protein scaffolds in the coupling of synaptic exocytosis and endocytosis. Nat. Rev. Neurosci. *12*, 127–138. https://doi.org/10.1038/NRN2948.

He, E., Wierda, K., Van Westen, R., Broeke, J.H., Toonen, R.F., Cornelisse, L.N., and Verhage, M. (2017a). Munc13-1 and Munc18-1 together prevent NSF-dependent de-priming of synaptic vesicles. Nat. Commun. *8*. https://doi.org/10.1038/ncomms15915.

He, E., Wierda, K., Van Westen, R., Broeke, J.H., Toonen, R.F., Cornelisse, L.N., and Verhage, M. (2017b). Munc13-1 and Munc18-1 together prevent NSF-dependent de-priming of synaptic vesicles. Nat. Commun. *8*, 1–10. https://doi.org/10.1038/ncomms15915.

He, K., Huertas, M., Hong, S.Z., Tie, X.X., Hell, J.W., Shouval, H., and Kirkwood, A. (2015). Distinct Eligibility Traces for LTP and LTD in Cortical Synapses. Neuron *88*, 528–538. https://doi.org/10.1016/j.neuron.2015.09.037.

Henderson, D., Eibl, H., and Weber, K. (1979). Structure and biochemistry of mouse hepatic gap junctions. J. Mol. Biol. *132*, 193–218. https://doi.org/10.1016/0022-2836(79)90391-7.

Hibino, H., Pironkova, R., Onwumere, O., Vologodskaia, M., Hudspeth, A.J., and Lesage, F. (2002). RIM binding proteins (RBPs) couple Rab3-interacting molecules (RIMs) to voltage-gated Ca2+ channels. Neuron *34*, 411–423. https://doi.org/10.1016/S0896-6273(02)00667-0.

Hodgkin, A.L. (1948). The local electric changes associated with repetitive action in a non-medullated

axon. J. Physiol. *107*, 165–181. .

Hodgkin, A.L., and Huxley, A.F. (1952a). The components of membrane conductance in the giant axon of Loligo. J. Physiol. *116*, 473–496. https://doi.org/10.1113/JPHYSIOL.1952.SP004718.

Hodgkin, A.L., and Huxley, A.F. (1952b). Currents carried by sodium and potassium ions through the membrane of the giant axon of Loligo. J. Physiol. *116*, 449–472. https://doi.org/10.1113/JPHYSIOL.1952.SP004717.

Hodgkin, A.L., Huxley, A.F., and Katz, B. (1952). Measurement of current-voltage relations in the membrane of the giant axon of Loligo. J. Physiol. *116*, 424–448. https://doi.org/10.1113/JPHYSIOL.1952.SP004716.

HODGKIN, A.L., and HUXLEY, A.F. (1952). Propagation of electrical signals along giant nerve fibers. Proc. R. Soc. London. Ser. B, Biol. Sci. *140*, 177–183. https://doi.org/10.1098/RSPB.1952.0054.

Hoffman, D.A., and Johnston, D. (1999). Neuromodulation of dendritic action potentials. J. Neurophysiol. *81*, 408–411. https://doi.org/10.1152/JN.1999.81.1.408/ASSET/IMAGES/LARGE/JNP.JA24F2.JPEG.

Hoffman, D.A., Magee, J.C., Colbert, C.M., and Johnston, D. (1997). K+ channel regulation of signal propagation in dendrites of hippocampal pyramidal neurons. Nat. 1997 3876636 *387*, 869–875. https://doi.org/10.1038/43119.

Hori, Y., Endo, K., and Takahashi, T. (1996). Long-lasting synaptic facilitation induced by serotonin in superficial dorsal horn neurones of the rat spinal cord. J. Physiol. *492*, 867–876. https://doi.org/10.1113/jphysiol.1996.sp021352.

Hormuzdi, S.G., Filippov, M.A., Mitropoulou, G., Monyer, H., and Bruzzone, R. (2004). Electrical synapses: A dynamic signaling system that shapes the activity of neuronal networks. Biochim. Biophys. Acta - Biomembr. *1662*, 113–137. https://doi.org/10.1016/j.bbamem.2003.10.023.

Howard, M.A., and Rubel, E.W. (2010). Dynamic Spike Thresholds during Synaptic Integration Preserve and Enhance Temporal Response Properties in the Avian Cochlear Nucleus. J. Neurosci. *30*, 12063–12074. https://doi.org/10.1523/JNEUROSCI.1840-10.2010.

Hu, H., Real, E., Takamiya, K., Kang, M.G., Ledoux, J., Huganir, R.L., and Malinow, R. (2007a). Emotion Enhances Learning via Norepinephrine Regulation of AMPA-Receptor Trafficking. Cell *131*, 160–173. https://doi.org/10.1016/J.CELL.2007.09.017.

Hu, H., Real, E., Takamiya, K., Kang, M.G., Ledoux, J., Huganir, R.L., and Malinow, R. (2007b). Emotion enhances learning via norepinephrine regulation of AMPA-receptor trafficking. Cell *131*, 160–173. https://doi.org/10.1016/J.CELL.2007.09.017.

Imig, C., Min, S.W., Krinner, S., Arancillo, M., Rosenmund, C., Südhof, T.C., Rhee, J.S., Brose, N., and Cooper, B.H. (2014). The Morphological and Molecular Nature of Synaptic Vesicle Priming at Presynaptic Active Zones. Neuron *84*, 416–431. https://doi.org/10.1016/j.neuron.2014.10.009.

Inoue, E., Deguchi-Tawarada, M., Takao-Rikitsu, E., Inoue, M., Kitajima, I., Ohtsuka, T., and Takai, Y. (2006). ELKS, a protein structurally related to the active zone protein CAST, is involved in Ca2+-dependent exocytosis from PC12 cells. Genes to Cells *11*, 659–672. https://doi.org/10.1111/j.1365-2443.2006.00970.x.

Itoh, T., and De Camilli, P. (2006). BAR, F-BAR (EFC) and ENTH/ANTH domains in the regulation of membrane-cytosol interfaces and membrane curvature. Biochim. Biophys. Acta *1761*, 897–912. https://doi.org/10.1016/J.BBALIP.2006.06.015.

de Jong, A.P., and Verhage, M. (2009). Pre-synaptic signal transduction pathways that modulate

synaptic transmission. Curr. Opin. Neurobiol. *19*, 245–253. https://doi.org/10.1016/J.CONB.2009.06.005.

Joris, P.X., Carney, L.H., Smith, P.H., and Yin, T.C. (1994). Enhancement of neural synchronization in the anteroventral cochlear nucleus. I. Responses to tones at the characteristic frequency. J. Neurophysiol. *71*, 1022–1036. https://doi.org/10.1152/jn.1994.71.3.1022.

Jung, S., Maritzen, T., Wichmann, C., Jing, Z., Neef, A., Revelo, N.H., Al-Moyed, H., Meese, S., Wojcik, S.M., Panou, I., et al. (2015a). Disruption of adaptor protein 2 (AP-2) in cochlear hair cells impairs vesicle reloading of synaptic release sites and hearing. EMBO J. *34*, 2686–2702. https://doi.org/10.15252/embj.201591885.

Jung, S., Oshima-Takago, T., Chakrabarti, R., Wong, A.B., Jing, Z., Yamanbaeva, G., Picher, M.M., Wojcik, S.M., Göttfert, F., Predoehl, F., et al. (2015b). Rab3-interacting molecules 2α and 2β promote the abundance of voltage-gated CaV1.3 Ca2+ channels at hair cell active zones. Proc. Natl. Acad. Sci. U. S. A. *112*, E3141–E3149. https://doi.org/10.1073/PNAS.1417207112.

Junge, H.J., Rhee, J.S., Jahn, O., Varoqueaux, F., Spiess, J., Waxham, M.N., Rosenmund, C., and Brose, N. (2004). Calmodulin and Munc13 form a Ca2+ sensor/effector complex that controls short-term synaptic plasticity. Cell *118*, 389–401. https://doi.org/10.1016/j.cell.2004.06.029.

Juranek, J.K., Mukherjee, K., Jahn, R., and Li, J.Y. (2021). Coordinated bi-directional trafficking of synaptic vesicle and active zone proteins in peripheral nerves. Biochem. Biophys. Res. Commun. *559*, 92–98. https://doi.org/10.1016/J.BBRC.2021.04.041.

Kaeser-Woo, Y.J., Yang, X., and Südhof, T.C. (2012). C-terminal complexin sequence is selectively required for clamping and priming but not for Ca 2+ triggering of synaptic exocytosis. J. Neurosci. *32*, 2877–2885. https://doi.org/10.1523/JNEUROSCI.3360-11.2012.

Kaeser, P.S., and Regehr, W.G. (2013). Molecular Mechanisms for Synchronous, Asynchronous, and Spontaneous Neurotransmitter Release. Annu. Rev. Physiol. *76*, 333–363. https://doi.org/10.1146/annurev-physiol-021113-170338.

Kaeser, P.S., and Regehr, W.G. (2014). Molecular Mechanisms for Synchronous, Asynchronous, and Spontaneous Neurotransmitter Release. Annu. Rev. Physiol. *76*, 333–363. https://doi.org/10.1146/annurev-physiol-021113-170338.

Kaeser, P.S., Deng, L., Chávez, A.E., Liu, X., Castillo, P.E., and Südhof, T.C. (2009). ELKS2alpha/CAST deletion selectively increases neurotransmitter release at inhibitory synapses. Neuron *64*, 227–239. https://doi.org/10.1016/J.NEURON.2009.09.019.

Kaeser, P.S., Deng, L., Wang, Y., Dulubova, I., Liu, X., Rizo, J., and Südhof, T.C. (2011). RIM proteins tether Ca2+ channels to pre-synaptic active zones via a direct PDZ-domain interaction. Cell *144*, 282–295. https://doi.org/10.1016/j.cell.2010.12.029.

Kamin, D., Revelo, N.H., and Rizzoli, S.O. (2014). FM Dye Photo-Oxidation as a Tool for Monitoring Membrane Recycling in Inner Hair Cells. PLoS One *9*, e88353. https://doi.org/10.1371/journal.pone.0088353.

Kaneko, M., and Takahashi, T. (2004). Pre-synaptic Mechanism Underlying cAMP-Dependent Synaptic Potentiation. J. Neurosci. *24*, 5202–5208. https://doi.org/10.1523/JNEUROSCI.0999-04.2004.

Kang, G., Joseph, J.W., Chepurny, O.G., Monaco, M., Wheeler, M.B., Bos, J.L., Schwede, F., Genieser, H.G., and Holz, G.G. (2003). Epac-selective cAMP analog 8-pCPT-2'-O-Me-cAMP as a stimulus for Ca2+-induced Ca2+ release and exocytosis in pancreatic beta-cells. J. Biol. Chem. *278*, 8279–8285. https://doi.org/10.1074/JBC.M211682200.

Katz, B., and Miledi, R. (1968). The role of calcium in neuromuscular facilitation. J. Physiol. *195*, 481–492. https://doi.org/10.1113/JPHYSIOL.1968.SP008469.

Kaufmann, N., DeProto, J., Ranjan, R., Wan, H., and Van Vactor, D. (2002). Drosophila liprin-α and the receptor phosphatase Dlar control synapse morphogenesis. Neuron *34*, 27–38. https://doi.org/10.1016/S0896-6273(02)00643-8.

Kawasaki, H., Springett, G.M., Mochizuki, N., Toki, S., Nakaya, M., Matsuda, M., Housman, D.E., and Graybiel, A.M. (1998). A family of cAMP-binding proteins that directly activate Rap1. Science *282*, 2275–2279. https://doi.org/10.1126/SCIENCE.282.5397.2275.

Keine, C., and Rübsamen, R. (2015). Inhibition Shapes Acoustic Responsiveness in Spherical Bushy Cells. J. Neurosci. *35*, 8579–8592. https://doi.org/10.1523/JNEUROSCI.0133-15.2015.

Kiyonaka, S., Nakajima, H., Takada, Y., Hida, Y., Yoshioka, T., Hagiwara, A., Kitajima, I., Mori, Y., and Ohtsuka, T. (2012). Physical and Functional Interaction of the Active Zone Protein CAST/ERC2 and the β-subunit of the Voltage-dependent Ca2+ Channel. J. Biochem. https://doi.org/10.1093/jb/mvs054.

Klepper, A., and Herbert, H. (1991). Distribution and origin of noradrenergic and serotonergic fibers in the cochlear nucleus and inferior colliculus of the rat. Brain Res. *557*, 190–201. https://doi.org/10.1016/0006-8993(91)90134-H.

Ko, K.W., Rasband, M.N., Meseguer, V., Kramer, R.H., and Golding, N.L. (2016). Serotonin modulates spike probability in the axon initial segment through HCN channels. Nat. Neurosci. 2016 196 *19*, 826–834. https://doi.org/10.1038/nn.4293.

Kononenko, N.L., Puchkov, D., Classen, G.A., Walter, A.M., Pechstein, A., Sawade, L., Kaempf, N., Trimbuch, T., Lorenz, D., Rosenmund, C., et al. (2014). Clathrin/AP-2 mediate synaptic vesicle reformation from endosome-like vacuoles but are not essential for membrane retrieval at central synapses. Neuron *82*, 981–988. https://doi.org/10.1016/j.neuron.2014.05.007.

Kopp-Scheinpflug, C., and Tempel, B.L. (2015). Decreased temporal precision of neuronal signaling as a candidate mechanism of auditory processing disorder. Hear. Res. *330*, 213–220. https://doi.org/10.1016/J.HEARES.2015.06.014.

Körber, C., Horstmann, H., Venkataramani, V., Herrmannsdörfer, F., Kremer, T., Kaiser, M., Schwenger, D.B., Ahmed, S., Dean, C., Dresbach, T., et al. (2015). Modulation of Pre-synaptic Release Probability by the Vertebrate-Specific Protein Mover. Neuron *87*, 521–533. https://doi.org/10.1016/J.NEURON.2015.07.001.

Koyama, S., Kubo, C., Rhee, J.S., and Akaike, N. (1999). Pre-synaptic serotonergic inhibition of GABAergic synaptic transmission in mechanically dissociated rat basolateral amygdala neurons. J. Physiol. *518*, 525–538. https://doi.org/10.1111/J.1469-7793.1999.0525P.X.

Kremer, T., Kempf, C., Wittenmayer, N., Nawrotzki, R., Kuner, T., Kirsch, J., and Dresbach, T. (2007). Mover is a novel vertebrate-specific pre-synaptic protein with differential distribution at subsets of CNS synapses. FEBS Lett. *581*, 4727–4733. https://doi.org/10.1016/J.FEBSLET.2007.08.070.

Krinner, S., Butola, T., Jung, S., Wichmann, C., and Moser, T. (2017). Rim-binding protein 2 promotes a large number of Cav1.3 Ca2+-channels and contributes to fast synaptic vesicle replenishment at hair cell active zones. Front. Cell. Neurosci. *11*, 1–20. https://doi.org/10.3389/fncel.2017.00334.

Krinner, S., Predoehl, F., Burfeind, D., Vogl, C., and Moser, T. (2021). RIM-Binding Proteins Are Required for Normal Sound-Encoding at Afferent Inner Hair Cell Synapses. Front. Mol. Neurosci. *14*, 33. https://doi.org/10.3389/FNMOL.2021.651935/BIBTEX.

Kuenzel, T. (2019). Modulatory influences on time-coding neurons in the ventral cochlear nucleus.

Hear. Res. *384*, 107824. https://doi.org/10.1016/j.heares.2019.107824.

Kuenzel, T., Borst, J.G.G., and Van Der Heijden, M. (2011). Factors controlling the input-output relationship of spherical bushy cells in the gerbil cochlear nucleus. J. Neurosci. *31*, 4260–4273. https://doi.org/10.1523/JNEUROSCI.5433-10.2011.

Kushibiki, Y., Suzuki, T., Jin, Y., and Taru, H. (2019). RIMB-1/RIM-Binding Protein and UNC-10/RIM Redundantly Regulate Pre-synaptic Localization of the Voltage-Gated Calcium Channel in Caenorhabditis elegans. J. Neurosci. *39*, 8617–8631. https://doi.org/10.1523/JNEUROSCI.0506-19.2019.

Kusick, G.F., Chin, M., Raychaudhuri, S., Lippmann, K., Adula, K.P., Hujber, E.J., Vu, T., Davis, M.W., Jorgensen, E.M., and Watanabe, S. (2020). Synaptic vesicles transiently dock to refill release sites. Nat. Neurosci. 2020 2311 *23*, 1329–1338. https://doi.org/10.1038/s41593-020-00716-1.

LaConte, L.E.W., Chavan, V., Liang, C., Willis, J., Schönhense, E.M., Schoch, S., and Mukherjee, K. (2016). CASK stabilizes neurexin and links it to liprin-α in a neuronal activity-dependent manner. Cell. Mol. Life Sci. *73*, 3599–3621. https://doi.org/10.1007/S00018-016-2183-4/FIGURES/8.

Lauer, A.M., Connelly, C.J., Graham, H., and Ryugo, D.K. (2013). Morphological characterization of bushy cells and their inputs in the laboratory mouse (Mus musculus) anteroventral cochlear nucleus. PLoS One *8*. https://doi.org/10.1371/JOURNAL.PONE.0073308.

Leal-Ortiz, S., Waites, C.L., Terry-Lorenzo, R., Zamorano, P., Gundelfinger, E.D., and Garner, C.C. (2008). Piccolo modulation of Synapsin1a dynamics regulates synaptic vesicle exocytosis. J. Cell Biol. *181*, 831–846. https://doi.org/10.1083/jcb.200711167.

Leão, R.M., and Von Gersdorff, H. (2002). Noradrenaline Increases High-Frequency Firing at the Calyx of Held Synapse During Development by Inhibiting Glutamate Release. J. Neurophysiol. *87*, 2297–2306. https://doi.org/10.1152/jn.2002.87.5.2297.

Leão, R.M., Kushmerick, C., Pinaud, R., Renden, R., Li, G.L., Taschenberger, H., Spirou, G., Levinson, S.R., and Von Gersdorff, H. (2005). Pre-synaptic Na+ channels: locus, development, and recovery from inactivation at a high-fidelity synapse. J. Neurosci. *25*, 3724–3738. https://doi.org/10.1523/JNEUROSCI.3983-04.2005.

Lee, J.S., Ho, W.K., and Lee, S.H. (2010). Post-tetanic increase in the fast-releasing synaptic vesicle pool at the expense of the slowly releasing pool. J. Gen. Physiol. *136*, 259–272. https://doi.org/10.1085/jgp.201010437.

Lee, J.S., Ho, W.K., and Lee, S.H. (2012). Actin-dependent rapid recruitment of reluctant synaptic vesicles into a fast-releasing vesicle pool. Proc. Natl. Acad. Sci. U. S. A. *109*. https://doi.org/10.1073/pnas.1114072109.

Lee, J.S., Ho, W.K., Neher, E., and Lee, S.H. (2013a). Superpriming of synaptic vesicles after their recruitment to the readily releasable pool. Proc. Natl. Acad. Sci. U. S. A. *110*, 15079–15084. https://doi.org/10.1073/pnas.1314427110.

Lee, J.S., Ho, W.K., Neher, E., and Lee, S.H. (2013b). Superpriming of synaptic vesicles after their recruitment to the readily releasable pool. Proc. Natl. Acad. Sci. U. S. A. *110*, 15079–15084. https://doi.org/10.1073/pnas.1314427110.

Lee, P.D.K., Conover, C.A., and Powell, D.R. (1993). Regulation and function of insulin-like growth factor-binding protein-1. Proc. Soc. Exp. Biol. Med. *204*, 4–29. https://doi.org/10.3181/00379727-204-43630.

Letellier, M., Park, Y.K., Chater, T.E., Chipman, P.H., Gautam, S.G., Oshima-Takago, T., and Goda, Y.

(2016). Astrocytes regulate heterogeneity of pre-synaptic strengths in hippocampal networks. Proc. Natl. Acad. Sci. U. S. A. *113*, E2685–E2694. https://doi.org/10.1073/PNAS.1523717113.

Li, C., Li, X., Bi, Z., Sugino, K., Wang, G., Zhu, T., and Liu, Z. (2020). Comprehensive transcriptome analysis of cochlear spiral ganglion neurons at multiple ages. Elife *9*. https://doi.org/10.7554/eLife.50491.

Li, W., Ma, C., Guan, R., Xu, Y., Tomchick, D.R., and Rizo, J. (2011). The crystal structure of a Munc13 C-terminal module exhibits a remarkable similarity to vesicle tethering factors. Struct. (London, Engl. 1993) *19*, 1443–1455. https://doi.org/10.1016/j.str.2011.07.012.

Liang, L., Lu, T., and Wang, X. (2002). Neural representations of sinusoidal amplitude and frequency modulations in the primary auditory cortex of awake primates. J. Neurophysiol. *87*, 2237–2261. .

Liang, M., Jin, G., Xie, X., Zhang, W., Li, K., Niu, F., Yu, C., and Wei, Z. (2021). Oligomerized liprin-α promotes phase separation of ELKS for compartmentalization of pre-synaptic active zone proteins. Cell Rep. *34*, 108901. https://doi.org/10.1016/J.CELREP.2021.108901.

Liberman, M.C. (1982). Single-neuron labeling in the cat auditory nerve. Science *216*, 1239–1241. https://doi.org/10.1126/SCIENCE.7079757.

Liberman, M.C., Gao, J., He, D.Z.Z., Wu, X., Jia, S., and Zuo, J. (2002). Prestin is required for electromotility of the outer hair cell and for the cochlear amplifier. Nature *419*, 300–304. https://doi.org/10.1038/NATURE01059.

Lin, K.-H., Taschenberger, H., and Neher, E. (2022). A sequential two-step priming scheme reproduces diversity in synaptic strength and short-term plasticity. Proc. Natl. Acad. Sci. U. S. A. *119*. https://doi.org/10.1073/PNAS.2207987119.

Lin, K.H., Oleskevich, S., and Taschenberger, H. (2011). Pre-synaptic Ca2+ influx and vesicle exocytosis at the mouse endbulb of Held: A comparison of two auditory nerve terminals. J. Physiol. *589*, 4301–4320. https://doi.org/10.1113/jphysiol.2011.209189.

Lipstein, N., Chang, S., Lin, K.-H., López-Murcia, F.J., Neher, E., Taschenberger, H., and Brose, N. (2021). Munc13-1 is a Ca2+-phospholipid-dependent vesicle priming hub that shapes synaptic short-term plasticity and enables sustained neurotransmission. Neuron https://doi.org/10.1016/j.neuron.2021.09.054.

Liu, C., Goel, P., and Kaeser, P.S. (2021). Spatial and temporal scales of dopamine transmission. Nat. Rev. Neurosci. 1–14. https://doi.org/10.1038/s41583-021-00455-7.

Liu, K.S.Y., Siebert, M., Mertel, S., Knoche, E., Wegener, S., Wichmann, C., Matkovic, T., Muhammad, K., Depner, H., Mettke, C., et al. (2011). RIM-binding protein, a central part of the active zone, is essential for neurotransmitter release. Science (80-.). *334*, 1565–1569. https://doi.org/10.1126/science.1212991.

Liu, X., Seven, A.B., Camacho, M., Esser, V., Xu, J., Trimbuch, T., Quade, B., Su, L., Ma, C., Rosenmund, C., et al. (2016). Functional synergy between the Munc13 C-terminal C1 and C2 domains. Elife *5*. https://doi.org/10.7554/ELIFE.13696.

López-Murcia, F.J., Reim, K., Jahn, O., Taschenberger, H., and Brose, N. (2019). Acute Complexin Knockout Abates Spontaneous and Evoked Transmitter Release. Cell Rep. *26*, 2521-2530.e5. https://doi.org/10.1016/j.celrep.2019.02.030.

Lou, X., Scheuss, V., and Schneggenburger, R. (2005). Allosteric modulation of the pre-synaptic Ca2+ sensor for vesicle fusion. Nature *435*, 497–501. https://doi.org/10.1038/nature03568.

Lu, J., Machius, M., Dulubova, I., Dai, H., Südhof, T.C., Tomchick, D.R., and Rizo, J. (2006). Structural

basis for a Munc13-1 homodimer to Munc13-1/RIM heterodimer switch. PLoS Biol. *4*, 1159–1172. https://doi.org/10.1371/journal.pbio.0040192.

Lujan, B., Dagostin, A., and Von Gersdorff, H. (2019). Pre-synaptic Diversity Revealed by Ca 2+-Permeable AMPA Receptors at the Calyx of Held Synapse. J. Neurosci. *39*, 2981–2994. https://doi.org/10.1523/JNEUROSCI.2565-18.2019.

Luo, F., Liu, X., Südhof, T.C., and Acuna, C. (2017). Efficient stimulus-secretion coupling at ribbon synapses requires RIM-binding protein tethering of L-type Ca2+ channels. Proc. Natl. Acad. Sci. U. S. A. *114*, E8081–E8090. https://doi.org/10.1073/pnas.1702991114.

Ma, C., Li, W., Xu, Y., and Rizo, J. (2011). Munc13 Mediates the Transition from the Closed Syntaxin–Munc18 complex to the SNARE complex. Nat. Struct. Mol. Biol. *18*, 542–549. https://doi.org/10.1038/nsmb.2047.

Ma, C., Su, L., Seven, A.B., Xu, Y., and Rizo, J. (2013). Reconstitution of the vital functions of Munc18 and Munc13 in neurotransmitter release. Science *339*, 421–425. https://doi.org/10.1126/SCIENCE.1230473.

Ma, L., Kang, Y., Jiao, J., Rebane, A.A., Cha, H.K., Xi, Z., Qu, H., and Zhang, Y. (2016). α-SNAP Enhances SNARE Zippering by Stabilizing the SNARE Four-Helix Bundle. Cell Rep. *15*, 531–539. https://doi.org/10.1016/J.CELREP.2016.03.050.

Maas, C., Torres, V.I., Altrock, W.D., Leal-Ortiz, S., Wagh, D., Terry-Lorenzo, R.T., Fejtova, A., Gundelfinger, E.D., Ziv, N.E., and Garner, C.C. (2012). Formation of Golgi-derived active zone precursor vesicles. J. Neurosci. *32*, 11095–11108. https://doi.org/10.1523/JNEUROSCI.0195-12.2012.

Malsam, J., Bärfuss, S., Trimbuch, T., Zarebidaki, F., Sonnen, A.F.P., Wild, K., Scheutzow, A., Rohland, L., Mayer, M.P., Sinning, I., et al. (2020). Complexin Suppresses Spontaneous Exocytosis by Capturing the Membrane-Proximal Regions of VAMP2 and SNAP25. Cell Rep. *32*, 107926. https://doi.org/10.1016/j.celrep.2020.107926.

Marin-Burgin, A., Eisenhart, F.J., Baca, S.M., Kristan, W.B., and French, K.A. (2005). Sequential development of electrical and chemical synaptic connections generates a specific behavioral circuit in the leech. J. Neurosci. *25*, 2478–2489. https://doi.org/10.1523/JNEUROSCI.4787-04.2005.

Martín, R., García-Font, N., Suárez-Pinilla, A.S., Bartolomé-Martín, D., Ferrero, J.J., Luján, R., Torres, M., and Sánchez-Prieto, J. (2020). β-adrenergic receptors/epac signaling increases the size of the readily releasable pool of synaptic vesicles required for parallel fiber LTP. J. Neurosci. *40*, 8604–8617. https://doi.org/10.1523/JNEUROSCI.0716-20.2020.

Martineau, M., Guzman, R.E., Fahlke, C., and Klingauf, J. VGLUT1 functions as a glutamate/proton exchanger with chloride channel activity in hippocampal glutamatergic synapses. https://doi.org/10.1038/s41467-017-02367-6.

McGaugh, J.L., and Roozendaal, B. (2002). Role of adrenal stress hormones in forming lasting memories in the brain. Curr. Opin. Neurobiol. *12*, 205–210. https://doi.org/10.1016/S0959-4388(02)00306-9.

McGinley, M.J., and Oertel, D. (2006). Rate thresholds determine the precision of temporal integration in principal cells of the ventral cochlear nucleus. Hear. Res. *216–217*, 52–63. https://doi.org/10.1016/j.heares.2006.02.006.

McMahon, H.T., and Boucrot, E. (2011). Molecular mechanism and physiological functions of clathrin-mediated endocytosis. Nat. Rev. Mol. Cell Biol. *12*, 517–533. https://doi.org/10.1038/nrm3151.

McMahon, H.T., Missler, M., Li, C., and Südhof, T.C. (1995). Complexins: Cytosolic proteins that

regulate SNAP receptor function. Cell *83*, 111–119. https://doi.org/10.1016/0092-8674(95)90239-2.

Meinrenken, C.J., Borst, J.G.G., and Sakmann, B. (2002). Calcium secretion coupling at calyx of held governed by nonuniform channel-vesicle topography. J. Neurosci. *22*, 1648–1667. https://doi.org/10.1523/jneurosci.22-05-01648.2002.

Melia, T.J. (2007). Putting the clamps on membrane fusion: How complexin sets the stage for calcium-mediated exocytosis. FEBS Lett. *581*, 2131–2139. https://doi.org/10.1016/j.febslet.2007.02.066.

Mendoza Schulz, A., Jing, Z., María Sánchez Caro, J., Wetzel, F., Dresbach, T., Strenzke, N., Wichmann, C., and Moser, T. (2014). Bassoon-disruption slows vesicle replenishment and induces homeostatic plasticity at a CNS synapse. EMBO J. *33*, 512–527. https://doi.org/10.1002/embj.201385887.

Meyer, A.C., Neher, E., and Schneggenburger, R. (2001). Estimation of quantal size and number of functional active zones at the calyx of held synapse by nonstationary EPSC variance analysis. J. Neurosci. *21*, 7889–7900. https://doi.org/10.1523/jneurosci.21-20-07889.2001.

Milosevic, I., Giovedi, S., Lou, X., Raimondi, A., Collesi, C., Shen, H., Paradise, S., O'Toole, E., Ferguson, S., Cremona, O., et al. (2011). Recruitment of endophilin to clathrin-coated pit necks is required for efficient vesicle uncoating after fission. Neuron *72*, 587–601. https://doi.org/10.1016/J.NEURON.2011.08.029.

Milovanovic, D., Wu, Y., Bian, X., and De Camilli, P. (2018). A liquid phase of synapsin and lipid vesicles. Science *361*, 604–607. https://doi.org/10.1126/SCIENCE.AAT5671.

Misura, K.M.S., Scheller, R.H., and Weis, W.I. (2000). Three-dimensional structure of the neuronal-Sec1–syntaxin 1a complex. Nat. 2000 4046776 *404*, 355–362. https://doi.org/10.1038/35006120.

Mizutani, H., Hori, T., and Takahashi, T. (2006). 5-HT1B receptor-mediated pre-synaptic inhibition at the calyx of Held of immature rats. Eur. J. Neurosci. *24*, 1946–1954. https://doi.org/10.1111/j.1460-9568.2006.05063.x.

Mohrmann, R., De Wit, H., Verhage, M., Neher, E., and Sørensen, J.B. (2010). Fast vesicle fusion in living cells requires at least three SNARE complexes. Science (80-.). *330*, 502–505. https://doi.org/10.1126/SCIENCE.1193134/SUPPL_FILE/MOHRMANN.SOM.PDF.

Monier, S., Jollivet, F., Janoueix-Lerosey, I., Johannes, L., and Goud, B. (2002). Characterization of novel Rab6-interacting proteins involved in endosome-to-TGN transport. Traffic *3*, 289–297. https://doi.org/10.1034/J.1600-0854.2002.030406.X.

Moser, T., and Beutner, D. (2000). Kinetics of exocytosis and endocytosis at the cochlear inner hair cell afferent synapse of the mouse. Proc Natl Acad Sci U S A *97*, 883–888. https://doi.org/10.1073/pnas.97.2.883.

Moser, T., Neef, A., and Khimich, D. (2006). Mechanisms underlying the temporal precision of sound coding at the inner hair cell ribbon synapse. J. Physiol. *576*, 55–62. https://doi.org/10.1113/JPHYSIOL.2006.114835.

Mukherjee, K., Yang, X., Gerber, S.H., Kwon, H.B., Ho, A., Castillo, P.E., Liu, X., and Südhof, T.C. (2010). Piccolo and bassoon maintain synaptic vesicle clustering without directly participating in vesicle exocytosis. Proc. Natl. Acad. Sci. U. S. A. *107*, 6504–6509. https://doi.org/10.1073/pnas.1002307107.

Nakata, T., Kitamura, Y., Shimizu, K., Tanaka, S., Fujimori, M., Yokoyama, S., Ito, K., and Emi, M. (1999). Fusion of a novel gene, ELKS, to RET due to translocation t(10;12)(q11;p13) in a papillary thyroid carcinoma. Genes. Chromosomes Cancer *25*, 97–103. https://doi.org/10.1002/(SICI)1098-2264(199906)25:2.

Neef, J., Jung, S., Wong, A.B., Reuter, K., Pangrsic, T., Chakrabarti, R., Kügler, S., Lenz, C., Nouvian, R.,

Boumil, R.M., et al. (2014). Modes and regulation of endocytic membrane retrieval in mouse auditory hair cells. J. Neurosci. *34*, 705–716. https://doi.org/10.1523/JNEUROSCI.3313-13.2014.

Neher, E. (1998). Vesicle pools and Ca2+ microdomains: new tools for understanding their roles in neurotransmitter release. Neuron *20*, 389–399. https://doi.org/10.1016/S0896-6273(00)80983-6.

Neher, E. (2010). What is rate-limiting during sustained synaptic activity: Vesicle supply or the availability of release sites. Front. Synaptic Neurosci. *2*, 1–6. https://doi.org/10.3389/fnsyn.2010.00144.

Neher, E. (2017). Some Subtle Lessons from the Calyx of Held Synapse. Biophys. J. *112*, 215–223. https://doi.org/10.1016/j.bpj.2016.12.017.

Neher, E., and Brose, N. (2018). Dynamically Primed Synaptic Vesicle States: Key to Understand Synaptic Short-Term Plasticity. Neuron *100*, 1283–1291. https://doi.org/10.1016/j.neuron.2018.11.024.

Neher, E., and Taschenberger, H. (2021). Non-negative Matrix Factorization as a Tool to Distinguish Between Synaptic Vesicles in Different Functional States. Neuroscience 1–21. https://doi.org/10.1016/j.neuroscience.2020.10.012.

Nouvian, R., Beutner, D., Parsons, T.D., and Moser, T. (2006). Structure and function of the hair cell ribbon synapse. J. Membr. Biol. *209*, 153–165. https://doi.org/10.1007/s00232-005-0854-4.

Nyitrai, H., Wang, S.S.H., and Kaeser, P.S. (2020). ELKS1 Captures Rab6-Marked Vesicular Cargo in Pre-synaptic Nerve Terminals. Cell Rep. *31*. https://doi.org/10.1016/j.celrep.2020.107712.

O'Dell, T.J., Connor, S.A., Gelinas, J.N., and Nguyen, P. V. (2010). Viagra for your synapses: Enhancement of hippocampal long-term potentiation by activation of beta-adrenergic receptors. Cell. Signal. *22*, 728–736. https://doi.org/10.1016/j.cellsig.2009.12.004.

Oertel, D., Shatadal, S., and Cao, X.J. (2008). In the ventral cochlear nucleus Kv1.1 and subunits of HCN1 are colocalized at surfaces of neurons that have low-voltage-activated and hyperpolarization-activated conductances. Neuroscience *154*, 77–86. https://doi.org/10.1016/j.neuroscience.2008.01.085.

Oestreich, E.A., Malik, S., Goonasekera, S.A., Blaxall, B.C., Kelley, G.G., Dirksen, R.T., and Smrcka, A. V. (2009). Epac and phospholipase Cepsilon regulate Ca2+ release in the heart by activation of protein kinase Cepsilon and calcium-calmodulin kinase II. J. Biol. Chem. *284*, 1514–1522. https://doi.org/10.1074/JBC.M806994200.

Okada, Y., Yamazaki, H., Sekine-Aizawa, Y., and Hirokawa, N. (1995). The neuron-specific kinesin superfamily protein KIF1A is a unique monomeric motor for anterograde axonal transport of synaptic vesicle precursors. Cell *81*, 769–780. https://doi.org/10.1016/0092-8674(95)90538-3.

Okerlund, N.D., Schneider, K., Leal-Ortiz, S., Montenegro-Venegas, C., Kim, S.A., Garner, L.C., Waites, C.L., Gundelfinger, E.D., Reimer, R.J., and Garner, C.C. (2018). Bassoon Controls Pre-synaptic Autophagy through Atg5. Neuron *97*, 727. https://doi.org/10.1016/J.NEURON.2018.01.010.

Oleskevich, S., Clements, J., and Walmsley, B. (2000). Release probability modulates short-term plasticity at a rat giant terminal. J. Physiol. *524*, 513–523. https://doi.org/10.1111/j.1469-7793.2000.00513.x.

Oleskevich, S., Youssoufian, M., and Walmsley, B. (2004). Pre-synaptic plasticity at two giant auditory synapses in normal and deaf mice. J. Physiol. *560*, 709–719. https://doi.org/10.1113/jphysiol.2004.066662.

Ortner, N.J., Pinggera, A., Hofer, N.T., Siller, A., Brandt, N., Raffeiner, A., Vilusic, K., Lang, I., Blum, K.,

Obermair, G.J., et al. (2020). RBP2 stabilizes slow Cav1.3 Ca2+ channel inactivation properties of cochlear inner hair cells. Pflugers Arch. Eur. J. Physiol. *472*, 3–25. https://doi.org/10.1007/s00424-019-02338-4.

Pan, B., and Zucker, R.S. (2009). A General Model of Synaptic Transmission and Short-Term Plasticity. Neuron *62*, 539–554. https://doi.org/10.1016/j.neuron.2009.03.025.

Pang, Z.P., Bacaj, T., Yang, X., Zhou, P., Xu, W., and Südhof, T.C. (2011). Doc2 Supports Spontaneous Synaptic Transmission by a Ca2+-Independent Mechanism. Neuron *70*, 244–251. https://doi.org/10.1016/j.neuron.2011.03.011.

Parisotto, D., Pfau, M., Scheutzow, A., Wild, K., Mayer, M.P., Malsam, J., Sinning, I., and Söllner, T.H. (2014). An extended helical conformation in domain 3a of Munc18-1 provides a template for SNARE (soluble N-ethylmaleimide-sensitive factor attachment protein receptor) complex assembly. J. Biol. Chem. *289*, 9639–9650. https://doi.org/10.1074/JBC.M113.514273.

Patzke, C., Brockmann, M.M., Dai, J., Gan, K.J., Grauel, M.K., Fenske, P., Liu, Y., Acuna, C., Rosenmund, C., and Südhof, T.C. (2019). Neuromodulator Signaling Bidirectionally Controls Vesicle Numbers in Human Synapses. Cell *179*, 498-513.e22. https://doi.org/10.1016/J.CELL.2019.09.011.

Patzke, C., Dai, J., Brockmann, M.M., Sun, Z., Fenske, P., Rosenmund, C., and Südhof, T.C. (2021). Cannabinoid receptor activation acutely increases synaptic vesicle numbers by activating synapsins in human synapses. Mol. Psychiatry *26*, 6253–6268. https://doi.org/10.1038/S41380-021-01095-0.

Payton, B.W., Bennett, M.V.L., and Pappas, G.D. (1969). Permeability and structure of junctional membranes at an electrotonic synapse. Science (80-.). *166*, 1641–1643. https://doi.org/10.1126/SCIENCE.166.3913.1641.

Pei, J., Ma, C., Rizo, J., and Grishin, N. V. (2009). Remote homology between Munc13 MUN domain and vesicle tethering complexes. J. Mol. Biol. *391*, 509–517. https://doi.org/10.1016/J.JMB.2009.06.054.

Pereda, A.E. (2014). Electrical synapses and their functional interactions with chemical synapses. Nat. Rev. Neurosci. *15*, 250–263. https://doi.org/10.1038/NRN3708.

Petzoldt, A.G., Götz, T.W.B., Driller, J.H., Lützkendorf, J., Reddy-Alla, S., Matkovic-Rachid, T., Liu, S., Knoche, E., Mertel, S., Ugorets, V., et al. (2020). RIM-binding protein couples synaptic vesicle recruitment to release sites. J. Cell Biol. *219*. https://doi.org/10.1083/jcb.201902059.

Picher, M.M., Oprişoreanu, A.M., Jung, S.Y., Michel, K., Schoch, S., and Moser, T. (2017). Rab interacting molecules 2 and 3 directly interact with the pore-forming Cav 1.3 Ca2+ channel subunit and promote its membrane expression. Front. Cell. Neurosci. *11*, 1–11. https://doi.org/10.3389/fncel.2017.00160.

Pofantis, E., Neher, E., and Dresbach, T. (2021). Regulation of a subset of release-ready vesicles by the pre-synaptic protein Mover. Proc. Natl. Acad. Sci. *118*, e2022551118. https://doi.org/10.1073/PNAS.2022551118.

Qin, Y., Zhu, Y., Baumgart, J.P., Stornetta, R.L., Seidenman, K., Mack, V., Van Aelst, L., and Zhu, J.J. (2005). State-dependent Ras signaling and AMPA receptor trafficking. Genes Dev. *19*, 2000–2015. https://doi.org/10.1101/GAD.342205.

Quade, B., Camacho, M., Zhao, X., Orlando, M., Trimbuch, T., Xu, J., Li, W., Nicastro, D., Rosenmund, C., and Rizo, J. (2019). Membrane bridging by Munc13-1 is crucial for neurotransmitter release. Elife *8*. https://doi.org/10.7554/ELIFE.42806.

Radulovic, T., Dong, W., Goral, R.O., Thomas, C.I., Veeraraghavan, P., Montesinos, M.S., Guerrero-

Given, D., Goff, K., Lübbert, M., Kamasawa, N., et al. (2020). Pre-synaptic development is controlled by the core active zone proteins CAST/ELKS. J. Physiol. *598*, 2431–2452. https://doi.org/10.1113/JP279736.

Regehr, W.G. (2012). Short-Term Pre-synaptic Plasticity. Cold Spring Harb. Perspect. Biol. *4*, a005702. https://doi.org/10.1101/CSHPERSPECT.A005702.

Ren, Y., Barnwell, L.F., Alexander, J.C., Lubin, F.D., Adelman, J.P., Pfaffinger, P.J., Schrader, L.A., and Anderson, A.E. (2006). Regulation of surface localization of the small conductance Ca2+-activated potassium channel, Sk2, through direct phosphorylation by cAMP-dependent protein kinase. J. Biol. Chem. *281*, 11769–11779. https://doi.org/10.1074/JBC.M513125200.

Rettig, J., and Neher, E. (2002). Emerging roles of pre-synaptic proteins in Ca++-triggered exocytosis. Science (80-.). *298*, 781–785. https://doi.org/10.1126/SCIENCE.1075375/ASSET/41DF6F51-915F-4B6B-94F0-68CDCBE70E67/ASSETS/GRAPHIC/SE4220977001.JPEG.

Rhee, J.-S., Betz, A., Pyott, S., Reim, K., Varoqueaux, F., Augustin, I., Hesse, D., Südhof, T.C., Takahashi, M., Rosenmund, C., et al. (2002). Beta phorbol ester- and diacylglycerol-induced augmentation of transmitter release is mediated by Munc13s and not by PKCs. Cell *108*, 121–133. https://doi.org/10.1016/S0092-8674(01)00635-3.

Richards, D.A., Guatimosim, C., Rizzoli, S.O., and Betz, W.J. (2003). Synaptic vesicle pools at the frog neuromuscular junction. Neuron *39*, 529–541. https://doi.org/10.1016/S0896-6273(03)00405-7.

Richmond, J.E., Weimer, R.M., and Jorgensen, E.M. (2001). An open form of syntaxin bypasses the requirement for UNC-13 in vesicle priming. Nature *412*, 338–341. https://doi.org/10.1038/35085583.

Rizo, J. (2022). Molecular Mechanisms Underlying Neurotransmitter Release. Https://Doi.Org/10.1146/Annurev-Biophys-111821-104732 *51*, 377–408. https://doi.org/10.1146/ANNUREV-BIOPHYS-111821-104732.

Rizo, J., and Südhof, T.C. (1998). C2-domains, Structure and Function of a Universal Ca2+-binding Domain. J. Biol. Chem. *273*, 15879–15882. https://doi.org/10.1074/jbc.273.26.15879.

Rizzoli, S.O. (2014). Synaptic vesicle recycling: steps and principles. EMBO J. *33*, 788–822. https://doi.org/10.1002/EMBJ.201386357.

Rizzoli, S.O., and Betz, W.J. (2004). The structural organization of the readily releasable pool of synaptic vesicles. Science *303*, 2037–2039. https://doi.org/10.1126/SCIENCE.1094682.

Rizzoli, S.O., and Betz, W.J. (2005). Synaptic vesicle pools. Nat. Rev. Neurosci. *6*, 57–69. https://doi.org/10.1038/NRN1583.

Rosenmund, C., and Stevens, C.F. (1996). Definition of the readily releasable pool of vesicles at hippocampal synapses. Neuron *16*, 1197–1207. https://doi.org/10.1016/S0896-6273(00)80146-4.

Rubio, M.E., Matsui, K., Fukazawa, Y., Kamasawa, N., Harada, H., Itakura, M., Molnár, E., Abe, M., Sakimura, K., and Shigemoto, R. (2017). The number and distribution of AMPA receptor channels containing fast kinetic GluA3 and GluA4 subunits at auditory nerve synapses depend on the target cells. Brain Struct. Funct. *222*, 3375–3393. https://doi.org/10.1007/S00429-017-1408-0/FIGURES/9.

Rutherford, M.A., Chapochnikov, N.M., and Moser, T. (2012). Spike Encoding of Neurotransmitter Release Timing by Spiral Ganglion Neurons of the Cochlea. J. Neurosci. *32*, 4773–4789. https://doi.org/10.1523/JNEUROSCI.4511-11.2012.

Sabatini, B.L., and Tian, L. (2020). Imaging Neurotransmitter and Neuromodulator Dynamics In Vivo with Genetically Encoded Indicators. Neuron *108*, 17–32. https://doi.org/10.1016/j.neuron.2020.09.036.

Saheki, Y., and De Camilli, P. (2012). Synaptic vesicle endocytosis. Cold Spring Harb. Perspect. Biol. *4*. https://doi.org/10.1101/CSHPERSPECT.A005645.

Sakaba, T., and Neher, E. (2001). Calmodulin mediates rapid recruitment of fast-releasing synaptic vesicles at a calyx-type synapse. Neuron *32*, 1119–1131. https://doi.org/10.1016/S0896-6273(01)00543-8.

Sakaba, T., and Neher, E. (2003). Direct modulation of synaptic vesicle priming by GABAB receptor activation at a glutamatergic synapse. Nature *424*, 775–778. https://doi.org/10.1038/nature01859.

Sara, Y., Virmani, T., Deák, F., Liu, X., and Kavalali, E.T. (2005). An Isolated Pool of Vesicles Recycles at Rest and Drives Spontaneous Neurotransmission. Neuron *45*, 563–573. https://doi.org/10.1016/j.neuron.2004.12.056.

Scheuss, V., Schneggenburger, R., and Neher, E. (2002). Separation of pre-synaptic and post-synaptic contributions to depression by covariance analysis of successive EPSCs at the calyx of held synapse. J. Neurosci. *22*, 728–739. https://doi.org/10.1523/jneurosci.22-03-00728.2002.

Schikorski, T., and Stevens, C.F. (2001). Morphological correlates of functionally defined synaptic vesicle populations. Nat. Neurosci. *4*, 391–395. https://doi.org/10.1038/86042.

Schlüter, O.M., Basu, J., Südhof, T.C., and Rosenmund, C. (2006). Rab3 superprimes synaptic vesicles for release: Implications for short-term synaptic plasticity. J. Neurosci. *26*, 1239–1246. https://doi.org/10.1523/JNEUROSCI.3553-05.2006.

Schneggenburger, R., and Neher, E. (2000). Intracellular calcium dependence of transmitter release rates at a fast central synapse. Nature *406*, 889–993. https://doi.org/10.1038/35022702.

Schneggenburger, R., Meyer, A.C., and Neher, E. (1999). Released fraction and total size of a pool of immediately available transmitter quanta at a calyx synapse. Neuron *23*, 399–409. https://doi.org/10.1016/S0896-6273(00)80789-8.

Sento, S., and Ryugo, D.K. (1989). Endbulbs of held and spherical bushy cells in cats: morphological correlates with physiological properties. J. Comp. Neurol. *280*, 553–562. https://doi.org/10.1002/CNE.902800406.

Serra-Pages, C., Kedersha, N.L., Fazikas, L., Medleyl, Q., Debant, A., and Streuli, M. (1995). The LAR transmembrane protein tyrosine phosphatase and a coiled-coil LAR-interacting protein co-localize at focal adhesions. EMBO J. *14*, 2827–2838. https://doi.org/10.1002/j.1460-2075.1995.tb07282.x.

Shapira, M., Zhai, R.G., Dresbach, T., Bresler, T., Torres, V.I., Gundelfinger, E.D., Ziv, N.E., and Garner, C.C. (2003). Unitary assembly of pre-synaptic active zones from Piccolo-Bassoon transport vesicles. Neuron *38*, 237–252. https://doi.org/10.1016/S0896-6273(03)00207-1.

Shen, H.H. (2018). Core Concept: Perineuronal nets gain prominence for their role in learning, memory, and plasticity. Proc. Natl. Acad. Sci. U. S. A. *115*, 9813–9815. https://doi.org/10.1073/PNAS.1815273115.

Shibasaki, T., Sunaga, Y., Fujimoto, K., Kashima, Y., and Seino, S. (2004). Interaction of ATP Sensor, cAMP Sensor, Ca2+ Sensor, and Voltage-dependent Ca2+ Channel in Insulin Granule Exocytosis. J. Biol. Chem. *279*, 7956–7961. https://doi.org/10.1074/jbc.M309068200.

Shin, O.H., Lu, J., Rhee, J.S., Tomchick, D.R., Pang, Z.P., Wojcik, S.M., Camacho-Perez, M., Brose, N., MacHius, M., Rizo, J., et al. (2010). Munc13 C 2 B domain is an activity-dependent Ca 2+ regulator of synaptic exocytosis. Nat. Struct. Mol. Biol. *17*, 280–288. https://doi.org/10.1038/nsmb.1758.

Shrestha, B.R., Chia, C., Wu, L., Kujawa, S.G., Liberman, M.C., and Goodrich, L. V (2018). Sensory Neuron Diversity in the Inner Ear Is Shaped by Activity. Cell *174*, 1229-1246.e17.

https://doi.org/10.1016/j.cell.2018.07.007.

Siddiqui, T.J., and Craig, A.M. (2011). Synaptic organizing complexes. Curr. Opin. Neurobiol. *21*, 132–143. https://doi.org/10.1016/J.CONB.2010.08.016.

Singer, J.H., and Berger, A.J. (1996). Pre-synaptic inhibition by serotonin: a possible mechanism for switching motor output of the hypoglossal nucleus. Sleep *19*. https://doi.org/10.1093/SLEEP/19.SUPPL_10.146.

Singer, J.H., Bellingham, M.C., and Berger, A.J. (1996). Pre-synaptic inhibition of glutamatergic synaptic transmission to rat motoneurons by serotonin. J. Neurophysiol. *76*, 799–807. https://doi.org/10.1152/jn.1996.76.2.799.

Skou, J.C., and Hoffman, J.F. (1998). The influence of some cations on an adenosine triphosphatase from peripheral nerves. J. Am. Soc. Nephrol. *9*, 2170–2177. https://doi.org/10.1681/asn.v9112170.

Smith, P.H., Joris, P.X., and Yin, T.C.T. (1993). Projections of physiologically characterized spherical bushy cell axons from the cochlear nucleus of the cat: Evidence for delay lines to the medial superior olive. J. Comp. Neurol. *331*, 245–260. https://doi.org/https://doi.org/10.1002/cne.903310208.

Söllner, T., Whiteheart, S.W., Brunner, M., Erdjument-Bromage, H., Geromanos, S., Tempst, P., and Rothman, J.E. (1993). SNAP receptors implicated in vesicle targeting and fusion. Nature *362*, 318–324. https://doi.org/10.1038/362318a0.

Spirou, G.A., Rager, J., and Manis, P.B. (2005). Convergence of auditory-nerve fiber projections onto globular bushy cells. Neuroscience *136*, 843–863. https://doi.org/10.1016/J.NEUROSCIENCE.2005.08.068.

Stevens, C.F., and Wesseling, J.F. (1999). Identification of a novel process limiting the rate of synaptic vesicle cycling at hippocampal synapses. Neuron *24*, 1017–1028. .

Strenzke, N., Chanda, S., Kopp-Scheinpflug, C., Khimich, D., Reim, K., Bulankina, A. V., Neef, A., Wolf, F., Brose, N., Xu-Friedman, M.A., et al. (2009). Complexin-I is required for high-fidelity transmission at the endbulb of held auditory synapse. J. Neurosci. *29*, 7991–8004. https://doi.org/10.1523/JNEUROSCI.0632-09.2009.

Südhof, T.C. (2012). The Pre-synaptic Active Zone. Neuron *75*, 11–25. https://doi.org/10.1016/J.NEURON.2012.06.012.

Sun, S., Babola, T., Pregernig, G., So, K.S., Nguyen, M., Su, S.S.M., Palermo, A.T., Bergles, D.E., Burns, J.C., and Müller, U. (2018). Hair Cell Mechanotransduction Regulates Spontaneous Activity and Spiral Ganglion Subtype Specification in the Auditory System. Cell *174*, 1247-1263.e15. https://doi.org/10.1016/j.cell.2018.07.008.

Takahashi, T., Forsythe, L.D., Tsujimoto, T., Barnes-Davies, M., and Onodera, K. (1996). Pre-synaptic calcium current modulation by a metabotropic glutamate receptor. Science *274*, 594–597. https://doi.org/10.1126/SCIENCE.274.5287.594.

Takamori, S., Holt, M., Stenius, K., Lemke, E.A., Grønborg, M., Riedel, D., Urlaub, H., Schenck, S., Brügger, B., Ringler, P., et al. (2006). Molecular Anatomy of a Trafficking Organelle. Cell *127*, 831–846. https://doi.org/10.1016/J.CELL.2006.10.030.

Takeuchi, T., Duszkiewicz, A.J., Sonneborn, A., Spooner, P.A., Yamasaki, M., Watanabe, M., Smith, C.C., Fernández, G., Deisseroth, K., Greene, R.W., et al. (2016). Locus coeruleus and dopaminergic consolidation of everyday memory. Nature *537*, 357–362. https://doi.org/10.1038/NATURE19325.

Tang, A.H., Chen, H., Li, T.P., Metzbower, S.R., MacGillavry, H.D., and Blanpied, T.A. (2016). A trans-synaptic nanocolumn aligns neurotransmitter release to receptors. Nature *536*, 210–214.

https://doi.org/10.1038/NATURE19058.

Tao-Cheng, J.H. (2007a). Ultrastructural localization of active zone and synaptic vesicle proteins in a preassembled multi-vesicle transport aggregate. Neuroscience *150*, 575–584. https://doi.org/10.1016/J.NEUROSCIENCE.2007.09.031.

Tao-Cheng, J.H. (2007b). Ultrastructural localization of active zone and synaptic vesicle proteins in a preassembled multi-vesicle transport aggregate. Neuroscience *150*, 575–584. https://doi.org/10.1016/j.neuroscience.2007.09.031.

Taschenberger, H., Scheuss, V., and Neher, E. (2005). Release kinetics, quantal parameters and their modulation during short-term depression at a developing synapse in the rat CNS. J. Physiol. *568*, 513–537. https://doi.org/10.1113/jphysiol.2005.093468.

Taschenberger, H., Woehler, A., and Neher, E. (2016). Superpriming of synaptic vesicles as a common basis for intersynapse variability and modulation of synaptic strength. Proc. Natl. Acad. Sci. *113*, E4548–E4557. https://doi.org/10.1073/pnas.1606383113.

Terhune, D.B., Sullivan, J.G., and Simola, J.M. (2016). Time dilates after spontaneous blinking. Curr. Biol. *26*, R459–R460. https://doi.org/10.1016/J.CUB.2016.04.010.

Thalhammer, A., Contestabile, A., Ermolyuk, Y.S., Ng, T., Volynski, K.E., Soong, T.W., Goda, Y., and Cingolani, L.A. (2017). Alternative Splicing of P/Q-Type Ca2+ Channels Shapes Pre-synaptic Plasticity. Cell Rep. *20*, 333–343. https://doi.org/10.1016/j.celrep.2017.06.055.

Thompson, A.M., and Thompson, G.C. (2001). Serotonin projection patterns to the cochlear nucleus. Brain Res. *907*, 195–207. https://doi.org/10.1016/S0006-8993(01)02483-0.

Thorp, J., Clewett, D., and Riegel, M. (2020). Two Routes to Incidental Memory under Arousal: Dopamine and Norepinephrine. J. Neurosci. *40*, 1790–1792. https://doi.org/10.1523/JNEUROSCI.2698-19.2020.

Tom Dieck, S., Sanmartí-Vila, L., Langnaese, K., Richter, K., Kindler, S., Soyke, A., Wex, H., Smalla, K.H., Kämpf, U., Fränzer, J.T., et al. (1998). Bassoon, a novel zinc-finger CAG/glutamine-repeat protein selectively localized at the active zone of pre-synaptic nerve terminals. J. Cell Biol. *142*, 499–509. https://doi.org/10.1083/jcb.142.2.499.

Tom Dieck, S., Altrock, W.D., Kessels, M.M., Qualmann, B., Regus, H., Brauner, D., Fejtová, A., Bracko, O., Gundelfinger, E.D., and Brandstätter, J.H. (2005). Molecular dissection of the photoreceptor ribbon synapse: physical interaction of Bassoon and RIBEYE is essential for the assembly of the ribbon complex. J. Cell Biol. *168*, 825–836. https://doi.org/10.1083/JCB.200408157.

Trussell, L.O. (1997). Cellular mechanisms for preservation of timing in central auditory pathways. Curr. Opin. Neurobiol. *7*, 487–492. https://doi.org/16/S0959-4388(97)80027-X.

Trussell, L.O. (1999). Synaptic mechanisms for coding timing in auditory neurons. Annu. Rev. Physiol. *61*, 477–496. https://doi.org/10.1146/ANNUREV.PHYSIOL.61.1.477.

Varoqueaux, F., Sigler, A., Rhee, J.S., Brose, N., Enk, C., Reim, K., and Rosenmund, C. (2002). Total arrest of spontaneous and evoked synaptic transmission but normal synaptogenesis in the absence of Munc13-mediated vesicle priming. Proc. Natl. Acad. Sci. U. S. A. *99*, 9037–9042. https://doi.org/10.1073/pnas.122623799.

Verhage, M., Maia, A.S., Plomp, J.J., Brussaard, A.B., Heeroma, J.H., Vermeer, H., Toonen, R.F., Hammer, R.E., Den, T.K. van, Berg, et al. (2000). Synaptic Assembly of the Brain in the Absence of Neurotransmitter Secretion. Science (80-.). *287*, 864–869. https://doi.org/10.1126/science.287.5454.864.

Viotti, J.S., and Dresbach, T. (2019). Differential Effect on Hippocampal Synaptic Facilitation by the Pre-synaptic Protein Mover. Front. Synaptic Neurosci. *11*. https://doi.org/10.3389/FNSYN.2019.00030.

Voleti, R., Jaczynska, K., and Rizo, J. (2020). Ca 2+-dependent release of synaptotagmin-1 from the SNARE complex on phosphatidylinositol 4,5-bisphosphate-containing membranes. Elife *9*, 1–95. https://doi.org/10.7554/ELIFE.57154.

Wadel, K., Neher, E., and Sakaba, T. (2007). The Coupling between Synaptic Vesicles and Ca2+ Channels Determines Fast Neurotransmitter Release. Neuron *53*, 563–575. https://doi.org/10.1016/j.neuron.2007.01.021.

Waites, C.L., Craig, A.M., and Garner, C.C. (2005). Mechanisms of vertebrate synaptogenesis. Annu. Rev. Neurosci. *28*, 251–274. https://doi.org/10.1146/ANNUREV.NEURO.27.070203.144336.

Waites, C.L., Leal-Ortiz, S.A., Andlauer, T.F.M., Sigrist, S.J., and Garner, C.C. (2011). Piccolo regulates the dynamic assembly of pre-synaptic F-actin. J. Neurosci. *31*, 14250–14263. https://doi.org/10.1523/JNEUROSCI.1835-11.2011.

Waites, C.L., Leal-Ortiz, S.A., Okerlund, N., Dalke, H., Fejtova, A., Altrock, W.D., Gundelfinger, E.D., and Garner, C.C. (2013). Bassoon and Piccolo maintain synapse integrity by regulating protein ubiquitination and degradation. EMBO J. *32*, 954–969. https://doi.org/10.1038/emboj.2013.27.

Wang, Y., and Südhof, T.C. (2003). Genomic definition of RIM proteins: Evolutionary amplification of a family of synaptic regulatory proteins. Genomics *81*, 126–137. https://doi.org/10.1016/S0888-7543(02)00024-1.

Wang, H., Isik, M., Borst, A., and Hemmert, W. (2010). Auditory information coding by modeled cochlear nucleus neurons. J. Comput. Neurosci. *30*, 529–542. https://doi.org/10.1007/s10827-010-0276-x.

Wang, S., Choi, U.B., Gong, J., Yang, X., Li, Y., Wang, A.L., Yang, X., Brunger, A.T., and Ma, C. (2017). Conformational change of syntaxin linker region induced by Munc13s initiates SNARE complex formation in synaptic exocytosis. EMBO J. *36*, 816–829. https://doi.org/10.15252/EMBJ.201695775.

Wang, X., Kibschull, M., Laue, M.M., Lichte, B., Petrasch-Parwez, E., and Kilimann, M.W. (1999). Aczonin, a 550-kD putative scaffolding protein of pre-synaptic active zones, shares homology regions with Rim and Bassoon and binds profilin. J. Cell Biol. *147*, 151–162. https://doi.org/10.1083/jcb.147.1.151.

Wang, Y., Okamoto, M., Schmitz, F., Hofmann, K., and Südhof, T.C. (1997). Rim is a putative rab3 effector in regulating synaptic-vesicle fusion. Nature *388*, 593–598. https://doi.org/10.1038/41580.

Wang, Y., Sugita, S., and Südhof, T.C. (2000). The RIM/NIM family of neuronal C2 domain proteins: Interactions with Rab3 and a new class of Src homology 3 domain proteins. J. Biol. Chem. *275*, 20033–20044. https://doi.org/10.1074/jbc.M909008199.

Watanabe, S., Rost, B.R., Camacho-Pérez, M., Davis, M.W., Söhl-Kielczynski, B., Rosenmund, C., and Jorgensen, E.M. (2013). Ultrafast endocytosis at mouse hippocampal synapses. Nat. 2013 5047479 *504*, 242–247. https://doi.org/10.1038/nature12809.

Weber, T., Zemelman, B. V., McNew, J.A., Westermann, B., Gmachl, M., Parlati, F., Söllner, T.H., and Rothman, J.E. (1998). SNAREpins: minimal machinery for membrane fusion. Cell *92*, 759–772. https://doi.org/10.1016/S0092-8674(00)81404-X.

Weyrer, C., Turecek, J., Harrison, B., and Regehr, W.G. (2021). Introduction of synaptotagmin 7 promotes facilitation at the climbing fiber to Purkinje cell synapse. Cell Rep. *36*. https://doi.org/10.1016/J.CELREP.2021.109719.

Wichmann, C. (2015). Molecularly and structurally distinct synapses mediate reliable encoding and processing of auditory information. Hear. Res. *330*, 178–190. https://doi.org/10.1016/J.HEARES.2015.07.008.

Wierda, K.D.B., Toonen, R.F.G., de Wit, H., Brussaard, A.B., and Verhage, M. (2007). Interdependence of PKC-dependent and PKC-independent pathways for pre-synaptic plasticity. Neuron *54*, 275–290. https://doi.org/10.1016/J.NEURON.2007.04.001.

Wilhelm, B.G., Groemer, T.W., and Rizzoli, S.O. (2010). The same synaptic vesicles drive active and spontaneous release. Nat Neurosci *13*, 1454–1456. https://doi.org/10.1038/nn.2690.

Winter, U., Chen, X., and Fasshauer, D. (2009). A conserved membrane attachment site in α-SNAP facilitates N-ethylmaleimide-sensitive factor (NSF)-driven SNARE complex disassembly. J. Biol. Chem. *284*, 31817–31826. https://doi.org/10.1074/jbc.M109.045286.

Wölfel, M., Lou, X., and Schneggenburger, R. (2007). A Mechanism Intrinsic to the Vesicle Fusion Machinery Determines Fast and Slow Transmitter Release at a Large CNS Synapse. J. Neurosci. *27*, 3198–3210. https://doi.org/10.1523/JNEUROSCI.4471-06.2007.

Wong, M.Y., Liu, C., Wang, S.S.H., Roquas, A.C.F., Fowler, S.C., and Kaeser, P.S. (2018). Liprin-α3 controls vesicle docking and exocytosis at the active zone of hippocampal synapses. Proc. Natl. Acad. Sci. U. S. A. *115*, 2234–2239. https://doi.org/10.1073/PNAS.1719012115/-/DCSUPPLEMENTAL.

Xu-Friedman, M.A., and Regehr, W.G. (2005). Dynamic-Clamp Analysis of the Effects of Convergence on Spike Timing. II. Few Synaptic Inputs. J. Neurophysiol. *94*, 2526–2534. https://doi.org/10.1152/jn.01308.2004.

Xu, J., Camacho, M., Xu, Y., Esser, V., Liu, X., Trimbuch, T., Pan, Y.Z., Ma, C., Tomchick, D.R., Rosenmund, C., et al. (2017). Mechanistic insights into neurotransmitter release and pre-synaptic plasticity from the crystal structure of Munc13-1 C 1 C 2 BMUN. Elife *6*. https://doi.org/10.7554/ELIFE.22567.

Xu, Y., Su, L., and Rizot, J. (2010). Binding of Munc18-1 to synaptobrevin and to the SNARE four-helix bundle. Biochemistry *49*, 1568–1576. https://doi.org/10.1021/BI9021878.

Xue, M., Stradomska, A., Chen, H., Brose, N., Zhang, W., Rosenmund, C., and Reim, K. (2008). Complexins facilitate neurotransmitter release at excitatory and inhibitory synapses in mammalian central nervous system. Proc. Natl. Acad. Sci. *105*, 7875. .

Xue, R., Ruhl, D.A., Briguglio, J.S., Figueroa, A.G., Pearce, R.A., and Chapman, E.R. (2018). Doc2-mediated superpriming supports synaptic augmentation. Proc. Natl. Acad. Sci. U. S. A. *115*, E5605–E5613. https://doi.org/10.1073/pnas.1802104115.

Yang, H., and Xu-Friedman, M.A. (2009). Impact of Synaptic Depression on Spike Timing at the Endbulb of Held. J. Neurophysiol. *102*, 1699–1710. https://doi.org/10.1152/jn.00072.2009.

Yang, H., and Xu-Friedman, M.A. (2010). Developmental Mechanisms for Suppressing the Effects of Delayed Release at the Endbulb of Held. J. Neurosci. *30*, 11466–11475. https://doi.org/10.1523/JNEUROSCI.2300-10.2010.

Yang, H., and Xu-Friedman, M.A. (2012a). Emergence of Coordinated Plasticity in the Cochlear Nucleus and Cerebellum. J. Neurosci. *32*, 7862–7868. https://doi.org/10.1523/jneurosci.0167-12.2012.

Yang, H., and Xu-Friedman, M.A. (2012b). Emergence of Coordinated Plasticity in the Cochlear Nucleus and Cerebellum. J. Neurosci. *32*, 7862–7868. https://doi.org/10.1523/JNEUROSCI.0167-12.2012.

Yang, X., Wang, S., Sheng, Y., Zhang, M., Zou, W., Wu, L., Kang, L., Rizo, J., Zhang, R., Xu, T., et al. (2015). Syntaxin opening by the MUN domain underlies the function of Munc13 in synaptic-vesicle priming.

Nat. Struct. Mol. Biol. *22*, 547–554. https://doi.org/10.1038/NSMB.3038.

Yin, T.C.T., and Chan, J.C.K. (1990). Interaural time sensitivity in medial superior olive of cat. J. Neurophysiol. *64*, 465–488. https://doi.org/10.1152/JN.1990.64.2.465.

Yu, W.M., and Goodrich, L. V. (2014). Morphological and physiological development of auditory synapses. Hear. Res. *311*, 3–16. https://doi.org/10.1016/j.heares.2014.01.007.

Zhai, R.G., Vardinon-Friedman, H., Cases-Langhoff, C., Becker, B., Gundelfinger, E.D., Ziv, N.E., and Garner, C.C. (2001). Assembling the pre-synaptic active zone: A characterization of an active zone precursor vesicle. Neuron *29*, 131–143. https://doi.org/10.1016/S0896-6273(01)00185-4.

Zhen, M., and Jin, Y. (1999). The liprin protein SYD-2 regulates the differentiation of pre-synaptic termini in C. elegans. Nature *401*, 371–375. https://doi.org/10.1038/43886.

Zucker, R.S., and Regehr, W.G. (2002). Short-term synaptic plasticity. Annu. Rev. Physiol. *64*, 355–405. https://doi.org/10.1146/annurev.physiol.64.092501.114547.

List of Figures

Figures in General Introduction

List of Tables

List of Abbreviations

5-HT	5-Hydroxy Tryptamine (Serotonin)	LTP	Long-Term Potentiation
5HTR	5-HT (Serotonin) Receptor	mEPSC	Minature EPSC (mini)
5HTT	Serotonin Transporter	mGluR	Metabotropic Glutamate Receptor
aCSF	Artificial Cerebro Spinal Fluid	MNTB	Medial nucleus of the Trapezoid Body
AMPA	α-amino-3-hydroxy5-methyl-4-isoxazolepropioninc acid	MSO	Medial Syperior Olive
AMPAR	AMPA receptor	N	Number of release Sites
ANF	Auditory Nerve Fiber	Na_V	Votage Gated sodium channel
AP	Action Potential	*NE*	Norepinephrine (noradrenaline)
AP-2	Adaptor Protein 2	*NET*	Norepinephrine transporter

AR	Adrenaline receptor	*NMDA*	N-Methyl-D-aspartate
ATP	Adenosine triphosphate	*NMDAR*	N-Methyl-D-aspartate receptor
AVCN	Antero Ventral Cochlear Nucleus	*NSF*	N-ethylmaleimide-sensitive factor
AZ	Active Zone	*OHC*	Outer Hair Cell
BC	Bushy Cell	*PB*	Phosphate Buffer
BLA	Basolateral Amygdala	*PBS*	Phosphate Buffer Saline
CAMKII	Calcium/Calmodulin dependent kinase II	*PFA*	Paraformaldehyde
cAMP	Cyclic Adenosine monophosphate	*PIP2*	Phosphatidylinositol 4,5-bisphosphate
CAST	CAZ associated structural protein	*PKA*	Protein kinase A
Ca_V	Votage Gated calcium channel	*PKC*	Protein kinase C
CAZ	Cytomatrix of the Active Zone	*PLC*	Phospholipase C
CC	Coiled Coil Domain	*PN*	Principal Neuron
cKO	Conditional kncok-out	P_{occ}	Probability of occupancy
CP-AMPAR	Calcium permeable AMPAR	*PPD*	Paired Pulse Depression
CTZ	Cyclothiazide	*PPF*	Paired Pulse Facilitation
DA	Dopamine	*PS*	Phosphatidyl serine
DAG	Di-acyl glycerol	*PSC*	Post-synaptic current
DAT	Dopamine Transporter	*PSD*	Post-synaptic Density
DCN	Dorsal Cochlear Nucleus	P_{succ}	Probability of successful release
dKO	Double Knock-out	P_{TS}	Probability of occupancy by a TS vesicle
eEPSC	Evoked EPSC	P_{vr}	Release probability
EPSC	Excitatory post-synaptic current	*qKO*	Quadruple knock-out
FA	Formaldehyde	*RRP*	Readily Releasable Pool
GABA	γ-aminobutyric acid	*SBC*	Spherical Bushy Cell
GBC	Globular Bushy Cell	*SGN*	Spiral Ganglion Neuron
GDP	Guanosine Diphosphate	*SH3*	SRC Homology 3 Domain
g_{KVLA}	Low-voltage activated potassium conductance	*SM*	Sec1/Munc18-1
GPCR	G-protein Coupled Receptor	*SNARE*	Soluble NSF Attachment Receptor protein
GTP	Guanosine Triphosphate	*ST*	Spike Timing
HCN	Hyperpolarization activated cyclic nucleotide gated channels	*STD*	Shor-term Depression
I_{ca}	Calcium Current	*STDP*	Spike Timing Dependent Plasticity
IHC	Inner Hair Cell	*STF*	Short-term Facilitation
ILD	Interaural Level Difference	*STP*	Short-term Plasticity
IP3	Inositol triphosphate	*SV*	Synaptic Vesicle
IPSC	Inhibitory post-synaptic current	*τ*	Tau
ITD	Interaural Time Difference	*TGN*	Trans-Golgi Network
KO	Knock-out	*TS*	Tight primed state
K_V	Votage Gated potassium channel	*tSNARE*	Target SNARE
LC	Locus Coeruleus	*VGCC*	Voltage gated calcium channel
LLPS	Liquid liquid phase separation	*vGlut*	Vesivular Glutamate transporter
LS	Loose primed state	V_m	Membrane Voltage
LSO	Lateral Superio Olive	*vMAT2*	Vesicular monoamine transporter 2
LTD	Long-term Depression	*vSNARE*	Vesicle SNARE

Acknowledgements

I would like to thank Prof. Dr. Tobias Moser for giving me the opportunity to join a world class laboratory, develop my skills and collaborate with such amazing and highly achieving colleagues. I thank him for entrusting me with the exciting world of the auditory brainstem, fostering my interest in neurons and for his excellent mentoring and support throughout the PhD. I am particularly thankful for his kind words during any and all stressful moments that appeared in this journey. I would like to thank my thesis committee member, Prof. Dr. Erwin Neher and Prof. Dr. Silvio Rizzoli for their generous feedback, their inspiring perspective and interesting ideas.

Special thanks go to Dr. Tanvi Butola, without whom I would not have patched a single cell. I thank her for her teaching, sharing her expertise, being an excellent collaborator and for her support. I am grateful to Dr. Jakob Neef, for co-supervising and teaching me superresolution imaging and the secrets of Igor programming and finally for providing analysis solutions with his custom scripts. Without their help and support this work would not have been possible. I thank Dr. Anika Hintze for being an amazing collaborator during the first study and for the stimulating scientific discussions.

Thank you to Sandra Gerke and Christiane Senger-Freitag for the mouse genotyping and guidance for utilizing the lab's resources. Thank you to Ina Herfort for her constant support and in the MPI NAT Fassberg Campus. I am grateful also to Patricia Raeke-Kügler for making my journey through the German bureaucracy easy and, almost fun and to Susann Meyer for her continuous support. Thanks goes to Gerhard Hoch for developing Matlab scripts for image analysis and teaching me how to be safe around laser equipment. I thank Dominik Riemenschneider for his help with all IT-related issues and the fun talks in the kitchen of the UMG. I want to thank the animal caretakers of both the MPI-NAT Fassberg and City Campus as well as those in the UMG, without whom our projects would not go that far.

I am grateful to the IMPRS neuroscience office, to the late Michael Hörner, to Sandra Drübe, Jonas Barth and Franziska Kühne. Their support during the entire MSc/PhD programme made its completion possible.

In the years of working in the institute for auditory neuroscience I have seen many of my relationships with colleagues turn into wonderful friendships. I want to specially thank Dr. Lina Maria Jaime for taking the role of an older sister, for her support during the days of covid-19 quarantine and empty floor in Fassberg tower 6 and during the most difficult moments in this journey. I wanna thank Dr. Antoine Huet, Habakuk Hain, Chad Paul Grabner, Dr. Tommi Antonnen, Christoph Kampshoff, Roos

Voorn, Dominik Riemneschneider and Dr. Carlos Duque Alfonso for fun times, stimulating and creative discussions and support. Here are “cheers” to many more fun experiences ahead.

I am very grateful to my friends Yunus Can Erol, Deniz Yuzak, Chrystalleni Vasilleiou, Meike Wiegand, Jennifer Rachel, Juan Diego Prieto and all the others from our IMPRS batch for making my time in Germany so much fun, for their support and awesome discussions about science, philosophy and life. I am thankful to Dimos Karamanlis, Nikos Sirmpiladze and Hanna Rula for all the times we spent together and wish to see them many more times, visiting the places of their new beginnings.

I am grateful to Myrto Panopoulou for her companionship during the first, hardest years of the PhD journey. I wish her all the best.

I want to thank Lucia Alana Rojas for her kind support and compassion, for sharing her enthusiasm for science, movies, music and travelling. Lucia, I am convinced that our journey ahead will be equally, if not more exciting and I cannot wait to neuromodulate our synapses and sculpt our brains together in the future.

Last, but, most certainly not least, I am grateful to my parents, Kyriakos and Olga, my brother, Dinos and to all my friends in Greece not only for their support and understanding, but also for fostering and entertaining my bottomless curiosity and borderline nerdiness.

Declaration

I hereby declare that I prepared the thesis “Quantitative molecular physiology at active zones of calyceal synapses in the auditory pathway” independently and with no other sources and aids than quoted

Theocharis Alvanos

Göttingen, 8. September, 2022

Curriculum Vitae

Theocharis Alvanos

Personal Information

Bürgerstrasse 32A,
37073 Göttingen
Germany

Date of Birth: 05 May 1993
+49 17677134134
theocharis.alvanos@gmail.com
Nationality: Greek

Education

2018 – Present

Doctoral Student – Synaptic Nanophysiology at Max Planck Institute for Multidisciplinary Sciences Fassberg Campus, Göttingen, Germany

1st Project: The role of RIM-binding proteins at the endbulb of Held synapse of the auditory pathway

Resulting Publications: Butola, Alvanos et al., 2021, RIM-Binding Protein 2 Organizes Ca2+ Channel Topography and Regulates Release Probability and Vesicle Replenishment at a Fast Central Synapse, Journal of Neuroscience

2nd Project: Pre-synaptic Neuromodulation at the mouse endbulb of Held synapse

Advisors: Tobias Moser, Erwin Neher, Silvio Rizzoli

2016 – 2018

International Max Planck Research School for Neuroscience: MSc / PhD Programme, Göttingen, Germany

Master thesis: "The role of RIM-binding proteins at the Endbulb of Held synapse of the auditory pathway"

Advisors: Tobias Moser, Erwin Neher

2011 – 2016

Bachelor's Degree in Biology from the National Kapodistrian University of Athens, Greece

BachelorThesis: "Role of Huntingtin in the long term memory of Drosophila melanogaster: The effects of a huntingtin homologue knock out and knock down in D.melanogaster's olfactory memory."

Advisors: Efthimios M.C. Skoulakis, Spiros Efthimiopoulos

Awards & Fellowships

IMPRS Neuroscience Stipend for MSc studies in Göttingen 2016 – 2018

Publications

Butola T, Alvanos T, Hintze A, Koppensteiner P, Kleindienst D, Shigemoto R, Wichmann C, Moser T. "RIM-Binding Protein 2 Organizes Ca2+ Channel Topography and Regulates Release Probability and Vesicle Replenishment at a Fast Central Synapse". J Neurosci. 2021 Sep 15;41(37):7742-7767. doi: 10.1523/JNEUROSCI.0586-21.2021.

Conferences & Symposia

Poster presentations

26.05.2020 **8th Biennial Neuroscience conference Neurizons, Göttingen, Germany**

RIM-Binding Protein 2 positively regulates the abundance and release site coupling of pre-synaptic Ca^{2+} channels at a fast central synapse

05.12.2019 **Core-to-Core Symposium, Berlin, Germany, Understanding Synapses – From Molecules to Function**

The role of RIM-Binding Protein 2 in neurotransmission at the endbulb of Held Synapse

29.05.2018 **7th Biennial Neuroscience conference Neurizons, Göttingen, Germany**

The role of RIM-Binding Protein 2 in neurotransmission at a central auditory synapse

Appendix

RIM-Binding Protein 2 Organizes Ca2+ Channel Topography and Regulates Release Probability and Vesicle Replenishment at a Fast Central Synapse

Tanvi Butola*, Theocharis Alvanos*, Anika Hintze, Peter Koppensteiner, David Kleindienst, Ryuichi Shigemoto, Carolin Wichmann and Tobias Moser

* These authors contributed equally to the work

Journal of Neuroscience 2021; 7742

DOI: https://doi.org/10.1523/JNEUROSCI.0586-21.2021

Cellular/Molecular

RIM-Binding Protein 2 Organizes Ca^{2+} Channel Topography and Regulates Release Probability and Vesicle Replenishment at a Fast Central Synapse

Tanvi Butola,[1,2,3,4]* Theocharis Alvanos,[1,2,3,4]* Anika Hintze,[1,4,5] Peter Koppensteiner,[6] David Kleindienst,[6] Ryuichi Shigemoto,[6] Carolin Wichmann,[1,4,5,7] and Tobias Moser[1,2,4,7]

[1]Institute for Auditory Neuroscience and InnerEarLab, University Medical Center Göttingen, Göttingen 37075, Germany, [2]Synaptic Nanophysiology Group, Max Planck Institute for Biophysical Chemistry, 37077 Göttingen, Germany, [3]International Max Planck Research School for Neurosciences and Göttingen Graduate Center for Neurosciences, Biophysics, and Molecular Biosciences (GGNB), University of Göttingen, 37075 Göttingen, Germany, [4]Collaborative Research Center 1286, University of Göttingen, 37075 Göttingen, Germany, [5]Molecular Architecture of Synapses Group, Institute for Auditory Neuroscience and Center for Biostructural Imaging of Neurodegeneration, 37075 Göttingen, Germany, [6]Institute of Science and Technology Austria (IST Austria), 3400 Klosterneuburg, Austria, and [7]Cluster of Excellence "Multiscale Bioimaging: from molecular machines to networks of excitable cells," University of Göttingen, Göttingen 37075, Germany

Rab-interacting molecule (RIM)-binding protein 2 (BP2) is a multidomain protein of the presynaptic active zone (AZ). By binding to RIM, bassoon (Bsn), and voltage-gated Ca^{2+} channels (Ca_V), it is considered to be a central organizer of the topography of Ca_V and release sites of synaptic vesicles (SVs) at the AZ. Here, we used RIM-BP2 knock-out (KO) mice and their wild-type (WT) littermates of either sex to investigate the role of RIM-BP2 at the endbulb of Held synapse of auditory nerve fibers (ANFs) with bushy cells (BCs) of the cochlear nucleus, a fast relay of the auditory pathway with high release probability. Disruption of RIM-BP2 lowered release probability altering short-term plasticity and reduced evoked EPSCs. Analysis of SV pool dynamics during high-frequency train stimulation indicated a reduction of SVs with high release probability but an overall normal size of the readily releasable SV pool (RRP). The Ca^{2+}-dependent fast component of SV replenishment after RRP depletion was slowed. Ultrastructural analysis by superresolution light and electron microscopy revealed an impaired topography of presynaptic Ca_V and a reduction of docked and membrane-proximal SVs at the AZ. We conclude that RIM-BP2 organizes the topography of Ca_V, and promotes SV tethering and docking. This way RIM-BP2 is critical for establishing a high initial release probability as required to reliably signal sound onset information that we found to be degraded in BCs of RIM-BP2-deficient mice *in vivo*.

Key words: active zone topography; calyceal synapses; $Ca_V2.1$ control of transmitter release; endbulb of Held; RIM-binding protein 2; short-term plasticity

Significance Statement

Rab-interacting molecule (RIM)-binding proteins (BPs) are key organizers of the active zone (AZ). Using a multidisciplinary approach to the calyceal endbulb of Held synapse that transmits auditory information at rates of up to hundreds of Hertz with submillisecond precision we demonstrate a requirement for RIM-BP2 for normal auditory signaling. Endbulb synapses lacking RIM-BP2 show a reduced release probability despite normal whole-terminal Ca^{2+} influx and abundance of the key priming protein Munc13-1, a reduced rate of SV replenishment, as well as an altered topography of voltage-gated (Ca_V)2.1 Ca^{2+} channels, and fewer docked and membrane proximal synaptic vesicles (SVs). This hampers transmission of sound onset information likely affecting downstream neural computations such as of sound localization.

Received Mar. 16, 2021; revised July 16, 2021; accepted July 20, 2021.

Author contributions: T.B., T.A., P.K., R.S., C.W., and T.M. designed research; T.B., T.A., A.H., P.K., and D.K. performed research; P.K. and D.K. contributed unpublished reagents/analytic tools; T.B., T.A., A.H., P.K., and D.K. analyzed data; T.M. wrote the first draft of the paper; T.B., T.A., A.H., P.K., D.K., R.S., C.W., and T.M. edited the paper; T.B., T.A., A.H., P.K., C.W., and T.M. wrote the final version of the paper.

This work was supported by the Deutsche Forschungsgemeinschaft (DFG, German Research Foundation) through the Collaborative Sensory Research Center 1286 [to C.W. (A4) and T.M. (B5)] and under Germany's Excellence Strategy Grant EXC 2067/1-390729940. We thank S. Gerke, A.J. Goldak, and C. Senger-Freitag for expert technical assistance; G. Hoch for developing image analysis routines; and S. Chepurwar and N. Strenzke for technical support and discussion regarding *in vivo* experiments. We also thank Dr. Christian Rosenmund, Dr. Katharina Grauel, and Dr. Stephan Sigrist for providing RIM-BP2 KO mice and Dr. Masahiko Watanabe for providing the anti-neurexin-antibody, and Dr. Toshihisa Ohtsuka for the anti-ELKS-antibody. J. Neef for help with the STED imaging and image analysis; E. Neher and S. Rizzoli for discussion and comments on the manuscript; K. Eguchi for help with the statistical analysis; and C. H. Huang and J. Neef for constant support and scientific discussion.

*T.B. and T.A. contributed equally to this work.

The authors declare no competing financial interests.

Correspondence should be addressed to Tobias Moser at tmoser@gwdg.de.

https://doi.org/10.1523/JNEUROSCI.0586-21.2021

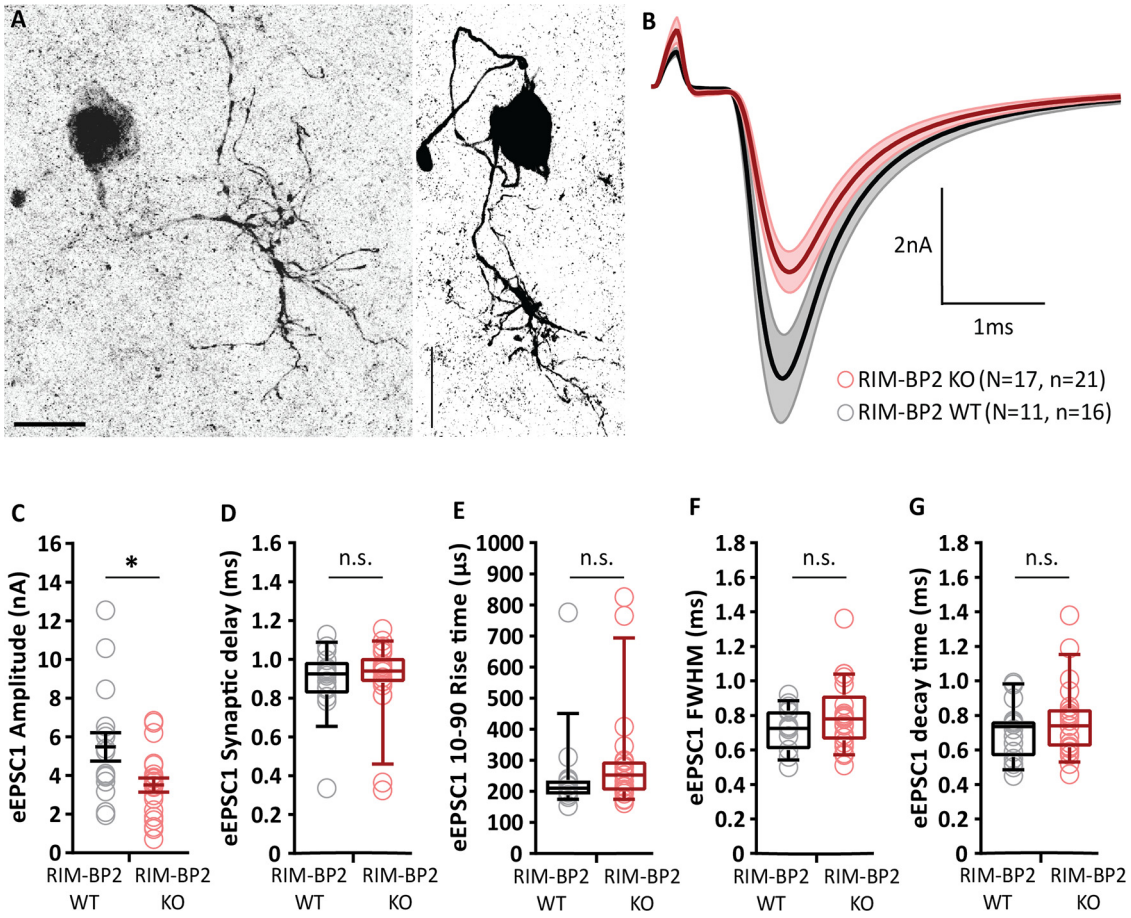

Figure 1. Reduced amplitude of evoked EPSCs in RIM-BP2-deficient endbulb synapses. ***A***, BCs (left and right panels showing dye-filled BCs) were distinguished from stellate cells (another major cell type in the aVCN) by the faster kinetics of their postsynaptic currents (Isaacson and Walmsley, 1995) and their characteristic short-term plasticity (Chanda and Xu-Friedman, 2010). In addition to such functional identification, each recorded cell was filled with fluorescent dye Alexa Fluor 488 via the patch pipette for morphologic distinction. BCs are spherical in appearance with one primary dendrite terminating in a dense bush-like dendritic tree (Wu and Oertel, 1984), distinct from stellate cells, which are asymmetrical in shape and have multiple dendrites branching off in various directions giving them a star-like appearance. Scale bars: 20 µm. ***B***, Average traces (±SEM) of eEPSCs in RIM-BP2 KO (red) and WT (black) endbulbs. ***C***, Reduced eEPSC amplitude in RIM-BP2 KO compared to WT. ***D–G***, No significant differences in eEPSC kinetics: (***D***) synaptic delay, (***E***) 10–90% rise time, (***F***) full width at half-maximum (FWHM), and (***G***) decay time. For an assessment of evoked release in the absence of kynurenic acid and CTZ, see Figure 2. To test whether the observed differences could be accounted for by changes in spontaneous release, sEPSC amplitude and kinetics were compared between genotypes in Figure 3 and Table 1. Data points represent the mean estimate of each BC included in the analysis. Normality was tested with the Jarque–Bera test. Normally distributed data (***C***) are shown as grand mean (of the means of all BCs) ± SEM. Non-normally distributed data (***D–G***) are presented as box and whisker plots (grand median of all BC means, lower/upper quartiles, 10–90th percentiles); *$p < 0.05$, n.s. $p \geq 0.05$, Mann–Whitney *U* test. *N*: number of animals, *n*: number of BCs.

Introduction

Active zones (AZs) are specialized regions at the presynaptic terminals where neurotransmitter release occurs. AZs employ a sophisticated machinery to enable ultrafast coupling of the incoming action potential to the release of transmitter via Ca^{2+}-triggered synaptic vesicle (SV) fusion. Voltage-gated Ca^{2+} channels (Ca_V) and SV release sites represent the core machinery, and their relative topography at the AZ co-determines the release probability (for recent review, see Kaeser and Regehr, 2014; Schneggenburger and Rosenmund, 2015; Walter et al., 2018; Dittman and Ryan, 2019). The function and abundance of Ca_V (for recent review, see Pangrsic et al., 2018; Dolphin and Lee, 2020) is positively regulated by auxiliary subunits and multidomain proteins of the AZ such as Rab-interacting molecule (RIM)-binding protein (BP), RIM, piccolo, bassoon (Bsn), CAST, and ELKS.

Several of these proteins promote the clustering of Ca^{2+} channels at the AZ and/or their interaction with the SV release sites (Gundelfinger and Fejtova, 2012; Südhof, 2012; Moser et al., 2020). RIM and RIM-BPs, in particular, have been considered as molecular linkers of Ca_V and vesicular release sites. Direct and indirect interactions of RIMs with Ca_V are well established (Kiyonaka et al., 2007; Gebhart et al., 2010; Kaeser et al., 2011; Picher et al., 2017). Proline-rich sequences of RIMs have been shown to bind the SH3 domains of RIM-BP that directly interacts with Ca_V (Hibino et al., 2002; Kaeser et al., 2011). Deletion of *Drosophila* RIM-BP disrupted Ca_V clustering at the AZs of larval neuromuscular junctions consequently impairing their functional coupling to SV release: altered short-term plasticity demonstrating a reduced release probability (Liu et al., 2011). Of the three mammalian RIM-BP isoforms, RIM-BP1 and RIM-BP2 are neuron specific, whereby RIM-BP2 seems to be the isoform that is most relevant for synaptic transmission (Acuna et al., 2015; Grauel et al., 2016; Krinner et al., 2021). Disruption of RIM-BP1 and RIM-BP2 did not alter the Ca^{2+} current at the calyx of Held synapse (Acuna et al., 2015), while lack of RIM-BP2 (Krinner et al., 2017; Luo et al., 2017) and of RIM-BP1 (Luo et al., 2017) reduced the Ca_V number at ribbon-type AZs. An

alteration of the Ca_V topography at the AZs has been reported based on superresolution immunofluorescence microscopy (Grauel et al., 2016; Krinner et al., 2017).

A loosening of the otherwise tight spatial relationship of Ca_V and SV release sites was indicated by the reduced release probability and a greater sensitivity to the intracellular presence of the "slow" Ca^{2+} chelator EGTA in the absence of RIM-BP(1)/2 (Acuna et al., 2015; Grauel et al., 2016; Luo et al., 2017). A similar conclusion was reached in sensory hair cells where, unlike in CNS synapses, SV replenishment was impaired in the absence of RIM-BP2 (Krinner et al., 2017). However, in contrast to the dramatic impairment of synaptic transmission at RIM-BP-deficient neuromuscular junctions in *Drosophila* (Liu et al., 2011), transmission was affected more subtly by RIM-BP deletion at mammalian synapses (Acuna et al., 2015; Grauel et al., 2016; Krinner et al., 2017; Luo et al., 2017). This might relate to partial compensation by other candidate linkers of Ca_V and SV release sites such as long RIM isoforms (Acuna et al., 2016). Recently, two alternative actions of RIM-BPs were indicated based on molecular perturbations studies in hippocampal neurons: (1) binding to Ca_V enabling their tight coupling to SVs or (2) promoting SV priming by interaction with Munc13-1 (Brockmann et al., 2020). Here, we aimed to further characterize the function of RIM-BP2 at the endbulb of Held synapse, the first central auditory synapse (von Gersdorff and Borst, 2002; Yu and Goodrich, 2014), that employs high vesicular release probability at its >100 AZs for reliable and temporally precise signal transmission from auditory nerve fibers (ANFs) to bushy cells (BCs) at frequencies of hundreds of Hertz (Trussell, 1999; Wang et al., 2011). We combined electrophysiological analysis with studies of the molecular composition and ultrastructure of the AZ in RIM-BP2-deficient endbulbs.

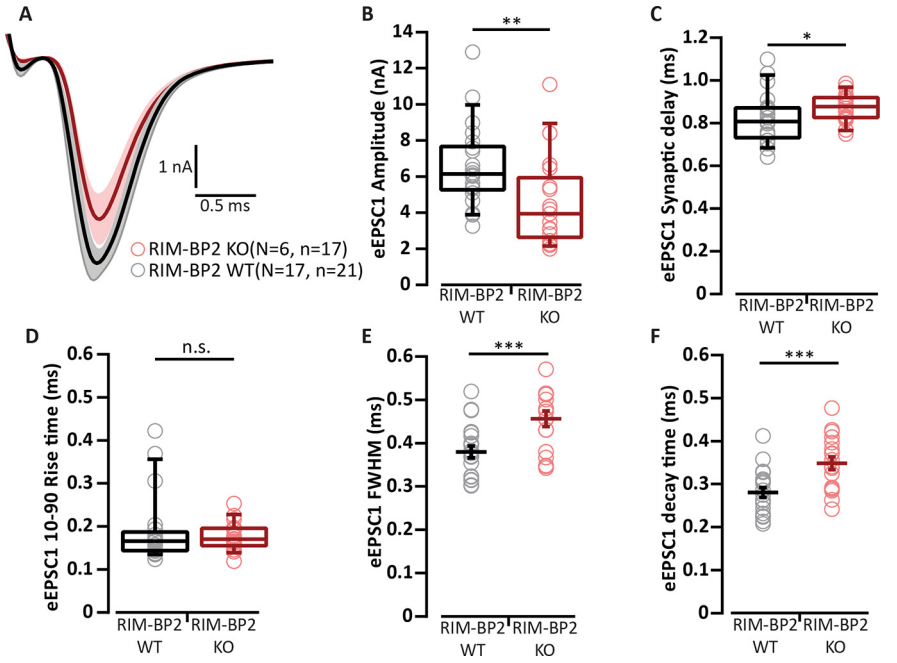

Figure 2. Evoked EPSC recordings in the absence of kynurenic acid and CTZ. ***A***, Average traces (±SEM) of eEPSCs in RIM-BP2 KO (red) endbulbs and WT (black) in the absence of kynurenic acid and CTZ. ***B***, Reduced eEPSC amplitude in RIM-BP2 KO compared to WT. (***C–F***) eEPSC kinetics: (***C***) a larger synaptic delay, (***D***) unchanged 10–90% rise time, (***E***) wider full-width at half-maximum (FWHM), and (***F***) slower decay time. Data points represent the mean estimate of each BC included in the analysis. Normality was tested with the Jarque–Bera test. Normally distributed data (***E***, ***F***) are shown as grand mean (of the means of all BCs) ± SEM, and significance was tested with Student's *t* test. Non-normally distributed data (***B–D***) are presented as box and whisker plots (grand median of all BC means, lower/upper quartiles, 10–90th percentiles), and significance was tested with Mann–Whitney *U* test; n.s. $p \geq 0.05$; *$p < 0.05$, **$p < 0.01$, ***$p < 0.001$. *N*: number of animals, *n*: number of BCs.

Materials and Methods

Animals

The constitutive RIM-BP2 knock-out (RIM-BP2 KO) mice were described previously (Grauel et al., 2016) and kindly provided to us by Dr. Christian Rosenmund, Dr. Katharina Grauel, and Dr. Stephan Sigrist. RIM-BP2 KO mice and their wild-type littermates (RIM-BP2 WT) of either sex were studied after the onset of hearing (postnatal day 13). For specific animal ages, please refer to the relevant Materials and Methods sections. All experiments were performed in compliance with the guidelines of the German animal welfare act and were approved by the board for animal welfare of the University Medical Center Göttingen and the animal welfare office of the state of Lower Saxony.

Slice electrophysiology

Slice preparation

Acute parasagittal slices (150 µm) from the anteroventral cochlear nucleus (aVCN) were obtained as described previously (Mendoza Schulz et al., 2014). Briefly, after killing by decapitation, brains were dissected out and quickly immersed in ice-cold low Na^+ and low Ca^{2+} cutting solution containing the following: 50 mM NaCl, 26 mM $NaHCO_3$, 120 mM sucrose, 1.25 mM $NaH_2PO_4.H_2O$, 2.5 mM KCl, 20 mM glucose, 0.2 mM $CaCl_2$, 6 mM $MgCl_2$, 0.7 mM Na L-ascorbate, 2 mM Na pyruvate, 3 mM myo-inositol, and 3 mM Na L-lactate with pH adjusted to 7.4 and osmolarity of around 310 mOsm/l. After removal of the meninges from the ventral face of the brainstem, the two hemispheres were separated by a midsagittal cut, and the forebrain was removed at the pons-midbrain junction. The brain blocks containing brain stem and cerebellum were then glued (cyanoacrylate glue; Loctite 401, Henkel) to the stage of a VT 1200S vibratome (Leica Microsystems) such that the medial side was glued on, the ventral side was facing the blade and the lateral side was facing upwards, submerged in ice-cold cutting solution. For sectioning, the blade was positioned at the height of cerebellar flocculus and sections were cut at a blade feed rate of 0.02 mm/s with an amplitude of 1.50 mm. Slices were incubated for 30 min in artificial CSF (aCSF) maintained at 35°C, and then kept at room temperature (22–24°C) until recording. Composition of aCSF was identical to the cutting solution except 125 mM NaCl, 13 mM glucose, 2 mM $CaCl_2$, and 1 mM $MgCl_2$. The pH of the solution was adjusted to 7.4 and osmolarity was around 310 mOsm/l. All solutions were continuously aerated with carbogen (95% O_2, 5% CO_2). For presynaptic endbulb recordings, coronal sections were made instead of parasagittal as described above. The only difference was that after the forebrain was removed at the pons-midbrain junction, the dissected brain was not cut midsagitally and the brain block containing the brain stem and the cerebellum was then glued to the vibratome stage with the caudal aspect facing upwards and the ventral side toward the blade.

Electrophysiology

Patch-clamp recordings were made from BCs of aVCN using EPC10 USB Patch clamp amplifier controlled by the Patchmaster software (HEKA Elektronik). Sampling interval and filter settings were 25 µs and 7.3 kHz, respectively. Cells were visualized by differential interference

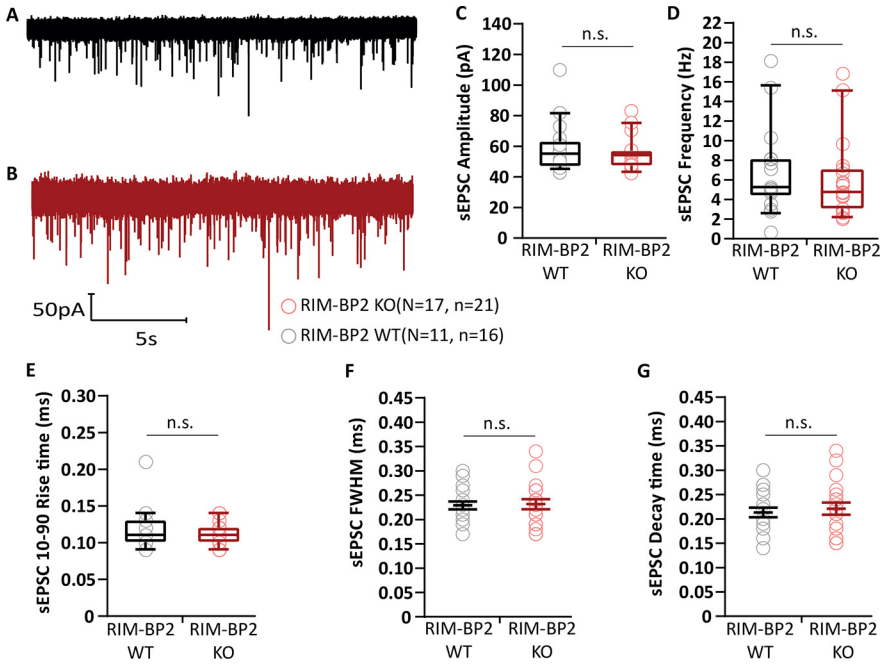

Figure 3. Unaltered amplitude, kinetics and frequency of sEPSCs in RIM-BP2-deficient endbulb synapses. ***A***, ***B***, Representative sEPSCs at WT (***A***, black) and RIM-BP2 KO (***B***, red) endbulbs of held: continuous traces are shown. No significant differences in (***C***) amplitude, (***D***) frequency, (***E***) 10–90% rise time, (***F***) full-width at half-maximum (FWHM), and (***G***) decay time in RIM-BP2-deficient endbulbs. sEPSC were recorded while intracellularly blocking BC action potential generation with QX-314. Each data point represents the mean estimate of each BC included in the analysis. Normality was tested with the Jarque–Bera test. Normally distributed data are depicted as mean (grand average of all BC means) ± SEM (***F***, ***G***; n.s. $p \geq 0.05$, unpaired Student's *t* test). Non-normally distributed data are presented as box and whisker plots (grand median of all BC means, lower/upper quartiles, 10–90th percentiles; ***C–E***); n.s. $p \geq 0.05$, Mann–Whitney *U* test, *N*: number of animals, *n*: number of BCs.

Table 1. Unaltered sEPSC at the RIM-BP2-deficient endbulb of Held in the absence of kynurenic acid and CTZ

Parameter	RIM-BP2 WT	RIM-BP2 KO	*p* value
Amplitude (pA)	130.54 ± 12.06	112.48 ± 4.03	0.22, M
10–90% rise time (ms)	0.09 ± 0.003	0.09 ± 0.002	0.85, T
FWHM (ms)	0.18 ± 0.008	0.19 ± 0.004	0.46, T
Decay time (ms)	0.16 ± 0.010	0.17 ± 0.005	0.36, T
Frequency (Hz)	7.65 ± 1.28	8.01 ± 1.09	0.83, T

Data presented as mean (grand average of the means of all BCs) ± SEM. Statistical significance between groups was determined by either unpaired Student's *t* test (in case of normally distributed data with comparable variances between the groups, indicated as T) or Mann–Whitney *U* test (when data distribution did not satisfy the criteria, indicated at M). Normality of distribution was tested with Jarque–Bera test and variances were compared with *F* test. WT $N = 4$; $n = 10$, RIM-BP2 KO $N = 7$; $n = 19$ (*N*: number of animals; *n*: number of BCs).

contrast (DIC) microscopy through a 40× water-immersion objective (NA 0.8; Zeiss) using an Axioscope 2 FS plus microscope (Zeiss). All experiments were conducted at a temperature of 33–35°C, maintained by constant superfusion (flow rate 3–4 ml/min) of aCSF, heated by an inline solution heater (SH-27B with TC-324B controller; Warner Instruments) and monitored by a thermistor placed between the inflow site and the slice, in the recording chamber.

Patch pipettes were pulled with P-87 micropipette puller (Sutter Instruments Co) from borosilicate glass capillaries with filament (GB150F, 0.86 × 1.50 × 80 mm; Science Products). Open tip pipette resistance was 1.5–3 MΩ when filled with intracellular solution containing the following: 115 mM K-gluconate, 10 mM HEPES, 8 mM EGTA, 10 mM Na_2phosphocreatine, 4 mM ATP-Mg, 0.3 mM GTP-Na, 4.5 mM $MgCl_2$, 10 mM NaCl, and 1 mM *N*-(2,6-dimethylphenyl carbamoylmethyl) triethylammonium chloride (QX-314; Alomone Labs) to block sodium channels, with a pH of 7.35 and an osmolarity of 300 mOsm/l. Additionally, 1 mM of fluorescent dye Alexa Fluor 488 (Invitrogen) was added to the recording pipette and cell structure was examined during experiments using a HXP 120 mercury lamp, with FITC filter (Semrock hardcoat). BCs were identified by the faster kinetics of their postsynaptic currents (Isaacson and Walmsley, 1995) and their characteristic short-term plasticity (Chanda and Xu-Friedman, 2010) and selection confirmed by their spherical in appearance with one primary dendrite terminating in a dense bush-like dendritic tree (Wu and Oertel, 1984), Cells were voltage-clamped at a holding potential of −70 mV, after correction for a liquid junction potential of 12 mV. Mean series resistance was around 5 MΩ and was compensated up to 70% with a 10-µs lag. Presynaptic ANF were minimally stimulated with a monopolar electrode in a patch pipette filled with aCSF, placed at a distance of at least three cell diameters from the cell being recorded. Stimulating currents of 10–20 µA were delivered through a stimulus isolator (A360 World Precision Instruments). For the main set of recordings, bath solution (aCSF) was supplemented with the following: 1 mM kynurenic acid sodium salt (Abcam Biochemicals), a low-affinity AMPAR antagonist, to prevent receptor saturation/desensitization, 100 µM cyclothiazide (CTZ) to prevent AMPAR desensitization, 10 µM bicuculline methchloride, a $GABA_A$ receptor antagonist and 2 µM strychnine hydrochloride, a glycine receptor antagonist.

For patch-clamp experiments at the endbulbs of Held, patch-pipettes were coated with either dental wax or Sylgard to minimize fast capacitive transients and stray capacitance during voltage-clamp experiments. Open tip pipette resistance was 4–5 MΩ with an intracellular solution containing the following: 130 mM Cs-methanesulfonate, 20 mM TEA-Cl, 10 mM HEPES, 0.5 mM EGTA, 5 mM Na_2phosphocreatine, 4 mM ATP-Mg, and 0.3 mM GTP-Na, with pH adjusted to 7.3 with CsOH and an osmolarity of 320 mOsm/l. For anatomic confirmation 1 mM of fluorescent dye Alexa Fluor 488 (Invitrogen) was added to the recording pipette. The bath solution differed from the aCSF normally used in the following: 85 mM NaCl, 25 mM glucose, 2 mM $CaCl_2$, and 1 mM $MgCl_2$. The pH of the solution was adjusted to 7.4 and osmolarity was around 310 mOsm/l. Additionally, the bath solution was supplemented with 1 µM TTX, 1 mM 4-AP, and 40 mM TEA-Cl to suppress voltage-gated Na^+ and K^+ currents. Presynaptic terminals were voltage-clamped at a holding potential of −80 mV, a liquid junction potential of 3 mV was ignored. Series resistance was <30 MΩ and was compensated up to 50% with a 10-µs lag.

Systems physiology: extracellular recordings from single BCs

Extracellular recordings from single units of BCs in the aVCN were performed as described before (Jing et al., 2013; Strenzke et al., 2016) in 9- to 10-week-old mice. After anesthetizing the mice with intraperitoneal injection of urethane (1.32 mg/kg), xylazine (5 mg/kg), and buprenorphine (0.1 mg/kg), a tracheostomy was performed, their cartilaginous ear canals were removed and then they were positioned in a custom-designed headholder and stereotactic system. After partial removal of the occipital bone and cerebellum to expose the surface of the cochlear nucleus, a glass microelectrode was advanced through the anterior portion of the aVCN to avoid the ANFs and instead target the area with a higher fraction of spherical BCs. Acoustic stimulation was provided by an open field Avisoft ScanSpeak Ultrasonic Speaker (Avisoft Bioacoustics). "Putative" spherical BCs were identified and differentiated from other cell types in the cochlear nucleus by their characteristic "primary-like" peristimulus time histogram (PSTH; Taberner and Liberman, 2005), irregular firing pattern demonstrated by a ≥0.5 coefficient of variation (c.v.) of interspike intervals of

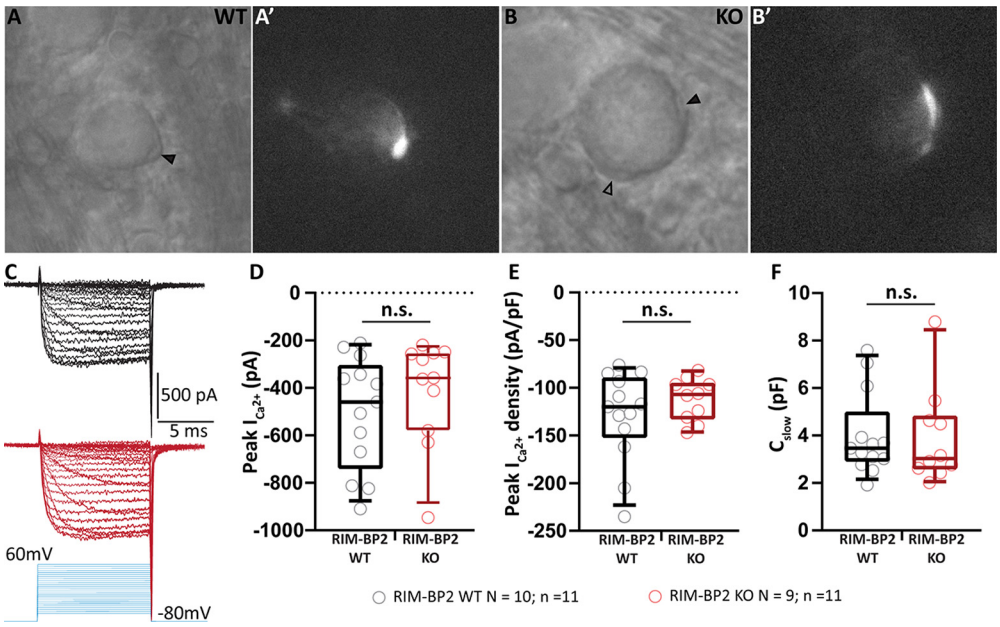

Figure 4. Ca^{2+} influx is unaltered in RIM-BP2-deficient endbulbs. ***A***, ***B***, Bright-field images of the WT (***A***) and RIM-BP2 KO (***B***) BCs under DIC. The recorded endbulb is demarcated by a solid black arrowhead (***A***, ***B***), while another endbulb onto to the same BC is shown by an open black arrowhead (***B***). Each recorded endbulb was filled with Alexa Fluor 488 to confirm that only the presynaptic terminal was accessed, and not the postsynaptic cell. Fluorescent endbulbs are shown in ***A'***, ***B'***. ***C***, Representative traces of presynaptic Ca^{2+} currents in WT (black) and RIM-BP2 KO (red) in response to stepped increase in holding potential (stimulus protocol in blue). ***D–F***, No significant difference was observed between the two genotypes in the peak Ca^{2+} current (***D***), peak Ca^{2+} density (***E***; peak current/C_{slow}), and the size of the endbulb (***F***; estimated by C_{slow}). Each data point represents the mean estimate of each endbulb included in the analysis. Normality was tested with the Shapiro–Wilk test, and variance with *F* test. All data are presented as box and whisker plots (grand median of all BC means, lower/upper quartiles, 10–90th percentiles). Significance of normally distributed data with equal variances (***D–E***) was tested with Student's *t* test, while non-normally distributed data (***F***) was tested with Mann–Whitney *U* test, n.s. $p \geq 0.05$, *N*: number of animals, *n*: number of endbulbs of Held.

adapted responses, and a first spike latency of ≤5 ms. BCs units were distinguished from ANF (also having primary-like PSTH) based on their stereotactic position (<1.1 mm below the surface of the cochlear nucleus). Recordings were performed using TDT system III hardware and an ELC-03XS amplifier (NPI Electronics).

Immunohistochemistry and confocal imaging

Mice at postnatal days 20–24 were deeply and terminally anesthetized with xylazin (5 mg/kg) and ketamin (10 mg/ml) in 0.9% saline and then transcardially perfused with 2% freshly prepared ice-cold paraformaldehyde with pH adjusted to 7.4. The fixed brain was then removed and brainstem was dissected with a coronal cut few millimeters nasal to the junction between occipital cortex and cerebellum. The brain block was washed overnight in 30% sucrose solution in PBS. For sectioning, the brain block was embedded in Tissue Tek Cryomatrix (Thermo Fisher Scientific) and then fixed on the stage of the cryostat (Figocut E cryotome, Reichert-Jung) such that the caudal aspect was facing upwards and the dorsal side was toward the blade. Advancing from caudal to nasal, 30-µm coronal sections were cut (chamber temperature: −20°C, object temperature: −22°C) and discarded until the appearance of the seventh cranial nerve. Subsequent sections containing aVCN were collected onto electrostatically charged microscope slides (SuperFrost Plus, Thermo Fisher Scientific). For parallel processing, one slice of each genotype was collected per slide. Thereafter, the slices were washed for 10 min in PBS and incubated in goat serum dilution buffer [GSDB; 16% normal goat serum, 450 mM NaCl, 0.3% Triton X-100, and 20 mM phosphate buffer (PB), pH 7.4] for 1 h, followed by incubation in primary antibodies diluted in GSDB, for 3 h, in a wet chamber at room temperature. After washing 2 × 10 min with wash buffer (450 mM NaCl, 0.3% Triton X-100, and 20 mM PB) and 2 × 10 min with PBS, the slices were incubated with secondary antibodies diluted in GSDB, for 1 h, in a light-protected wet chamber at room temperature. The slices were then washed 2 × 10 min with wash buffer, 2 × 10 min with PBS and 1 × 10 min in 5 mM PB, and finally mounted with a drop of fluorescence mounting medium based on Mowiol 4–88 (Carl Roth) and covered with a thin glass coverslip. The above-described perfusion fixation method was used to stain for RIM-BP2. The remaining immunofluorescence experiments (Munc13-1, RIM2, CAST, Bsn) were done on samples taken from RIM-BP2 KO mice aged between postnatal day (p)15 and p23 and WT littermates. After obtaining coronal sections of the unfixed mouse brain from the cryostat the slices were maintained frozen at −20°C until immersion fixation or fixed directly on ice in a solution of PBS containing 3% w/v heat depolymerized PFA (70°C) for 3 min. This alternative method of fixation showed robust labeling with less background than perfusion fixed samples labeled against the same markers. For the comparison of $Ca_V2.1$ immunofluorescence levels in confocal microscopy and the stimulated emission depletion (STED) analysis of $Ca_V2.1$ and Bsn clusters, we used very brief fixation with 3% PFA for <1 min (30–40 s) as $Ca_V2.1$ labeling was impeded by stronger fixation. Thereafter, the blocking and immunolabeling protocols were followed exactly as described above for the perfusion fixed samples.

Primary antibodies used were: rabbit anti-RIM-BP2 (1:200), guinea pig anti-VGLUT1 (1:500), rabbit anti-VGLUT1 (1:1000), mouse anti-Gephyrin (1:500), mouse anti-Sap7f407 to Bsn (1:500; Abcam), guinea pig anti-Bsn (1:500), rabbit anti-Munc13-1 (1:200), rabbit anti-RIM1 (1:200), rabbit anti-RIM2 (1:200), rabbit anti-CAST (1:200), rabbit anti-P/Q Ca^{2+} channel (1:500), chicken anti-Homer1 (1:200). Unless stated otherwise, primary antibodies were purchased from Synaptic Systems. Secondary antibodies used were: Alexa Fluor 488-, Alexa Fluor 568-, and Alexa Fluor 647-labeled antibodies (1:200, Invitrogen), goat anti-guinea pig STAR580, and goat anti-rabbit STAR 635p (1:200, Abberior GmbH).

Confocal images were acquired using a laser-scanning confocal microscope (Leica TCS SP5; Leica Microsystems) equipped with 488-nm (Ar) and 561/633-nm (He-Ne) lasers and 63×/1.4 NA oil-immersion objective. STED and confocal images ($Ca_V2.1$ and Bsn analyses) were acquired using a two-color STED microscope (Abberior Instruments) equipped with 561- and 640-nm excitation lasers, a 775-nm laser for STED (1.2 W) and a 100× oil immersion objective (1.4 NA, Olympus). Confocal *z*-stacks were processed with Imaris (Bit-plane) for spot detection, co-localization analysis and fluorescence intensity calculation using custom MATLAB scripts. STED images of $Ca_V2.1$ and Bsn were analyzed using Igor Pro7 (Wavemetrics). Samples of both genotypes: RIM-

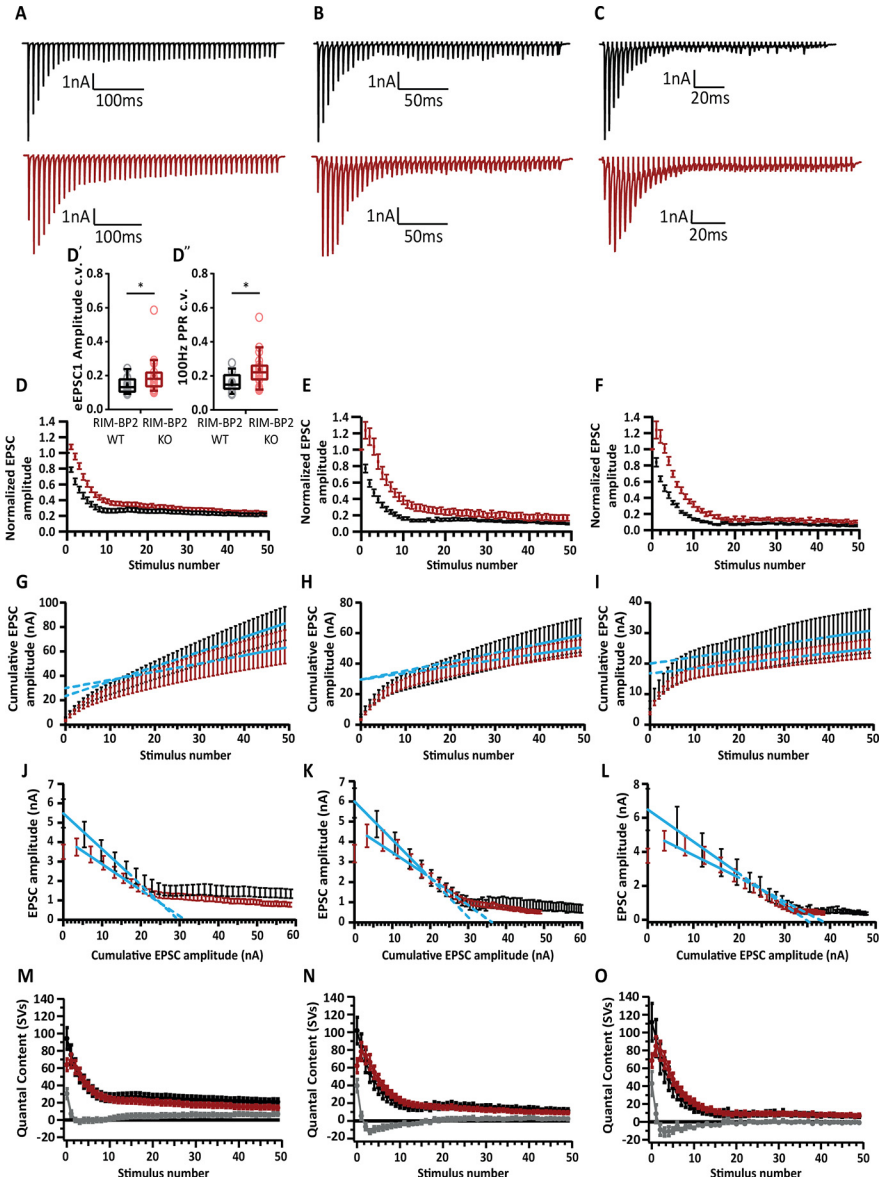

Figure 5. Analysis of release probability (P_r) as well as the size and dynamics of the RRP. ***A–C***, Representative traces of eEPSCs in response to trains of 50 action potentials delivered at frequencies of 100 Hz (***A***), 200 Hz (***B***), and 333 Hz (***C***) recorded from WT (top, black traces) and RIM-BP2 KO (bottom, red traces). Note the characteristic fast short-term depression of WT BC EPSCs that is altered in the mutant. The mutant BCs show a delayed short-term depression with the first EPSC amplitude not being the largest in the train, indicating that the naive mutant synapse releases most of its vesicles later in the train. ***D–F***, Average EPSC amplitudes, normalized to the first EPSC of the train plotted against the stimulus number. ***D′***, For each cell included in the 100-Hz dataset, the trial-to-trial variability of SV release was assessed by calculating the eEPSC1 amplitude c.v. The KO shows significantly higher variability than the WT. ***D″***, The trial-to-trial variability of P_r was similarly assessed using the PPR c.v. as a proxy. Here, again, the KO endbulbs display higher PPR variability than WT endbulbs. ***G–I***, To estimate the size of the RRP, the rate of vesicle replenishment and the P_r using the SMN method, the EPSC amplitudes of the 100-Hz (***G***), 200-Hz (***H***), and 333-Hz (***I***) trains were plotted cumulatively against the stimulus number. The linear fit (solid blue line) to the last ten steady-state values was back-extrapolated to the *y*-axis (dotted blue line). The *y*-intercept value, divided by the average sEPSC amplitude yields the number of vesicles in the RRP. To calculate P_r, the vesicle content of eEPSC1 is divided by the size of the RRP. The slope of the linear fit approximates the rate of vesicle replenishment during the train. Quantitative analysis is further elaborated in Table 2. ***J–L***, To estimate the RRP size and P_r using the EQ method, absolute EPSC amplitudes were plotted against the cumulative amplitude of all the EPSCs preceding the corresponding EPSC. The linear fit to the first three to five points for the 100-Hz (***J***), 200-Hz (***K***), and 333-Hz (***L***) trains (solid blue line) was forward extrapolated (dotted blue line) to the *x*-axis. Dividing the *x* intercept value by the average sEPSC size yields the size of the RRP, while the slope of the linear fit defines the P_r. To assess whether the reduced P_r results from fewer superprimed SVs in the RRP, a subtraction analysis was performed. We first divided the average eEPSC amplitudes by the average sEPSC amplitude to calculate the SV number released during each eEPSC (quantal content) of the averaged responses to 100-, 200-, and 333-Hz train stimulation. Traces plot the quantal content released during each one of 50 eEPSCs in 100-Hz (***M***), 200-Hz (***N***), and 333-Hz (***O***) trains against the stimulus number. After subtracting the quantal content for each RIM-BP2 KO eEPSC from the respective WT eEPSC, we plot the subtraction curves (gray curves at the bottom of each panel). For an assessment of P_r and RRP dynamics in the absence of kynurenic acid and CTZ along with the changes of RIM-BP2 KO short-term plasticity in response to increased $[Ca^{2+}]_e$, see Figure 6. For 100 Hz: RIM-BP2 WT $N = 14$; $n = 16$, RIM-BP2 KO $N = 17$; $n = 21$. For 200 Hz: RIM-BP2 WT $N = 13$; $n = 16$, RIM-BP2 KO $N = 13$; $n = 16$. For 333 Hz: RIM-BP2 WT $N = 6$; $n = 12$, RIM-BP2 KO $N = 14$; $n = 17$. *N*: number of animals; *n*: number of BCs.

BP2 WT and RIM-BP2 KO were processed and imaged in parallel, using same laser power, gain, and microscope settings.

SDS–freeze-fracture replica immunolabeling (SDS-FRIL)

Mice at postnatal days 20–24 were deeply and terminally anesthetized with xylazin (5 mg/kg) and ketamin (10 mg/ml) in 0.9% saline, and perfused transcardially with ice-cold PBS followed by perfusion with freshly-prepared 2% PFA with 15% saturated picric acid solution in 0.1 M PB with pH adjusted to 7.3. The fixed brain was then removed and brainstem was dissected with a coronal cut few millimeters nasal to the junction between occipital cortex and cerebellum. The brain block was washed over night in 30% sucrose solution in PBS. Coronal slices (130 µm thick) were cut from the fixed brain block fusing a vibratome microslicer (Linear-Pro7, Dosaka) in ice-cold PBS. The rostral aVCNs were trimmed by hand from the slices. The trimmed sections were then immersed in graded glycerol concentrations of 10−20% at room temperature for 20 min each, followed by 30% at 4°C overnight. The trimmed sections were sandwiched between two metal carriers and then rapidly frozen by a high-pressure freezing machine (HPM010, BAL-TEC, Balzers). Using a freeze etching device (BAF060, BAL-TEC), frozen samples were then fractured into two parts at −115°C, and the fractured faces were replicated by sequential deposition of carbon (thickness: 5 nm from 90° angle), platinum (thickness: 2 nm from 60° angle, unidirectional), and carbon again (thickness: 20 nm from 90° angle). After thawing, the tissue debris attached to the replica was digested with gentle shaking at 80°C for 18 h, in a solution containing 2.5% SDS, 20% sucrose, and 15 mM of Tris-HCl with pH set to 8.3. The replicas were washed 3 × 10 min in wash buffer (0.1% Tween 20, 0.05% BSA, and 0.05% NaN_3 in TBS, pH 7.4), and then the non-specific binding sites were blocked with 5% BSA in wash buffer for 1 h at 4°C.

For multiple immunolabeling against $Ca_V2.1$ and AZ proteins, replicas were first incubated with guinea pig anti-$Ca_V2.1$ antibody (8 µg/ml in 1% BSA; Frontier Institute AB_2571851) at 15°C for 3 d, then with anti-guinea pig secondary antibodies conjugated with 10-nm gold particles (1:30 diluted in 5% BSA; British Biocell International) at 15°C overnight, followed by incubation with a cocktail of rabbit anti-AZ proteins antibodies (anti-ELKS at 2 µg/ml in 1% BSA; gift from Dr. Toshihisa Ohtsuka raised against rat ELKS aa117-142, anti-Neurexin at 4 µg/ml in

1% BSA; gift from Dr. Masahiko Watanabe raised against aa1499–1507 and anti-RIM at 4 µg/ml in 1% BSA; Synaptic Systems 140203) at 15°C overnight, and finally with anti-rabbit secondary antibodies conjugated with 5-nm gold particles (1:30 diluted in 5% BSA; British Biocell International) at 15°C overnight. After immunolabeling, replicas were rinsed three times with 0.05% BSA in TBS, washed with TBS and distilled water, and mounted on formvar-coated copper grids.

The labeled replicas were imaged using a Tecnai-12 transmission electron microscope (FEI; AV 120 kV). To obtain a planar view for quantitative measurement of immuno-gold particle number and densities, profile of synaptic structures (AZ and PSD) were tilted in the electron beam. IMP-clusters representing PSDs were manually demarcated and the area was measured using ImageJ software (Rubio et al., 2017). AZ areas were marked by hand with the experimenter being blinded to the identity of the two genotypes. Quantitative analysis of immune-gold particles was done using an in-house software tool, Gold Particle Detection and Quantification (Luján et al., 2018). To define clusters of gold particles the threshold for the distance between particles belonging to the same cluster was calculated as $\mu + 2\sigma$, where μ and σ are the mean and SD obtained from a Gaussian fit to the distribution of nearest neighbor distances (NNDs) between particles. $\mu + 2\sigma$ was 43.02 and 43.92 nm for $Ca_V2.1$ gold particles in RIM-BP2 WT and KO, respectively. We set the threshold at 40 nm to match the value used in a previous analysis (Miki et al., 2017). The distances between particles were measured from their centers of mass, and the minimum number of particles required to form a cluster was set to three. We additionally compared our "real" distribution of NNDs between gold particles and their clustering to 500 random generated by Monte Carlo simulations (as described in Luján et al., 2018; Kleindienst et al., 2020) to confirm that the clusters visualized through our analysis are not generated by chance.

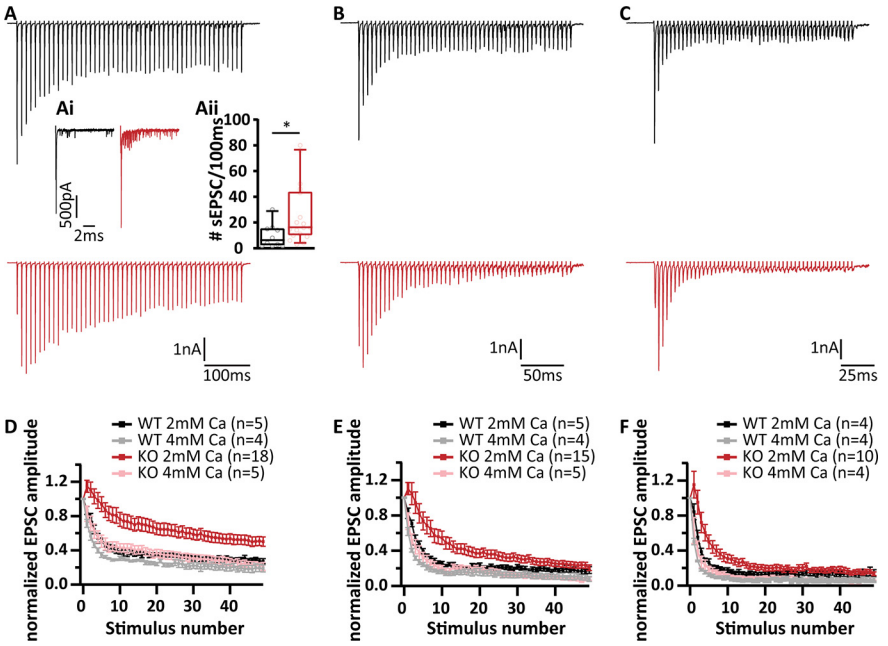

Figure 6. Short-term depression replaced by facilitation at endbulbs of Held in RIM-BP2 KO mice in the absence of kynurenic acid and CTZ. Representative traces of eEPSCs in response to trains of 50 action potentials delivered at frequencies of 100 Hz (***A***), 200 Hz (***B***), and 333 Hz (***C***) recorded from WT (top, black traces) and RIM-BP2 KO (bottom, red traces). Inset (***Ai***, ***Aii***), Asynchronous release calculated as the number of sEPSC events within 100 ms following the synchronous release elicited by a train of 50 pulses delivered at 100 Hz. A significantly higher asynchronous release was observed in the RIM-BP2 KO (red, 25.67 ± 5.55 sEPSC/100 ms) as compared to the WT (black, 9.60 ± 2.90 sEPSC/100 ms; $p = 0.02$, Mann–Whitney *U* test). Note the characteristic fast short-term depression of WT BC EPSCs that is altered in the mutant. The mutant BCs show a delayed short-term depression with the first EPSC amplitude not being the largest in the train, indicating that the naive mutant synapse releases most of its vesicles later in the train. This effect is more pronounced in the higher frequencies of stimulation, as is demonstrated when the EPSC amplitudes, normalized to the first EPSC of the train are plotted against the stimulus number (***D–F***). This effect was abolished when extracellular Ca^{2+} was increased to 4 mM (WT traces in gray and KO traces in pink).

High-pressure freezing, freeze substitution, and electron tomography

Parasagittal slices from cochlear nuclei were obtained as described for slice electrophysiology. Slices containing the cochlear nucleus were trimmed and mounted onto type A specimen carriers (Leica Microsystems) filled with cutting solution. The flat side of the type B carriers (Leica Microsystems) was dipped in 1-hexadecene (Sigma-Aldrich) and placed onto the type A carriers. Samples were frozen immediately using a HPM100 (Leica Microsystems) and transferred into liquid nitrogen. Freeze-substitution was performed in an EM AFS2 (Leica Microsystems) according to Wong et al. (2014). The slices were incubated in 0.1% (w/v) tannic acid in acetone at −90°C for 4 d and afterward washed three times for 1 h each in acetone at −90°C. 2% (w/v) osmium tetroxide in acetone was applied and incubated for 40.4 h. During that time the temperature was raised slowly to 4°C (10°C/h). At 4°C, osmium tetroxide was removed, and the samples were washed with acetone three times and brought to room temperature. Slices were infiltrated in epoxy resin (Agar-100 kit, Plano; epoxy/acetone 1:1 3–6 h; 100% epoxy overnight). Finally, samples were further incubated in fresh 100% epoxy and placed in embedding molds.

After polymerization for 48 h at 70°C, excess resin was removed with a fine file (DiAtome) and the block was trimmed to a pyramid using a razor blade. To check the region and the structural preservation, 65-nm ultrathin sections were cut with a diamond knife (DiAtome) using an EM UC7 (Leica Microsystems) ultramicrotome. Sections were collected on formvar-coated copper slot grids (Athene, Plano, for ultrathin sections). For electron tomography, 250-nm semi-thin sections were obtained and collected on mesh grids (100 mesh; Athene, Plano, for semi-thin sections). Poststaining was performed with Uranyless (EMS) for 20 min.

The region and quality of the tissue was checked at 80 kV using a JEM1011 transmission electron microscope (JEOL) equipped with a GatanOrius 1200A camera (Gatan). Electron tomography was essentially performed as described previously (Jung et al., 2015; Wong et al., 2014); 10-nm gold beads (British Bio Cell/Plano) were applied to both sides of the stained grids. Big synaptic terminals BCs were identified, and tilt series from endbulb AZs were acquired at 200 kV using a JEM2100 transmission electron microscope (JEOL) mostly from −60° to +60° with a 1° increment at 15,000× using the Serial-EM software package with an image pixel size of 0.95 nm (Mastronarde, 2005). Tomograms were generated using the IMOD package etomo (Kremer et al., 1996).

Only asymmetric synapses with clearly identifiable PSDs were analyzed. However, in high-pressure frozen samples, PSDs appear less electron-dense compared to chemical fixed synapses. Only AZs that showed a PSD and a clear synaptic cleft, originating from large presynaptic terminals were analyzed to exclude inhibitory synapses.

Tomograms were segmented semi-automatically using 3dmod (Kremer et al., 1996). The AZ membrane was manually segmented every 15 virtual sections for five consecutive virtual sections and then interpolated across the *z*-stack, following the extent of the PSD and the parallel synaptic cleft. Moreover, virtual sections were corrected manually after interpolation. The total surface area of this object was then divided by two to calculate the AZ area.

Table 2. Analysis of P_r as well as the size and dynamics of the RRP

Stimulation frequency	Parameter	RIM-BP2 WT	RIM-BP2 KO	*p* value
100 Hz	eEPSC1 amplitude (nA)	5.48 ± 0.73 (4.7)	3.5 ± 0.37 (3.6)	**0.022, M**
	tau (ms)	33.60 ± 3.64 (27.2)	56.95 ± 3.76 (58.03)	**0.0001, T**
	$eEPSC_{30–50}$ (nA)	1.29 ± 0.22 (1.09)	0.87 ± 0.12 (0.84)	0.1015, M
	$eEPSC_{30–50}/EPSC_{max}$	0.23 ± 0.02 (0.21)	0.24 ± 0.03 (0.24)	0.8205, T
	Replenishment	2.09 ± 0.35 (1.79)	1.44 ± 0.20 (1.2)	0.1015, T
	RRP_{SMN} (SVs)	398.60 ± 72.50 (341.56)	455.61 ± 63.00 (446.32)	0.4038, M
	RRP_{EQ} (SVs)	575.11 ± 102.11 (504.25)	593.62 ± 73.45 (610.12)	0.6826, M
	$P_{r\ SMN}$	0.26 ± 0.02 (0.28)	0.17 ± 0.01 (0.15)	**0.0004, T**
	$P_{r\ EQ}$	0.2 ± 0.02 (0.21)	0.14 ± 0.01 (0.13)	**0.0336, T**
	PPR	0.79 ± 0.03 (0.72)	1.08 ± 0.10 (0.97)	**0.0004, M**
200 Hz	tau (ms)	33.05 ± 3.04 (32.46)	70.51 ± 5.85 (65.43)	**<0.0001, M**
	$eEPSC_{30–50}$ (nA)	0.76 ± 0.13 (0.70)	0.59 ± 0.07 (0.56)	0.0608, M
	$eEPSC_{30–50}/EPSC_{max}$	0.13 ± 0.01 (0.14)	0.17 ± 0.03 (0.13)	0.0608, M
	Replenishment	2.16 ± 0.37 (1.98)	1.53 ± 0.24 (1.45)	0.1756, T
	RRP_{SMN} (SVs)	479.11 ± 110.23 (351.27)	544.42 ± 77.85 (545.76)	0.3168, M
	RRP_{EQ} (SVs)	554.34 ± 123.03 (441.21)	771.93 ± 108 (663.17)	0.0883, M
	$P_{r\ SMN}$	0.25 ± 0.02 (0.26)	0.14 ± 0.01 (0.13)	**<0.0001, M**
	$P_{r\ EQ}$	0.22 ± 0.02 (0.20)	0.13 ± 0.01 (0.13)	**0.0002, T**
	PPR	0.81 ± 0.05 (0.79)	1.28 ± 0.10 (1.21)	**<0.0001, M**
333 Hz	tau (ms)	19.34 ± 2.50 (19.77)	39.97 ± 3.92 (40.97)	**0.0002, T**
	$eEPSC_{30–50}$ (nA)	0.45 ± 0.09 (0.38)	0.48 ± 0.08 (0.41)	0.1523, M
	$eEPSC_{30–50}/EPSC_{max}$	0.07 ± 0.01 (0.07)	0.10 ± 0.02 (0.08)	0.6106, M
	Replenishment	1.24 ± 0.21 (1.22)	1 ± 0.25 (0.89)	0.1656, M
	RRP_{SMN} (SVs)	345.21 ± 96.42 (253.09)	306.16 ± 36.91 (331.58)	0.6471, M
	RRP_{EQ}(SVs)	595.52 ± 155.74 (450.19)	674.17 ± 76.94 (787.59)	**0.0043, T**
	$P_{r\ EQ}$	0.23 ± 0.03 (0.21)	0.15 ± 0.01 (0.15)	**0.0022, T**
	PPR	0.8 ± 0.05 (0.84)	1.28 ± 0.11 (1.21)	**0.0009, T**

Tau (τ): time constant of single exponential fit to the decay of eEPSC during the stimulation train. $eEPSC_{30–50}/EPSC_{max}$: average amplitude of the last 20 EPSCs (30–50) in the train, normalized to the amplitude of the largest EPSC of the train. Replenishment: rate of vesicle replenishment. RRP: readily releasable pool. P_r: release probability. PPR: paired pulse ratio, amplitude of the second EPSC of the train normalized to the amplitude of the first EPSC. Data are presented as mean ± SEM, and medians are shown in parentheses. Normality of data distribution was tested with Jarque–Bera test, and the variances were compared with *F* test. Statistical significance of differences was assessed with unpaired Student's *t* test (shown in the table as T), when the data satisfied the criteria of normality and variance comparability. When the data did not satisfy these criteria, Mann–Whitney *U* test was used instead (shown in the table as M); $p < 0.05$, set as threshold for statistical significance. Statistically significant differences are shown in bold.

SVs were reconstructed at their maximum projection and the sphere size was adjusted for each vesicle. The smallest distances from the outer leaflet of the SV membrane to the inner leaflet of the AZ membrane were measured and SVs in contact with the AZ membrane were defined as morphologically docked SVs (0- to 2-nm distance). Moreover, all vesicles within 200 nm of the AZ were quantified and categorized in 20-nm bins. The radii of the SVs were determined with the program "imodinfo" of the IMOD software package and the diameters were calculated. For quantification of lateral distances of docked SVs, models of tomogram top views with docked SVs were imported in ImageJ and the center of the captured AZ area was defined by setting two diagonal lines from respective edges of the AZ. The crossing point was defined as the center and the distances were measured from the outer membrane of the SV toward the center point.

Experimental design and statistical analysis

We investigated the role of RIM-BP2 in synaptic transmission at the endbulb of Held both functionally and morphologically. We used patch-clamp electrophysiology in acute mouse brains slices to assess the Ca^{2+} influx at the presynapse by direct presynaptic terminal recordings. Afferent fiber stimulation was used to assess synaptic strength, synaptic plasticity, SV pool size, and SV release and recovery dynamics. We employed *in vivo* extracellular recordings from single units of BCs in live anesthetised animals to assess the effect of RIM-BP2 deletion on sound processing. To analyze the molecular composition at the endbulb AZs, we employed confocal and STED imaging of immunostained mouse brain slices. We used electron tomography, and immuno-electron microscopy to assess the ultrastructure of the endbulb synapse–SV complement at the AZ, and spatial coupling of SV and Ca^{2+} channels.

Electrophysiology data were analyzed using Igor Pro (Wavemetrics), MATLAB (MathWorks), Mini Analysis (Synaptosoft Inc.), and GraphPad Prism software. Synaptic delay was calculated as the time between the start of stimulus (voltage output of the amplifier as dictated by the experiment protocol) and the time when the respective EPSC response reached 10% of its peak amplitude.

Confocal images were analyzed using ImageJ software, Imaris (Bitplane AG), and MATLAB (MathWorks). STED images of $Ca_V2.1$ channels were analyzed using custom Igor pro scripts. Single plane slices of the top (coverslip proximal) and/or bottom (distal from coverslip) membranes of BCs were imaged to capture the $Ca_V2.1$ spots on a flat surface top view and enable 2D Gaussian fitting. The $Ca_V2.1$ spots that were simultaneously closely juxtaposed to puncta of both Homer1 and Bsn were fitted with Igor Pro's 2D Gaussian function.

Figures were assembled for display using Adobe Illustrator (Adobe Systems). Unless reported otherwise, statistical significance between groups was determined by either unpaired Student's *t* test (in case of normally distributed data with comparable variances between the groups) or Mann–Whitney *U* test (when data distribution did not satisfy the criteria). Normality of distribution was tested with Jarque–Bera test and variances were compared with *F* test. Data are presented as mean ± SEM when normally distributed data with comparable variances between the groups, and otherwise as box and whisker plots showing grand median (of the means of all recordings), lower/upper quartiles, 10–90th percentiles; $*p < 0.05$, $**p < 0.01$, $***p < 0.001$, and $****p < 0.0001$.

Hierarchical Bayesian modeling

Data of Nearest Neighbor Distances (NNDs) were analyzed with a hierarchical Bayesian model (Kruschke and Vanpaemel, 2015). The γ distribution was chosen as a continuous probability distribution with a low number of parameters and a positive domain. Appropriate to the statistical model, genotypes were used as a fixed effect, while animals were used as a random effect. For this experiment, three animals per genotype were used. The priors for each parameter were set as the default of brm function (RStudio), except for β-coefficients (overall fixed effects for model intercepts) and shapes. Specifically, we used a half-Cauchy prior with

location 0 and scale 5 on β-coefficients, and with location 0 and scale 2 on shapes. The modeling was performed using the R language (version 4.0.2) on RStudio (version 1.3.1056) with brms (version 2.13.3) and rstan (version 2.21.1) packages (Buerkner, 2017). Models were estimated via Markov Chain Monte Carlo (MCMC) sampling, running four parallel chains for 10,000 iterations each with a 5000-iteration burn-in. The model comparison was assessed by a Bayes factor and wide-applicable Akaike Information Criteria (WAIC Watanabe, 2010) with models in which the fixed effect had been dropped (null models) from the original models (full models).

Results

Deletion of RIM-BP2 impairs synchronous transmitter release at the endbulb of held synapse

To determine the functional role of RIM-BP2, we studied synaptic transmission at the endbulb of Held synapse in acute parasagittal slices of the brainstem of constitutive RIM-BP2 KO mice (RIM-BP2 KO; Grauel et al., 2016) recording spontaneous EPSCs (sEPSCs) (no stimulation, no TTX applied) and evoked EPSCs (eEPSCs) from BCs of the aVCN (Fig. 1*A*) at postnatal days 15–21. eEPSCs were elicited by minimal electrical stimulation of the presynaptic ANF by a monopolar electrode placed in the proximity (approximately three cell diameters away) of the recorded BC, whereby each stimulus is aimed to elicit one action potential in one endbulb (Yang and Xu-Friedman, 2008).

Experiments of Figure 1 were performed in the presence of 1 mM kynurenic acid and 100 μM CTZ to avoid saturation and desensitization of AMPA receptors (Chanda and Xu-Friedman, 2010), respectively. The concentration of CTZ used here, was adopted from previous reports at the calyx of Held (Sakaba and Neher, 2001; Thanawala and Regehr, 2013). The former study (Sakaba and Neher, 2001) examined the NMDA current in the presence of 100 μM CTZ and found no evidence for a presynaptic CTZ effect at the calyx of Held. The eEPSC amplitude was reduced in RIM-BP2 KO BCs compared to littermate WT [3.50 ± 0.37 nA (KO) vs 5.48 ± 0.73 nA (WT), $p = 0.022$, Mann–Whitney *U* test; Fig. 1*B*,*C*]. Both the eEPSC synaptic delay [0.89 ± 0.04 ms (KO) vs 0.89 ± 0.2 ms (WT) $p = 0.5691$, Mann–Whitney *U* test; Fig. 1*D*] and 10–90 rise time [297.76 ± 38.47 μs (KO) vs 247.77 ± 61.93 μs (WT) $p = 0.1650$, Mann–Whitney *U* test; Fig. 1*E*] were comparable between the two genotypes. The eEPSC full width at half maximum [0.80 ± 0.04 ms (KO) vs 0.72 ± 0.18 ms (WT) $p = 0.3119$, Mann–Whitney *U* test; Fig. 1*F*] and the decay time [0.77 ± 0.04 ms (KO) vs 0.71 ± 0.18 ms (WT) $p = 0.4163$, Mann–Whitney *U* test; Fig. 1*G*] also remained unchanged. EPSC recordings in the absence of kynurenic acid and CTZ confirmed the eEPSC amplitude reduction [4.54 ± 0.75 nA (KO) vs 6.57 ± 0.47 nA (WT), $p = 0.004$, Mann–Whitney *U* test; Fig. 2*A*,*B*], eliminating the possibility of CTZ obscuring the changes in AMPA receptor composition or inducing membrane potential changes. The eEPSC synaptic delay was longer [0.89 ± 0.02 ms (KO) vs 0.82 ± 0.03 ms (WT) $p = 0.013$, Mann–Whitney *U* test; Fig. 2*C*], 10–90 rise time remained unchanged [0.18 ± 0.01 ms (KO) vs 0.19 ± 0.02 ms (WT) $p = 0.49$, Mann–Whitney *U* test; Fig. 2*D*], and decay kinetics were significantly slower for RIM-BP2 KO BCs under these conditions [full width at half maximum was 0.46 ± 0.02 ms (KO) vs 0.38 ± 0.01 ms (WT) $p = 0.0005$, Student's *t* test, and decay time was 0.35 ± 0.02 ms (KO) vs 0.28 ± 0.02 ms (WT) $p = 0.0004$, Student's *t* test; Fig. 2*E*,*F*].

In order to test for potential changes in the quantal release properties we recorded sEPSCs from BCs (Fig. 3). We did not observe differences in the sEPSC amplitude [54.91 ± 1.46 pA (KO) vs 58.17 ± 3.70 pA (WT), $p = 0.5781$, Mann–Whitney *U* test; Fig. 3*A*–*C*]. Similarly, the sEPSC frequency [6.02 ± 2.10 pA (KO) vs 9.02 ± 2.40 pA (WT), $p = 0.3127$, Mann–Whitney *U* test; Fig. 3*D*], 10–90 rise time [0.11 ± 0.002 ms (KO) vs 0.11 ± 0.006 ms (WT), $p = 0.9353$, Mann–Whitney *U* test; Fig. 3*E*], full-width at half-maximum [0.23 ± 0.006 ms (KO) vs 0.23 ± 0.008 ms (WT), $p = 0.9364$, Mann–Whitney *U* test; Fig. 3*F*], and decay time [0.22 ± 0.007 ms (KO) vs 0.21 ± 0.010 ms

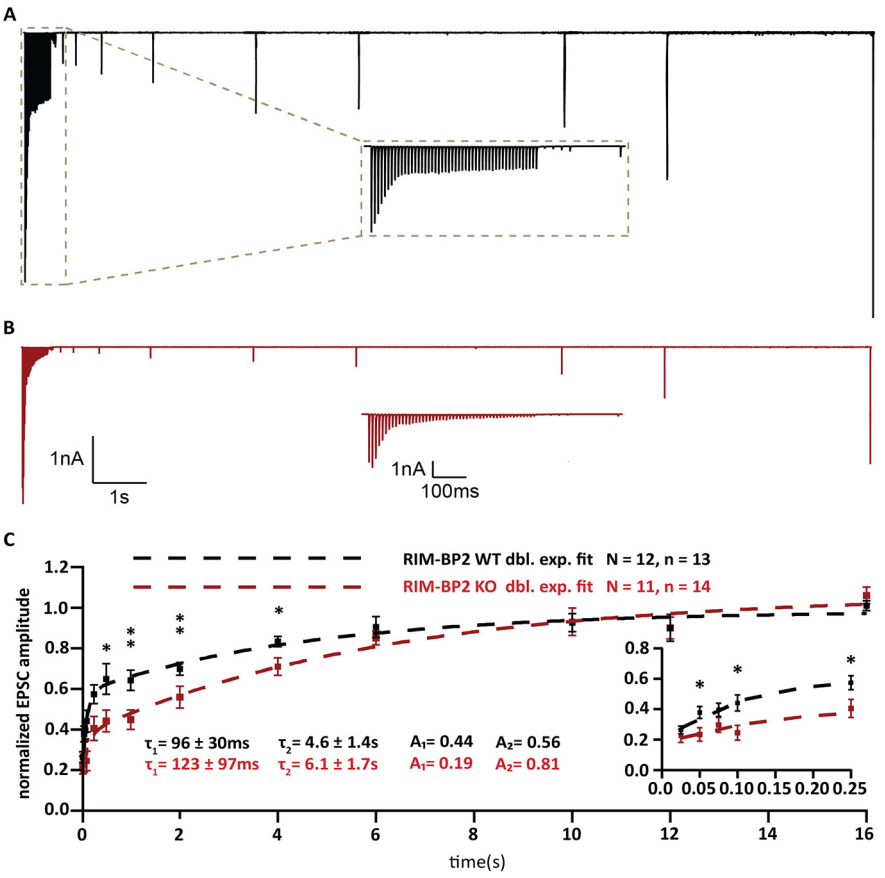

Figure 7. Slowed RRP recovery in RIM-BP2-deficient endbulb synapses. ***A***, ***B***, Representative traces of RIM-BP2 WT (***A***) and RIM-BP2 KO (***B***) illustrate the recovery experiment. After a 100-Hz conditioning train of 50 stimuli, single test pulses were delivered at time intervals of (in ms) 25, 50, 75, 100, 250, 500 (further intervals in s), 1, 2, 4, 6, 10, 12, and 16. To assess recovery, the EPSC amplitude in response to the test pulse is normalized to the first EPSC amplitude of the conditioning train. Insets (***A***, ***B***) show the time course of recovery during the first five test stimuli in subsecond detail. ***C***, Recovery is plotted as mean ± SEM EPSC amplitude in response to test pulses normalized to the first EPSC amplitude of the conditioning train. The double exponential fits are represented by the dashed lines for RIM-BP2 WT (black) and RIM-BP2 KO (red). The time constants (τ) and fractional contributions (***A***) of fast (τ_1, A_1) and slow (τ_2, A_2) recovery components are provided on the graph. Inset shows the first five responses in detail. Normality was tested with Jarque–Bera test. Statistical significance between groups was tested with Mann–Whitney *U* test; $^{**}p < 0.01$, $^{*}p < 0.05$. *N*: number of animals, *n*: number of BCs.

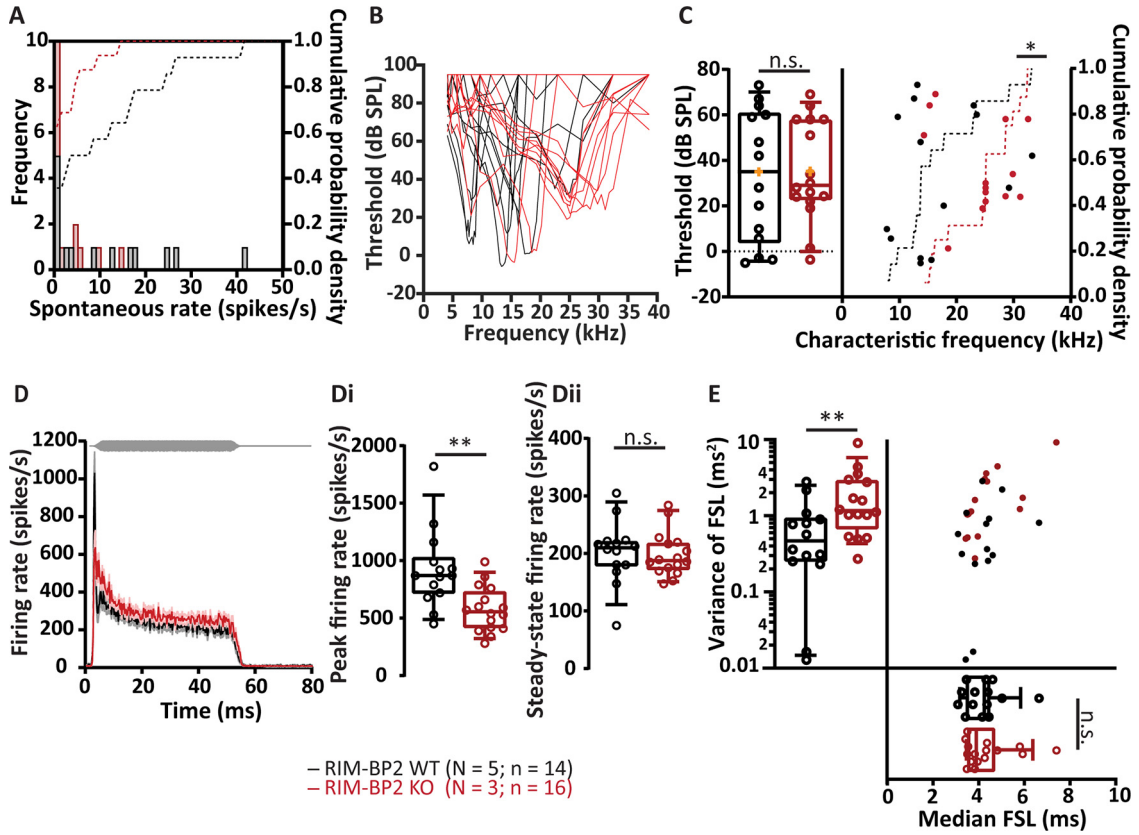

Figure 8. Impaired transmission of sound information in aVCN of RIM-BP2 KO mice *in vivo*. ***A***, Comparable distribution of spontaneous firing rates of single BCs in RIM-BP2 WT (black) and RIM-BP2 KO (red). The histograms represent the frequency distribution (left *y*-axis) and the dotted lines represent the cumulative probability density (right *y*-axis) of spontaneous firing rates. ***B***, ***C***, Representative tuning curves of BCs from RIM-BP2 WT (black) and RIM-BP2 KO (red) demonstrate preserved sharp frequency tuning and low thresholds at the characteristic frequencies (frequency for which spike rate increase requires least sound intensity; ***C***, left) in RIM-BP2 KO BCs. For unknown reasons, we encountered more BCs with high characteristic frequency in RIM-BP2 KO (***C***, right). ***D***, Rise-aligned PSTH of the BC response to 50-ms tone burst stimulation (at characteristic frequency, 30 dB above threshold, stimulus represented in gray) in RIM-BP2 WT (black; $N = 5$; $n = 14$) and RIM-BP2 KO (red; $N = 3$; $n = 16$). PSTH presented as mean (solid lines) ± SEM (shaded area). Peak onset firing rate was significantly reduced in RIM-BP2 KO BCs (***Di***) while the steady-state firing rate was comparable between the two genotypes (***Dii***). Variance in the first spike latency of PSTH (in ***D***) was increased in RIM-BP2 KO units while the median first spike latency remained unperturbed (***E***). Data information: Significance levels: n.s. $p \geq 0.05$, $^{*}p < 0.05$, $^{**}p < 0.01$; n = number of BCs; and N = number of mice. Box and whisker plot represents median, lower/upper quartiles and 10–90th percentiles. Each data point represents the response of a BC. For details about mean ± SEM, median, sample size, and statistics, see Table 3.

Table 3. Analysis of *in vivo* extracellular recordings from single BCs

Parameter	RIM-BP2 WT ($N = 5$; $n = 14$)	RIM-BP2 KO ($N = 3$; $n = 16$)	*p* value
Spontaneous rate (spikes/s)	10.90 ± 3.42 (5.88)	2.74 ± 1.07 (0.60)	0.18, M
Threshold (dB SPL)	33.20 ± 7.76 (35.00)	35.20 ± 5.50 (29.00)	0.83, T
Characteristic frequency (kHz)	16.75 ± 2.06 (13.66)	24.21 ± 1.59 (25.05)	**0.015, K**
Peak firing rate (spikes/s)	922.10 ± 91.65 (870.00)	575.60 ± 49.24 (555.00)	**0.0033, TW**
Steady-state firing rate (spikes/s)	202.30 ± 14.53 (209.80)	197.80 ± 9.6 (187.40)	0.79, T
Variance of FSL (ms^2)	0.76 ± 0.22 (0.47)	2.11 ± 0.56 (1.18)	**0.008, M**
Median FSL (ms)	4.20 ± 0.24 (4.25)	4.36 ± 0.28 (3.90)	0.93, M

Data are presented as mean ± SEM, and medians are shown in parentheses. Normality of data distribution was tested with Kolmogorov–Smirnov test, and the variances were compared with *F* test. Statistical test used to assess the significance of differences is indicated in the column of *p* value. Unpaired Student's *t* test (shown in the table as T) was used, when the data satisfied the criteria of normality and variance comparability. Normally distributed data with unequal variances were compared using Student's *t* test with Welch's correction (shown in the table as TW). Non-normally distributed data were tested with Mann–Whitney *U* test or Kolmogorov–Smirnov test (shown in the table as M and K, respectively); $p < 0.05$, set as threshold for statistical significance. Statistically significant differences are shown in bold.

(WT), $p = 0.8336$, Mann–Whitney *U* test; Fig. 3*G*] were unaltered in the RIM-BP2 KO. This was also the case when recording in the absence of kynurenic acid and CTZ (Table 1). Unaltered sEPSCs suggest that the properties of single SV release and of postsynaptic glutamate response are intact in RIM-BP2-deficient endbulb synapses at BCs.

Quantal size being unaltered, the reduced eEPSC alteration could result from either: (1) an impaired stimulus-secretion coupling because of reduced Ca^{2+} influx and/or altered topography of Ca^{2+} channels (Krinner et al., 2017) and fusion competent SVs (Acuna et al., 2015; Grauel et al., 2016; Luo et al., 2017), or (2) because of an impaired SV priming that has recently been shown to involve RIM-BP2 interaction with Munc13-1 (Brockmann, 2020). We first checked for changes in presynaptic Ca^{2+} influx in the absence of RIM-BP2 using ruptured-patch recordings from

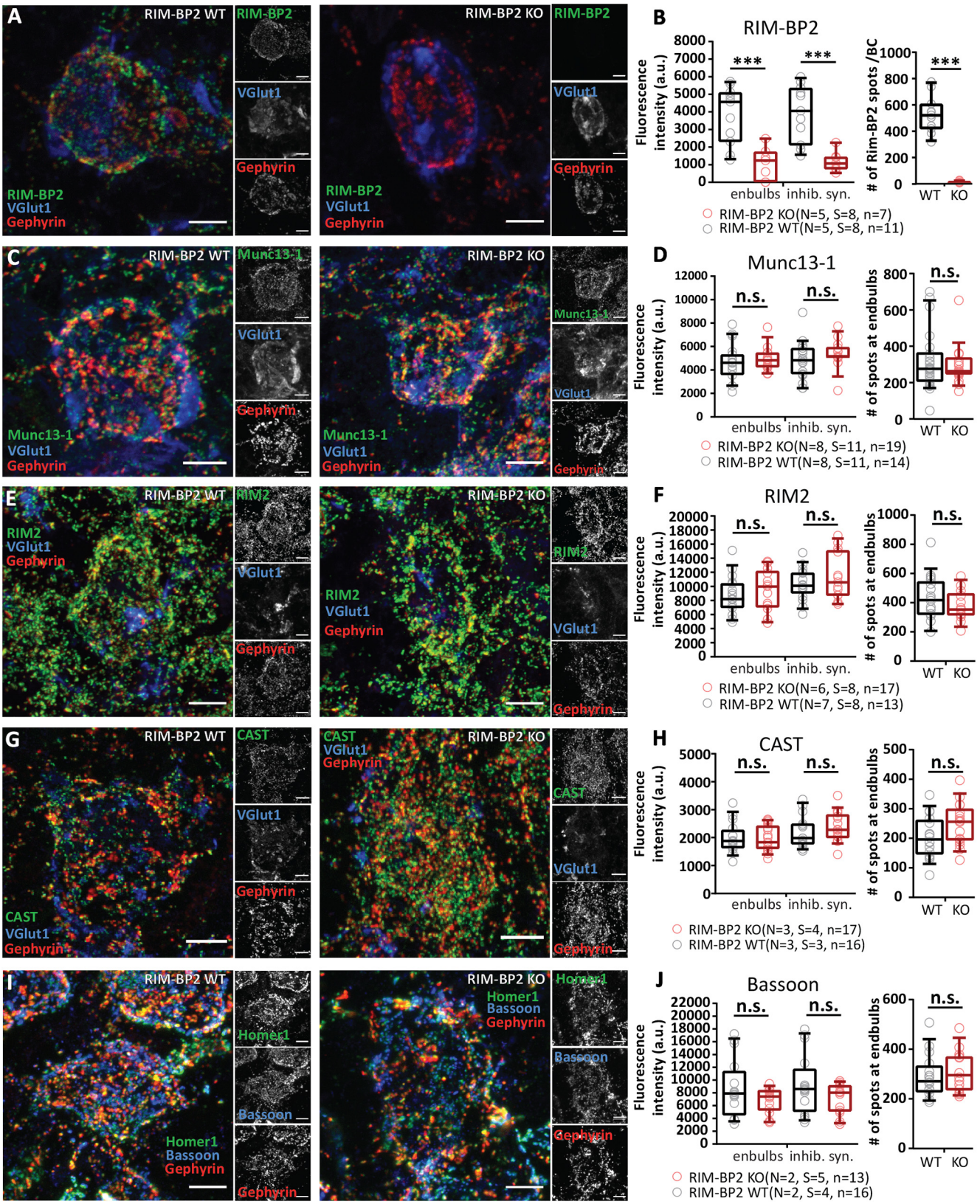

Figure 9. RIM-BP2 disruption does not seem to alter the molecular composition of the endbulb AZs. ***A, C, E, G, I***, Representative maximal *z*-projections of confocal image stacks of BCs in RIM-BP2 WT shown on left and RIM-BP2 KO on right; 30-μm coronal brainstem slices were immunolabelled for RIM-BP2 (***A***), Munc13-1 (***C***), RIM2 (***E***), and CAST (***G***) and co-stained for VGlut1 to outline endbulbs and Gephyrin for inhibitory synapse labeling. For Bsn immunolabeling (***I***), we co-stained for Homer1 (excitatory postsynapses) and Gephyrin. ***B, D, F, H, J***, Quantification of fluorescence intensity of CAZ proteins at endbulbs and inhibitory synapses of BCs (left), and the number of spots of the target CAZ protein at endbulbs (right). ***A***, Representative *z*-projection shows loss of RIM-BP2 immunoreactivity in the RIM-BP2 KO brainstem slices. There was only a faint residual and likely unspecific signal remaining at excitatory and inhibitory synapses (***B***, left), RIM-BP2 immunofluorescent spots were nearly abolished (***B***, right). The immunofluorescence intensity of Munc13-1 (***D***), RIM2 (***F***), CAST (***H***), and Bsn (***J***) were unaltered at RIM-BP2 KO endbulbs. Right columns of ***D***, ***F***, ***H***, ***J*** show similar number of CAZ protein spots localized at KO endbulb AZs as in the WT AZs. The numbers were calculated by subtracting the Gephyrin

the endbulb of Held (Lin et al., 2011) in mice after the hearing onset (postnatal days 13–16; Fig. 4*A*,*B*). We did not observe significant changes in the peak Ca^{2+} current amplitude [413.50 ± 67.17 pA (KO) vs 504.90 ± 65.97 pA, p = 0.34, Student's t test; Fig. 4*C*,*D*] or peak Ca^{2+} current density in KO endbulbs of Held [112.00 ± 7.06 pA/pF (KO) vs 129.60 ± 13.16 pA/pF, p = 0.29, Student's t test; Fig. 4*E*]. The size of the endbulbs estimated by the C_{slow} was comparable between the genotypes [3.92 ± 0.64 pF (KO) vs 4.00 ± 0.49 pA, p = 0.65, Mann–Whitney U test; Fig. 4*F*].

Next, we investigated whether eEPSC alteration is caused by a reduction in release probability or altered vesicle pool dynamics. We used high-frequency stimulation to assess short-term plasticity, release probability as well as the size and dynamics of the readily releasable pool (RRP) during quasi physiological regimes of synaptic transmission. Fifty consecutive stimuli were delivered at 100, 200, and 333 Hz [in the presence of 1 mM kynurenic acid and 100 μM CTZ (Fig. 5); in the absence of both drugs (Fig. 6)]. Different from the prominent short-term depression typical for the endbulb of Held (Oleskevich and Walmsley, 2002; Yang and Xu-Friedman, 2008), RIM-BP2-deficient endbulb synapses showed an initial facilitation followed by slower depression (Figs. 5, 6; Table 2). Facilitation was evident from the paired pulse ratio (PPR) >1 in RIM-BP2-deficient endbulb synapses for all interstimulus intervals tested, while PPR was consistently ~0.8 in WT (100 Hz Mann–Whitney U test, 200 Hz: Mann–Whitney U test, 333 Hz: Student's t test, $p < 0.05$; Table 2). eEPSC1 and PPR were not only altered on average, but also showed greater variance. Consistent with a prior analysis of RIM-BP1/2-deficient calyx of Held (Acuna et al., 2015), the trial-to-trial coefficient of variation (c.v.) of eEPSC1 was significantly increased compared to WT [0.18 ± 0.02 (KO) vs 0.14 ± 0.01 (WT), Mann–Whitney U test p = 0.035; Fig. 5*D'*]. We also assessed the trial-to-trial variability of PPR as a proxy for P_r variability and found the c.v. also increased in the RIM-BP2-edicient endbulb synapses exposed to 100-Hz trains of stimulation [0.22 ± 0.02 (KO) vs 0.17 ± 0.02 (WT), Mann–Whitney U test p = 0.015; Fig. 5*D"*]. Interestingly, at 200 and 333 Hz stimulation, there was no significant difference in PPR c.v. (Mann–Whitney U test p = 0.8039; data not shown). In contrast to (Acuna et al., 2015), we did not find a significantly more variable EPSC rise time in the absence of RIM-BP2. The extent of depression assessed as $EPSC_{30–50}/EPSC_{max}$ (Figs. 5, 6; Table 2) tended to be less in RIM-BP2-deficient endbulb synapses without reaching statistical significance. Release probability (P_r) as well as the size and dynamics of the RRP were estimated by applying two variants of the cumulative analysis to the EPSC trains (Fig. 5): Schneggenburger–Meyer–Neher (SMN) method (Schneggenburger et al., 1999) and Elmqvist and Quastel (EQ) method (Elmqvist and Quastel, 1965; for review, see Neher, 2015). Both methods revealed a significant reduction of P_r in RIM-BP2 KO synapses while RRP size and the replenishment rate were not significantly altered (Table 2). In an attempt to address the question whether the reduced release probability reflects a smaller complement of high release probability SVs ("tightly docked" or "super-primed" SVs; Neher and Brose, 2018), we followed a previously

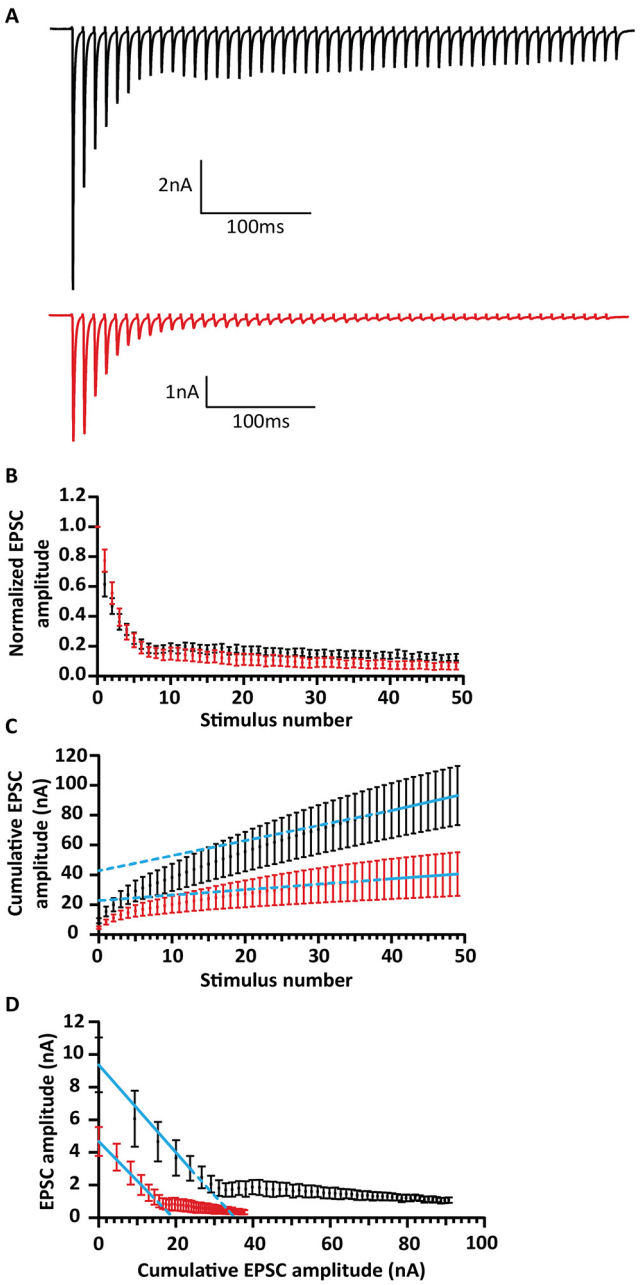

Figure 10. Analysis of release probability (P_r) as well as the size and dynamics of the RRP at 4 mM $[Ca^{2+}]_e$. ***A***, Representative traces of eEPSCs in response to trains of 50 action potentials delivered at a 100-Hz frequency, recorded from WT (top, black traces) and RIM-BP2 KO (bottom, red traces). When the mutant terminals are exposed to 4 mM $[Ca^{2+}]_e$, a WT-like depression pattern is restored. ***B***, This is even more obvious when the mean EPSC amplitudes, normalized to the first EPSC of the train are plotted against the stimulus number. ***C***, We estimate the size of the RRP, the rate of vesicle replenishment during the train and the P_r using the SMN method. ***D***, We estimate the RRP size and P_r using the EQ method. For 100 Hz: RIM-BP2 WT $N = 7$; $n = 7$, RIM-BP2 KO $N = 5$; $n = 5$. N: number of animals; n: number of BCs. Quantitative analysis is further elaborated in Table 4.

←

colocalized spots from the total number of spots per BC. The data are presented as box and whiskers plots (grand median of mean estimates for all BCs, lower/upper quartiles, 10–90th percentiles). Each data point represents the mean estimate of fluorescence intensity of all the AZs of each BC included in the analysis. Statistical significance of differences between groups was determined with unpaired Student's t test (with Welch's correction, when variances differed significantly), if the data's distribution did not differ from a normal distribution or with Mann–Whitney U test in case of non-normally distributed data. Normality of distribution was tested with Jarque–Bera test, and variances were compared with F test; $^*p \leq 0.05$, $^{**}p \leq 0.01$, $^{***}p \leq 0.001$, n.s. $p \geq 0.05$. Samples from RIM-BP2 WT and RIM-BP2 KO mice, aged p15–p21, were harvested and processed strictly in parallel, and images were acquired in parallel using the same laser power and gain settings at the same confocal microscope. Data information: N: number of animals, S: number of slices, n: number of BCs. All scale bars: 5 μm.

Table 4. Analysis of P_r as well as the size and dynamics of the RRP at 4 mM $[Ca^{2+}]_e$

Stimulation frequency	Parameter	RIM-BP2 WT	RIM-BP2 KO	*p* value
100 Hz	eEPSC1 amplitude (nA)	9.36 ± 1.67 (8.07)	4.67 ± 0.88 (4.05)	**0.035, T**
	tau (ms)	21.76 ± 3.44 (20.17)	29.19 ± 4.50 (32.89)	0.2115, T
	$eEPSC_{30–50}$	1.22 ± 0.21 (1.23)	0.41 ± 0.18 (0.46)	0.2020, M
	$eEPSC_{30–50}/EPSC_{max}$	0.14 ± 0.02 (0.13)	0.08 ± 0.03 (0.10)	0.1125, T
	Replenishment	1.91 ± 0.29 (1.96)	0.66 ± 0.26 (0.78)	**0.0116, T**
	RRP_{SMN} (SVs)	666.43 ± 219.15 (363.98)	415.15 ± 155.94 (331.33)	0.5303, M
	RRP_{EQ} (SVs)	602.61 ± 168.87 (518.41)	358.88 ± 102.66 (320.26)	0.3434, M
	$P_{r\ SMN}$	0.31 ± 0.04 (0.27)	0.26 ± 0.04 (0.22)	0.4168, T
	$P_{r\ EQ}$	0.30 ± 0.04 (0.30)	0.27 ± 0.04 (0.24)	0.6034, T
	PPR	0.62 ± 0.08 (0.63)	0.77 ± 0.07 (0.79)	0.2677, M

Tau (τ): time constant of single exponential fit to the decay of eEPSC amplitudes during the stimulation train. $eEPSC_{30–50}/EPSC_{max}$: average amplitude of the last 20 EPSCs (30–50) in the train, normalized to the amplitude of the largest EPSC of the train. Replenishment: rate of vesicle replenishment during the train. RRP: readily releasable pool. P_r: release probability. PPR: paired pulse ratio, amplitude of the second EPSC of the train normalized to the amplitude of the first EPSC. Data are presented as mean ± SEM, and medians are shown in parentheses. Normality of data distribution was tested with Jarque–Bera test, and the variances were compared with *F* test. Statistical significance of differences was assessed with unpaired Student's *t* test (shown in the table as T), when the data satisfied the criteria of normality and variance comparability. When the data did not satisfy these criteria, the Mann–Whitney *U* test was used instead (shown in the table as M); $p < 0.05$, set as threshold for statistical significance. Statistically significant differences are shown in bold.

described analysis that found a reduction of superprimed SVs on genetic deletion of all rab3 isoforms (Schlüter et al., 2006). We subtracted the quantal content of each RIM-BP2 KO response from the respective RIM-BP2 WT response during train stimulation (Fig. 5*M–O*). This analysis revealed the strongest difference between the two genotypes occurs at the beginning of the train, where the RIM-BP2 KO endbulbs release 30–40 SVs less than the RIM-BP2 WT, which is consistent with a reduction of high release probability (superprimed) SVs in the absence of RIM-BP2. The difference vanishes already after the first two eEPSCs, when the subtraction curves for 200 and 333 Hz cross the zero line, indicating that release from KO-synapses is actually slightly larger than that from WT. Possible reasons for this small difference include (1) protracted release of low release probability SVs that could result from impaired Ca_V-release site coupling and (2) residual desensitization that is more prominent for RIM-BP2 WT synapses with larger eEPSCs (despite 100 µM CTZ and 1 mM kynurenic acid). During the steady state response to the train stimulation, the WT synapses tended to release more SVs than the KO (average difference: six SVs for 100 Hz, three SVs for 200 Hz, no difference for 333 Hz). After cessation of the stimulus train, RIM-BP2 KO synapses showed enhanced asychronous release (Fig. 6*Ai* and *Aii*).

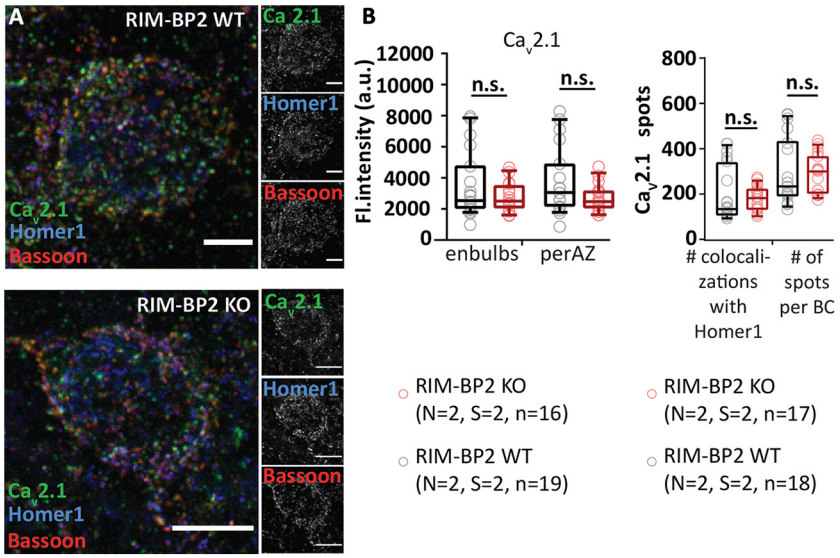

Figure 11. Unaltered $Ca_V2.1$ immunofluorescence intensity in RIM-BP2-deficient endbulbs of Held. ***A***, Maximal *z*-projections from confocal image stacks display the immunolabeling against $Ca_V2.1$, Bsn, and Homer1 at endbulb AZs in coronal brain stem slices of mouse aVCN. ***B***, No quantitative change was found in the integrated immunofluorescence (left) or number (right) of $Ca_V2.1$ puncta in either the excitatory endbulb AZs (juxtaposed to Homer1 immunofluorescence) or all AZs (endbulb + inhibitory AZ) facing BC of RIM-BP2 KOs. n.s. $p \geq 0.05$. *N*: number of animals, *S*: number of slices, *n*: number of BCs.

In order to further scrutinize RRP dynamics, we studied the recovery from short-term depression, by measuring eEPSC amplitudes elicited by single stimuli presented at varying time intervals after a conditioning 100-Hz train of 50 pulses (Fig. 7). Recovery is displayed as the eEPSC amplitudes normalized to the amplitude of the first eEPSC of the conditioning train (Fig. 7*A*, *B*): RIM-BP2-deficient endbulb synapses showed a major reduction of fast recovery. The time course was fitted with a double exponential function revealing the following tau values and fractional contributions of the fast and slow components of recovery: $\tau_1 = 123 \pm 97$ ms, $A_1 = 0.19$; $\tau_2 = 6.1 \pm 1.7$ s, $A_2 = 0.81$ for RIMBP2 KO and $\tau_1 = 96 \pm 30$ ms, $A_1 = 0.44$; $\tau_2 = 4.6 \pm 1.4$ s, $A_2 = 0.56$ for WT. (Fig. 7*C*).

Next, we evaluated the impact of the impaired synaptic transmission on processing of auditory information using juxtacellular recordings from putative spherical BCs (for simplicity referred to as "BCs") *in vivo* (Fig. 8). Glass microelectrodes were stereotactically navigated to the aVCN from an occipital craniotomy, sound stimuli were presented in the open field, and BCs identified based on electrode position, first spike latency, regularity of firing and shape of the peristimulus time histogram (see Materials and Methods). The (non-significant) trend toward lower spontaneous firing rate (Fig. 8*A*; Table 3) is consistent with the reduced spontaneous ANF input (Krinner et al., 2017) and the trend toward a lower frequency of sEPSCs in RIM-BP2 KO BCs (Fig. 3). Sound threshold and quality of frequency tuning were unaltered, whereby the RIM-BP2 KO data set contained more BCs with higher characteristic frequency (Fig. 8*B*,*C*; Table 3).

The peak firing rate at sound onset was significantly reduced in RIM-BP2 KO BCs (Fig. 8*D*, *Di*, by ~40%; Table 3) compatible with the reduced initial release probability. The adapted firing rates were not significantly reduced (Fig. 8*D*, *Dii*; Table 3), which is consistent with the better maintained EPSC amplitudes during steady

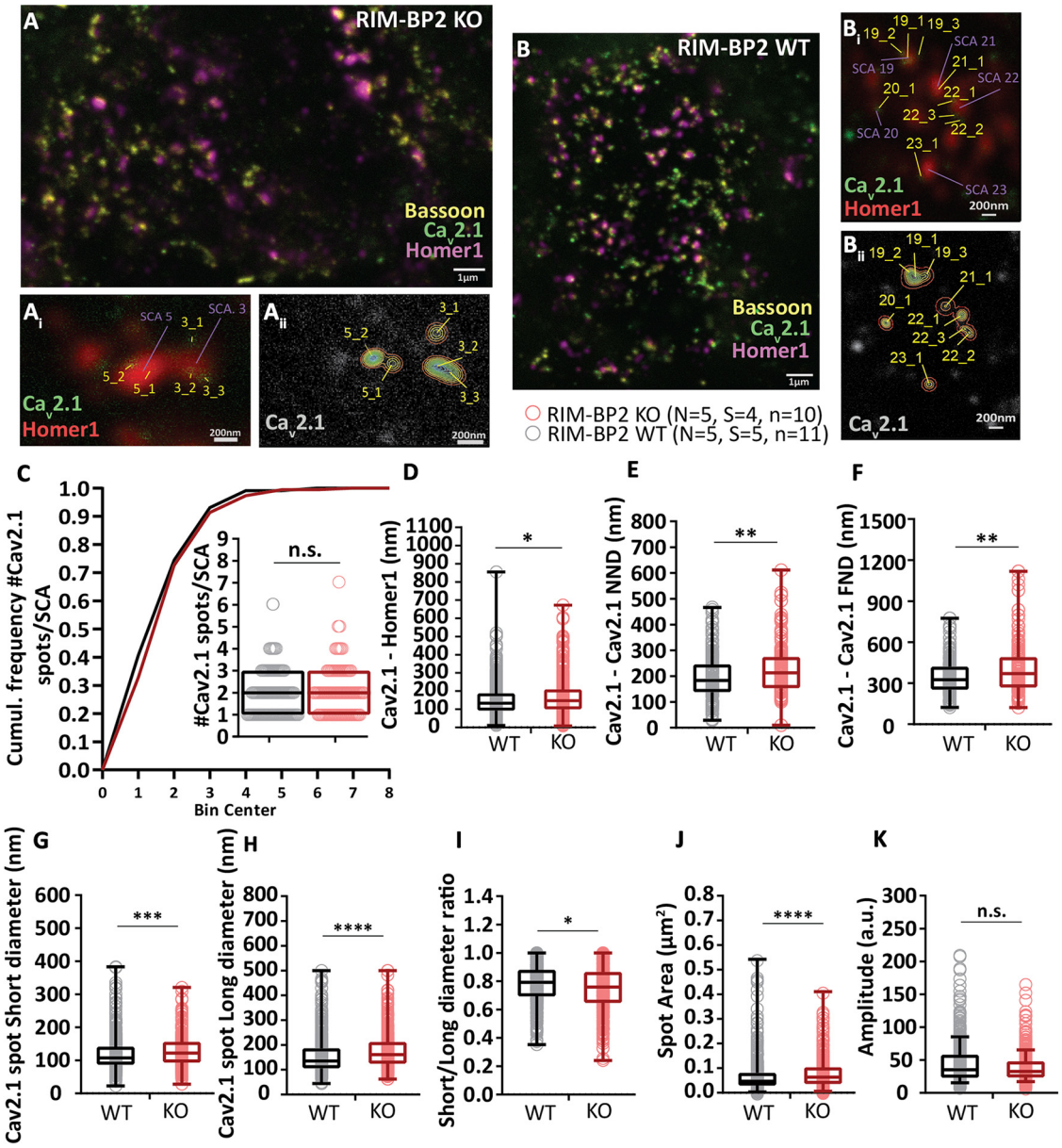

Figure 12. RIM-BP2 disruption alters the topography of Ca^{2+} channels at endbulb AZs. ***A***, ***B***, Analyzing sections from 20-µm-thick brain slices stained for $Ca_V2.1$ (STED), Bsn (STED), and Homer1 (Confocal) with STED nanoscopy, uncovered differences in the topography and dimensions of $Ca_V2.1$ clusters at AZ–to–PSD SCAs of RIM-BP2 WT (***A***, ***A$_i$***, ***A$_{ii}$***) and RIM-BP2 KO (***B***, ***B$_i$***, ***B$_{ii}$***) endbulb terminals. ***C***, The number of clusters per SCA is unchanged in the KO. In the absence of RIM-BP2, the $Ca_V2.1$ puncta (yellow tags ***A$_i$***, ***A$_{ii}$***, ***B$_i$***, ***B$_{ii}$***) are located further from the center of the SCA (***D***), defined as the center of the Homer1 puncta (violet tags ***A$_i$***, ***B$_i$***). The clusters are also located further apart from each other, shown by increased NND (***E***) and FND (***F***) within SCAs. ***G***, ***H***, ***J***, 2D–Gaussian fitting yielded the short and long cluster diameters at half maximum. ***I***, The deletion of RIM-BP2 leads to larger and more elongated $Ca_V2.1$ puncta at the endbulb of Held AZs. ***K***, The amplitude of fluorescence at the center of $Ca_V2.1$ puncta does not differ significantly between RIM-BP2 WT and RIM-BP2 KO AZs. A semiquantitative assessment of $Ca_V2.1$ abundance in endbulb is depicted in Figure 11. The lack of RIM-BP2 also affects the precise localization of the presynaptic protein bassoon. A similar STED–2D Gaussian fitting analysis was employed to dissect the effect on bassoon and the results are summarized in Figure 13. Finally, a comparison of the NND between bassoon and $Ca_V2.1$ puncta within SCAs is depicted in Figure 14. Statistical significance between groups was tested with Mann–Whitney *U* test for non-normally distributed data or with Student's *t* test;for normally distributed data with equal variance. $^{****}p < 0.0001$, $^{***}p < 0.001$, $^{**}p < 0.01$, $^{*}p < 0.05$. *N*: number of animals, *S*: number of slices, *n*: number of BCs. The effect sizes and statistics of the performed comparisons are summarized in Table 5.

state response to train stimulation in BCs (RIM-BP2 WT: 1.2 ± 0.2 nA, RIM-BP2 KO: 0.9 ± 0.1 nA; Fig. 5*A–F*; Table 2) and the normal adapted firing rate of ANFs (Krinner et al., 2017).

In addition, we found the temporal jitter of the first spike after stimulus onset to be greater in RIM-BP2 KO BCs, while the first spike latency was comparable between the two genotypes (Fig. 8*E*; Table 3). The stronger reduction of the peak rate and increased first spike latency jitter of BCs in comparison to ANF likely reflects the impaired transmission at the RIM-BP2-deficient endbulb, which degrades information processing in the lower auditory pathway beyond what is caused by the mildly affected synaptic sound encoding in the cochlea. This hypothesis is further supported by the auditory brainstem responses of RIM-BP2 KO mice, which show a more pronounced amplitude decline for the aVCN related Wave III than for the auditory nerve related Wave I (Krinner et al., 2017). In conclusion, the reduced release probability of the endbulbs impairs the transmission of sound onset information, which is likely to hamper hearing and auditory tasks such as gap detection and sound localization in particular.

Table 5. Altered $Ca_V2.1$ shape properties and spatial distribution in endbulb SCAs

	RIM-BP WT VGCCs	RIM-BP KO VGCCs	*p* value
Amplitude	44.77 ± 1.54 (35.14)	38.55 ± 1.16 (32.55)	n.s. 0.1061, M
Short diameter	120.39 ± 2.47 nm (106.98)	127.6 ± 2.39 nm (121.98)	*****0.0005, M**
Long diameter	158.97 ± 3.58 nm (135.58)	178.72 ± 3.91 nm (160.98)	******<0.0001, M**
Area (μm^2)	0.071 ± 0.004 μm^2 (0.047)	0.079 ± 0.003 μm^2 (0.064)	******<0.0001, M**
Ratio	0.78 ± 0.007 (0.79)	0.74 ± 0.008 (0.76)	****0.0019, M**
Distance from left (nm)	151.47 ± 4.3 nm (133.12)	167.84 ± 5.45 nm (146.71)	***0.0399, M**
NND (nm)	196.25 ± 6.3 nm (183.78)	227.6 ± 7.58 nm (212.72)	****0.0032, M**
FND (nm)	347 ± 9.4 nm (325.27)	411.43 ± 14.87 nm (370.03)	****0.0037, M**

Data are presented as mean ± SEM (median). Statistical significance of differences was assessed with unpaired Student's *t* test (shown in the table as T), when the data satisfied the criteria of normality and variance comparability. When the data did not satisfy these criteria, the Mann–Whitney *U* test was used instead (shown in the table as M); $p < 0.05$, set as threshold for statistical significance. Statistically significant differences are shown in bold; ****$p < 0.0001$, ***$p < 0.001$, **$p < 0.01$, *$p < 0.05$.

RIM-BP2 disruption appears not to alter the molecular composition of the endbulb AZs

Given the scope of protein interactions of RIM-BP that includes Ca^{2+} channels, large conductance Ca^{2+} activated K^+ channels (Sclip et al., 2018) and multidomain proteins of the AZ, we considered the possibility that some of the above described physiological alterations might reflect changes in the abundance of other AZ proteins. In order to test for potential effects of RIM-BP2 disruption on the molecular composition of the AZs, we performed semi-quantitative, confocal immunofluorescence microscopy in coronal brain slices. RIM-BP2 WT and RIM-BP2 KO samples were harvested and processed strictly in parallel. Likewise, images were acquired using the same laser power and gain settings at the same confocal microscope. Excitatory AZs facing the postsynaptic BC were identified by co-localization of immunofluorescence of the targeted AZ protein with the immunofluorescence of the vesicular glutamate transporter VGlut1 or a juxtaposition to the immunofluorescence of Homer 1, a scaffold of excitatory synapses and a lack of juxtaposition to immunofluorescence of Gephyrin, a scaffold of inhibitory synapses (Fig. 9). We focused our analysis on the spherical or ovoid BC soma which are engaged by a corona of synapses. Staining for RIM-BP2 showed the expected corona of immunofluorescence spots in WT slices, but no obvious synaptic immunofluorescence in RIM-BP2 KO slices (Fig. 9*A*,*B*, left: integrated fluorescence within the Vglut1-positive volume, endbulbs: $p = 0.0008$, inhibitory synapses: $p = 0.0002$, right: lack of RIM-BP2 spots in the KO $p < 0.0001$, Student's *t* test). We did not observe significant differences in the integrated immunofluorescence or the number of puncta of Munc13-1 (Fig. 9*C*,*D*), RIM2 (Fig. 9*E*,*F*), CAST (Fig. 9*G*,*H*), and Bsn (Fig. 9*I*,*J*) in RIM-BP2 KO slices ($p \geq 0.05$), suggesting an unaltered abundance of these multidomain proteins at the excitatory AZs facing the BC in the absence of RIM-BP2.

Increased Ca^{2+} influx improves release probability but unmasks impaired SV replenishment during train stimulation

Unaltered Ca^{2+} influx and RRP size but reduced P_r led us to focus the analysis on the coupling of Ca^{2+} channels to SV release. As a first approach we increased the presynaptic Ca^{2+} influx by elevating the extracellular Ca^{2+} concentration $[Ca^{2+}]_e$ from physiological (2 mM) to 4 mM. This manipulation abolished the differences in P_r (both time course of depression and PPR were WT-like; Fig. 10; Table 4). This is consistent with a greater diffusional distance between Ca^{2+} channels and SV release sites that can be overcome when more Ca^{2+} enters per channel opening. Alternatively, or in addition, greater Ca^{2+} influx might foster Ca^{2+}-dependent priming or facilitation of release. Finally, increased Ca^{2+} influx unmasked a slowed SV replenishment during train stimulation in RIM-BP2-deficient endbulbs (Fig. 10; Table 4).

RIM-BP2 disruption alters the topography of Ca^{2+} channels at endbulb AZs

In order to probe for potential morphologic correlates of altered release probability we employed immunofluorescence microscopy and electron microscopy of immunolabeled Ca^{2+} channels. First, we performed a strictly parallel study of $Ca_V2.1$ distribution at excitatory synapses around the BCs of RIM-BP2 KO and WT mice using confocal microscopy (as described above; Fig. 11*A*,*B*) as well as STED nanoscopy (Fig. 12*A*-*K*). We used Bsn and Homer1 as context markers to analyze the presynaptic $Ca_V2.1$ immunofluorescence intensity at endbulbs and at all BC facing AZs, including inhibitory ones. The integrated fluorescence intensity was comparable at both endbulbs ($p = 0.65$, Mann–Whitney *U* test; Fig. 11*B*), and at all BC facing AZs ($p = 0.11$, Student's *t* test; Fig. 11*B*). The number of $Ca_V2.1$ spots neighboring Homer1 appositions ($p = 0.60$, Student's *t* test; Fig. 11*B*) and total number of spots facing BC ($p = 0.87$, Student's *t* test; Fig. 11*B*) were unaltered at the confocal level, which is consistent with finding normal presynaptic Ca^{2+} influx (Fig. 4).

For our two-color STED analysis, we focused on AZ/PSD appositions ($Ca_V2.1$/Homer1, Bsn/Homer1) of endbulbs of Held. We interpret the $Ca_V2.1$ and Bsn puncta discerned by STED to represent individual AZs. As the PSD was studied at confocal resolution, we assume the larger Homer1-spots represent a merger of several small PSDs. We operationally defined the organization of several $Ca_V2.1$ or Bsn puncta around a single Homer1 spot a synaptic contact assembly (SCA) whereby its center corresponds to the center of the Homer1 punctum. The number of $Ca_V2.1$ puncta per SCA was comparable between RIM-BP2 WT and KO endbulbs (Fig. 12*C*). However, the Cav2.1 puncta were located further from the center of the SCA (Fig. 12*D*). The distance between $Ca_V2.1$ puncta was increased as assessed by NND and furthest neighbor distance (FND) in the SCA (Fig. 12*E*,*F*; Table 5). 2D Gaussian fitting of the $Ca_V2.1$ puncta showed that the KO puncta are wider and longer but also more round-shaped than WT (Fig. 12*G*–*J*), while the fluorescence amplitude at the center of the fitted $Ca_V2.1$ puncta was comparable between WT and KO (Fig. 12*K*). Similar findings were made for Bsn when comparing WT and KO SCAs (Fig. 13). Notably, the distance from the SCA center was increased from 138.5 ± 4.6 nm to 160.9 ± 5.7 nm in the KO ($p = 0.0074$, Mann–Whitney *U* test; Fig. 13*D*). The NND between Bsn puncta was not significantly increased in the absence of RIM-

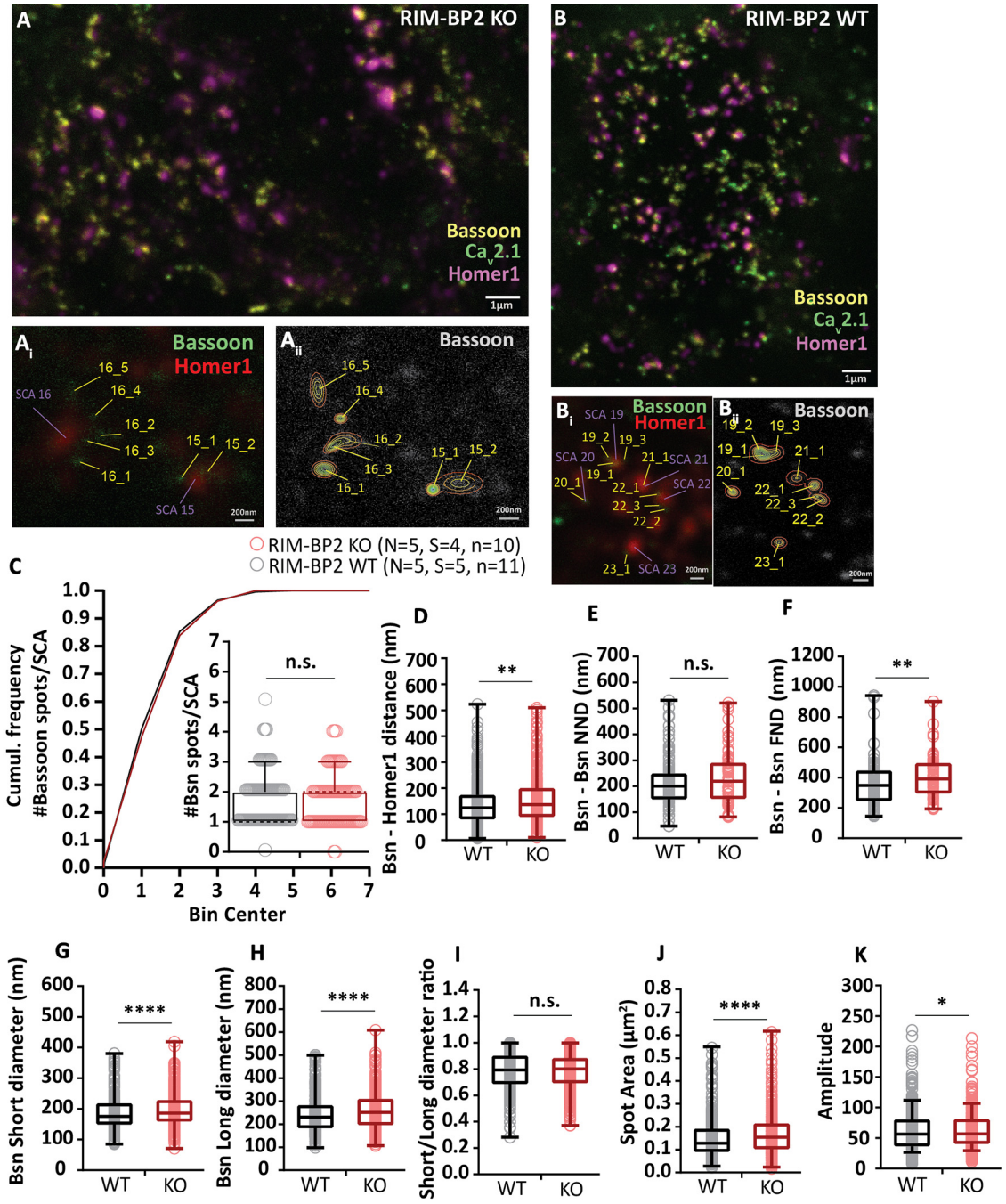

Figure 13. RIM-BP2 disruption alters distribution and extent of Bsn clusters marking the presynaptic density of endbulb AZs. Analyzing sections (***A***, ***B***) from 20-µm-thick brain slices stained for $Ca_V2.1$ (STED), Bsn (STED), and Homer1 (confocal) with STED nanoscopy, uncovered differences in the amplitude of fluorescence, topography, and dimensions of Bsn-positive puncta in the absence of RIM-BP2. The Bsn puncta were detected and fitted with 2D–Gaussian functions at AZ–to–PSD SCAs of RIM-BP2 WT (***A***, ***A$_i$***, ***A$_{ii}$***) and RIM-BP2 KO (***B***, ***B$_i$***, ***B$_{ii}$***) endbulb terminals. The number of puncta per SCA is unchanged in the KO (***C***). In the absence of RIM-BP2, the Bsn puncta (yellow tags ***A$_i$***, ***A$_{ii}$***, ***B$_i$***, ***B$_{ii}$***) are located further from the center of the SCA (***D***), defined as the center of the postsynaptic Homer1 puncta (violet tags ***A$_i$***, ***B$_i$***). We found no significant difference in the NND (***E***). FND (***F***) was significantly increased in the mutant. Comparing the short and long puncta diameters at half maxima shows that the deletion of RIM-BP2 leads to proportionally (no change in short/long diameter ratio, ***I***) larger (***G***, ***H***, ***J***) Bsn puncta at endbulb of Held AZs. The amplitude of fluorescence at the center of Bsn puncta is significantly increased RIM-BP2 KO AZs (***K***). Normality was tested with Jarque–Bera test. Statistical significance between groups was tested with Mann–Whitney *U* test for non-normally distributed data and with Student's *t* test for normally distributed data with equal variance. $^{****}p < 0.0001$, $^{***}p < 0.001$, $^{**}p < 0.01$, $^{*}p < 0.05$. *N*: number of animals, *S*: number of slices, *n*: number of BCs.

BP2 ($p = 0.156$, Mann–Whitney *U* test; Fig. 13*E*), but the FND was altered from 357.5 ± 13.3 nm in WT to 408 ± 15.2 nm in the KO ($p = 0.0042$, Mann–Whitney *U* test; Fig. 13*F*). The Bsn puncta short diameter was increased from 181.7 ± 2.7 nm in the WT to 197.8 ± 3.1 nm in the KO ($p < 0.0001$, Mann–Whitney *U* test; Fig. 13*G*), while the long diameter changed from an average of 239.4 ± 4.3 nm in WT to 261.2 ± 4.6 nm in the KO ($p < 0.0001$, Mann–Whitney *U* test; Fig. 13*H*).In contrast to our $Ca_V2.1$ findings, the lack of RIM-BP2 did not affect the Bsn puncta short/long diameter ratio ($p = 0.6043$, Mann–Whitney *U* test; Fig. 13*I*), while the amplitude of Bsn fluorescence was slightly increased in AZs of RIM-BP2

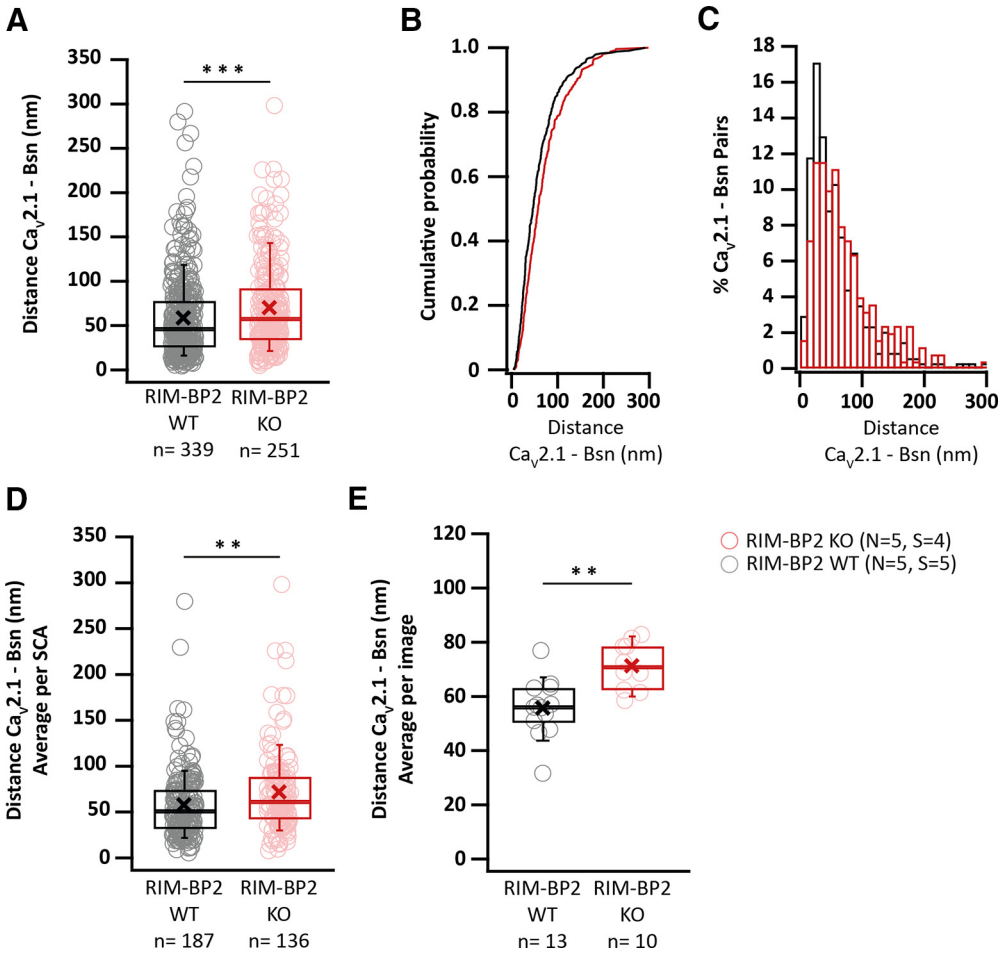

Figure 14. Increased NND between $Ca_V2.1$ and Bsn puncta. ***A***, $Ca_V2.1$–Bsn, defined at the distance cutoff of 300 nm, show significantly higher NND in the absence of RIM-BP2 compared to WT (WT pairs: $n = 339$, KO pairs: $n = 251$). Cumulative probability (***B***) and histogram (***C***) representations of the NND estimates for $Ca_V2.1$–Bsn pairs show that RIM-BP2 KO pairs are less likely to have small NND values compared to WT and more RIM-BP2 KO pairs occupy the higher NND bins. ***D***, The increase in NND is robust and remains statistically significant when averaging the NNDs per-SCA (WT SCAs: $n = 187$, KO SCAs: $n = 136$) and (***E***) also when averaging the NNDs per image taken typically including the SCAs of one BC (WT images: $n = 13$, KO images: $n = 10$) Non-normally distributed data are presented as box and whisker plots with grand median of all BC means (***A***), all SCA means (***D***), and all image means (***E***). Lower/upper quartiles represent the 25/75th percentiles, while the X represents the grand mean (***A***, ***C***, ***D***); n.s. $p \geq 0.05$; *$p \leq 0.05$, **$p \leq 0.01$, ***$p \leq 0.001$, Mann–Whitney *U* test). *N*: number of animals, *S*: number of imaged slides, *n*: number of pairs (***A***), number of SCAs (***D***), number of images (***E***).

lacking endbulbs [63.9 ± 1.9 (KO) vs 60.3 ± 1.9 (WT), Mann–Whitney *U* test $p = 0.0363$; Fig. 13*K*]. The area of Bsn puncta was increased on average from 0.15 ± 0.005 to 0.17 ± 0.006 μm^2 ($p < 0.0001$, Mann–Whitney *U* test; Fig. 13*J*) in the absence of RIM-BP2.

We then assessed the NND between $Ca_V2.1$ and Bsn puncta. To calculate the NND we used the x, y coordinates of each punctum's center, yielded from the 2D Gaussian fitting that was applied to analyze the punctum's shape as mentioned above. To define a $Ca_V2.1$–Bsn pair, we set a distance cutoff at 300 nm, since <3% of all pairs had NNDs higher than 300 nm. By averaging over all the $Ca_V2.1$–Bsn pairs, we found an NND of 58.93 ± 2.6 nm (mean ± *SEM*, $n = 339$) for WT and a significantly higher NND of 70.3 ± 3.1 nm (mean ± SEM, $n = 251$, $p = 0.0006$) in the absence of RIM-BP2 (Fig. 14*A*). $Ca_V2.1$–Bsn pairs of RIM-BP2-deficient SCAs were found less frequently than WT ones in the small NND bins, while being more abundant than WT in the higher NND bins (Fig. 14*B*,*C*). The significant increase in NND was robust and persisted when averaging NNDs per SCA (WT mean NND ± SEM = 57.9 ± 2.7 nm, $n = 187$, KO mean NND ± SEM = 71.9 ± 4.5 nm, $n = 136$, $p = 0.00134$; Fig. 14*D*) or per image taken (WT mean NND ± SEM = 55.7 ± 2.9 nm, $n = 13$, KO mean NND ± SEM = 71.3 ± 2.8 nm, $p = 0.00101$; Fig. 14*E*). We also assessed the potential contribution of unspecific labeling for $Ca_V2.1$ and Bsn in shaping this effect. To that end we defined orphaned $Ca_V2.1$ and Bsn puncta in each SCA, as those that were not found in the proximity of Bsn and $Ca_V2.1$, respectively, and quantified their abundance per SCA. We found no significant differences in the amount of orphaned $Ca_V2.1$ or Bsn puncta between WT and RIM-BP2 KO SCAs (data not shown).

We then turned to immunolabeling of $Ca_V2.1$ in SDS-treated freeze-fracture replica (SDS-FRIL; Nakamura et al., 2015). To image the endbulbs onto the BCs, we focused on the BC rich rostral-most aVCN sections of the brainstem. Endbulb terminals were prominently distinguishable in our replicas by their large size synapsing on to the BC soma (Fig. 15*A*). We also validated that we were imaging the correct area and cell type, by analyzing the intramembrane particle (IMP) clusters representing PSDs on the exoplasmic face (E-face) of the BC soma (Fig. 15*C*–*F*). Our estimates of PSD areas (Fig. 15*B*; Table 6) were comparable to the ones previously reported for ANF-BC synapses (Rubio et al., 2017). We then assessed the protoplasmic face (P-face) of the replicas for the analysis of AZ proteins and $Ca_V2.1$ channel

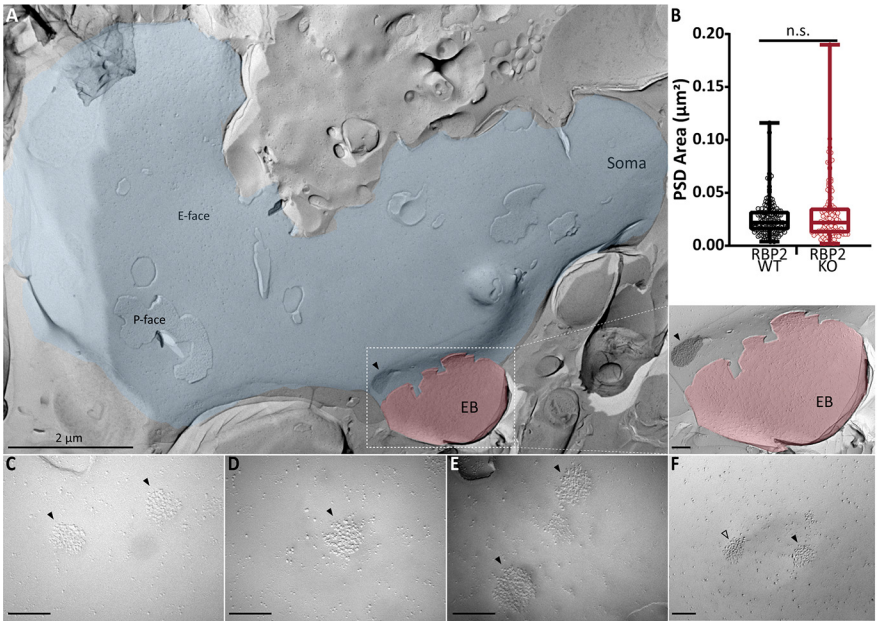

Figure 15. Identification of endbulb of Held synapses. ***A***, SDS-FRIL electron micrograph at low magnification (9700×) showing E-face of a BC soma (blue) with patches of P-face, contacted by an endbulb (red). IMP-cluster representing the PSD of auditory nerve fiber on the BC soma highlighted in black with a solid black arrowhead. Inset shows the magnified (97,000×) view of the endbulb synapse on to the BC with a PSD IMP-cluster. ***B***, Comparable PSD areas at endbulbs of Held in RIM-BP2 WT and KO. ***C–F***, High-magnification (***C–E***, 93,000×; ***F***, 97,000×) images of IMP-clusters of BC soma facing the endbulb. PSD IMP-clusters indicated by solid black arrowheads. Open black arrowhead in ***F*** marks the PSD IMP-cluster that lies on the curvature of the synaptic cleft depression and hence was not included in the analysis. All unmarked scale bars are 200 nm. For details about PSD values, sample size, and statistics, see Table 6.

distribution (Fig. 16). AZs were located by simultaneous immunolabeling of three characteristic AZ proteins: RIM, neurexin, and ELKS with 5-nm gold particles. The number of AZ particles was less than that previously observed in other types of synapses (Miki et al., 2017) which might reflect lower expression of ELKS in the endbulb synapses. Since the samples from both genotypes were handled simultaneously by the same experimenter, the comparison between the genotypes remains valid. Nonetheless, given the low labeling efficiency for AZ proteins, we used AZ markers primarily to identify the location of AZs. AZ area was characterized by IMPs of distinct shape, number and size compared to those in surrounding areas, and demarcated manually by connecting the outermost IMPs (Fig. 16*B*,*C*). The estimated AZ area was comparable between RIM-BP2 KO and WT (Fig. 16*D*). When analyzing the distribution of $Ca_V2.1$ channels labeled with 10-nm gold particles within the AZ area, both the number and density of $Ca_V2.1$ particles were significantly reduced in the RIM-BP2 KO (Fig. 16*G*,*H*; Table 6).

A low labeling efficiency for AZ proteins would overestimate the AZ to AZ and $Ca_V2.1$ to AZ particles NNDs. Hence, we only compared the NND for $Ca_V2.1$ to $Ca_V2.1$ and AZ to $Ca_V2.1$ particles. The value of mean ± 2 SD s of the Gaussian fit to the distribution of $Ca_V2.1$ to $Ca_V2.1$ NNDs was considered the threshold for the maximum distance by which two particles can be separated and still belong to the same cluster (Fig. 16*A-C*; see Materials and Methods): mean ± 2 SD were 43.09 and 43.92 nm for WT and RIM-BP2 KO, respectively. The threshold used for defining a cluster in our analysis was 40 nm as used in previous analysis (Miki et al., 2017). In many KO AZ images, there were not even the minimum required three $Ca_V2.1$ gold particles to qualify as a cluster (Fig. 16*C*). Within the qualified clusters, we still found a

Table 6. Quantitative analysis SDS-FRIL electron micrographs

Au particles		Parameter	RIM-BP2 WT	RIM-BP2 KO	*p* value
		# of animals	3	3	-
		# of replicas	6	5	-
		# of images	437	196	-
		# of PSD	136	102	-
		AZ area (μm^2)	0.040 ± 0.001 (0.036)	0.041 ± 0.002 (0.034)	0.75, M
		PSD area (μm^2)	0.026 ± 0.002 (0.022)	0.030 ± 0.003 (0.022)	0.89, M
AZ (5 nm)		# of particles/AZ area	2.74 ± 0.14 (2.00)	1.34 ± 0.12 (1)	**<0.0001, M**
		Density (#/μm^2)	76.65 ± 4.72 (54.13)	47.91 ± 6.21 (21.41)	**<0.0001, M**
$Ca_V2.1$ (10 nm)		# of particles/AZ area	6.30 ± 0.22 (5.00)	3.31 ± 0.23 (3.00)	**<0.0001, M**
		Density (#/μm^2)	181.10 ± 5.93 (151.30)	96.88 ± 6.19 (73.72)	**<0.0001, M**
$Ca_V2.1$ (10 nm)		# of clusters	342	74	-
		# of particles/cluster	4.36 ± 0.13 (4.00)	3.80 ± 0.16 (3.00)	**0.0011, M**
		Area of cluster (nm^2)	976.25 ± 88.99 (590.90)	659.50 ± 95.37 (418.3)	**0.013, M**
			NND analysis		
			95% CI	Model comparison (vs null model)	
		Mean ± SEM	Lower–higher	BF (full/null)	ΔWAIC (null–full)
$Ca_V2.1$–$Ca_V2.1$	WT	37.8 ± 1.52	33.4–43.8	0.458	−0.2
	KO	47 ± 2.43	40.2–54.6		
AZ–$Ca_V2.1$	WT	62.8 ± 7.67	44.6–89.7	0.083	−0.4
	KO	77.4 ± 11.05	51.8–111.3		

Data are presented as mean ± SEM with median in parentheses (except for the NND analysis). Data were distributed non-normally as determined by Kolmogorov–Smirnov test. Statistical significance of the comparison between RIM-BP2 WT, and KO was determined by Mann–Whitney *U* test (denoted in the table as M). $p < 0.05$ set as threshold for statistical significance. Statistically significant differences shown in bold.

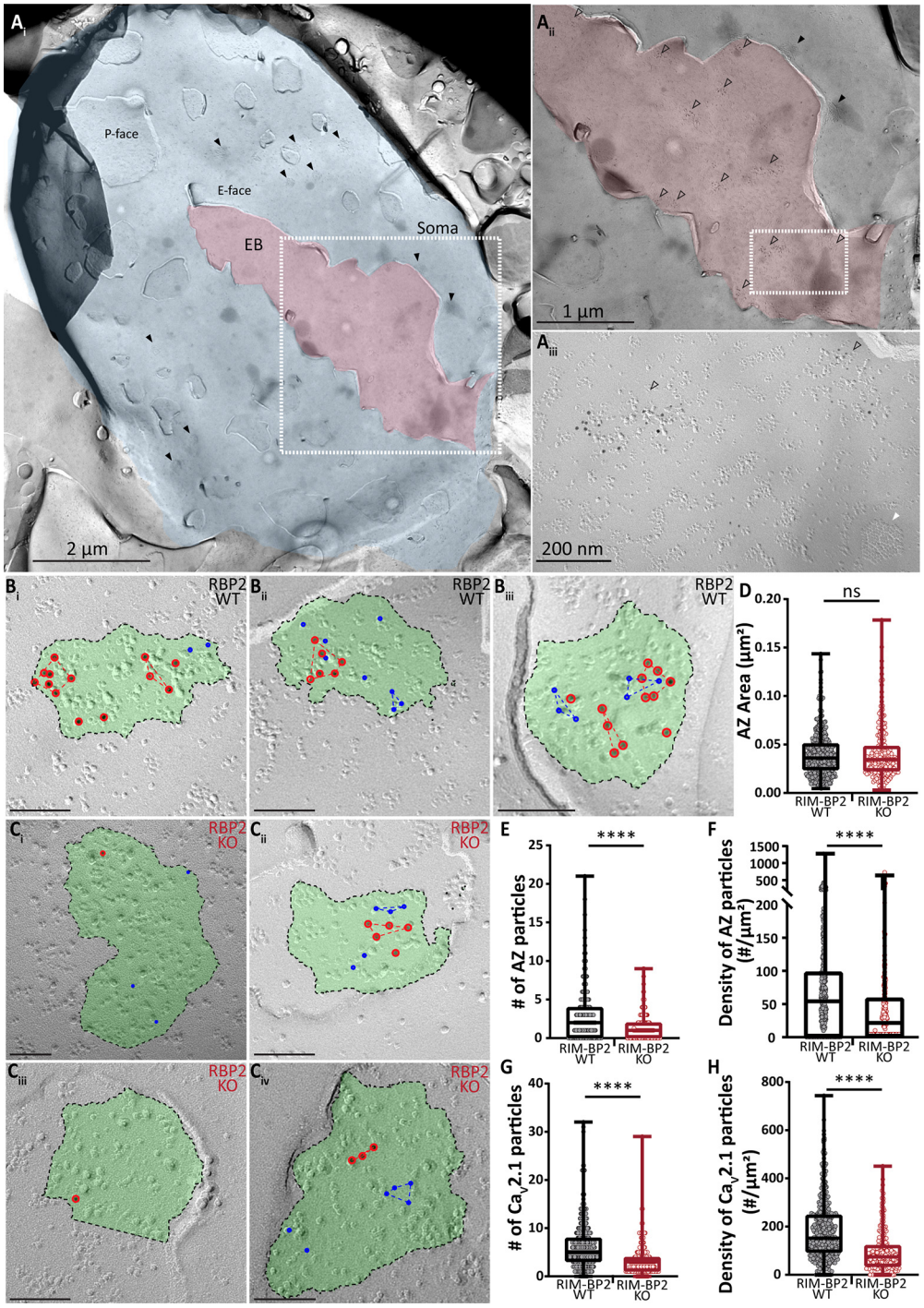

Figure 16. Similar AZ size but reduced number of AZ and $Ca_V2.1$ labels in endbulbs of RIM-BP2 KO. ***A***, SDS-FRIL electron micrograph at low magnification (9700×) showing E-face of a BC soma (blue) with patches of P-face, connected to an endbulb (red). ***Ai***, Some of the IMP-clusters representing the PSDs of ANF on the BC soma highlighted by solid black arrowheads. ***Aii***, Magnified (18,500×) view of the box in ***Ai*** of endbulb synapse (red) on to the BC soma (blue) with IMP-clusters for AZ and PSD indicated by open and solid black arrows, respectively. ***Aiii***, Magnified (97,000×) view of the box in ***Aii*** with IMP-clusters for AZ indicated by open arrows and P-face of a gap junction indicated by a solid white arrow. ***B***, ***C***, FRIL images showing endbulb AZs (green) in RIM-BP2 WT (***B***) and KO (***C***), immunolabelled for AZ molecules (RIM, neurexin, ELKS) and $Ca_V2.1$ channels with 5-nm (blue circles) and 10-nm (red circles) gold particles, respectively. ***D–H***, Quantitative analysis of AZ area (***D***), number of AZ (***E***), and $Ca_V2.1$ (***G***) gold particles, and density of AZ (***F***) and $Ca_V2.1$ (***H***) gold particles. All unlabeled scale bars are 100 nm. ns: not significant, $^{****}p < 0.0001$. For details about mean ± SEM, median, sample size, and statistics, see Table 6.

significantly reduced number of $Ca_V2.1$ particles per cluster in the RIM-BP2 KO (Table 6) which is consistent with a more dispersed $Ca_V2.1$ topography at the AZ as indicated in the STED analysis. Since there were no significant differences between the animals within the groups (RIM-BP2 WT and RIM-BP2 KO; data not shown), data across animals of one genotype were pooled to represent that genotype group. To confirm that the clusters obtained in our analysis were valid and not reflecting chance occurrence, we compared our real data to 500 random simulations of cluster arrangements (see Materials and Methods; Luján et al., 2018; Kleindienst et al., 2020). Table 7 confirms the validity of AZ and $Ca_V2.1$ clusters. We then used hierarchical

Table 7. Comparison of real and simulated distribution of gold particles

		Cluster analysis			
Genotype	Au particles	Parameter	Real data	Simulated data	*p* value
RIM-BP2 WT	AZ (5 nm)	# of clusters/AZ	0.29 ± 0.03	0.14 ± 0.01	**3.68e-16**
		# of particles/cluster	3.99 ± 0.15	3.50 ± 0.09	**8.57e-08**
		Area of cluster (nm^2)	663.30 ± 80.9	503.78 ± 45.30	**0.007**
	$Ca_V2.1$ (10 nm)	# of clusters/AZ	0.78 ± 0.04	0.48 ± 0.03	**6.44e-29**
		# of particles/cluster	4.36 ± 0.13	3.79 ± 0.08	**5.72e-13**
		Area of cluster (nm^2)	976.25 ± 88.99	695.77 ± 55.90	**2.26e-08**
RIM-BP2 KO	AZ (5 nm)	# of clusters/AZ	0.08 ± 0.02	0.05 ± 0.01	**0.015**
		# of particles/cluster	4.33 ± 0.43	3.71 ± 0.33	**0.006**
		Area of cluster (nm^2)	759.82 ± 186.11	542.89 ± 125.05	0.09
	$Ca_V2.1$ (10 nm)	# of clusters/AZ	0.38 ± 0.04	0.15 ± 0.02	**6.13 e-13**
		# of particles/cluster	3.80 ± 0.16	3.35 ± 0.06	**0.0003**
		Area of cluster (nm^2)	659.50 ± 95.37	438.90 ± 29.90	**0.005**

Data are presented as mean ± SEM. Real data were compared to 500 random simulations to confirm that the observed clusters are significantly different from chance (random) occurrence. Student's *t* test was used to determine the statistical significance. $p < 0.05$ set as threshold for statistical significance. Statistically significant differences shown in bold.

Table 8. Quantitative analysis of electron tomograms

Parameter		RIM-BP2 WT	RIM-BP2 KO	*p* value
AZ area (μm^2)		0.0820 ± 0.0052 (0.0809)	0.1031 ± 0.0039 (0.0981)	**0.0022, T**
No. of SVs		49.81 ± 4.49 (46.50)	51.57 ± 4.63 (41.00)	0.79, T
Number of SVs per μm^2 AZ	All SVs	662.3 ± 77.4 (543.1)	523.7 ± 53.4 (443.2)	0.14, W
	Docked SVs	27.52 ± 5.24 (18.58)	14.64 ± 4.77 (1.72)	**0.015, W**
	2–20 nm	109.1 ± 12.8 (98.4)	68.16 ± 9.22 (59.32)	**0.006, W**
	20–40 nm	58.59 ± 7.14 (45.26)	49.68 ± 5.40 (45.20)	0.61, W
	40–60 nm	83.25 ± 8.23 (82.21)	53.59 ± 5.36 (53.69)	**0.004, W**
	60–80 nm	79.81 ± 10.62 (64.31)	55.80 ± 6.26 (48.54)	0.09, W
	80–100 nm	70.43 ± 10.52 (54.67)	59.51 ± 7.92 (43.09)	0.39, W
	100–120 nm	61.41 ± 11.08 (43.38)	51.56 ± 9.16 (36.31)	0.51, W
	120–140 nm	50.51 ± 10.47 (41.23)	48.79 ± 7.41 (41.68)	0.64, W
	140–160 nm	55.12 ± 11.25 (42.14)	47.62 ± 6.21 (38.58)	0.82, W
	160–180 nm	37.59 ± 7.70 (25.56)	40.12 ± 8.33 (27.80)	0.92, W
	180–200 nm	29.68 ± 8.40 (15.05)	33.26 ± 4.97 (31.13)	0.20, W
Diameter (nm)	All SVs	50.99 ± 0.59 (51.68)	52.14 ± 0.68 (52.44)	0.73, T

Data are presented as mean ± SEM, and medians are shown in parentheses. Normal distribution was assessed with the Jarque–Bera test, and equality of variances was assessed with the *F* test in normally distributed data. Statistical significance of normally distributed data was determined by unpaired Student's *t* test (denoted as T), while that of the non-normally distributed data was determined by the Wilcoxon rank test (denoted as W). $p < 0.05$ set as threshold for statistical significance. Statistically significant differences shown in bold.

Bayesian modeling of the data to test for differences between the $Ca_V2.1$ to $Ca_V2.1$ NNDs and AZ to $Ca_V2.1$ NNDs of RIM-BP2 WT and RIM-BP2 KO, respectively (Fig. 17). In our limited data sample of AZs from three mice each, we did not observe statistically significant differences for either $Ca_V2.1$ to $Ca_V2.1$ NNDs (Bayes factor K: 0.46 and Watanabe–Akaike Information Criterion: −0.2; Table 6) or AZ to $Ca_V2.1$ NNDs (Bayes factor K: 0.08 and Watanabe–Akaike Information Criterion: −0.4; Table 6). In summary, the major findings of our FRIL analysis are the significantly lower number and density of $Ca_V2.1$ channels.

RIM-BP2 disruption alters the SV organization at the endbulb AZs

Next, we high-pressure froze aVCNs slices, acutely prepared as for physiology to best relate structure and function, for electron tomography analysis of SV organization at the endbulb AZ. Following freeze-substitution, embedding, sectioning and tomography, we rigorously analyzed and reconstructed AZ of RIM-BP2-deficient and WT endbulb synapses (Fig. 18). The AZ area, approximated from the extent of the postsynaptic density, was significantly larger in RIM-BP2-deficient endbulbs (Fig. 18*C*; Table 8, $p < 0.01$, Student's *t* test). The number (Fig. 18*D*) and density (Fig. 18*E*) of SVs per AZ were not altered. For a more comprehensive analysis we compared the SV distribution within 200 nm of the presynaptic AZ membrane (perpendicular to the presynaptic membrane into the cytosol of the presynaptic terminal) in 20-nm bins. Morphologically docked SVs (0- to 2-nm distance), analyzed separately, were significantly fewer in number at RIM-BP2 KO AZs. Significantly fewer SVs were also found for non-docked membrane proximal SVs (2–20 nm) and SVs within 40–60 nm from the AZ membrane (Fig. 18*F*, $p < 0.01$, Wilcoxon rank test; Table 8). We also analyzed top views of the AZs showing only the docked SVs in the models generated from the tomograms and quantified the percentage of AZs with zero to eight docked SVs. We found that 50% of the analyzed RIM-BP2 KO AZs showed zero docked SVs, while two docked SVs per AZ were most frequently encountered in WT (27% of the AZs; Fig. 18*G*). We further tested for effects of RIM-BP2 disruption on the lateral distribution of the docked SVs by setting a central point within the generated top views and quantifying the distances of all docked SVs from the center (we note that the AZ area captured in the tomograms might not necessarily allow proper definition of the AZ center). The docked SVs appeared to be further away from the center in RIM-BP2 KO synapses, possibly representing a broader distribution over the whole AZs area (Fig. 18*J*). To analyze the membrane proximal,

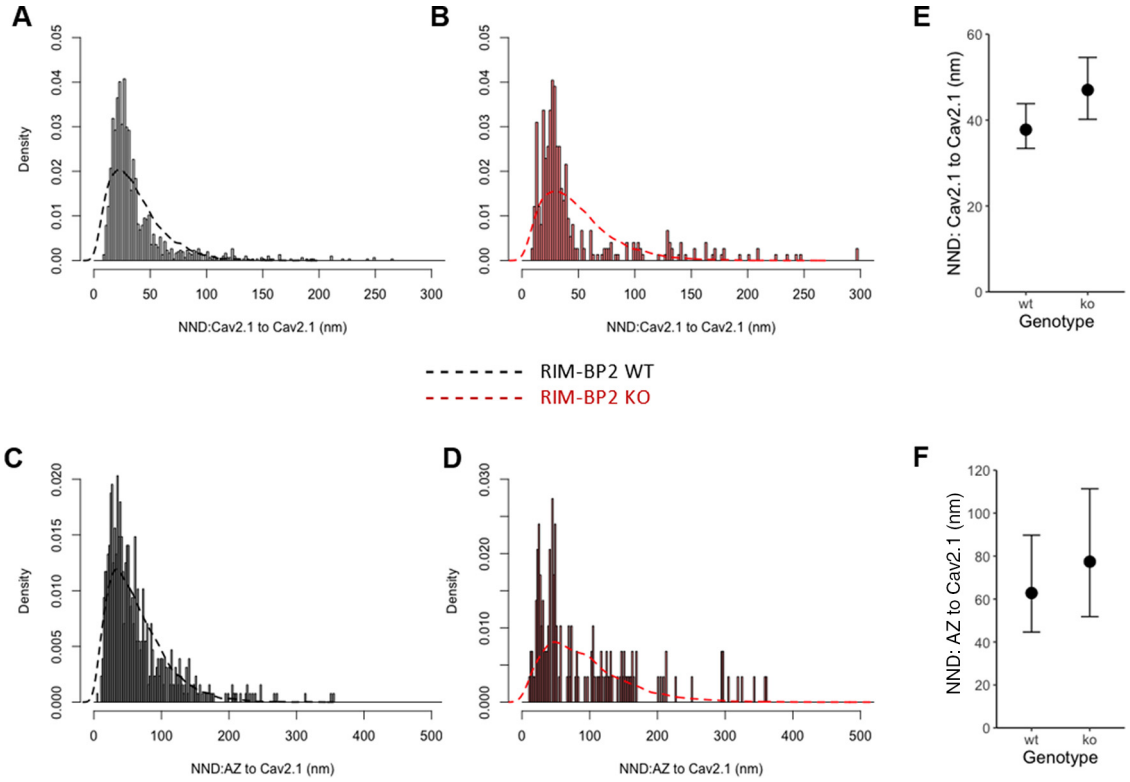

Figure 17. Altered topography of Ca_V channels relative to AZ proteins. ***A***, ***B***, Example histograms of NNDs between $Ca_V2.1$ to $Ca_V2.1$ gold particles in RIM-BP2 WT (***A***) and KO (***B***). ***C***, ***D***, Histogram of NNDs between AZ to $Ca_V2.1$ gold particles in RIM-BP2 WT (***C***) and KO (***D***). The dashed lines in (***A–D***) represent kernel density estimators of the predicted NND distributions in each genotype simulated from the hierarchical Bayesian models (see Materials and Methods). ***E***, ***F***, Marginal means of NNDs between $Ca_V2.1$ and $Ca_V2.1$ (***E***) and AZ-$Ca_V2.1$ (***F***) in WT and RIM-BP2 KO animals. Error bars indicate 95% credible intervals (CIs) of the means. For details about the statistics including mean, SEM, 95% CI, and model comparisons, see Table 6. For reference images of endbulbs as seen in the freeze fracture replica, and an analysis of PSD size, see Figure 15. For an assessment of AZ size, and labeling efficiency of AZ and $Ca_V2.1$ particles, see Figure 16. Data were from different animals within a genotype and were pooled together for the final analysis. Observed gold particle distributions were compared to 500 random simulations of gold particle distributions to ensure that the reported results did not occur by chance. For a comparison of real and simulated data, see Table 7.

non-docked SVs in more detail, we quantified the proportion of SVs in the 2- to 20-nm bin and observed a shift toward fewer SVs at mutant AZs. Whereas most of the WT (15%) AZs contained six SVs within 2–20 nm from the AZ membrane, most mutant AZs showed only two or five SVs within this distance (Fig. 18*K*). Lastly, by measuring the diameter of SVs, we found that they exhibited comparable sizes at RIM-BP2 KO and RIM-BP2 WT endbulb AZs (WT: 51.94 ± 0.55 nm; KO: 52.67 ± 0.54 nm). We conclude that RIM-BP2 contributes to normal SV docking and SV organization in close proximity to the membrane of the presynaptic AZ. These changes seem compatible with the lower number of superprimed SVs, impaired SV replenishment (Figs. 5, 7, 10) and the reduced release probability (Fig. 5).

Discussion

Priming of SVs, Ca_V function as well as the topography of Ca_V and the SV release sites at the AZ, co-determine the probability of SV release in response to the action potential invading the presynaptic terminal. Here, we probed the role of RIM-BP2, thought to serve as molecular linker between Ca_V and release sites, and alternatively in SV priming via Munc13, in synaptic transmission at the endbulb of Held synapse. Using superresolution immunofluorescence and immuno-electron microscopy we demonstrate that RIM-BP2 disruption alters the topography of $Ca_V2.1$ channels at the AZs. Electron tomography revealed fewer docked and membrane-proximal SVs at the AZ. As a physiological corollary of these structural changes, we found a reduction in the amplitude of evoked EPSCs, reduced release probability, and slowed SV replenishment to the RRP. We postulate that RIM-BP2, likely via interaction with Munc13-1, promotes a superprimed (Taschenberger et al., 2016) or tightly docked (Neher and Brose, 2018) SV state. Moreover, RIM-BP2 organizes the topography of $Ca_V2.1$ channels tightly coupling them to SV release sites.

Synaptic transmission at calyceal synapses of the lower auditory pathway shows impressive temporal fidelity. At the first central relay of the auditory pathway, co-incident transmission from endbulbs formed by ANF drives the postsynaptic BCs at hundreds of Hertz and with microsecond precision as required for time-critical neural computations such as in sound localization (Trussell, 1999; von Gersdorff and Borst, 2002). Such fidelity is enabled by synergistic adaptations on molecular, synaptic and network levels. In the mouse aVCN, BCs receive input from on average three to four endbulbs (Cao and Oertel, 2010; Butola et al., 2017) with ~400 excitatory AZs (Nicol and Walmsley, 2002; Mendoza Schulz et al., 2014; Butola et al., 2017). Endbulbs feature a large RRP (Lin et al., 2011) and high release probability (estimates range from 0.2 to 0.7: Oleskevich and Walmsley, 2002; Wang and Manis, 2005; Chanda and Xu-Friedman, 2010; Mendoza Schulz et al., 2014; Butola et al., 2017) which enable massive synchronous parallel release for powerful excitation of BCs. RIM-BP2 deletion hampers this reliable and temporally precise transmission of auditory information: firing at sound

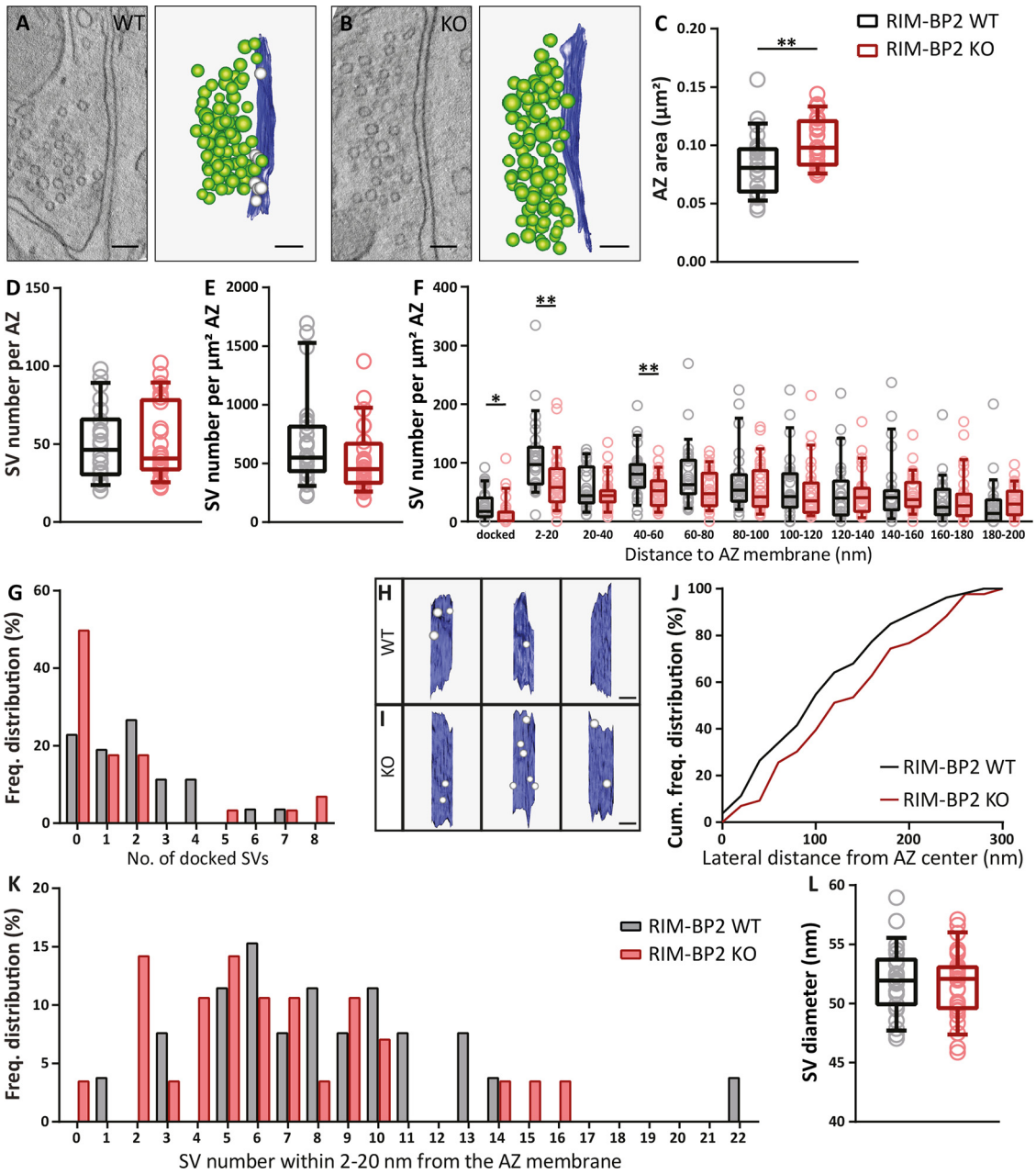

Figure 18. RIM-BP2 disruption alter the axial SV distribution at the endbulb AZs. ***A***, ***B***, Single virtual sections and corresponding models of representative tomograms of RIM-BP2 WT (***A***) and KO (***B***) AZs showing the AZ membrane (blue), SVs (green), and morphologically docked SVs (gray). Scale bars: 100 nm. ***C***, The AZ area estimated by the PSD, is significantly larger in the KO endbulb synapses; $^{**}p < 0.01$, Student's *t* test. Each data point represents the AZ area of individual synapses. ***D***, The total number of SVs is not significantly different in mutant AZs; $p > 0.05$, Student's *t* test. Each data point represents the number of SVs per AZ of individual synapses. ***E***, SV number normalized to the AZ area is not significantly altered in KO endbulb AZs; $p > 0.05$, Wilcoxon rank test. Each data point represents the number of SVs normalized to the AZ area of individual synapses. ***F***, The number of morphologically docked SVs (0–2 nm) and SVs within 200 nm from the AZ membrane normalized to the AZ area divided into 20-nm bins. The number of docked as well as SVs within 2-20 and 40-60 nm is significantly lower in mutant AZs. The number of SVs in the other bins is not significantly different.; $^{*}p < 0.05$, $^{**}p < 0.01$, Wilcoxon rank test. Each data point represents the number of SVs in each bin normalized to the AZ area of individual AZs. ***G***, Frequency distribution of the number of morphologically docked SVs. ***H***, ***I***, Top views of representative tomogram models of RIM-BP2 WT (***H***) and KO (***I***) AZs with docked SVs. Scale bars: 100 nm. ***J***, Cumulative distribution of the lateral distances of morphologically docked SVs to the assumed center of the reconstructed AZ. ***K***, Frequency distribution of the SV number within 2–20 nm from the AZ membrane. (***L***) Mean SV diameter is not significantly altered in mutant synapses; $p > 0.05$, Student's *t* test. Each data point represents the mean diameter of SVs of individual synapses. Box and whisker plots present median, lower/upper quartiles, 10–90th percentiles. RIM-BP2 WT ($N = 4$; $n = 26$) in black and RIM-BP2 KO ($N = 3$; $n = 28$) in red (*N*: number of animals; *n*: number of AZs). For details about mean ± SEM, median, and statistics, see Table 8.

onset was impaired both in rate and temporal precision (Fig. 8). We mainly attribute the reduced firing at sound onset (40% reduction) to the observed impairment of endbulb transmission ($EPSC_1$ amplitude reduction: 36%; Fig. 1), as the deficit in sound onset coding in RIM-BP2 KO ANF was mild (~10% reduction in peak onset firing rate; Krinner et al., 2017) and convergent ANF input to BCs is expected to alleviate consequences of impaired ANF coding for BC firing (Joris et al., 1994; Buran et al., 2010). These results from single-neuron recordings are in good agreement with previously reported auditory brainstem responses (Krinner et al., 2017), in which the amplitude reduction was lower for Wave I

(~30%) than for Wave III (~70%). Waves I and III are attributed to the synchronized firing of ANFs and cochlear nucleus neurons, respectively (Melcher et al., 1996). Future studies, also employing analysis of gap detection or sound localization should evaluate the behavioral consequences of this temporal processing deficit.

Impaired transmission of sound onset information at RIM-BP2-deficient endbulbs is primarily rooted in a nearly halved initial release probability, which could be restored to WT levels on increasing Ca^{2+} influx (Fig. 10). We attribute the decreased release probability to (1) the altered topography of $Ca_V2.1$ and SVs and (2) to the impaired SV docking at RIM-BP2-deficient endbulb AZs. Whole-cell patch-clamp recordings showed normal Ca^{2+} currents in RIM-BP2-deficient endbulbs (Fig. 4) and confocal imaging of $Ca_V2.1$ immunofluorescence semi-quantitatively reported a normal Ca^{2+} channel complement of the AZs (Fig. 11). This suggests that unlike ribbon synapses (Krinner et al., 2017; Luo et al., 2017), RIM-BP2 is not strictly required for establishing a normal presynaptic Ca_V complement at the endbulb of Held synapse. However, both, FRIL and STED imaging of immunolabeled $Ca_V2.1$ channels revealed an impaired clustering of $Ca_V2.1$ at RIM-BP2-deficient endbulb AZs. The number and density of $Ca_V2.1$ immunogold particles was reduced at the AZs (Table 6). Nonetheless, distribution of the $Ca_V2.1$ immunogold particles was significantly different from random, likely reflecting the presynaptic Ca_V organization by other multidomain proteins of the AZ such as RIMs (Han et al., 2011; Kaeser et al., 2011; Jung et al., 2015) and CAST (Dong et al., 2018; Hagiwara et al., 2018). Immunofluorescence of $Ca_V2.1$ as well as of Bsn (marking the presynaptic density) was less confined in space and immunofluorescent spots were more oval in shape in the absence of RIM-BP2 as compared to compact, round spots in the WT (Fig. 12, 13). The nearest neighboring immunofluorescence spot was further away both for $Ca_V2.1$ and Bsn, implying that both $Ca_V2.1$ and Bsn clusters were further apart from their respective $Ca_V2.1$ and Bsn clusters in the mutant synapses. In addition, when checking the $Ca_V2.1$ to Bsn distance, we found that the $Ca_V2.1$ clusters were further apart from the Bsn clusters in the mutant (Fig. 14), implying an increased distance between the $Ca_V2.1$ and SV release machinery marked by Bsn. In summary, our data indicate that RIM-BP2 contributes to orchestrating $Ca_V2.1$ channels at the AZ. Based on our data and in line with previous studies on other synapses (Liu et al., 2011; Acuna et al., 2015; Brockmann et al., 2020; Petzoldt et al., 2020), we hypothesize that RIM-BP2 via its interaction with $Ca_V2.1$ and AZ proteins, contributes to tight coupling of Ca^{2+} channels and vesicular release sites also at the endbulb of Held synapse. Future experimental and theoretical studies will be needed to further test this hypothesis.

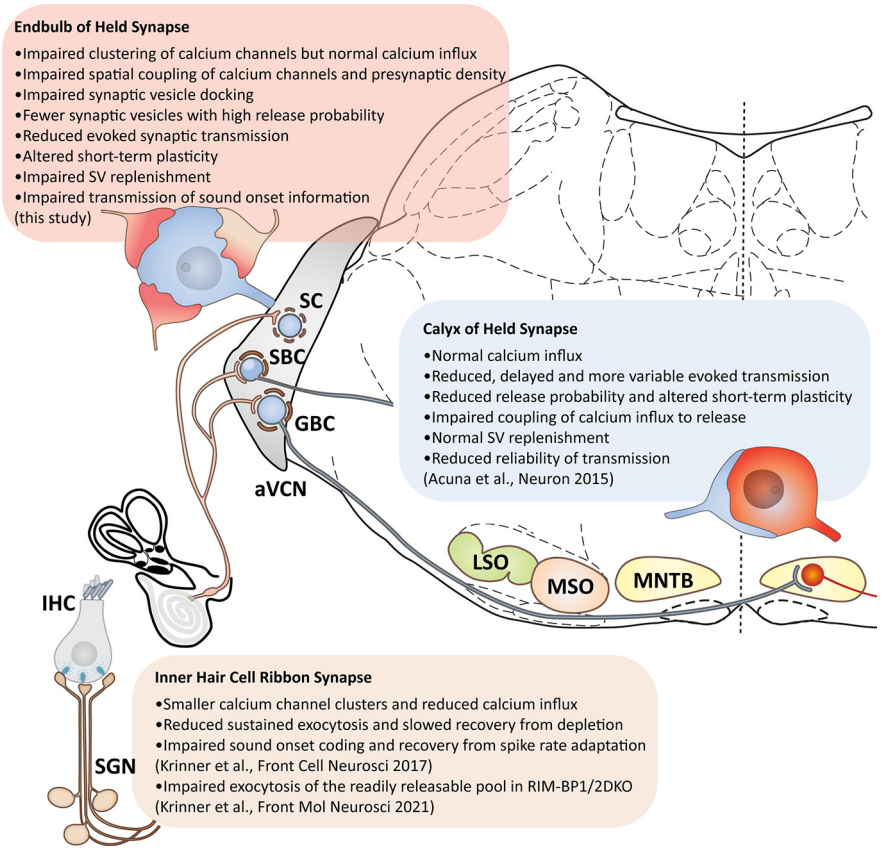

Figure 19. Compilation of findings on RIM-BP-deficient auditory synapses. RIM-BP2 is required for normal transmission at inner hair cell ribbon synapses as well as at endbulb and calyx of Held synapses. The roles of RIM-BP2 and RIM-BP1 have been addressed at the hair cell and the calyx of Held synapses, while our study focused on effects of deleting RIM-BP2 at the endbulb. The requirement for presynaptic tethering of Ca^{2+} channels seems most stringent at the hair cell synapse, but an altered localization of Ca^{2+} channels is manifested at all three synapses. Tight Ca^{2+} nanodomain coupling of Ca^{2+} channels and release ready SVs is maintained at hair cell synapses, while coupling is impaired at the calyx of Held, and this also seems to be case at the endbulb of Held. Both calyceal synapses show a major reduction in release probability, explanations of which include (1) impaired coupling of Ca^{2+} channels and release ready SVs and (2) impaired priming/docking of SVs (Fig. 18 of this study revealed a reduction of membrane proximal and docked SVs). This might relate to the interaction of RIM-BP to Munc13-1 described recently (Brockmann et al., 2020).

Recently, an alternative interaction of RIM-BP2 with the C2B domain of Munc13-1 has been reported by which RIM-BP promotes release probability via SV docking/priming (Brockmann et al., 2020). The Munc13-1 C2B domain carrying the KW mutation (Shin et al., 2010), showed the highest affinity for RIM-BP2 binding. Of note, we did not observe a reduction in Munc13-1 or in any other major AZ protein in our semi-quantitative analysis of AZs in RIM-BP2-deficient endbulbs of Held (Fig. 9). This provides confidence in attributing functional and morphologic alterations to the lack of RIM-BP2 function rather than to quantitative changes in other AZ proteins. Our functional and electron tomographic analysis of SV pool organization at RIM-BP2-deficient endbulbs now provides evidence for a role of RIM-BP in SV priming, likely via its interaction with Munc13-1. Rigorous electron tomography analysis of docking showed that the numbers of morphologically docked SVs (defined in a distance from 0 to 2 nm to the AZ membrane) were nearly halved at RIM-BP2-deficient AZs, which might represent a reduced tight docking (Neher and Brose, 2018). We speculate this to indicate that Munc13-1-mediated docking that generates primed

SVs (Siksou et al., 2009; Imig et al., 2014) partially depends on the interaction with RIM-BP2. The reduction of both docked SVs and those at a distance of 2–20 nm (membrane proximal SVs) from the plasma membrane might then suggest that the upstream loose-docking is rate limiting or less stable in the absence of RIM-BP2. An alternative explanation for retarded recovery from depression might be that RIM-BP2 facilitates release site clearance (Neher and Sakaba, 2008).

However, our analysis of pool dynamics in regular $[Ca^{2+}]_e$ indicated an unaltered RRP size despite the fact that the numbers of docked and membrane-proximal SVs were nearly halved. Interestingly, we found a trend toward a smaller RRP in RIM-BP2-deficient endbulbs when restoring release probability by enhanced Ca^{2+} influx. Despite this partial restoration, the first evoked EPSC amplitude in the absence of RIM-BP2 was still only 50% of that in the WT synapses (Fig. 10; Table 4). This persisting difference alludes to a deficit in superprimed (Fig. 5; Table 2) or tightly docked SVs (Fig. 18; Table 8). It is tempting to speculate that the impaired SV docking is uncovered under conditions that occlude the effect of altered spatial coupling of Ca^{2+} channel-release site on release probability. Our morphologic analysis of Ca^{2+} channel-release site coupling is hampered by (1) the low number of docked SVs in electron tomography and (2) the lack of information on the Ca_V position in electron tomography and of SV docking in FRIL electron micrographs. Nonetheless, there was a trend for docked SVs to be further away from the estimated AZ center, possibly reflecting a more random SV topography because of lack of RIM-BP2-mediated interaction with Ca_Vs. In addition, or alternatively, the RRP estimated by SMN/EQ analyses of responses to train stimulation might contain SVs that undergo tethering, docking and fusion during the train. Recent work by Pofantis et al. (2021), showed that deleting the presynaptic protein Mover specifically affects the high P_r component of the RRP at the Calyx of Held. eEPSC trains were analyzed with non-negative matrix factorization to reveal components representing subpools of SVs with different contributions to transmitter release during the train. Future studies that tackle how such subpools deplete and how they recover from depletion in synapses lacking both RIM-BP2 and Mover will help to further dissect the contributions of RIM-BP2 to SV superpriming and Ca_V clustering as determinants of P_r.

Exciting topics for future studies include i) the relative contributions of altered Ca^{2+} channel-release site coupling and impaired SV docking to the reduced release probability, ii) a potential contribution of release site clearance to the observed deficit in SV docking, and iii) the molecular mechanisms and structure-function relationship of SV replenishment. Our morphologic and functional experiments indicate that RIM-BP2 takes a role in tethering SVs near the plasma membrane en route to docking. Functionally, the fast, Ca^{2+}-dependent component of recovery from depression because of trains stimulation was hampered. This could reflect a lower local $[Ca^{2+}]$ because of mislocalization of $Ca_V2.1$ channels. Indeed, a key role of Ca^{2+} in regulating SV replenishment at calyceal synapses has been reported in multiple studies (Wang and Kaczmarek, 1998; Hosoi et al., 2007). Interestingly, enhancing Ca^{2+} influx by elevated $[Ca^{2+}]_e$ uncovered a reduced SV replenishment during train stimulation, which would seem to reflect a Ca^{2+} independent limitation e.g., of SV priming. Future studies on calyceal synapses of mice carrying mutations that target Ca^{2+}-dependent effects on Munc13-1 function and/or the RIM-BP2-Munc13-1 interactions by combined functional and ultrastructural analyses will be required to elucidate this intricate process. To best relate AZ structure and function, future studies will ideally employ optogenetic or electric field stimulation followed by high-pressure freezing and EM tomography (Watanabe et al., 2013; Imig et al., 2020).

References

Acuna C, Liu X, Gonzalez A, Südhof TC (2015) RIM-BPs mediate tight coupling of action potentials to Ca(2+)-triggered neurotransmitter release. Neuron 87:1234–1247.

Acuna C, Liu X, Südhof TC (2016) How to make an active zone: unexpected universal functional redundancy between RIMs and RIM-BPs. Neuron 91:792–807.

Brockmann MM, Zarebidaki F, Camacho M, Grauel MK, Trimbuch T, Südhof TC, Rosenmund C (2020) A trio of active zone proteins comprised of RIM-BPs, RIMs, and Munc13s governs neurotransmitter release. Cell Rep 32:107960.

Buerkner PC (2017) brms: an R package for Bayesian multilevel models using Stan. J Stat Softw 80:1–28.

Buran BN, Strenzke N, Neef A, Gundelfinger ED, Moser T, Liberman MC (2010) Onset coding is degraded in auditory nerve fibers from mutant mice lacking synaptic ribbons. J Neurosci 30:7587–7597.

Butola T, Wichmann C, Moser T (2017) Piccolo promotes vesicle replenishment at a fast central auditory synapse. Front Synaptic Neurosci 9:14.

Cao XJ, Oertel D (2010) Auditory nerve fibers excite targets through synapses that vary in convergence, strength, and short-term plasticity. J Neurophysiol 104:2308–2320.

Chanda S, Xu-Friedman MA (2010) A low-affinity antagonist reveals saturation and desensitization in mature synapses in the auditory brain stem. J Neurophysiol 103:1915–1926.

Dittman JS, Ryan TA (2019) The control of release probability at nerve terminals. Nat Rev Neurosci 20:177–186.

Dolphin AC, Lee A (2020) Presynaptic calcium channels: specialized control of synaptic neurotransmitter release. Nat Rev Neurosci 21:213–229.

Dong W, Radulovic T, Goral RO, Thomas C, Suarez Montesinos M, Guerrero-Given D, Hagiwara A, Putzke T, Hida Y, Abe M, Sakimura K, Kamasawa N, Ohtsuka T, Young SM (2018) CAST/ELKS proteins control voltage-gated Ca2+ channel density and synaptic release probability at a mammalian central synapse. Cell Rep 24:284–293.e6.

Elmqvist D, Quastel DM (1965) A quantitative study of end-plate potentials in isolated human muscle. J Physiol 178:505–529.

Gebhart M, Juhasz-Vedres G, Zuccotti A, Brandt N, Engel J, Trockenbacher A, Kaur G, Obermair GJ, Knipper M, Koschak A, Striessnig J (2010) Modulation of Cav1.3 Ca2+ channel gating by Rab3 interacting molecule. Mol Cell Neurosci 44:246–259.

Grauel MK, Maglione M, Reddy-Alla S, Willmes CG, Brockmann MM, Trimbuch T, Rosenmund T, Pangalos M, Vardar G, Stumpf A, Walter AM, Rost BR, Eickholt BJ, Haucke V, Schmitz D, Sigrist SJ, Rosenmund C (2016) RIM-binding protein 2 regulates release probability by fine-tuning calcium channel localization at murine hippocampal synapses. Proc Natl Acad Sci USA 113:11615–11620.

Gundelfinger ED, Fejtova A (2012) Molecular organization and plasticity of the cytomatrix at the active zone. Curr Opin Neurobiol 22:423–430.

Hagiwara A, Kitahara Y, Grabner CP, Vogl C, Abe M, Kitta R, Ohta K, Nakamura K, Sakimura K, Moser T, Nishi A, Ohtsuka T (2018) Cytomatrix proteins CAST and ELKS regulate retinal photoreceptor development and maintenance. J Cell Biol 217:3993–4006.

Han Y, Kaeser PS, Südhof TC, Schneggenburger R (2011) RIM determines Ca^{2+} channel density and vesicle docking at the presynaptic active zone. Neuron 69:304–316.

Hibino H, Pironkova R, Onwumere O, Vologodskaia M, Hudspeth AJ, Lesage F (2002) RIM - binding proteins (RBPs) couple Rab3 - interacting molecules (RIMs) to voltage - gated Ca2+ channels. Neuron 34:411–423.

Hosoi N, Sakaba T, Neher E (2007) Quantitative analysis of calcium-dependent vesicle recruitment and its functional role at the calyx of Held synapse. J Neurosci 27:14286–14298.

Imig C, Min SW, Krinner S, Arancillo M, Rosenmund C, Südhof TC, Rhee J, Brose N, Cooper BH (2014) The morphological and molecular nature of synaptic vesicle priming at presynaptic active zones. Neuron 84:416–431.

Imig C, López-Murcia FJ, Maus L, García-Plaza IH, Mortensen LS, Schwark M, Schwarze V, Angibaud J, Nägerl UV, Taschenberger H, Brose N, Cooper BH (2020) Ultrastructural imaging of activity-dependent synaptic membrane-trafficking events in cultured brain slices. Neuron 108:843–860.e8.

Isaacson JS, Walmsley B (1995) Receptors underlying excitatory synaptic transmission in slices of the rat anteroventral cochlear nucleus. J Neurophysiol 73:964–973.

Jing Z, Rutherford MA, Takago H, Frank T, Fejtova A, Khimich D, Moser T, Strenzke N (2013) Disruption of the presynaptic cytomatrix protein bassoon degrades ribbon anchorage, multiquantal release, and sound encoding at the hair cell afferent synapse. J Neurosci 33:4456–4467.

Joris PX, Carney LH, Smith PH, Yin TC (1994) Enhancement of neural synchronization in the anteroventral cochlear nucleus. I. Responses to tones at the characteristic frequency. J Neurophysiol 71:1022–1036.

Jung S, Oshima-Takago T, Chakrabarti R, Wong AB, Jing Z, Yamanbaeva G, Picher MM, Wojcik SM, Göttfert F, Predoehl F, Michel K, Hell SW, Schoch S, Strenzke N, Wichmann C, Moser T (2015) Rab3-interacting molecules 2α and 2β promote the abundance of voltage-gated CaV1.3 Ca2+ channels at hair cell active zones. Proc Natl Acad Sci USA 112:E3141–E3149.

Kaeser PS, Regehr WG (2014) Molecular mechanisms for synchronous, asynchronous, and spontaneous neurotransmitter release. Annu Rev Physiol 76:333–363.

Kaeser PS, Deng L, Wang Y, Dulubova I, Liu X, Rizo J, Südhof TC (2011) RIM proteins tether Ca2+ channels to presynaptic active zones via a direct PDZ-domain interaction. Cell 144:282–295.

Kiyonaka S, Wakamori M, Miki T, Uriu Y, Nonaka M, Bito H, Beedle AM, Mori E, Hara Y, De Waard M, Kanagawa M, Itakura M, Takahashi M, Campbell KP, Mori Y (2007) RIM1 confers sustained activity and neurotransmitter vesicle anchoring to presynaptic Ca2+ channels. Nat Neurosci 10:691–701.

Kleindienst D, Montanaro J, Bhandari P, Case MJ, Fukazawa Y, Shigemoto R (2020) Deep learning-assisted high-throughput analysis of freeze-fracture replica images applied to glutamate receptors and calcium channels at hippocampal synapses. Int J Mol Sci 21:6737.

Kremer JR, Mastronarde DN, McIntosh JR (1996) Computer visualization of three-dimensional image data using IMOD. J Struct Biol 116:71–76.

Krinner S, Butola T, Jung S, Wichmann C, Moser T (2017) RIM-binding protein 2 promotes a large number of CaV1.3 Ca2+-channels and contributes to fast synaptic vesicle replenishment at hair cell active zones. Front Cell Neurosci 11:334.

Krinner S, Predoehl F, Burfeind D, Vogl C, Moser T (2021) RIM-binding proteins are required for normal sound-encoding at afferent inner hair cell synapses. Front Mol Neurosci 14:651935.

Kruschke JK, Vanpaemel W (2015) Bayesian estimation in hierarchical models. In: The Oxford handbook of computational and mathematical psychology (BusemeyerJR, WangZ, TownsendJT, and EidelsA, eds), pp 279–299. Oxford: Oxford University Press.

Lin KH, Oleskevich S, Taschenberger H (2011) Presynaptic Ca2+ influx and vesicle exocytosis at the mouse endbulb of Held: a comparison of two auditory nerve terminals. J Physiol 589:4301–4320.

Liu KSY, Siebert M, Mertel S, Knoche E, Wegener S, Wichmann C, Matkovic T, Muhammad K, Depner H, Mettke C, Bückers J, Hell SW, Müller M, Davis GW, Schmitz D, Sigrist SJ (2011) RIM-binding protein, a central part of the active zone, is essential for neurotransmitter release. Science 334:1565–1569.

Luján R, Aguado C, Ciruela F, Cózar J, Kleindienst D, de la Ossa L, Bettler B, Wickman K, Watanabe M, Shigemoto R, Fukazawa Y (2018) Differential association of GABAB receptors with their effector ion channels in Purkinje cells. Brain Struct Funct 223:1565–1587.

Luo F, Liu X, Südhof TC, Acuna C (2017) Efficient stimulus-secretion coupling at ribbon synapses requires RIM-binding protein tethering of L-type Ca^{2+} channels. Proc Natl Acad Sci USA 114:E8081–E8090.

Mastronarde DN (2005) Automated electron microscope tomography using robust prediction of specimen movements. J Struct Biol 152:36–51.

Melcher JR, Guinan JH Jr, Knudson IM, Kiang NYS (1996) Generators of the brainstem auditory evoked potential in cat II. Correlating lesion sites with waveform changes. Hear Res 93:28–51.

Mendoza Schulz A, Jing Z, Sánchez Caro JM, Wetzel F, Dresbach T, Strenzke N, Wichmann C, Moser T (2014) Bassoon-disruption slows vesicle replenishment and induces homeostatic plasticity at a CNS synapse. EMBO J 33:512–527.

Miki T, Kaufmann WA, Malagon G, Gomez L, Tabuchi K, Watanabe M, Shigemoto R, Marty A (2017) Numbers of presynaptic Ca2+ channel clusters match those of functionally defined vesicular docking sites in single central synapses. Proc Natl Acad Sci USA 114:E5246–E5255.

Moser T, Grabner CP, Schmitz F (2020) Sensory processing at ribbon synapses in the retina and the cochlea. Physiol Rev 100:103–144.

Nakamura Y, Harada H, Kamasawa N, Matsui K, Rothman JS, Shigemoto R, Silver RA, DiGregorio DA, Takahashi T (2015) Nanoscale distribution of presynaptic Ca(2+) channels and its impact on vesicular release during development. Neuron 85:145–158.

Neher E (2015) Merits and limitations of vesicle pool models in view of heterogeneous populations of synaptic vesicles. Neuron 87:1131–1142.

Neher E, Sakaba T (2008) Multiple roles of calcium ions in the regulation of neurotransmitter release. Neuron 59:861–872.

Neher E, Brose N (2018) Dynamically primed synaptic vesicle states: key to understand synaptic short-term plasticity. Neuron 100:1283–1291.

Nicol MJ, Walmsley B (2002) Ultrastructural basis of synaptic transmission between endbulbs of Held and bushy cells in the rat cochlear nucleus. J Physiol 539:713–723.

Oleskevich S, Walmsley B (2002) Synaptic transmission in the auditory brainstem of normal and congenitally deaf mice. J Physiol 540:447–455.

Pangrsic T, Singer JH, Koschak A (2018) Voltage-gated calcium channels: key players in sensory coding in the retina and the inner ear. Physiol Rev 98:2063–2096.

Petzoldt AG, Götz TWB, Driller JH, Lützkendorf J, Reddy-Alla S, Matkovic-Rachid T, Liu S, Knoche E, Mertel S, Ugorets V, Lehmann M, Ramesh N, Beuschel CB, Kuropka B, Freund C, Stelzl U, Loll B, Liu F, Wahl MC, Sigrist SJ (2020) RIM-binding protein couples synaptic vesicle recruitment to release sites. J Cell Biol 219:e201902059.

Picher MM, Oprişoreanu AM, Jung S, Michel K, Schoch S, Moser T (2017) Rab interacting molecules 2 and 3 directly interact with the pore-forming CaV1.3 Ca2+ channel subunit and promote its membrane expression. Front Cell Neurosci 11:160.

Pofantis E, Neher E, Dresbach T (2021) Regulation of a subset of release-ready vesicles by the presynaptic protein mover. Proc Natl Acad Sci USA 118:e2022551118.

Rubio ME, Matsui K, Fukazawa Y, Kamasawa N, Harada H, Itakura M, Molnár E, Abe M, Sakimura K, Shigemoto R (2017) The number and distribution of AMPA receptor channels containing fast kinetic GluA3 and GluA4 subunits at auditory nerve synapses depend on the target cells. Brain Struct Funct 222:3375–3393.

Sakaba T, Neher E (2001) Quantitative relationship between transmitter release and calcium current at the calyx of Held synapse. J Neurosci 21:462–476.

Schlüter OM, Basu J, Südhof TC, Rosenmund C (2006) Rab3 superprimes synaptic vesicles for release: implications for short-term synaptic plasticity. J Neurosci 26:1239–1246.

Schneggenburger R, Rosenmund C (2015) Molecular mechanisms governing Ca(2+) regulation of evoked and spontaneous release. Nat Neurosci 18:935–941.

Schneggenburger R, Meyer AC, Neher E (1999) Released fraction and total size of a pool of immediately available transmitter quanta at a calyx synapse. Neuron 23:399–409.

Sclip A, Acuna C, Luo F, Südhof TC (2018) RIM-binding proteins recruit BK-channels to presynaptic release sites adjacent to voltage-gated Ca2+-channels. EMBO J 37:e98637.

Shin OH, Lu J, Rhee JS, Tomchick DR, Pang ZP, Wojcik SM, Camacho-Perez M, Brose N, Machius M, Rizo J, Rosenmund C, Südhof TC (2010) Munc13 C2B domain is an activity-dependent Ca2+ regulator of synaptic exocytosis. Nat Struct Mol Biol 17:280–288.

Siksou L, Varoqueaux F, Pascual O, Triller A, Brose N, Marty S (2009) A common molecular basis for membrane docking and functional priming of synaptic vesicles. Eur J Neurosci 30:49–56.

Strenzke N, Chakrabarti R, Al-Moyed H, Müller A, Hoch G, Pangrsic T, Yamanbaeva G, Lenz C, Pan K-T, Auge E, Geiss-Friedlander R, Urlaub H, Brose N, Wichmann C, Reisinger E (2016) Hair cell synaptic dysfunction, auditory fatigue and thermal sensitivity in otoferlin Ile515Thr mutants. EMBO J 35:2519–2535.

Südhof TC (2012) The presynaptic active zone. Neuron 75:11–25.

Taberner AM, Liberman MC (2005) Response properties of single auditory nerve fibers in the mouse. J Neurophysiol 93:557–569.

Taschenberger H, Woehler A, Neher E (2016) Superpriming of synaptic vesicles as a common basis for intersynapse variability and modulation of synaptic strength. Proc Natl Acad Sci USA 113:E4548–E4557.

Thanawala MS, Regehr WG (2013) Presynaptic calcium influx controls neurotransmitter release in part by regulating the effective size of the readily releasable pool. J Neurosci 33:4625–4633.

Trussell LO (1999) Synaptic mechanisms for coding timing in auditory neurons. Annu Rev Physiol 61:477–496.

von Gersdorff H, Borst JGG (2002) Short-term plasticity at the calyx of held. Nat Rev Neurosci 3:53–64.

Walter AM, Böhme MA, Sigrist SJ (2018) Vesicle release site organization at synaptic active zones. Neurosci Res 127:3–13.

Wang LY, Kaczmarek LK (1998) High-frequency firing helps replenish the readily releasable pool of synaptic vesicles. Nature 394:384–388.

Wang Y, Manis PB (2005) Synaptic transmission at the cochlear nucleus endbulb synapse during age-related hearing loss in mice. J Neurophysiol 94:1814–1824.

Wang Y, O'Donohue H, Manis P (2011) Short-term plasticity and auditory processing in the ventral cochlear nucleus of normal and hearing-impaired animals. Hear Res 279:131–139.

Watanabe S (2010) Asymptotic equivalence of Bayes cross validation and widely applicable information criterion in singular learning theory. J Mach Learn Res 11:3571–3594.

Watanabe S, Rost BR, Camacho-Pérez M, Davis MW, Söhl-Kielczynski B, Rosenmund C, Jorgensen EM (2013) Ultrafast endocytosis at mouse hippocampal synapses. Nature 504:242–247.

Wong AB, Rutherford MA, Gabrielaitis M, Pangršič T, Göttfert F, Frank T, Michanski S, Hell S, Wolf F, Wichmann C et al. (2014) Developmental refinement of hair cell synapses tightens the coupling of Ca2+ influx to exocytosis. EMBO J 33:247–264.

Wu SH, Oertel D (1984) Intracellular injection with horseradish peroxidase of physiologically characterized stellate and bushy cells in slices of mouse anteroventral cochlear nucleus. J Neurosci 4:1577–1588.

Yang H, Xu-Friedman MA (2008) Relative roles of different mechanisms of depression at the mouse endbulb of Held. J Neurophysiol 99:2510–2521.

Yu WM, Goodrich LV (2014) Morphological and physiological development of auditory synapses. Hear Res 311:3–16.